Interpretation of Remote Sensing Data for Energy Performance Assessments of Existing Buildings

Interpretation von Fernerkundungsdaten für die energetische Bewertung von Bestandsgebäuden

Von der Fakultät für Bauingenieurwesen
der Rheinisch-Westfälischen Technischen Hochschule Aachen
zur Erlangung des akademischen Grades
eines Doktors der Ingenieurwissenschaften
genehmigte Dissertation

vorgelegt von

Philip Groesdonk geb. Gorzalka

Berichter:

Univ.-Prof. Dr.-Ing. Christoph van Treeck

Univ.-Prof. Dr.-Ing. Bernhard Hoffschmidt

Tag der mündlichen Prüfung: 03. Dezember 2024

Diese Dissertation ist auf den Internetseiten der Universitätsbibliothek online verfügbar.

Vorwort und Danksagung

Diese Dissertation wurde mir durch meine Anstellung als Doktorand am Institut für Solarforschung des Deutschen Zentrums für Luft- und Raumfahrt e. V. (DLR) in Jülich ermöglicht. Sie war Teil des durch das Bundesministerium für Wirtschaft und Energie geförderte Projekt "Gtom" (Förderkennzeichen 03ET1405A). Ich bin außerordentlich dankbar für die erstklassige Betreuung und Unterstützung, die mir in diesem Rahmen nicht nur durch meinen Doktorvater Univ.-Prof. Dr.-Ing. Bernhard Hoffschmidt und meinen Erstberichter an der Fakultät Univ.-Prof. Dr.-Ing. Christoph van Treeck, sondern auch durch Univ.-Prof. Dr.-Ing. Robert Pitz-Paal und Univ.-Prof. Dr. rer. nat. Christian Sattler zuteil wurde. Von unschätzbarem Wert war für mich die enge nicht nur fachliche Beratung und Betreuung während der gesamten Zeit, für die ich mich an dieser Stelle noch einmal ausdrücklich bei Dr. rer. nat. Jacob Estevam Schmiedt bedanken möchte. Mein herzlichen Dank gebührt außerdem apl. Prof. Dr.-Ing Jérôme Frisch für die Übernahme des Prüfungsvorsitzes im Rahmen meines Promotionsverfahrens an der RWTH Aachen.

Aufgrund der Einbettung in ein großes Forschungsprojekt liegen den Methoden und Ergebnissen, die ich in dieser Dissertation vorstelle, umfangreiche Arbeiten von Kolleginnen und Kollegen am DLR und anderen Institutionen zugrunde. Die hervorragende Zusammenarbeit bei Experimenten, in zahlreichen Gesprächen und im Rahmen von gemeinsamen Veröffentlichungen hat mir bei meiner eigenen Forschung sehr weitergeholfen bzw. sie teilweise erst ermöglicht. Die Messergebnisse für Materialeigenschaften von Baumaterialien verdanke ich zu einem großen Teil der Mitarbeit von Galina Golubeva im Rahmen ihres Praktikums am

DLR. Wichtigen Anteil am Erfolg dieser Untersuchungen hatten außerdem Stephan Dill, Resul Fener, Alexander Haas, Markus Peichl und Stefan Thurner sowie die zahlreichen Kolleginnen und Kollegen und Externen, die mir bei der Sammlung der Baumaterialproben geholfen bzw. diese zur Verfügung gestellt haben. Für die Modellierung der energetischen Eigenschaften von Gebäuden konnte ich auf Fernerkundungsdaten zurückgreifen, die aus den Arbeiten von Dirk Frommholz, Magdalena Linkiewicz und Stephan Plattner sowie Dennis Dahlke, Nan Ge, Martin Israel und Sebastian Pless hervorgingen. Ausdrücklich möchte ich mich in diesem Zusammenhang bei den drei Erstgenannten für die wertvollen Informationen über die photogrammetrische Erstellung von Punktwolken und die darauf basierende Ableitung von Gebäudegeometrien bedanken. Dank der unkomplizierten Unterstützung von Erwin Lindermeir konnte ich bei der Analyse von Infrarotbildern auf mit MODTRAN modellierte atmosphärische Parameter zurückgreifen. Die von mir genutzten Vergleichswerte für die Simulationsergebnisse am Einzelgebäude und Modellparameter im Quartier existieren nur dank der gemeinsamen Arbeit am Versuchsgebäude in Morschenich mit Virginia Gori (University College London), Dhruvkumar Patel und Christian Schorn (Solar-Institut Jülich) und an den Daten zum Testquartier in Berlin-Moabit mit Ivan Dochev (HCU Hamburg), Jacob Estevam Schmiedt und Verena Weiler (HFT Stuttgart).

Das kollegiale und freundschaftliche Umfeld im Institut für Solarforschung war für mich stets eine zusätzliche und wichtige Motivation für meine Arbeit. Geprägt wurde dies neben den unzähligen Unterhaltungen im Flur und am Mittagstisch vor allem von den vor dem pandemiebedingten Umzug ins Home Office fast täglichen und auch danach dank des hervorragenden Zusammenhalts regelmäßigen und zahlreichen Gesprächen mit meinen Mit-DoktorandInnen Kristina Blume, Benedikt Kölsch und Dhruvkumar Patel, der stets empathischen Begleitung durch meinen Gruppenleiter Björn Schiricke und dem Austausch mit den Kollegen, ohne die ich diesen meinen Weg eher nicht gefunden hätte, nämlich Eckhard Lüpfert, Arne Tiddens und ganz besonders Matthias Offergeld, in dem ich in den letzten Jahren einen sehr guten Freund gewonnen habe.

Auf die Unterstützung aller, die am DLR die Forschung von administrativer und technischer Seite unterstützen, und die ihre Arbeits- oder Freizeit in die Bereitstellung von Open-Source-Inhalten und freier Software investieren, war ich an so vielen Stellen angewiesen, dass eine Nennung hier unmöglich wäre – umso mehr bin ich dafür dankbar.

Teil meiner gewonnenen Erfahrung war auch, dass das Aufeinandertreffen von Promotionsprojekt und Privatleben sowie ab Anfang 2020 der Pandemie einige Schwierigkeiten mit sich brachte. Umso mehr bin ich glücklich über gute und langjährige Freundschaften, auf die ich mich stets verlassen kann – die quasilebenslangen mit Niklas, Nils, Philipp und Thorsten und auch alle anderen, die ich hier unerwähnt lasse. Dass meine Familie, vor allem Jana, Maike und meine Eltern Karin und Wolfgang sowie meine Schwiegereltern Marika und Frank, mich auf meinem Weg immer unterstützen und begleiten, ist für mich und war auch für das Gelingen dieser Arbeit unendlich wertvoll. Ganz besonders von Herzen danken möchte ich der wichtigsten und wunderbarsten Person in meinem Leben, meiner Frau Lara, für ihre Liebe und die tägliche Unterstützung auch in schwierigen Zeiten. Ohne dich – ohne euch – wäre ich nicht der, der ich bin, und hätte es auf diesen Weg nicht weit geschafft.

Kurzfassung

Die Nutzung von Energie in Gebäuden, insbesondere für die Beheizung, trägt wesentlich zur fortschreitenden Klimaerwärmung bei. Die dringend erforderliche Reduktion dieses Beitrags durch Gegenmaßnahmen wie die Umstellung von Energiesystemen und die Sanierung von Bestandsgebäuden geht bisher zu langsam voran. Ein Grund dafür ist fehlendes Wissen über den Zustand des Gebäudebestands. Diese Dissertation beschäftigt sich mit der Frage, wie die automatisierte Interpretation von Fernerkundungsdaten genutzt werden kann, um auf verschiedenen Skalen energetische Gebäudesimulationsmodelle zu erstellen bzw. zu verbessern. Für die Quartiersebene wird anhand eines Beispielquartiers vorgestellt, wie 3D-Modelle der Gebäude die Auswertung von Luftbild-Infrarotthermographie zur Ermittlung von Oberflächentemperaturen von Fassaden und Dächern verbessern können und wie die satellitenbasierte TomoSAR-Technologie Daten über den Beheizungszustand von Dachstühlen liefern kann. Für die Anwendung an Einzelgebäuden wird anhand eines Beispielgebäudes ein Gesamtprozess aufgezeigt, der auf Basis von Bildaufnahmen aus Drohnen Wärmebedarfe und Gebäude-Wärmetransferkoeffizienten vor und nach einer potenziellen Sanierung schnell, automatisierbar und dadurch kostengünstig abschätzen kann. Zu diesem Zweck werden eine Modellierungssoftware und Open-Source-Tools zur Gebäudesimulation (weiter-)entwickelt und eine Messkampagne am Beispielgebäude nachsimuliert. Zudem sind Materialuntersuchungen Teil dieser Arbeit, die die Permittivität und thermische Eigenschaften üblicher Baustoffe miteinander in Verbindung bringt. Mit den gewonnenen Daten kann eine Methode zur Vermessung des Innenaufbaus von Wänden mit Mikrowellenradar auch Erkenntnisse über U-Werte liefern.

Abstract

Energy usage in buildings, particularly for heating, contributes significantly to ongoing global warming. The urgently required reduction of this contribution by countermeasures like energy system transformations energy retrofits of existing buildings is progressing unsatisfactorily slowly so far. This is also caused by a lack of knowledge about the conditions of the building stock. This dissertation investigates how automated interpretation approaches for remote sensing data can contribute to creating and/or improving building energy simulation models on different scales. On district level, a case study quarter is used to demonstrate how 3D building models can enhance the evaluation of aerial infrared thermography for deriving surface temperatures of façades and roofs. Additionally, TomoSAR satellite data are presented as a possible way to generate information about which attics in a quarter are heated. For application on single buildings, the methods developed for the dissertation and in the project it was associated with enable a fast, automatable, and hence inexpensive overall approach to estimate heat demands and whole building heat transfer coefficients pre- and post-retrofit from drone imagery. For this purpose, modelling software was developed, open-source tools for building energy simulation were adapted, and the approach was applied to a case study building for demonstration. The resulting model was able to reproduce the temperatures during an actual measurement campaign on the building with satisfying accuracy. Furthermore, this work comprises material investigations that connect permittivity and thermal parameters of common building materials. With the measured values, a method for identifying the interior structure of walls using microwave radar can additionally deliver insights about U-values.

Contents

List of Figures

List of Tables

List of Symbols

Constants

Symbol	Name	Value (approx.) [1]
h	Planck's constant	$6.626 \times 10^{-34}\,\mathrm{J\,s}$
k	Boltzmann's constant	$1.381 \times 10^{-23}\,\mathrm{J\,K^{-1}}$
N_A	Avogadro constant	$6.022 \times 10^{23}\,\mathrm{mol^{-1}}$
v_l	Speed of light	$299\,792\,458\,\mathrm{m\,s^{-1}}$
ε_0	Permittivity of free space	$8.854 \times 10^{-12}\,\mathrm{F\,m^{-1}}$
μ_0	Magnetic permeability of free space	$4\pi \times 10^{-7}\,\mathrm{N\,A^{-2}}$
σ	Stefan–Boltzmann constant	$5.67 \times 10^{-8}\,\mathrm{W\,m^{-2}\,K^{-4}}$

Latin Symbols

Symbol	Description	Unit
a	Thermal diffusivity	$\mathrm{m^2\,s^{-1}}$
A	Area	$\mathrm{m^2}$
C	Thermal/heat capacity	$\mathrm{J\,K^{-1}}$
c (c_p)	Specific heat capacity (at constant pressure)	$\mathrm{J\,K^{-1}\,kg^{-1}}$

Symbol	Description	Unit
d	Distance or thickness	m
F	Sky view factor	-
F_{G}	Basement air temperature correction factor	
f_{r}	Bidirectional reflection distribution function (BRDF)	sr^{-1}
h	Height	m
h	Surface coefficient of heat transfer	$\mathrm{W\,m^{-2}\,K^{-1}}$
l	Length	m
L	Radiance	$\mathrm{W\,sr^{-1}\,m^{-3}}$
M_{e}	Radiant exitance	$\mathrm{W\,m^{-2}}$
$M_{\mathrm{e},\lambda}$	Spectral radiant exitance	$\mathrm{W\,m^{-3}}$
M_{m}	Molar mass	$\mathrm{kg\,mol^{-1}}$
n	Air change rate	$\mathrm{h^{-1}}$
n	Number (quantity)	-
n	Refractive index	-
q	Heat flux	$\mathrm{W\,m^{-2}}$
$\dot{Q}$	Heat flow	J
r	Reflectance	-
R	Thermal resistance	$\mathrm{m^2\,K\,W^{-1}}$ *or* $\mathrm{K\,W^{-1}}$
s	Volumetric heat capacity	$\mathrm{J\,m^{-3}\,K^{-1}}$
S	Sensitivity	-
t	Time	s
T	Temperature (thermodynamic scale)	K
U	U-value	$\mathrm{W\,m^{-2}\,K^{-1}}$
v	Velocity	$\mathrm{m\,s^{-1}}$
V	Volume	$\mathrm{m^3}$

Greek Symbols

Symbol	Description	Unit
α	Absorptance	-
α_p	Polarisability	$\mathrm{C\,m^2\,V^{-1}}$
β	Spectral response (of a thermal camera)	-
γ	Propagation constant	-
ε	Emissivity	$\mathrm{m^2\,s^{-1}}$
ε_r	Dielectric constant	-
ε'_r	Relative permittivity	-
ε''_r	Dielectric loss factor	-
η	Number density of oscillators	
ϑ	Nadir angle	$^\circ$ *or* rad
ϑ	Temperature (empiric scale)	°C
λ	Thermal conductivity	$\mathrm{W\,m^{-1}\,K^{-1}}$
λ_w	Wavelength	m
Λ	Mean free path	m
μ_λ	Spectral extinction coefficient	$\mathrm{m^{-1}}$
μ	Magnetic permeability	$\mathrm{H\,m^{-1}}$
ρ	Density	$\mathrm{kg\,m^{-3}}$
σ	Conductivity	$\mathrm{S\,m^{-1}}$
τ	Transmittance	-
φ	Azimuth angle	$^\circ$ *or* rad
Φ'	Dissipation	W
$\Phi_{\mathrm{e},\lambda}$	Spectral radiant flux	$\mathrm{W\,m^{-1}}$
ω	Solid angle	sr
ω	Angular frequency	$\mathrm{rad\,s^{-1}}$
Ω	Hemisphere	sr

Subscripts

Symbol	Description
adj	Adjacent (room or zone)
af	Attic floor
amb	Ambient
bb	Black body
bc	Basement ceiling
bs	Black sky
cd	Conduction
comb	Combined
cv	Convection
d	Downwelled
dem	Demand
dir	Directional
e	Radiant
eq	Equivalent
f	Flight
fl	Fluid
fp	Floor plate
ftf	Floor-to-floor
h	Heating
hb	Heat bridges
i	Incidence
inf	Infiltration
int	Interior (elements)
iw	Interior wall
l	Lattice vibration
lw	Long-wave
obs	Observation

Symbol	Description
ow	Outer wall
p	Phase
pre	Pre-retrofit
rad	Radiative
r	Reflected
rt	Rooftop
s	Surface
sol	Solar
se	Exterior surface
si	Interior surface
sw	Short-wave
t	Transmission
T	Total
tr	Transparent (elements of the building envelope)
u	Upwelled
ue	Between unconditioned space and exterior
v	Ventilation
win	Window
zb	Border to neighboured zone(s)
λ	Spectral
0	Free space (vacuum)
50	50 Pa (pressure difference)

Abbreviations

Symbol	Description
AAC	Autoclaved aerated concrete

Symbol	Description
AB	Apartment block (TABULA type)
ADE	Application Domain Extension
ALKIS	Amtliches Liegenschaftskatasterinformationssystem (German digital cadastre)
API	Application programming interface
BCB	Burnt clay brick
BEM	Building energy modelling
BIM	Building information modelling
BMVBS	Bundesministerium für Verkehr, Bau und Stadtentwicklung (German Federal Ministry for Transport, Building and Urban Development)
BRDF	Bidirectional reflection distribution function
CFD	Computational fluid dynamics
CIBSE	Institution of Building Service Engineers
CSB	Calcium silicate brick
C-S-Hs	Calcium silicate hydrates
DLR	Deutsches Zentrum für Luft- und Raumfahrt e. V. (German Aerospace Center)
DSM	Digital surface model
DTM	Digital terrain model
DWD	Deutscher Wetterdienst (German Meteorological Service)
GIS	Geographic information system(s)
HR	High-rise building (TABULA type)
HTC	Heat transfer coefficient
HVAC	Heating, ventilation, and air conditioning
IDF	EnergyPlus Input Data File
IPCC	Intergovernmental Panel on Climate Change
IR	Infrared
IRT	Infrared thermography
IWU	Institut Wohnen und Umwelt

Symbol	Description
LAC	Lightweight aggregated concrete
LOA	Level of accuracy
LOAD	Level of as-is documentation (BIM term [2])
LOAG	Level of as-is geometry (BIM term [2])
LOAI	Level of as-is information (BIM term [2])
LOD	Level of detail (of CityGML models)
LOD	Level of development (of a BIM model)
LOG	Level of geometry (of a BIM model)
LOI	Level of information (of a BIM model)
LOIN	Level of information need (BIM term)
MFH	Multi-family house (TABULA type)
NIR	Near infrared
NRW	North Rhine-Westphalia (German state)
np	NumPy
RC	Resistance-capacitance
ROM	Reduced-order model (of AixLib)
SAR	Synthetic aperture radar
SFH	Single family house (TABULA type)
SHD	Specific heat demand
SHGC	Solar heat gain coefficient
SIJ	Solar-Institute Jülich
TH	Terraced house (TABULA type)
TomoSAR	SAR tomography
UAV	Unmanned aerial vehicle (“drone”)
UBEM	Urban building energy modelling
UML	Unified Modeling Language
uPVC	Unplasticised polyvinyl chloride
U-value	Overall heat transfer coefficient (thermal transmittance)
WWR	Window-wall ratio

1. Introduction

According to the European Environment Agency (EEA), a share of 35 % of energy-related emissions in the European Union is caused by the building sector, either through direct use of fossil fuels in buildings or indirectly through the production of electricity and heat [3]. Therefore, the reduction of these emissions is a key component in the fight against global warming. Eventually, no fossil fuels should be consumed for uses such as space heating or domestic hot water. Key measures to reach this goal include switching to renewable energy sources, efficiency measures on the building itself (such as insulation) and the devices and systems therein, and other options including urban planning or district heating [4].

Although new buildings are often very energy-efficient during operation, refurbishments are preferable over demolition and new construction due to embodied carbon and other reasons [5]. As a consequence, modernising the building stock is essential for reaching ambitious emission reduction goals. Kuramochi et al. [6] find that a pathway aiming at a limitation of global warming to an average temperature increase of 1.5 °C includes renovating existing buildings at a rate of 5 % per year. In the EU, the "Renovation Wave" initiative intends to substantially increase the renovation rate of currently only about 1 %. National policies have preceded and will build up on that initiative, promoting adequate energy-efficient refurbishments and the decarbonisation of heating and cooling [7].

The individual preparation of these promoted measures or the implementation of successful policies (also on local level) require reliable knowledge about the status quo of the building stock. Similar knowledge is needed for the other key measures

mentioned above, namely switching to renewable energy sources, municipal heat planning, and district heating. This thesis focuses on the potential of different remote sensing methods to provide this knowledge on different levels from single building elements to urban districts.

1.1. Research Background, Objectives, and Hypothesis

The "Building Tomograph" project was jointly conducted by the German Aerospace Center (DLR) and the Solar-Institute Jülich (SIJ) between 2016 and 2020. It comprised tests and development of measurement techniques for a fast and accurate determination of physical building parameters on single-building and district scale [8–10]. This dissertation emerged from that project and deals with the general question how remote sensing data collected through the application of the measurement techniques can be used to create and/or improve energy performance simulation models for the investigated buildings. In that context, it encompasses three main topics. Each of them covers a different scale of observation, but they are all needed to close or reduce the gap between the results of the remote sensing methods treated in the project and their applicability for energy-related building analyses:

1. the investigation of building materials to facilitate the application of microwave radar for wall structure analyses, exploring a possible relationship between permittivity and thermal parameters;
2. energy-related modelling and simulation of a single building based on remotely sensed data, applied to the case study of a single family house;
3. the interpretation of remote sensing data to collect or enhance input data for urban building energy modelling (UBEM), including an exemplary execution on a case study quarter.

In that context, the hypothesis of this dissertation is that **those remote sensing methods have the potential to be used in automatable workflows that reduce the effort to gather data about existing buildings in a quality that is sufficient to inform the decision process about measures like efficiency improvements, district heat networks, and renewable energy implementations.**

1.2. Thesis Structure

This section, in combination with Figure 1.1, gives an overview of the structure of this thesis and how its parts are related to each other, to the "Building Tomograph" research project, and to the research articles and conference contributions published during this dissertation.

Chapter 2 (Theory and State of the Art) includes the theoretical background about heat transfer, electromagnetic wave propagation, and building materials in Sections 2.1 to 2.3. Sections 2.4 to 2.6 treat the state of the art regarding building data handling, modelling, and acquisition. Their contents were partly contributed to an inter-institutional publication [11] that emerged from the *IEA EBC Annex 70* ("Building Energy Epidemiology: Analysis of real building energy use at scale") project and to the final report of *IEA EBC Annex 71* ("Building Energy Performance Assessment Based on In-situ Measurements") [12].

Chapter 3 (Project Overview, Test Sites, and Complementary Work) includes information about the "Building Tomograph" project and presents corresponding complementary research by others performed within it. It elaborates the common background of the research conducted at the two test sites: Initial evaluations of the data gathered on the case study building in Morschenich, a single-family house, were presented at the *IEA EBC Annex 70 Third Working Meeting* [13] and at the *Building Simulation 2019* conference [14]. The case study quarter in Berlin-Moabit was also used for the comparison of different UBEM methods in the previously mentioned Annex 70-related article [11].

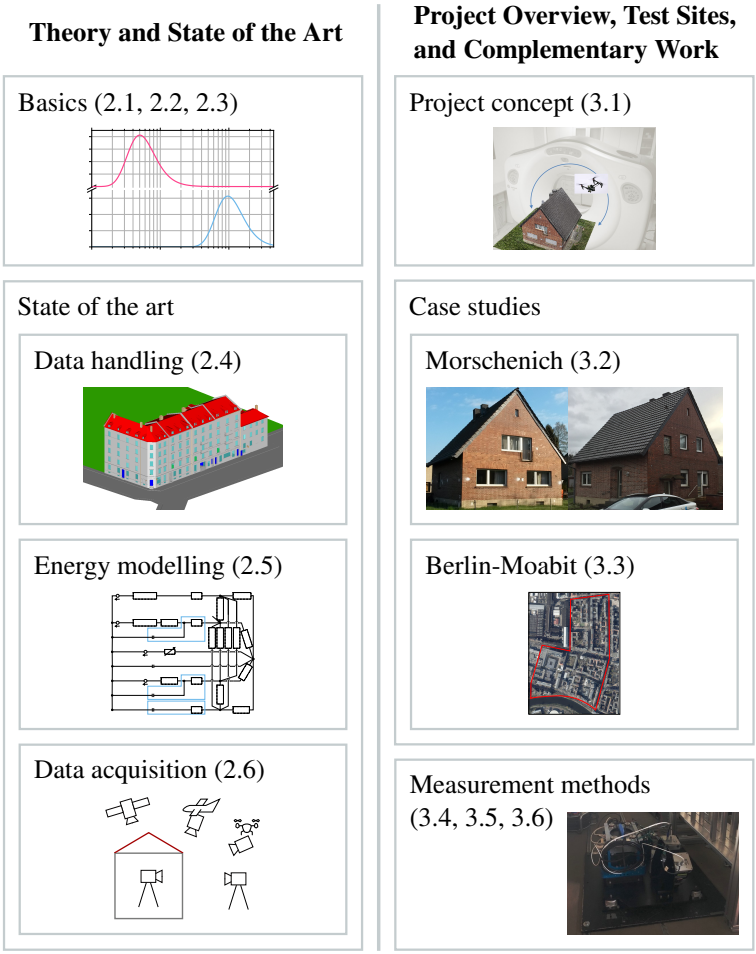

Figure 1.1.: *Overall structure of the thesis.*

Methods

Results and Discussion

Building material permittivity investigations (4.1, 5.1)

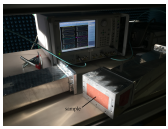

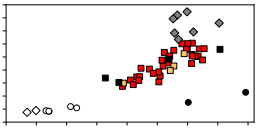

Data integration (4.2)

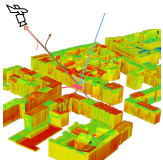

Simulation (4.3)

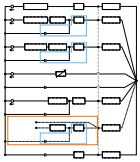

Case study results

District (5.2)

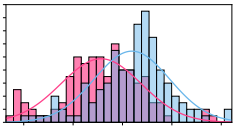

Single building (5.3)

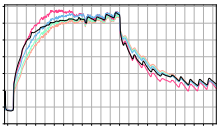

Sensitivity analysis (4.4, 5.4)

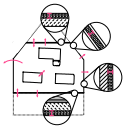

Practical relevance (5.5)

The Methods Chapter 4 explains the methodologies developed and applied as part of this dissertation. Its sections are partly mirrored by the Results and Discussion Chapter 5. Sections 4.1 and 5.1 close an important gap for making microwave radar useful for individual wall structure and thermal quality assessments. They follow the line of reasoning previously published in the *Materials and Structures* journal [15]. The other sections cover the integration of remotely sensed data into building models and the results drawn regarding energy performance assessments. This includes a common Python object model used for both single-building and district scale, the connection to simulation tools, evaluation results on the single-building and district case study, and a sensitivity analysis performed for the single-building case. Apart from the aforementioned *Energy & Buildings* article [11], the research was previously published at the *Workshop 3D-Stadtmodelle* [16], in the *Buildings* journal [17], and at the *15th International Modelica Conference* [18]. Additionally, it was used for contributions to the *Building Simulation 2021* [19] conference and to the *DGZfP DACH-Jahrestagung 2023* [20]. The Results and Discussion Chapter is wrapped up by Section 5.5 about the Practical Relevance of the methods and results of the thesis.

Chapter 6 summarises and concludes the thesis. Doing so, it treats the different scales of analysis separately, checks the results against the initial hypothesis, and gives and outlook about possible future investigations.

2. Theory and State of the Art

This chapter sums up the theory that the methods presented in this work are founded on, including the basics of temperature and heat transfer as well as of permittivity and electromagnetic wave propagation. Furthermore, for different topics related to building energy analysis, the state of the art is elaborated insofar it is relevant for the scope of this dissertation. This ranges from building material properties to building energy modelling and how data of the latter is collected, handled, and used in simulation.

2.1. Basics of Temperature and Heat Transfer

Any calculation approach that seeks to simulate the thermal behaviour of buildings is based on the physical laws of heat (and, to some extent, mass) transfer. In the following, the principles relevant for this thesis are explained, building up on Hens [21] and Hahn and Özisik [22] unless otherwise specified.

2.1.1. Temperature

For humans, an important factor of wellbeing is the temperature of their environment. Therefore and due to its interrelation with heat flows and energy consumption, it is an essential quantity in building simulation. Physically spoken, the temperature of an amount of matter is the scalar quantity describing its level

of thermodynamic energy. Among the scales with which it is quantified, the thermodynamic temperature T (in K) and the empiric temperature ϑ (in °C) are relevant here. As they have the same scaling, values can be converted through $T/[\mathrm{K}] = \vartheta/[°\mathrm{C}] + 273.15$. Higher temperatures stand for an increased kinetic energy of atoms and free electrons.

For the change in air temperature ϑ of an ideally mixed building zone as a result of heat flow, Hens [21] presents the simplified equation

$$\rho_{\mathrm{air}} \cdot c \cdot V \cdot \frac{\mathrm{d}\vartheta}{\mathrm{d}t} = \dot{Q}_{\mathrm{cv,s}} + \dot{H}_{\mathrm{inf}} + \dot{Q}_{\mathrm{g}} + \dot{Q}_{\mathrm{heating/cooling}}, \tag{2.1}$$

where ρ_{air} is the density of the air, V is the volume of the room, c is an equivalent specific heat capacity for the room covering air, furniture, and furnishing, $\dot{Q}_{\mathrm{cv,s}}$ is the heat transfer through convection from surrounding surfaces to the air, $\dot{H}_{\mathrm{inf}}$ is the enthalpy flow caused by infiltration or other air exchange, $\dot{Q}_{\mathrm{g}}$ is the convective share of internal heat gains, and $\dot{Q}_{\mathrm{heating/cooling}}$ is the convective heat flow from heating or cooling systems. The mechanisms of heat transfer are explained briefly in the following.

2.1.2. Heat Transfer

Heat is transferred through conduction, convection, or radiation. The heat flow between systems is intrinsically tied to their temperatures and can be assessed as presented in the following subsections.

Heat Transfer by Conduction

Fourier's Law

$$\boldsymbol{q}_{\mathrm{cd}} = -\lambda \cdot \nabla T \tag{2.2}$$

connects the (three-dimensional) conductive heat flux $\boldsymbol{q}_{\mathrm{cd}}$ to the gradient of temperature ∇T within a medium by means of the thermal conductivity λ, stating that the heat flux into each direction is proportional to the negative of the likewise oriented temperature gradient. As a consequence of sensible heat flow (meaning there is no phase change involved), the temperature of the medium is directly affected. Under the assumption of a constant thermal conductivity and volumetric heat capacity $s = \rho \cdot c$, the partial temporal derivative of the temperature $\partial T/\partial t$ can be connected to the divergence of its gradient

$$\nabla^2 T = \frac{\rho \cdot c}{\lambda} \cdot \frac{\partial T}{\partial t} - \frac{\Phi'}{\lambda}, \tag{2.3}$$

where ρ is the density of the medium, c is its specific heat capacity, and Φ' is the dissipation.

For application in practice, simplifications of these laws enable computational solutions in reasonable time. For example, in a single-layer one-dimensional flat assembly, the conductive heat flux q_{cd} from face 2 to face 1 in steady state can be expressed as proportional to the difference between the surface temperatures T_{s1} and T_{s2} and the layer thickness d, leading to

$$q_{\mathrm{cd}} = \lambda \cdot \frac{T_{\mathrm{s2}} - T_{\mathrm{s1}}}{d}. \tag{2.4}$$

By applying an analogy to the relationship between current and voltage difference as proportional to the resistance in an electrical circuit, the thermal resistance R of the layer is defined as

$$R = \frac{d}{\lambda}. \tag{2.5}$$

Heat Transfer by Convection

In convective heat transfer, fluids and the movement of molecules within them are involved. For the case of natural convection, the movement is interrelated with

temperature fields. Forced convection is driven by otherwise induced movement, such as wind or other imposed pressure differences. In reality, these two forms of convection are usually mixed, even though one may be dominant.

Presenting equations that describe the complex behaviour of fluids in the context of convection would be beyond the scope of this thesis. In modelling practice, the convective heat flux q_{cv} from a surface to a fluid is often described as

$$q_{\mathrm{cv}} = h_{\mathrm{cv}} \cdot \left(T_{\mathrm{fl}} - T_{\mathrm{s}}\right), \tag{2.6}$$

introducing a linear relation of the heat flux to the difference of fluid temperature T_{fl} and surface temperature T_{s} by defining the convective heat transfer coefficient h_{cv}. The coefficient accommodates the mentioned complex behaviour.

In gases like air, convective heat transfer usually dominates over conduction, which is why Equation (2.1) includes only convective heat flows.

Heat Transfer by Radiation

Via electromagnetic waves, non-connected bodies exchange heat through a transparent medium or even vacuum. The "thermal" radiation relevant for heat transfer comprises the ultraviolet (UV), the visible light, and the infrared (IR) range with wavelengths of 0.01–0.38 µm, 0.38–0.76 µm, and 0.76–10^3 µm respectively.

The background of radiative heat exchange is the emission of waves by any matter with a temperature of more than 0 K. Ideal emitters are called "black bodies". Their spectral radiant exitance $M_{\mathrm{e},\lambda,\mathrm{bb}}$ is given by Planck's law as

$$M_{\mathrm{e},\lambda,\mathrm{bb}} = \frac{2 \cdot \pi \cdot v_1^2 \cdot h \cdot \lambda_w^{-5}}{\exp\left(\frac{v_1 \cdot h}{k \cdot \lambda_w \cdot T_{\mathrm{bb}}}\right) - 1}, \tag{2.7}$$

where v_l is the speed of light, h is Planck's constant, λ_w is the wavelength, k is Boltzmann's constant, and T_{bb} is the black body's temperature. Figure 2.1 shows the spectral exitance for black bodies with ambient and with the sun's temperature over the wavelength. The graphs illustrate that bodies with higher temperature

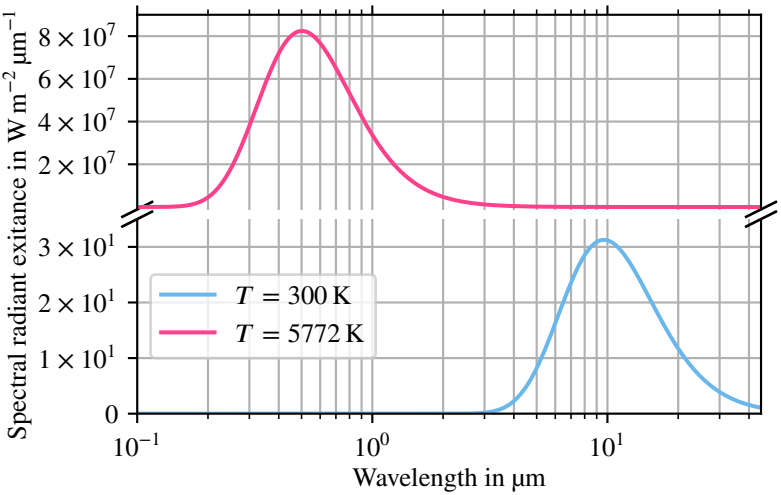

Figure 2.1.: *Spectral radiant exitance for black bodys with ambient and with the sun's temperature.*

emit more radiation. This is reflected in the Stefan-Boltzmann law

$$M_{e,bb} = \int_0^\infty M_{e,\lambda,bb}\, d\lambda_w = \sigma \cdot T_{bb}^4 \tag{2.8}$$

in which the Stefan–Boltzmann constant σ is introduced to connect the total radiant exitance $M_{e,bb}$ and the temperature. Furthermore, warmer black bodies display their maximal spectral exitance at smaller wavelengths.

Real bodies emit less radiation than black bodies. The emissivity

$$\varepsilon = M_e / M_{e,bb} \tag{2.9}$$

is defined as the quotient of the actual radiant exitance M_e and the radiant exitance of a black body at the same temperature. Kirchhoff's Law

$$\varepsilon(\lambda_w) = \alpha(\lambda_w) \tag{2.10}$$

connects the emissivity to the absorptance α. The latter quantifies the share of incident irradiance that is absorbed by a body. Yet apart from being absorbed, irradiance can also be transmitted or reflected. The law of conservation of energy leads to

$$\alpha + r + \tau = 1, \tag{2.11}$$

where r and τ are reflectance and transmittance respectively. They are defined in an analogous manner as the absorptance as shares of incident irradiance being reflected or transmitted. Likewise in general, they vary depending on the wavelength and the direction of incidence. Therefore, if α, r and τ are given as integrated values over a wavelength band and incidence directions, they describe the properties of a surface only under a particular radiative situation.

In most fluids and in transparent solids (e.g. glass), radiant flux through the medium decreases by absorption and scattering. The (spectral) linear extinction coeffient

$$\mu_\lambda(\lambda_w) = \frac{1}{\Phi_{e,\lambda}(\lambda_w)} \frac{\mathrm{d}\Phi_{e,\lambda}(\lambda_w)}{\mathrm{d}l} \tag{2.12}$$

describes the relative decrease in spectral radiant flux $\Phi_{e,\lambda}$ with respect to the propagation length l [23].

As a full spectral resolution is often impractical or impossible to model, spectral variations in the radiative behaviour of real bodies (such as building elements) are often considered separately only for short-wave (visible) and long-wave (thermal) radiation. A well-known example for the applicability of this simplification is the greenhouse effect: Glass is highly transparent for short-wave sunlight, but absorbs the long-wave thermal radiation emitted by indoor surfaces. This makes the interior temperature increase.

2.2. Permittivity and Electromagnetic Wave Propagation

To support the understanding of the part of this thesis that relates to the propagation of microwaves through building materials, some basic knowledge about electromagnetic wave propagation is summarised in this section mainly based on Ulaby and Long [24].

Electromagnetic waves are caused by travelling, time-varying, mutually induced electric and magnetic fields. Their propagation is possible with or without an underlying medium. To describe their behaviour, the constitutive parameters of the medium are the electrical permittivity $\varepsilon_r'\varepsilon_0$ which is usually written as the product of the relative permittivity $\varepsilon_r' \geq 1$ and the permittivity of free space ε_0, the magnetic permeability μ, the volume charge density, and the conductivity σ.

Permittivity measures the polarisability of a material in response to electric fields. Induced and permanent dipole moments arrange along these fields. Therefore high permittivities can be found for liquid water and other materials in which dipoles can move. Due to the different reorientation velocities of polarisation mechanisms, permittivity is generally frequency-dependent [25, p. 438].

For non-ferromagnetic materials, the magnetic permeability does not vary ($\mu = \mu_0$). In non-conducting media ($\sigma = 0$), waves propagate without loss with the phase velocity

$$v_p = \frac{1}{\sqrt{\mu \cdot \varepsilon_r'\varepsilon_0}} = \frac{v_l}{\sqrt{\varepsilon_r'}}. \tag{2.13}$$

In lossy media, the permittivity is amended by the dielectric loss factor ε_r'' to the complex dielectric constant

$$\varepsilon_r = \varepsilon_r' - j\varepsilon_r'' = \varepsilon_r' - j\frac{\sigma}{\omega \cdot \varepsilon_0}, \tag{2.14}$$

where ω is the angular frequency of the wave. The reduction of the wave magnitude is described by the propagation constant γ, a complex number that includes attenuation (in a generalised version of the extinction coefficient as defined in Equation (2.12)) and phase change. In nonmagnetic media, it can be expressed as

$$\gamma = j\omega \cdot \sqrt{\mu_0 \cdot \varepsilon_\mathrm{r}' \varepsilon_0} \cdot \left(1 - j\frac{\varepsilon_\mathrm{r}''}{\varepsilon_\mathrm{r}'}\right)^{\frac{1}{2}}. \tag{2.15}$$

Furthermore, Equation (2.13) for the phase velocity still holds. As a consequence, the permittivity is the only or most influential parameter for wave propagation in nonmagnetic media like most common building materials.

2.3. Building Materials and Their Properties

This section looks at building materials and their properties from both an empirical and a theoretical point of view. Regarding the further, it investigates the availability of measured or experiential values for material properties. The latter, which was also provided by a previous publication [15], serves to provide a basic idea of how thermal conductivity, specific heat capacity and also permittivity are related to the microstructure of four exemplary materials that will be considered in later parts of the thesis:

- **Burnt clay bricks** are made of clay, loam, sand and occasionally additional ingredients, meaning they mainly consist of aluminium silicates and silicon oxide. They are sintered at about 1000 °C, which results in a crystalline structure with small grain sizes. Porosity and, therefore, density depend on the conditions of the manufacturing process. Red bricks get their colour from a higher ratio of ferric oxide, while yellow ones have more calcium oxide. However, the concentration of both compounds is low and the colour also depends on the conditions of the sintering process [26, 27].

- **Calcium silicate bricks** (also called sand-lime bricks) are produced by hardening a mixture of burnt lime, sand and water at about 200 °C. The finished bricks consist of sand that is bound by calcium silicate hydrates (C-S-Hs), a mixture of calcium oxide, silicon oxide and water [28].
- **Autoclaved aerated concrete** is a light and comparatively new material and is, similar to calcium silicate bricks, made of burnt lime (and/or cement), fine sand and water. Before being hardened at about 200 °C, it is foamed using aluminium powder. The sand dissolves into C-S-Hs at production [27, 28].
- **Lightweight** (aggregated) **concrete** (with open or closed structure) is produced out of a light aggregate (e.g. (volcanic) pumice or blast furnace slag) bound by cement and water into a porous brick. As a result, the finished material consists of the aggregate and binding C-S-Hs [29, 30].

As a conclusion, all materials have a structure of small crystalline grains, partly also on a macroscopic scale. Some of them contain water (in C-S-Hs) and metal (in blast furnace slag). However, the macroscopic structure is unordered and like chemical composition and density depends on the (regionally different) ingredients and on the individual manufacturing process. Furthermore, all materials are at least nearly non-conducting solids (dielectrics). Electrons cannot move freely within the crystals, with the exception of potential metallic residuals in aggregates (e.g. blast furnace slag). The consequences for permittivity and thermal properties are treated in the following.

2.3.1. Permittivity

Permittivity does not only govern the propagation of microwave radar through materials, but also that of other electromagnetic radiation which is e. g. used for telecommunication signals. As a consequence, building material permittivity values

are interesting for modelling their propagation in buildings and multiple publications about the topic exist. The British broadcasting regulatory authority Ofcom published a report about radio scenarios in buildings in 2007 which includes a list of sources and a collection of values for building material permittivities extracted from them [31]. At the U.S. National Institute of Standards and Technology (NIST), a measurement system was developed and experiments were conducted with the purpose to create "a database of material permittivities for use by engineers for modeling wireless signal propagation in buildings and related applications" [32]. However, neither the database nor preliminary data could be provided by the authors on request. Safaai-Jazi et al. [33] measure the loss and dielectric constant of commonly used building materials over the 1–15 GHz frequency range. In the publication, materials are only named and not characterised further. The authors also look at the connection of dielectric constant versus frequency. While most models show a straight line with very small negative slope, the brick wall stands out with a small positive slope. The authors assume the non-homogeneity of the sample (hollow brick) as the reason, which also invalidates their results for deriving raw material properties here. Cuiñas and Sánchez [34], Muqaibel and Safaai-Jazi [35], Kubacki [36], and Ferreira et al. [37] do not only provide single values, but also treat their frequency dependence, observing low gradients and variances with few exceptions. In addition to that, single values can be found in several other sources [38–44]. Other properties of the samples, such as chemical composition or density, are hardly specified in the literature.

From a theoretical point of view, the Clausius-Mossotti equation

$$\frac{\varepsilon_\mathrm{r} - 1}{\varepsilon_\mathrm{r} + 2} = \frac{N_\mathrm{A} \cdot \rho \cdot \alpha_p}{3 \cdot M_\mathrm{m} \cdot \varepsilon_0} \tag{2.16}$$

allows for calculating the permittivity from other material parameters. Besides the Avogadro constant N_A, its application requires the knowledge of density ρ, molar mass M_m, and polarisability α_p. The equation is only valid if "individual field effects of the surrounding molecules on the particle [...] mutually cancel",

which is "reasonable [...] when the elementary particles are neutral and without permanent dipole moment, or when they are arranged either in complete disorder or in cubic or similar highly symmetrical arrays" [45, p. 20]. As the symmetrical arrays (crystals) are small in the case of the mentioned building materials, it is hard to say if the equation applies. Furthermore, values for polarisability are hardly available and grain borders and pores influence macroscopic permittivity. Nevertheless, for similarly composed materials with therefore similar molar mass and polarisability, Equation (2.16) indicates that mainly the density determines the permittivity. This suggests to build the hypothesis that a corresponding correlation may be empirically found.

2.3.2. Thermal Conductivity

Due to their importance for the assessment of the energy performance of buildings, common values for relevant thermal properties of commonly used materials are given in standards and guidelines. For example, ISO 10456 [46] and the "Environmental design" guide of the Chartered Institution of Building Service Engineers (CIBSE) [47] provide tables containing thermal conductivities and specific heat capacities. The CIBSE guide makes clear that "[p]articular masonry products can have thermal conductivities significantly lower than the corresponding values given" [47, p. 4]. Although this is not explicitly stated, an obvious reason for this approach is that engineers should design buildings conservatively and make sure that heat conductivity is not higher than specified. The values given in both sources also allow linking thermal conductivity to density. As an example, Table 2.1 shows the values provided by CIBSE for fired clay bricks.

In theory, thermal energy is transferred through the crystals as vibrations of the lattice (phonons) in the absence of free electron movement. For non-conducting solids, the thermal conductivity λ can be calculated as

$$\lambda = \frac{1}{3} \cdot (s \cdot v \cdot \Lambda)_l \tag{2.17}$$

Table 2.1.: *Thermal conductivity of homogeneous fired clay bricks at standard moisture content (1 %) provided by CIBSE [47].*

Dry density in $\mathrm{kg\,m^{-3}}$	Thermal conductivity in $\mathrm{W\,m^{-1}\,K^{-1}}$
1200	0.36
1300	0.40
1400	0.44
1500	0.47
1600	0.52
1700	0.56
1800	0.61
1900	0.66
2000	0.70

from the volumetric heat capacity s_l, the average velocity v_l and the mean free path Λ_l of the lattice vibration. s_l is related to the number density of oscillators $\eta = N_\mathrm{A} \cdot \rho \cdot M_\mathrm{m}^{-1}$ through both Dulong-Petit law and T^3 law. Additionally, the Cahill-Pohl model directly connects thermal conductivity to η [22, pp. 661–667]. Neither of these equations allows linking to polarisability or permittivity, but the connection to density stands out. Moreover, air-filled pores will decrease both density and thermal conductivity. Again, as for the permittivity, the existence of an empirically detectable correlation seems likely.

2.3.3. Correlation of Permittivity and Thermal Conductivity

The preceding theoretical explanations lead to the conclusion that both permittivity and thermal conductivity are based on different microscopic properties, but are related to the macroscopic density within building materials that are similar regarding their chemical composition and visible structure.

From literature values for the two material parameters, the presence of a correlation can hardly be tested. Although some sources for building material permittivit-

ies exist, they are usually given for whole material types. Within such single types of stones, building materials show significant ranges of thermal properties [47]. The correlation between electrical and thermal conductivity of bricks that Johnson [48] found in 1938 was proposed by Powell [49] as base for thermal conductivity measurement of dry samples. Perinelli et al. [50] present an apparatus for electrical measurement of permittivity and, thereby, thermal conductivity, but they include only four material samples over a very wide range of thermal conductivity and permittivity. As a consequence, new material measurements are required to test the hypothesis, which is done within this work.

2.4. Building Data Handling

Today, information technology has replaced paper and filing shelves for technical drawings and cadastral entries as a method to handle building data. As a result of this development, standardised approaches and formats have emerged. When it comes to civil engineering, the concept of building information modelling (BIM) is the most prominent one. Geographical information systems (GIS) also cover the built environment, but from a large-scale viewpoint. This is e.g. covered by the CityGML format. As both BIM and especially CityGML are relevant in subsequent chapters, this section introduces them and gives an overview of relevant work in the field.

2.4.1. Building Information Modelling

Historically, buildings have been built and maintained based on design drawings and, for more elaborated projects, architectural sculptures. With the recent advances in digitisation, the architecture, engineering and construction industries

also seek to profit from the associated potential increase in productivity and quality. While the use of dedicated software for technical drawings, energy simulations, and similar steps during construction projects is well established, the BIM concept is overarching and, if applied consistently, has the benefit of heavily simplifying information handover between different steps and reducing error sources [51]. According to Borrmann et al. [51, p. 4],

> [a] building information model is a comprehensive digital representation of a built facility with great information depth. It typically includes the three-dimensional geometry of the building components at a defined level of detail. In addition, it also comprises non-physical objects, such as spaces and zones, a hierarchical project structure, or schedules. Objects are typically associated with a well-defined set of semantic information, such as the component type, materials, technical properties, or costs, as well as the relationships between the components and other physical and logical entities [...]. The term Building Information Modeling (BIM) consequently describes both the process of creating such digital building models as well as the process of maintaining, using and exchanging them throughout the entire lifetime of the built facility [...].

The BIM concept encompasses all shareholders and all life cycle steps of the building, as shown in Figure 2.2, which is a version of a widespread visualisation of what BIM is designed to cover: For example, architects design the building digitally in multiple steps. They communicate with the owner, the authorities, and the actual builder using BIM interfaces during the process. After construction, as-built information is documented and facility managers and technical building services use BIM as a tool for their work. Deconstruction or refurbishment activities can be planned using BIM and profit from the information stored in the model.

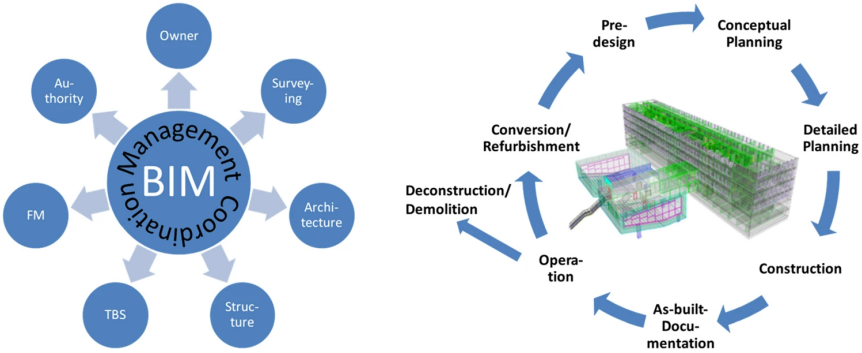

Figure 2.2.: *Shareholders (FM: facility management, TBS: technical building services) and life cycle of BIM according to Herle et al. [52].*

BIM Dimensions

The practical implementation of the concept brings multiple challenges. First, the model needs to include all information needed to fulfill the tasks that it is meant to be used for. This includes the 3D geometry that Borrmann et al. name as "[t]he most obvious feature of a Building Information Model" [51, p. 5]. Geometric objects are attributed with semantic information following the principle of object-oriented programming and can have a type (e.g. walls, doors or windows) and hold numerous other pieces of information. They can afterwards be linked to phases of the construction process, which gives the model a fourth dimension, and associated with costs for fabrication and/or purchase (5D). Additional standard dimensions are sustainability and efficiency (6D) and facility management (7D) [53, 54]. On top of these, common definitions for 8D (prevention through design [54, 55]), 9D (lean construction and total quality management [54, 56]), and 10D (industrial and modular construction [53, 57]) exist, but these definitions are not always consistently used [53]. Even mentions for 11D (monitoring) can be found in literature [58]. This huge amount of application dimensions gives an impression of the size of the second challenge: All use cases have their own information requirements, and the model needs to provide them. As a consequence, use cases

must be defined in advance as “a very important point of departure” [51, p. 6]. This preparation ensures that the data is complete and minimises the effort for creating and filling the model. For supporting the preparation process, several use cases are defined e.g. by Messner et al. [59].

Standards and Implementation

Practical implementation of BIM requires software tools (a wide range of commercial and non-commercial programs are available) and data formats for exchanging information between the people involved and the software tools used by them. Besides proprietary formats developed by different software companies, the vendor-independent standard IFC (Industry Foundation Classes) was developed by the buildingSMART association. It follows the schema defined in ISO 16739-1 [60]. Looking at standardisation, support by BIM-authoring software, and research activity, Fichter [61] comes to the conclusion that IFC is the most important open data format for exchanging geometry and semantic information in the field of building construction. Nevertheless, the huge amount and complexity of data and tasks that BIM covers, the wide range of software products used around the world, and new developments regarding e.g. computational potential, building practice, official requirements, and technical standards makes interoperability an ambitious goal. Common issues exist regarding data losses and misinterpretations when files are read by software that did not create them. However, there is no alternative to neutral formats to reach efficient data exchange for the always existing need for purpose-specific software or stakeholder-individual solutions [51].

BIM in Existing Buildings

At the time of writing, BIM is still on the way to full implementation in the industry. The rate of BIM construction projects differs from country to country [51]. However, in existing buildings, the cumbersome capture of “as-built” information

to "digitise" its status quo limits the implementation to cases in which stakeholders benefit substantially from the result, i.e. if the implementation of computer-aided facility management is desired [62]. Volk, Stengel and Schultmann [63] give a literature review over BIM in existing buildings as of 2014. In their conclusion, gathering data in the first place, updating the model, and handling uncertainties are the main challenges. The review's focus is on efficient deconstruction. In a follow-up publication, they present a system called "ResourceApp", "a hardware sensor with software modules for building information acquisition, 3D reconstruction, object detection, building inventory generation and optimized project planning" [64]. Although the results are promising for demolition project planning, the approach does not include automated BIM generation. Scherer and Katranuschkov [65] present a process called "BIMification" aimed at creating models for existing buildings and using it for retrofits. Although the article has a focus on energy issues, they name interoperability issues to energy domain tools as an important challenge. The "BIMification" idea was later implemented for a service providing automated damage identification and renovation recommendations for natural stone walls [66, 67]. Becker et al. [2] present the levels of as-is documentation (LOAD), subclassified into level of as-is geometry (LOAG), level of as-is information (LOAI), and level of accuracy (LOA). They state that different purposes in facility management have different data quality requirements and develop the LOAD system to judge as-built BIM capturing methods by the quality of their results. In the framework, LOAD has four different levels. Regarding LOAI, the authors refer to the application-specific custom property sets defined by IFC. The five levels of LOA are derived from the USIBD Level of Accuracy (LOA) Specification Guide. The framework shadows the established level of development (LOD) system that is built up from level of geometry (LOG) and level of information (LOI) [68]. It is used to compare information stored in the model with the needs for a specific application defined by the level of information need (LOIN), a process also specified (without the listed terms explicitly mentioned) in the standard EN 17412 [69, 70]. However, the publication is not very specific and mainly focuses on the generation of BIM geometry from point clouds, a topic

treated by Section 2.6 of this thesis.

BIM and Energy Analysis

Regarding energy analysis, BIM is currently "only supported by some of the established calculation programs" and although "the support is mostly limited to the geometric aspect", "the current development status is still characterized by a high error rate and interpretation problems". As of 2018, research projects aimed at "defining energy-specific data representation schemes and [...] unify[ing] them" [71, p. 345]. Practical implementation is still confronted with interoperability issues [72]. One important issue is the difference between three-dimensional construction elements and thermal boundary surfaces, which are usually located in the centre of elements that are bordered by heated rooms on both sides and on the non-heated or exterior surface otherwise [71]. Fichter [61] finds a high need for additional research regarding thermal building simulation based on BIM in his literature review and concludes from a survey among practitioners that producing suitable geometry information is the most time-consuming part of building simulation. As a contribution to a future reduction of these efforts, he develops a method (IFC2SB) to enrich IFC files with automatically generated space boundaries for use in simulation. The relevance of thermal boundary surfaces and space boundaries for building energy simulation is shown in Section 2.5.1. Fichter's work contributed to the project BIM2SIM by RWTH Aachen University and Rud. Otto Meyer Technik GmbH & Co. KG [73]. The project led to the development of a library to convert BIM models in the IFC format to models for building performance simulation (BPS), heating, ventilation and air conditioning (HVAC), computational fluid dynamics (CFD), and life cycle assessment (LCA) [74]. Two of the most important features for the BPS interface are the Modelica and Python libraries presented in Sections 2.5.3 and 2.5.4.

Relevance of BIM for the Presented Work

For the purpose of this work, the issues of collecting as-built information, combining data from different sources, and using stored information for simulation purposes are relevant and will be further discussed in the following sections. The tasks of feeding as-built data into BIM and using BIM geometry data in open-source building energy modelling software were not sufficiently covered by established tools at the time of conducting the research for this thesis. As a consequence, neither BIM tools nor data formats were applied for the research within its scope. Nevertheless, the presented methods do not rely on specific data formats, which is why they could be implemented into a BIM-based workflow in the future.

2.4.2. CityGML

Digital building models on large scale are increasingly used by public bodies for maintenance and planning purposes. For modelling cities and landscapes in 3D, i.e. for three-dimensional GIS, CityGML is internationally the most important format. It is described by the encoding standard OGC 12-019 [75]. CityGML files are plain text (XML) files. The standard definition allows them to include a wide range of information [76].

To understand the concept of CityGML, a short introduction into the underlying XML standard is given in the following based on Watson [77]. XML stands for eXtensible Markup Language and is a standard to structure plain text files that contain information. In comparison to the very popular markup language HTML (HyperText Markup Language) that many web pages are build up on, it is designed for storing and exchanging data and information rather than for presenting them. Furthermore, it is extensible regarding the pieces of information it can include. The most important way for storing data is the use of tags. An opening tag `<tag>` and a closing tag `</tag>` enclose the information associated with it. Furthermore,

smaller pieces of data can be inserted using attributes. XML documents have to follow a strict syntax to be valid. XML schemas define obligatory and optional tags, their hierarchy, their order, and the attributes that are allowed to add. In this way, schemas are an important way to simplify data exchange between different software tools.

Figure 2.3 shows the visualisation of the "Frankfurt Street Setting" CityGML example [78]. The screenshot of an extract of its text file in Figure 2.4 is used in the following to explain the most relevant of the standard's features.

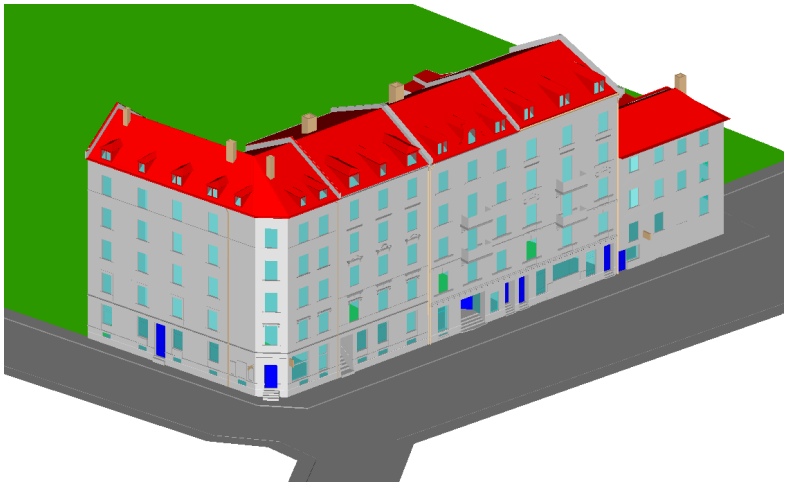

Figure 2.3.: *Visualisation of the "Frankfurt Street Setting" CityGML example dataset [78] in FZKViewer [79].*

The Frankfurt example CityGML file contains objects from the domains of buildings, transport infrastructure, and land cover as well as their appearance. Additional modules allow to model relief, bridges, tunnels, vegetation, water bodies, and city furniture [80, p. 90]. For the scope of this thesis, a focus on CityGML's building objects is sufficient. Their spatial description consists of only linear geometries, which means that triangles and more complex polygons describe areal

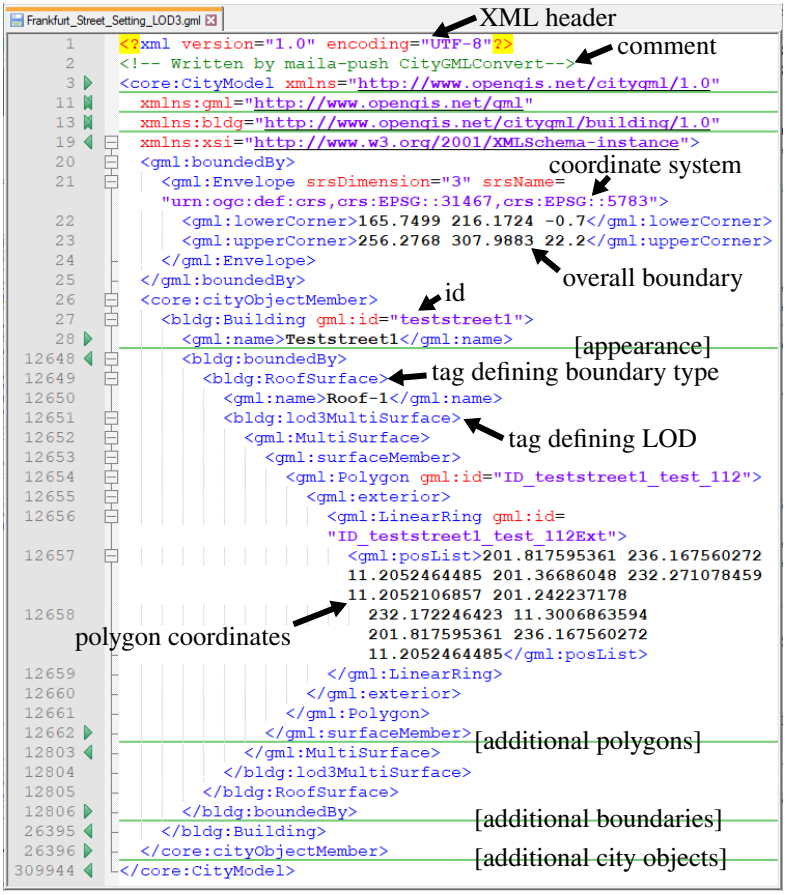

Figure 2.4.: *Screenshot of an extract from the text file of the "Frankfurt Street Setting" CityGML example [78] as visualised by Notepad++ with explanations. Bracketed descriptions stand for data in lines that were hidden for this image.*

features and a boundary representation scheme is used for volumetric geometries. One of the main features of the format is the LOD (level of detail) concept. It allows representing the same objects (even in the same file) in different complexities. A good overview of the different LODs is provided by Biljecki, Ledoux and Stoter's [81] graphic (Figure 2.5). LOD0 essentially covers footprints. LOD1

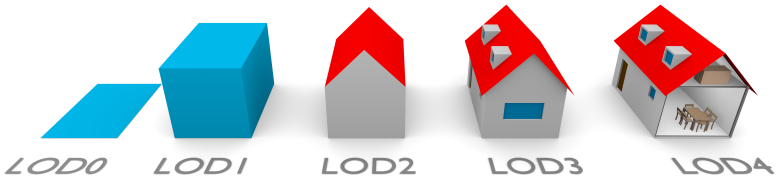

Figure 2.5.: *The five different LODs for building models in CityGML [81]. Licensed under CC BY-NC-ND 4.0.*

contains blocks (i.e. extruded footprints). LOD2 describes volumes with generalised roof shapes. LOD3 specifies volumetric models with greater architectural details including windows (as well as other openings), roof overhangs, and more façade details. Finally, LOD4 extends LOD3 with additional indoor features like rooms or furniture. The choice of LOD for a particular model depends on the availability of appropriately acquired data and the intended use [76].

In recent years, more and more three-dimensional models, in particular of buildings, were produced for cities and regions all over the world. Due to the continuous publication of new models, lists of them tend to be incomplete, but show a first picture of the widespread application of the standard [82, 83]. Model quality ranges from textured LOD3 models [84] to simple LOD1 models. In Germany, LOD2 models for the whole country exist [85]. Data quality, semantic details, and openness vary by state and even more by country [86, 87].

Application

Several domains of public and private sector activities profit from the availabilty of three-dimensional city models. For city planning purposes, the visualisation of new buildings or other projects in the existing environment, damage predictions for floods, earthquakes, and bomb defusions, traffic simulation as well as underground land administration are supported. Climate adaptation projects profit from wind and urban heat simulations. Furthermore, the simulation of noise and radio-wave propagation as well as archaeological applications can be found in the literature besides building-related tasks like floorspace analysis, building classifications, solar energy prediction, and the use case of heat demand prediction and heat load simulation that this thesis focuses on [88–90]. The topic of urban building energy simulation (UBEM) is presented in Section 2.5.5.

As it is designed to be created from measurements, its descriptive character distinguishes CityGML from the prescriptive BIM formats. As a consequence, it is less applicable for construction planning purposes, but well-suited for surface-based modelling tasks [76, 91], which the remote-sensing based methods used in this thesis require.

2.5. Building Energy Modelling and Simulation

As a consequence of the importance of energy efficiency in the built environment, a wide range of calculation approaches and tools have been developed to support owners' and public bodies' decisions regarding its improvement. Foucquier et al. [92] classify them into three categories. Physical ("white-box") models are based on measurable properties of the objects. Statistical/machine-learning ("black-box") models predict their behaviour based on training data. Hybrid ("grey-box") models are a combination of the other two. As only the application of physical models is relevant for this thesis, the reader is referred to Foucquier et al. [92] for

information on the others. An overview of white-box building energy modelling (BEM) is given below, followed by more elaborate presentations of the approaches and tools that were applied for the tasks of this thesis, and an introduction to urban building energy modelling (UBEM).

2.5.1. Physical Models

According to Foucquier et al. [92], approaches applying computational fluid dynamics (CFD) form the most complete way of thermal building simulation. The CFD technique microscopically decomposes fluid volumes into small control volumes to calculate their behaviour, including flow fields and heat transfer, in great detail. While being advantageous if airflow, pollutant transport or specific constituents of technical supply systems should be described, it has the disadvantage of huge computation times and the need for complex model implementations. A simplified description is sufficient for many applications.

The "first degree of simplification" is the zonal method, a "two-dimensional approach" that divides "each building zone into several cells" [92]. It is helpful for estimating temperature distributions in rooms, for assessing thermal comfort, and for visualising airflows. However, flow profiles need to be known in advance and the detail needed for pollutant transport or airflow prediction is not provided.

In the multizone or nodal approach, each building zone is defined as a homogeneous volume with characteristic state variables, such as temperature and air pressure. Zones and (parts of) building elements are represented by nodes with individual thermal transfer equations which may also include defined loads from sources like occupancy, technical equipment, heating or cooling. Foucquier et al. [92] consider this a "one-dimensional approach". It is employed by several popular software tools, such as the open-source program EnergyPlus [93].

In constructional practice, BIM data serves as input for calculation approaches according to technical standards in various applications around energy in build-

ings [94]. The German standard DIN V 18599-2 [95] provides a monthly energy balance method to calculate the heat demand. It has a similar spatial discretisation to the multizone approach, but lacks a fine temporal resolution (see also Section 2.5.2). However, the automatisation of standard-specific interfacing is cumbersome and may lead to errors and misinterpretations of architectural and technical information [96]. Interfaces between BIM and BEM tools are also available for more detailed simulations, such as between SketchUp and EnergyPlus using OpenStudio [97] or within Autodesk® Revit® [98]. This work instead takes advantage of the customisability of the open-source tools AixLib and TEASER described in the following, not affecting the applicability of the developed methods in practice.

2.5.2. Heat Demand Calculation Standards

As soon as energy performance requirements are part of legislation, standard methods for calculating the regulated energy demand values need to be defined. Without a standard method, performance requirements cannot be enforced. This issue is named by Pernetti, Magnani and Magrini [99] to have caused a delayed implementation of the European Energy Performance of Buildings Directive (EPBD) in Italy. The EPBD includes a mandate to develop a common framework of standards for harmonised calculations in the EU [100]. Among these standards, ISO 52016-1 defines calculation procedures for both hourly and monthly thermal balances of buildings. Doing so, it supersedes ISO 13790, which was "the first International Standard with a simple monthly calculation method for residential and non-residential buildings, to calculate both heating and cooling needs" [101, p. 7].

In Germany, the formerly used combination of the standards DIN V 4108-6 (for the building) and DIN V 4701-10 (for the heating system) was replaced by the DIN V 18599 set of standards that follow a holistic calculation principle. In this case, holistic means that after the heating or cooling demands of a conditioned

zone are calculated, energy flows caused by producing and distributing the energy to satisfy the demand may influence its amount. This circumstance changes the required energy, and both energy demand and HVAC system need to be iteratively re-calculated until the flows match. In the simplified approach of DIN V 4108-6 and DIN V 4701-10, losses in the heating system were allocated to its own energy balance and no iterations were needed [102].

The holistic calculation principle is requested by European regulation. Although it was developed based on ISO 13790 [103], DIN V 18599 does not fully match the requirements of ISO 52016-1 according to Erhorn and Jagnow [102]. Comparing the multiple national and international standards is beyond the scope of this thesis. In the following, some basics needed to understand the useful heat demand calculations performed by implementing DIN V 18599-2 [95] are introduced. For a more detailed explanation, the reader is referred to the official text of the standard and to the illustrated elaborations by Erhorn and Jagnow [102].

In DIN V 18599-2 [95], the demand for useful heat (and, similarly, the cooling demand) is calculated on a monthly basis for each zone of a building. Assuming a continuous operation of the zone, the demand

$$Q_{\mathrm{h,dem}} = Q_{\mathrm{sink}} - \eta \cdot Q_{\mathrm{source}} \tag{2.18}$$

depends on the balance of sinks and sources, where the latter is reduced by a utilisation factor η. It is calculated on a daily basis, with exterior conditions averaged for each month of the year.

The term for heat sinks

$$Q_{\mathrm{sink}} = Q_{\mathrm{t}} + Q_{\mathrm{v}} + Q_{\mathrm{int,sink}} + Q_{\mathrm{rad}} \tag{2.19}$$

sums up heat losses by transmission Q_{t} and by ventilation Q_{v} as well as internal heat sinks $Q_{\mathrm{int,sink}}$ and losses by outgoing radiation under consideration of solar gains Q_{rad}. Transmission losses are calculated for each part of the zone envelope

separately, with defined boundary conditions depending on the type of envelope element, and completed with losses due to heat bridges $\Delta Q_{\mathrm{t,hb}}$. Ventilation losses consider infiltration losses as well as air exchange due to operation, e.g. caused by opening windows or by an air handling unit.

The term for heat sources

$$Q_{\mathrm{source}} = Q_{\mathrm{sol,tr}} + Q_{\mathrm{t}} + Q_{\mathrm{v}} + Q_{\mathrm{int,source}} \tag{2.20}$$

includes the same terms for transmission and ventilation that can be found in Equation (2.19). Each contribution to the terms is calculated separately, meaning that a non-zero e.g. transmission term in both Equation (2.19) and (2.20) is possible for the same month. Solar gains through the windows Q_{s} and internal gains $Q_{\mathrm{int,source}}$ (including waste heat from the HVAC system as mentioned above) are added. The utilisation factor η in Equation 2.18 makes sure that gains do not reduce the overall heating demand to an implausible extent that could be caused by the daily and monthly aggregation.

The daily minimum or maximum interior (setpoint) temperature is an important parameter for heating and cooling demand respectively. In the case of heating demand, night setback is considered by reducing the minimum temperature depending on the monthly mean exterior temperature as well as on the time and extent of the setback.

2.5.3. AixLib's Reduced-order Model

AixLib [104] is an open-source library for building energy simulation based on the Modelica IBPSA Library [105]. It is written in Modelica, an object-oriented programming language in which not only deterministic functions, but first of all differential and algebraic equations specify models of physical systems [106]. AixLib contains a wide range of models covering heating, ventilation, and air conditioning (HVAC) equipment as well as two differently detailed thermal zone

modules, `HighOrder` and `ReducedOrder`. The development of the latter is described by Lauster [107]. As part of this thesis, the reduced-order model (ROM) of AixLib version 0.9.1 was used and expanded. Later, the changes were contributed to version 1.3.x of the library as presented in a contribution to the *15th International Modelica Conference* [18]. The corresponding paper explains the model structure and the equations governing the thermal behaviour partly in the same words as the following paragraphs.

The hierarchical concept of the ROM is visualised in Figure 2.6. A building is represented by a `Multizone` object. This object mainly serves to collect externally defined boundary conditions, such as weather data, setpoint temperatures, and internal gains as well as internally calculated quantities for use in other coupled models. Furthermore, it optionally contains a model of an air handling unit (e.g. for ventilation systems). Within the `Multizone` environment, an array of n_{zones} `ThermalZone` objects is specified. The boundary conditions are passed to these objects. Each thermal zone consists of a core resistance-capacitance (RC) module and supplementary components.

Core RC modules are available in different levels reaching from `OneElement` to `FourElement`. With decreasing number of elements, more building components (roof and floor plate, in that order) are lumped into the element for exterior walls. For the final step from `TwoElement` to `OneElement`, the inner walls, i.e. solid interior masses, are neglected. As roofs and exterior walls do not differ in their description, presenting the `ThreeElement` model is sufficient here. Figure 2.7 shows a visually adjusted version of the thermal network representation by Lauster [107].

In the network, nodes represent temperatures. If they are connected to capacities, a thermal mass with that temperature is present. Resistances govern the heat flow between temperature nodes. Some heat flows, represented by arrows in the figure, are prescribed boundary conditions. Blue-coloured boxes are parts of the network that may be repeated in a series connection. However, this feature is not used for

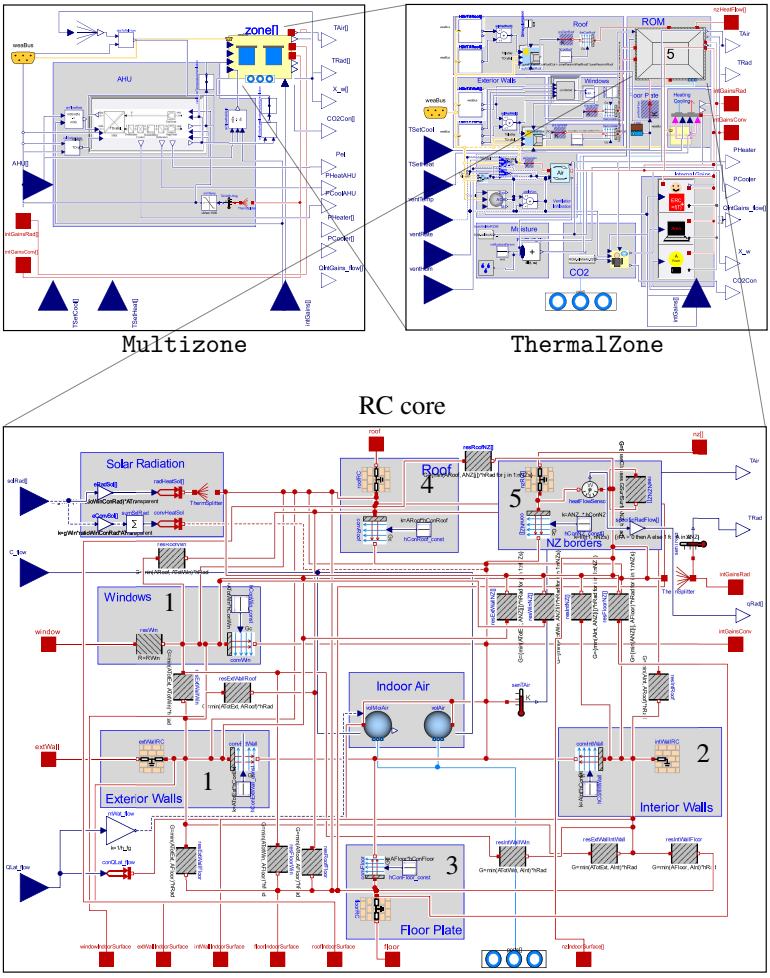

Figure 2.6.: *Visualisation of the ROM concept with the three model levels. Numbers in the RC core indicate which elements are added from* `OneElement` *up to the* `FiveElement` *model introduced as a part of this thesis [18].*

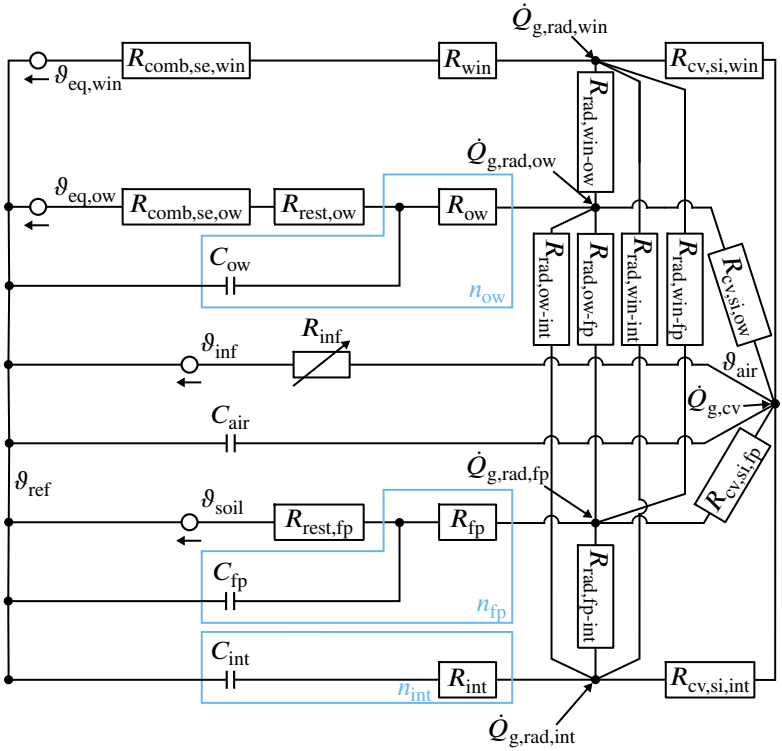

Figure 2.7.: *Thermal network representation of the AixLib* `ThreeElement` *model according to Lauster [107], visually adjusted. Other than in Equation* (2.21)*, infiltration is represented by a thermal resistance* R_{inf}.

the scope of this paper.

The centre-right node in the network represents the air inside the zone. Its energy balance equation can be written as

$$\begin{aligned}\frac{\mathrm{d}U(\vartheta_{\mathrm{air}}, p_{\mathrm{air}})}{\mathrm{d}t} &= \dot{Q}_{\mathrm{g,cv}} + n_{\mathrm{inf}} \cdot V_{\mathrm{air}} \cdot c_{p,\mathrm{air}} \cdot \rho_{\mathrm{air}} \cdot \left(\vartheta_{\mathrm{inf}} - \vartheta_{\mathrm{air}}\right) \\ &\quad + \sum_{i \in X} h_{\mathrm{cv,si},i} \cdot A_i \cdot \left(\vartheta_{\mathrm{si},i} - \vartheta_{\mathrm{air}}\right),\end{aligned} \tag{2.21}$$

where U is the inner energy of the air volume, ϑ_{air}, p_{air}, V_{air} and $c_{p,\text{air}}$ are its temperature, pressure, volume, and specific heat capacity respectively, n_{inf} is the air change rate for infiltration with temperature ϑ_{inf}, and $X = \{\text{win}, \text{ow}, \text{fp}, \text{int}\}$ is the set of heat-transferring elements i (windows, outer walls, floor plate, or interior elements) with effective area A_i, internal surface temperature $\vartheta_{\text{si},i}$ and internal surface coefficient of heat transfer $h_{\text{cv,si},i}$. $\dot{Q}_{\text{g,cv}}$ is the sum of convective heat gains, including the convective share of heat flow from solar gains through windows, heating/cooling, machines, lights, and humans. The main difference to Equation (2.1) is that the relation between temperature and inner energy is not linearised using the specific heat capacity, but modelled in greater complexity using a dedicated module for the mixing volume that includes temperature and pressure.

The impact of radiative heat transfer is calculated at all internal surfaces of the elements $i \in X$ with individual heat balances

$$\begin{aligned} 0 = {} & h_{\text{cv,si},i} \cdot A_i \cdot \left(\vartheta_{\text{air}} - \vartheta_{\text{si},i}\right) + \frac{\vartheta_{1,i} - \vartheta_{\text{si},i}}{R_{1,i}} + \frac{A_i}{\sum_{j \in X} A_j} \cdot \dot{Q}_{\text{g,rad}} \\ & + \sum_{j \in X, j \neq i} \min(A_i, A_j) \cdot h_{\text{rad}} \cdot \left(\vartheta_{\text{si},j} - \vartheta_{\text{si},i}\right), \end{aligned} \tag{2.22}$$

where h_{rad} is the (linearised and therefore approximated) radiative heat transfer coefficient for mutual direct heat transfer between all interior surfaces, $\dot{Q}_{\text{g,rad}}$ is the radiative counterpart to $\dot{Q}_{\text{g,cv}}$, and $R_{1,i}$ is the thermal resistance between the interior surface and the first capacity node of element i with temperature $\vartheta_{1,i}$. Other than in Equation (2.5), the definition of the thermal resistance in $\mathrm{K\,W^{-1}}$ used here includes the cross-sectional area of the heat-transferring element.

This leads to the description of the thermal behaviour of the elements, which is done with RC blocks. All elements but windows can store energy in n_i capacity

nodes. For $k \in \{1, \ldots, n_i\}$,

$$C_{k,i} \cdot \frac{\mathrm{d}\vartheta_{k,i}}{\mathrm{d}t} = \frac{\vartheta_{k-1,i} - \vartheta_{k,i}}{R_{k,i}} + \frac{\vartheta_{k+1,i} - \vartheta_{k,i}}{R_{k+1,i}} \tag{2.23}$$

connects the heat capacity value $C_{k,i}$ of node k and its temperature $\vartheta_{k,i}$ with the heat flows from its neighbours, including the interior ($\vartheta_{0,i} = \vartheta_{\mathrm{si},i}$) and exterior ($\vartheta_{n_i+1,i} = \vartheta_{\mathrm{se},i}$) surface. The latter drops out in the case of interior walls; so does $R_{n_i,i}$, which is denoted as $R_{\mathrm{rest},i}$ for the other elements.

For the ground plate, the exterior surface temperature is set equal to the soil temperature ($\vartheta_{\mathrm{se,fp}} = \vartheta_{\mathrm{soil}}$). For the window and outer wall elements, equivalent air temperatures $\vartheta_{\mathrm{eq},i}$ allow combining convective and radiative heat transfer into a combined surface heat transfer coefficient

$$h_{\mathrm{comb,se},i} = h_{\mathrm{cv,se},i} + h_{\mathrm{rad,se},i}, \tag{2.24}$$

such that the heat balance equation for the exterior surface becomes

$$0 = h_{\mathrm{comb,se,ow}} \cdot \left(\vartheta_{\mathrm{eq,ow}} - \vartheta_{\mathrm{se,ow}}\right) + \frac{\vartheta_{\mathrm{n_{ow},ow}} - \vartheta_{\mathrm{se,ow}}}{R_{\mathrm{rest,ow}}} \tag{2.25}$$

for the outer wall element and

$$0 = h_{\mathrm{comb,se,win}} \cdot \left(\vartheta_{\mathrm{eq,win}} - \vartheta_{\mathrm{se,win}}\right) + \frac{\vartheta_{\mathrm{si,win}} - \vartheta_{\mathrm{se,win}}}{R_{\mathrm{win}}} \tag{2.26}$$

for the window element.

The equivalent air temperatures are the sum of the ambient (dry-bulb) air temperature ϑ_{amb} and contributions from short-wave radiation $\Delta\vartheta_{\mathrm{eq,sw},i}$ and from long-wave radiation $\Delta\vartheta_{\mathrm{eq,lw},i}$:

$$\vartheta_{\mathrm{eq},i} = \vartheta_{\mathrm{amb}} + \Delta\vartheta_{\mathrm{eq,sw},i} + \Delta\vartheta_{\mathrm{eq,lw},i}. \tag{2.27}$$

For the long-wave contributions

$$\Delta\vartheta_{\mathrm{eq,lw},i} = \left(\vartheta_{\mathrm{bs}} - \vartheta_{\mathrm{amb}}\right) \cdot \frac{h_{\mathrm{rad,se},i}}{h_{\mathrm{comb,se},i}}, \tag{2.28}$$

the difference between ambient air and "black sky" temperature ϑ_{bs} as well as the ratios of the radiative and the combined surface heat transfer coeffients are taken into account. The black sky temperature is defined as the temperature of a black body that emits as much radiation as the sky (ignoring sunlight).

The total solar irradiances of the surfaces $E_{\mathrm{sol},i}$ (accounting for tilt and orientation) and their short-wave absorptances $\alpha_{\mathrm{se},i}$ are considered in the short-wave contributions

$$\Delta\vartheta_{\mathrm{eq,sw},i} = E_{\mathrm{sol},i} \cdot \frac{\alpha_{\mathrm{se},i}}{h_{\mathrm{comb,se},i}}. \tag{2.29}$$

Weather files with usually hourly resolution are used as input to fix $E_{\mathrm{sol},i}$, ϑ_{amb}, and ϑ_{bs} as boundary conditions of the model. $\vartheta_{\mathrm{soil}}$ is a fixed model parameter.

For the simulation, this means that the different zones are not interconnected, which reduces calculation complexity. In practice, the `TwoElement` model has shown to be a good trade-off between calculation times and accuracy [108]. Lumping to two elements is also suggested by VDI 6007 Part 1 [109], the standard on which the modelling approach of ROM is based.

2.5.4. TEASER

TEASER (short for "Tool for Energy Analysis and Simulation for Efficient Retrofit") [108] is a Python-written open-source software for the generation of AixLib ROM simulation models and for data enrichment in building energy models at the same time. The `logic` package of its object model is visualised in the functional universal markup language (UML) [110] diagram in Figure 2.8. In the hierarchical structure, the `project` object contains a list of `building` objects,

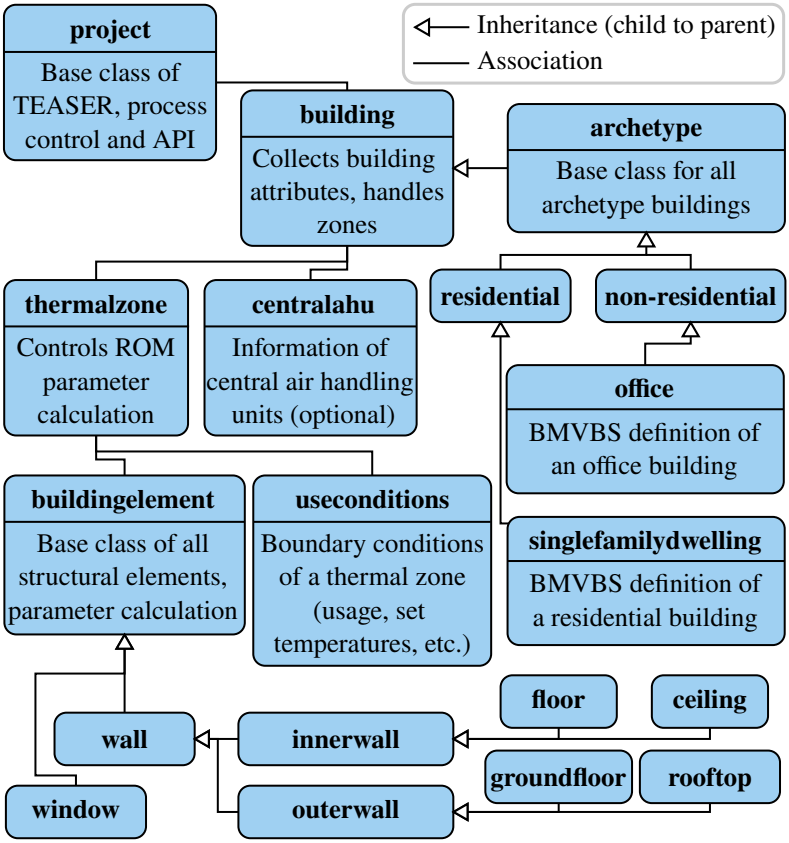

Figure 2.8.: *Functional UML diagram for the* `logic` *package of TEASER according to Remmen et al. [108] (API: Application programming interface, BMVBS: German Federal Ministry of Transport, Building and Urban Development).*

a `building` contains a list of `thermalzone` objects, a `thermalzone` contains a list of `buildingelement` objects, and a `buildingelement` contains a list of material layers (which are part of the `buildingphysics` package and therefore not in the figure). All relevant parameters are stored as attributes on an appropriate aggregation level and serve as sources for the calculation of the ROM parameters when a TEASER model instance is converted to a Modelica representation.

For the parameters of the RC modules, Lauster [107, p. 29] describes the calculation approach as based on Beuken [111], Rouvel [112], and Rouvel and Zimmermann [113]: While every wall layer is represented by T circuits in such number that a further sub-division leads to no measurable increase in accuracy in the detailed model of Beuken [111], the walls are lumped to one T circuit each in Rouvel's n-K model. In the 2-K model of Rouvel and Zimmermann [113], all walls are lumped to two equivalent elements. Here, a "T circuit" connects two thermal resistances and one capacity as defined in Equation (2.23). "K" stands for "capacity". Rouvel and Zimmermann's model with two capacities, which finds its representation in AixLib's `TwoElement` model, can also be found in the guideline VDI 6007 Part 1 [109] and is selected by Lauster [107] as base model.

According to VDI 6007 Part 1 [109], the simplification step that leads from a two-capacity module (for every single one of "all exterior building components [...] and all interior building components between rooms with differing temperatures") to a single-capacity model is valid for building components "where the thermal load occurs on one side only", but it is needed for the lumping process presented. As visualised in Figure 2.9, it does not change the values of the three resistances, but cancels out the outer capacitance C_2 by converting the value of the inner one C_1 to $C_{1,\mathrm{korr}}$. As a result, TEASER includes algorithms to parametrise a single-capacity module that covers an arbitrary number of different building elements, but also for lumping single building elements to individual two-capacity modules.

Concerning data enrichment, the `archetype` classes offer typical parameter val-

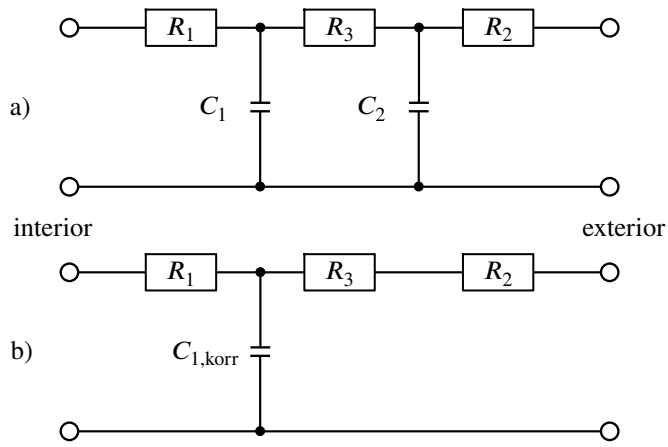

Figure 2.9.: *Simplification step from a dynamic model for a wall with two capacitances (a) to a model for the thermal response of building components with asymmetrical thermal load (b) according to VDI 6007 Part 1 [109].*

ues. The version 0.7.4 of TEASER that was used and expanded for this thesis includes more archetypes than those included in Figure 2.8. Among them are the single-family house (SFH), terraced house (TH), multi-family house (MFH) and apartment block (AB) archetypes of the German TABULA typology (see Section 2.6.4). For each building element type, the usual layer compositions of the TABULA are completed with fixed layer thicknesses and material parameters (e.g. thermal conductivity and capacity) in such a way that the U-values (thermal transmittances) of the elements match those listed in the typology. The convective coefficients of heat transfer that are necessary for U-value calculation are sourced from VDI 2078 [114] and amount to $20\,\mathrm{W\,m^{-2}\,K^{-1}}$ for exterior surfaces, $2.7\,\mathrm{W\,m^{-2}\,K^{-1}}$ for wall interior surfaces, and $1.7\,\mathrm{W\,m^{-2}\,K^{-1}}$ for rooftop and floor plate interior surfaces. The differences to the default values in ISO 6946 [115] for interior surfaces ($5.0\,\mathrm{W\,m^{-2}\,K^{-1}}$ for upward, $2.5\,\mathrm{W\,m^{-2}\,K^{-1}}$ for horizontal, and $0.7\,\mathrm{W\,m^{-2}\,K^{-1}}$ for downward heat flow) result from the necessity of coefficients that are fixed for the whole year [107, 116].

The thermal mass of the building interior is not specified in the archetypes. Instead, TEASER estimates the area of interior ceiling and floor surfaces as

$$A_{\text{ceiling}} = A_{\text{floor}} = \frac{n_{\text{floors}} - 1}{n_{\text{floors}}} \cdot A_{\text{zone}}, \tag{2.30}$$

considering the number of floors n_{floors} and the floor area of the zone A_{zone}, and of the interior wall surfaces as

$$A_{\text{iw}} = n_{\text{rooms}} \cdot h_{\text{ftf}} \cdot \left(l_{\text{room,typical}} + 2 \cdot b_{\text{room,typical}} \right), \tag{2.31}$$

where n_{rooms} is the number of rooms, h_{ftf} is the floor-to-floor height, and $l_{\text{room,typical}}$ and $b_{\text{room,typical}}$ are the typical length and width of a room respectively. Lauster [107, p. 43] defines them as depending on the usage, e.g. $l_{\text{room,typical}} = 6\,\text{m}$ and $b_{\text{room,typical}} = 3\,\text{m}$ for residential buildings. The number of rooms is derived from these measures as

$$n_{\text{rooms}} = \frac{A_{\text{zone}}}{l_{\text{room,typical}} \cdot b_{\text{room,typical}}}. \tag{2.32}$$

It is worth mentioning that the modelling simplifications lump all interior components. As a consequence, no heat flows through the centre between the two surfaces of interior slabs and walls. The respective RC block values are determined applying the aforementioned algorithms on the overall surface area associated with thermally active material of half the average actual thickness.

Having the goal to "enable the use of [building performance simulation] on urban-scale" [108], TEASER or the combination of TEASER and AixLib's ROM can be classified as a UBEM tool (see also Section 2.5.5). As a consequence, the need for low computational effort leads to a decrease in the modelling accuracy of individual buildings. Remmen et al. [108] and Lauster and Müller [117] confirm that a good accuracy is reached at an aggregated level. Combining the benefits of TEASER and AixLib with sufficient accuracy for single-building modelling based on individually acquired remote sensing data is part of this thesis.

2.5.5. Urban Building Energy Modelling

As a consequence of the need for strategies and plans aimed at reducing carbon emissions, public bodies are increasingly interested in modelling building energy use in districts or on urban scale. An example from regulatory practice is the municipal heat planning scheme developed in Denmark [118] and now included as obligatory local heating and cooling plans in the EU's revised Energy Efficiency Directive [119]. UBEM methods provide support for these tasks, helping to understand the status quo and to analyse strategies and scenarios for future development regarding their impact on the energy use [11, 120]. Recently, different methods and tools have been developed. In the following, a summary of a few bottom-up modelling approaches is given. For more information on the developments, tools and challenges in and of the field, the reader is referred to the pertinent review articles [120–124].

In an application at a research campus, the previously introduced **TEASER** and **AixLib ROM** were applied to compare simulated and measured time series for multiple buildings to check its applicability for the case of load forecasting [117]. Weak points were identified in the modelling of user profiles and temperature-independent base loads. Apart from this case, UBEM tool results are rarely cross-checked with measured time series data, although most of them are tested against reference scenarios.

DESCity

As mentioned in Section 2.5.4, TEASER is able to generate urban-scale simulation models in AixLib/Modelica, which can be used to calculate the demand for heating (and cooling, if desired) of each individual building in hourly resolution. With its enrichment features, TEASER is able to close a large part of the data availability gap that, among others, Malhotra et al. [124] identify in the youngest of the aforementioned review articles. However, building geometry needs to

be provided at the start of the TEASER-AixLib toolchain. Malhotra [125] seeks to solve this shortcoming with the development of the open-source tool collection **DESCity** (short for "District Energy Simulation using CityGML models"). It consists of six tools:

- The CityGML building interpolation tool (**CityBIT**) supports the user in developing new CityGML datasets for existing and planned buildings by either entering simple geometric and functional information or by interpolating properties of surrounding buildings.
- The CityGML analysis toolbox (**CityATB**) is able to validate CityGML files (against the XML schema), convert them between versions of the standard, and assists the user in selecting subsets of the often very large files.
- The CityGML geometrical transformation and validation tool (**CityGTV**) can validate the geometrical data stored in a file. To heal the issues found, a problem that often occurs in existing CityGML files, Malhotra points to Coors, Betz and Duminil's CityDoctor [126].
- The CityGML LOD transformation tool (**CityLDT**) makes conversions between LOD0, LOD1, and LOD2 possible. Thereby, users can bring LODs in line within a dataset or reach the LOD needed for a specific application. Necessary data for LOD increase can be entered in the process.
- The CityGML enrichment software (**CityEnrich**) allows to include information from the Energy Application Domain Extension (Energy ADE [127]) into previously purely geometric CityGML files manually.
- **TEASER+** has the same task, but provides an interface to TEASER such that TEASER models can be created from CityGML files up to LOD3 as well as re-exported as CityGML Energy ADE files or transferred to AixLib simulations models after enrichment.

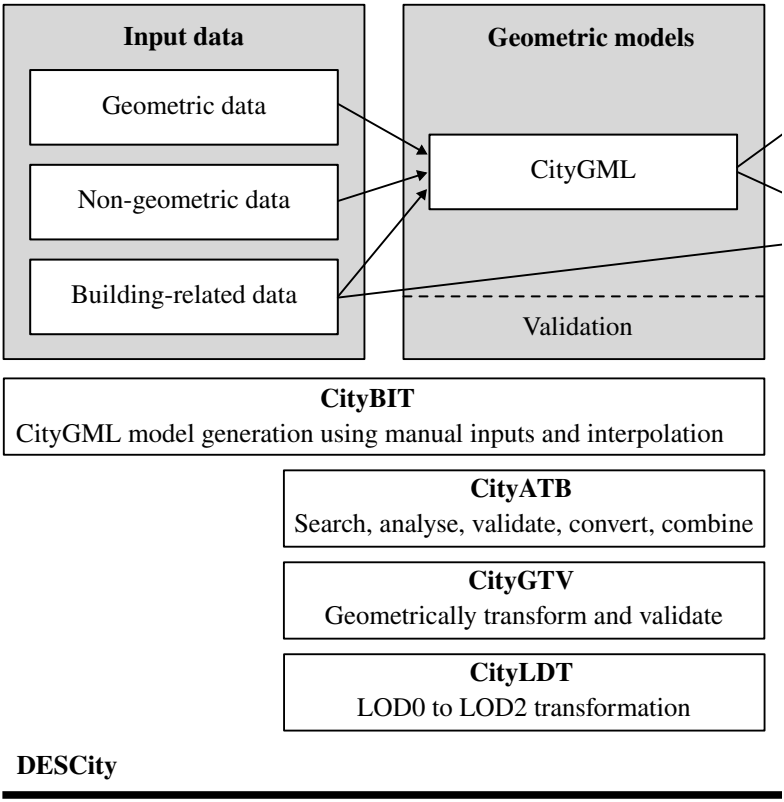

Figure 2.10.: *Overview of the tasks addressed by the tools developed for DESCity by Malhotra [125].*

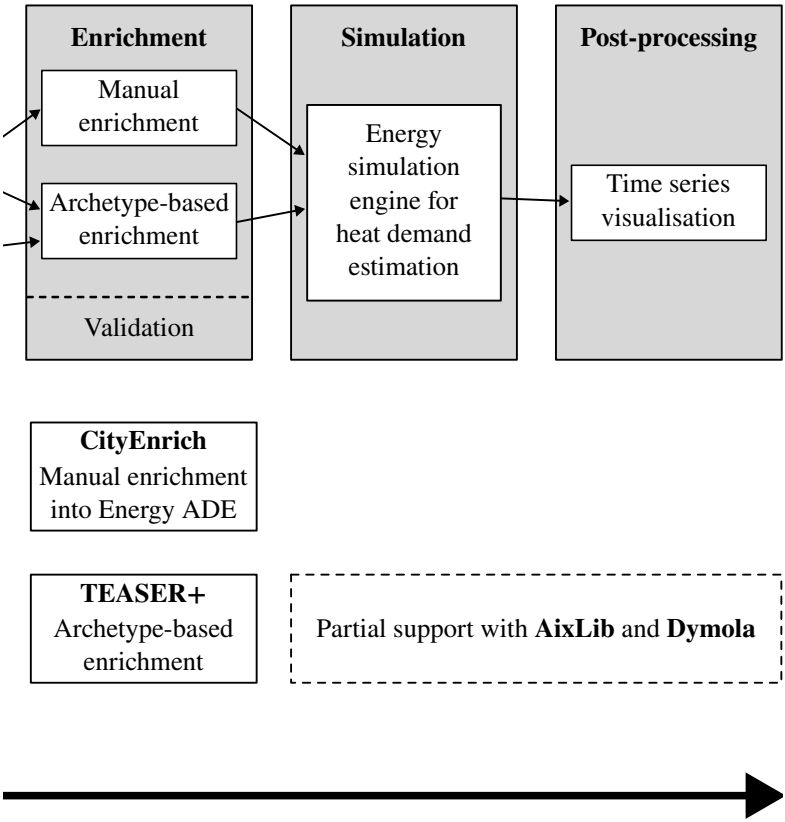
Enrichment
Manual enrichment
Archetype-based enrichment
Validation
Simulation
Energy simulation engine for heat demand estimation
Post-processing
Time series visualisation
CityEnrich
Manual enrichment into Energy ADE
TEASER+
Archetype-based enrichment
Partial support with AixLib and Dymola

Figure 2.10 shows an overview of the addressed tasks and the tools. They enable users to avoid complicated programming tasks or manual handling of enormous text files, which is why they have the potential to facilitate the adaptation of CityGML in practise. However, TEASER+ is a fork of TEASER and has not been maintained since 2021 at the time of writing [128]. Therefore, it has lost connection to recent developments of TEASER and AixLib, in particular the discontinued support for CityGML bindings [129] and the update to Modelica version 4.0.0 respectively. Nevertheless, Malhotra's exemplary application with CityGML files in the city of Hamburg shows the importance not only of the six tools for practical application, but above all of providing as much information as possible for energy simulations, especially those covered by the Energy ADE, such as thermal boundaries that differ from the outer envelope of the LOD geometry and interior thermal masses [125, 130].

Other Tools and Methods

Collected from reviews [120–123, 125] and previous inter-institutional work [11], a selection of other tools and methods for UBEM are summarised in the following.

Some of them use the building energy modelling core of **EnergyPlus**. For example, the Urban Energy Systems Lab of the Swiss Federal Laboratories for Materials Science and Technology applied their tool **CESAR** (Combined Energy Simulation and Retrofit) [131] to calculate current demand and future retrofit options in exemplary Swiss districts [132]. The City Building Energy Saver (**CityBES**) is described by its developers at the Lawrence Berkeley National Laboratory (LBNL) as "a web-based platform to support city-scale building energy efficiency" and provides an opportunity to both simulate buildings available from CityGML files in EnergyPlus and calculate possible retrofit savings [133]. EnergyPlus is also included as a simulation engine for the software development

kit **URBANopt** that aims to provide modules for the simulation of highly efficient districts, campuses, and district thermal systems during their design [134, 135].

CitySim [136] was developed at the Swiss École polytechnique fédérale de Lausanne (EPFL) "to provide a decision support for urban energy planners and stakeholders to minimize the net use of non-renewable energy sources as well as the associated emissions of greenhouse gases" [137]. The building simulations are performed with an RC model that is in most regards more complex than the `FourElement` ROM of AixLib. It was successfully tested against the Building Energy Simulation Test (BESTEST) of ASHRAE 140 [138] and experimentally verified on a campus building [139]. Data can be entered using a dedicated XML file format [137], via a graphical user interface in the free CitySim Pro version [140], and from CityGML Energy ADE files in the successor CitySim+ developed at the University of Nottingham [141].

City Energy Analyst (CEA) is "a computational framework for the analysis and optimization of energy systems in neighborhoods and city districts" [142]. Besides a model for the demand of electricity and heat (based on LOD1 geometries and calculated through a simplified RC model) [143], CEA features GIS-based renewable resource potential analysis as well as libraries of HVAC components and building archetypes of Switzerland, Singapore, and Germany. Initially based on the commercial software ArcGIS, the fully open-source tool maintained mainly by the Chair of Architecture and Building Systems of ETH Zürich now provides both a dashboard and a console for users [144].

CityBEM by Murshed, Picard and Koch [145], another open-source tool, implements ISO 13790 [146] to calculate monthly heating and cooling energy demands for 3D data imported from a CityGML dataset. It was validated against TRNSYS simulations.

The software tool **SimStadt** [147–150] builds up on LOD1 or LOD2 CityGML models, a building physics library for Germany based on the TABULA-equivalent typology of IWU (Institut Wohnen und Umwelt, see Section 2.6.4) [151], usage

libraries and weather databases. For the heat demand, a monthly energy balance according to DIN V 18599-2 [95] is applied [11].

In a more simplified method, Dochev, Seller and Peters [152] calculate heat demands from cadastral footprint areas, number of floors, and **specific heat demands** using the IWU typology for residential buildings and VDI 3807 Part 2 [153] for non-residential buildings [11].

Previous research has shown that initial data (e.g. geometry), calculation methods, and boundary conditions have a large impact on the results [11]. The two latter points call for tool developers to be transparent about their software and the assumptions it is based on, e.g. by providing open-source code. Unfortunately, this is not always the case and published studies lack reproducibility [124]. The collection of initial data has to be covered by tool users or their clients and can be very cumbersome.

Gathering Initial Data

Most of the tools listed above profit from accurate geometries and information on types and usages of the investigated buildings. In many places, cadastres provide a large share of the required data, namely footprints, types, and usages. CityGML 3D geometries are available in a growing number of regions and countries, such as in Germany, but usually in no more detail than LOD2 and often with simplified components [85, 86]. Due to missing window data, assumptions are required which have been shown to tend to overestimations of the window-wall ratio [11]. In many UBEM methods, typologies are the bridge between general information on the buildings (type, usage, age) and energy-related parameters. Another possibility for their acquisition is infrared thermography, which is covered in Section 2.6.3. Still, the varying content of available data as well as the high effort for collecting reliable input datasets remain to be open challenges [121, 123].

Malhotra [125, p. 19–23] concludes from Goy, Maréchal and Finn [154] that "obtaining the data that is adequate for computing the energy performance of buildings is always challenging at an urban scale" and identifies a set of 22 key input data categories, of which only eight are "[o]ften available in virtual 3D city models such as CityGML". As a consequence, other sources need to be found for the rest. Regarding open-access data, he finds that "the available data is generally inadequate for a precise 3D representation of individual buildings in the form of energy models".

These issues are addressed by the idea of introducing remote sensing data into UBEM, a task this thesis wants to contribute to.

2.6. Building Parameter Collection

As mentioned in previous sections and following a previously published line of reasoning [17], knowledge about certain boundary conditions as well as about the geometry and the fabric of the building is required for energy performance calculations. An assessment of individual parameters is possible, for example by blower door tests for the airtightness [155] and by heat flow sensors for the U-value of building parts [156]. In order to accomplish a reasonably low measurement effort for individual building analysis, standards and laws give room for assumptions and provide default values. For example, air exchange rates for certain situations [157] and heat conductivities of certain building materials (see Section 2.3) can be used. In Germany, the German Meteorological Service (DWD) offers representative weather data as test reference years [158]. Furthermore, the legislation allows to use "simplified measurements" and "empirical values for building parts and system components of comparable age classes" if no better knowledge about the building is available [159]. A similar approach exists as Reduced Standard Assessment Procedure (RdSAP) in the United Kingdom [160]; and simplified data

collection procedures are also part of Italian standards [99]. Although being important for keeping the effort appropriate, such simplifications cause inaccuracies that are one reason for the so-called "performance gap" between predicted demand and actual energy use [161]. Naturally, the issue also exists for UBEM with its aforementioned open challenge of data availability.

Possibilities for mitigating these inaccuracies include the improvement of conventional ways to measure and model geometry and heat loss as well as the utilisation of the heat transfer coefficient (HTC) and/or inverse modelling methods. The following sections provide introductions to these topics. Furthermore, the concept of building typologies is summarised.

2.6.1. Automation of Geometry Acquisition

The geometry of buildings is arguably one of their most important features. Floor plans and usable space values are key indicators when buildings and flats are rented and sold. On maps, building footprints are ubiquituous, and cadastral geometries have long been used as an important tool of government activities and taxation [162]. As a consequence, there are numerous methods for assessing the geometry of single buildings in detail [163] as well as of multiple buildings in a regional context [164, 165], in a wide range including yardsticks, ropes, lasers, tachymeters, three-dimensional scans, and photogrammetry. It is beyond the scope of this dissertation to give a full overview. In the following, some methods that are crucial for the context of the thesis are introduced. Section 3.4 explains the methods applied in the context of the project in greater detail.

To create accurate point cloud or mesh representations of building envelopes, authors have used terrestrial laser scans (TLS) or photogrammetry on images obtained from unmanned aerial vehicles (UAVs, also known as drones) [166–168]. From these, surfaces can be manually extracted and BIM representations can be created with the help of commercial software. Interior surface information may be

integrated from original [168] or TLS-reconstructed [169] floor plans. Although these approaches pragmatically make use of established software, the individual modelling effort is high [170]. Furthermore, the open issues in the application of BIM for energy purposes (see Section 2.4.1) call for a more direct measurement-to-BEM approach.

In UBEM, largely automated approaches for reconstruction and modelling have been developed in the face of large datasets. From remotely sensed point clouds, e.g. Frommholz et al. [171] and Malihi, Valadan Zoej and Hahn [172] reconstruct simplified geometries with semantic annotations. The former approach was used to generate important data for this dissertation on both single-building and district level and is presented in greater detail in Section 3.4. However, the most convenient way for acquiring the geometric features of UBEM models are existing databases from authorities or OpenStreetMaps [173].

2.6.2. In-situ Heat Loss Assessment and Close-range Infrared Thermography

For assessing building heat loss, several calculation-based, non-contactless, and invasive methods exist. Furthermore, infrared thermography (IRT) has been widely used for qualitative or quantitative analysis of surface temperatures and the related thermal parameters. In the following, the state of the art in close-range IRT for buildings is presented. Long-range applications are treated in Section 2.6.3. This section starts with an introduction to the former after briefly describing other methods for heat loss assessment.

In their *Review of in situ methods for assessing the thermal transmittance of walls*, Bienvenido-Huertas et al. [174] conclude:

> The theoretical estimation method [(ISO 6946 [115])] is often used in energy audits because no tests are required (the main advantage of this method) [and] because the composition of a wall can be assessed

> using various methods, such as [...] (i) endoscopy, (ii) using reliable technical documentation or databases describing the envelope of the building of interest, or (iii) using estimates based on analogous constructions.

As a consequence, this method has different disadvantages depending on its implementation. It is either (i) destructive, (ii) requires substantial a-priori knowledge that may have to be manually obtained from old plans, or (iii) is not necessarily representative for the observed building (see also Section 2.6.4). Bienvenido-Huertas et al. [174] continue:

> In situ measurements can give more representative values [...], but the use of such methods is affected by many factors, with environmental factors being the most important. In situ measurement methods require [...] (i) a high thermal gradient ($T_{in} - T_{out} > 10\,°C$), (ii) a wind speed of 0–1 $\frac{m}{s}$, (iii) zero rainfall, and (iv) no solar radiation or other radiation sources to affect the wall of interest.

The mentioned in-situ methods for U-value measurement include the heat flow meter method standardised in ISO 9869-1 [156], a simple hot-box heat flow meter method that creates a small volume with controlled temperature on one side of the wall, and a thermometric method that measures the interior surface temperature in addition to environment temperatures on both sides. All of them require the installation of measurement equipment on the walls, access to the building interior, and a measurement period of more than a day. Finally, Bienvenido-Huertas et al. [174] mention the quantitative infrared thermography (QIRT) methods. As shown in Figure 2.12, they may also be performed from the interior (e.g. in a standardised manner according to ISO 9869-2 [175]). Their implementation from the exterior enables a high variability and automatability including image acquisition from UAVs, even though the environmental requirements regarding temperature differences and gradients, wind, and solar radiation are demanding. This is also found by Patel et al. [176] in an uncertainty analysis of a practical application of

exterior QIRT. As a consequence of the dynamic nature of heat loss, Patel et al. [177] developed a dynamic method for U-value measurement from multiple IRT recordings as part of the project that this dissertation also emerged from. From other publications [20, 178, 179], it is concluded that UAV-based QIRT is currently more uncertain than using typology values. As close-range IRT results were not used for the content of this thesis, the reader is referred to the original sources for more information on the approach.

2.6.3. Long-range Aerial Infrared Thermography

For several decades, aerial IRT has been applied for mapping surface temperatures. The following explanation of physical backgrounds and state-of-the-art evaluations features parts of the contributions to an article in *Energy & Buildings* [11] and to the *DGZfP DACH-Jahrestagung 2023* [20].

Infrared thermography is commonly understood as recording thermal radiation with a camera to a pixel matrix that equals a greyscale image. Pixel values represent the amount of radiation that the sensor array has recorded at the respective spot. When measuring under exterior conditions, a band of 8–14 µm is often applied. In that range, the atmospheric influence on thermal radiation is comparatively small. Furthermore, the spectral emission peaks of black bodies between −66–90 °C makes commonly investigated objects differentiable [180].

The overview in Figure 2.12 features long-range thermography based on satellites and planes. Satellite imagery from space is sometimes applied for building analysis, but their resolution is too coarse for detailed evaluations [181]. Commercial aerial applications are used in a qualitative manner for building heat loss visualisation [182] or for leakage detection in district heating systems [183].

Quantitative evaluations of thermographic datasets require considering several influencing factors. The temperature of the pictured surface, usually being the parameter of interest, influences the measured quantity to a variable degree. According

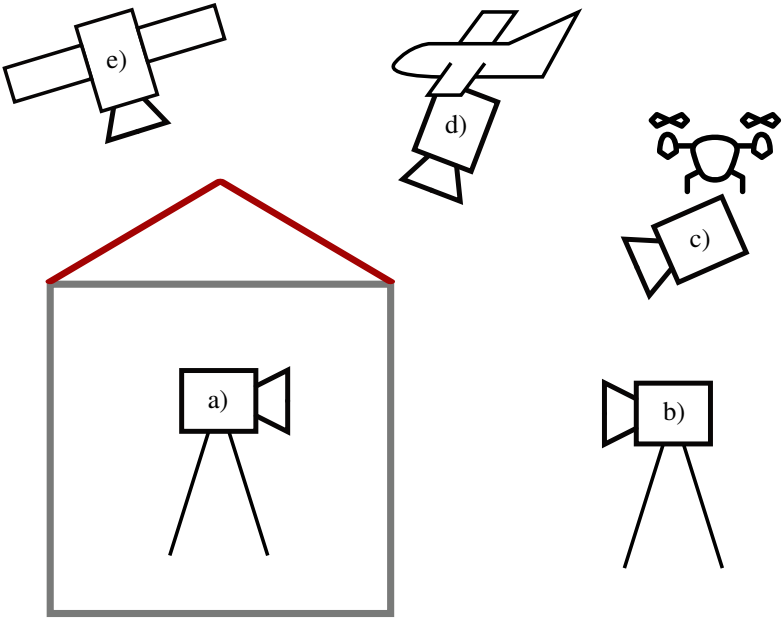

Figure 2.12.: *Different options for thermographic measurements on buildings: a) stationary (interior), b) stationary (exterior), c) UAV-based, d) aerial, e) satellite-based [20].*

to Schott, Biegel and Wilkinson [184], the radiance recorded at the sensor L is approximately equal to

$$\begin{aligned} L &= \left[\varepsilon \cdot L_{\mathrm{bb}}(T_{\mathrm{s}}) + r \cdot \left(F \cdot L_{\mathrm{d}} + (1-F) \cdot L_{\mathrm{b}}\right)\right] \cdot \tau + L_{\mathrm{u}} \\ &= L_0 \cdot \tau + L_{\mathrm{u}}, \end{aligned} \tag{2.33}$$

where ε is the surface emissivity, $L_{\mathrm{bb}}(T_{\mathrm{s}})$ is the blackbody radiance at the surface temperature, F is the sky view factor (the fraction of the hemisphere above the surface which is sky), L_{d} is the downwelled atmospheric radiance from the sky, L_{b} is the radiance from background objects, τ is the atmospheric transmittance between surface and camera, L_{u} is the effective upwelled radiance of the atmosphere between surface and camera, and L_0 is the total radiance leaving the

surface into the direction of the camera. Figure 4.6 shows these phenomena in an urban context. All radiance values are effective values for the recorded IR band, meaning they include the spectral response of the sensor, and those not defined otherwise are generally angle-dependant [180].

Equation (2.33) includes several simplifications.

- In general, radiation is different over the spectrum of interest. This is also true for radiative properties of objects like emissivity and reflectance (see Section 2.1.2), which we see as colours in the visual spectrum. Multiplications of spectrally integrated values inevitably cause inaccuracies [180]. Weighting by the spectral response the sensor is meant to reduce them to a minimum.

- In addition to the emission depending on the angle of observation, reflection properties similarly vary over both incidence and observation direction. $r \cdot \left(F \cdot L_\mathrm{d} + (1 - F) \cdot L_\mathrm{b}\right)$ lumps both different directional properties of reflectance and different incidence radiations to scalar reflectance and macroscopic values of sky view factor, background radiation, and downwelled radiation to make these contributions to the equation assessable with reasonable effort.

- Atmospheric properties depend on the composition of air that the radiation travels through, and are not generally equal for different positions in the field and viewing angles.

Efforts for efficiently modelling the contributions or making the approach more precise have been made by different authors in the meantime. Byrnes and Schott [185] present methods to correct thermal imagery for atmospheric effects, i.e. to determine τ and L_u. Among those is the "angular calibration technique" by Macleod [186] that assumes Lambertian behaviour of the surface (i.e. L_0 is dir-

ectionally constant) and uses the relation

$$\begin{aligned} L(h_\mathrm{f}, \vartheta_1) = {} & L(h_\mathrm{f}, 0°) \cdot \tau(h_\mathrm{f}, 0°)^{\sec \vartheta_1 - 1} \\ & + L_\mathrm{u}(h_\mathrm{f}, 0°) \cdot \left(\sec \vartheta_1 - 1\right) \cdot \tau(h_\mathrm{f}, 0°)^{\sec \vartheta_1 - 1} \end{aligned} \tag{2.34}$$

to derive the upwelled radiance and the atmospheric transmittance for nadir observations by two recordings from the same flight height h_f, but different view nadir angles ϑ_view, e.g. nadir ($\vartheta_\mathrm{view} = 0°$) and a different orientation ($\vartheta_\mathrm{view} = \vartheta_1$). Another possibility is to model the propagation and the atmospheric radiation based on knowledge about atmospheric conditions and physical equations, which was at the time performed by LOWTRAN. Today, the software MODTRAN [187] is also available for the task.

If viewing angles deviate largely from orthogonal view, the "Lambertian" approximation of constant emissivity made in Equation (2.33) does not hold anymore [188]. Monien et al. [189] encounter this limitation when recording façades from a car driving by. They solve it by deriving the directional emissivity ε_dir for each observation nadir angle ϑ_obs (relative to the surface normal) through the Fresnel equations. Using the comprehensive explanation by Koirala [190, pp. 24–28], ε_dir of opaque dielectrics becomes

$$\varepsilon_\mathrm{dir}(\vartheta_\mathrm{obs} = 0°) = \frac{4 \cdot n}{(n+1)^2} \tag{2.35}$$

for normal view and

$$\begin{aligned} \varepsilon_\mathrm{dir}\left(\vartheta_\mathrm{obs}\right) = {} & \frac{1 - \left(\frac{\sqrt{n^2 - \sin^2 \vartheta_\mathrm{obs}} - \cos \vartheta_\mathrm{obs}}{\sqrt{n^2 - \sin^2 \vartheta_\mathrm{obs}} + \cos \vartheta_\mathrm{obs}} \right)^2}{2} \\ & + \frac{1 - \left(\frac{\cos \vartheta_\mathrm{obs} \cdot n^2 - \sqrt{n^2 - \sin^2 \vartheta_\mathrm{obs}}}{\cos \vartheta_\mathrm{obs} \cdot n^2 + \sqrt{n^2 - \sin^2 \vartheta_\mathrm{obs}}} \right)^2}{2} \end{aligned} \tag{2.36}$$

for oblique view, where n is the refractive index of the dielectric.

The emissivity is a property of the observed surface material. If the ones prevalent for the investigated area are known, they may be assumed as representative and emissivities may be read from a table (as available e.g. in VDI 3511 [191]). For a higher accuracy, emissivities can be measured or materials can be recognised. Bitelli et al. [192] classify roof materials based on satellite images and use literature emissivity values for the identified materials.

With increasing ϑ_{obs} and therefore decreasing $\varepsilon_{\mathrm{dir}}$, the share of the recorded radiance that originated from reflection in Equation (2.33) becomes more important. Although the law of energy conservation results in

$$r_{\mathrm{dir}}(\vartheta_{\mathrm{i}}) = 1 - \varepsilon_{\mathrm{dir}}(\vartheta_{\mathrm{i}}), \tag{2.37}$$

for an intransparent medium and given radiation *incidence* angle ϑ_{i}, a calculated directional reflectivity r_{dir} to the *observation* angle can only be used as an approximation in Equation (2.33). To model reflection accurately, the bidirectional reflection distribution function (BRDF) f_{r} of the surface material should be taken into account. Following Nicodemus et al. [193], the radiance L_{r} reflected into the observation direction defined by the nadir angle ϑ_{obs} and the azimuth angle φ_{obs} can be written as

$$L_{\mathrm{r}}\left(\vartheta_{\mathrm{obs}}, \varphi_{\mathrm{obs}}\right) = \int_{\Omega_{\mathrm{i}}} f_{\mathrm{r}}(\vartheta_{\mathrm{i}}, \varphi_{\mathrm{i}}; \vartheta_{\mathrm{obs}}, \varphi_{\mathrm{obs}}) \cdot L_{\mathrm{i}}(\vartheta_{\mathrm{i}}, \varphi_{\mathrm{i}}) \cdot \cos\vartheta_{\mathrm{i}} \cdot \mathrm{d}\omega_{\mathrm{i}}, \tag{2.38}$$

accounting for incident radiance from the hemisphere Ω_{i}, where the solid angle of incidence ω_{i} is spanned by the nadir and azimuth angles ϑ_{i} and φ_{i}.

However, BRDFs are hardly available for urban surface materials [194]. The models highly popular in computer graphics, e.g. based on Oren and Nayar [195], unsurprisingly have a focus on visible fractions of light. Falling back on the assumption of a Lambertian reflective behaviour, BRDF values are determined from

the directional emissivity as

$$f_r(\vartheta_i, \varphi_i; \vartheta_{obs}, \varphi_{obs}) = \frac{1 - \varepsilon_{dir}(\vartheta_i)}{\pi}. \tag{2.39}$$

For the application in large-scale building characterisation, these considerations are merely theoretical. The complexity of the task requires using more pragmatic methods that reduce the most influential uncertain parts of the equation. Mandanici and Conte [196] focus on modelling accurate sky view factors and assume $L_b = L_{bb}(T_s)$, as their approach lacks a 3D model and therefore spatially resolved L_i values. At the same time, observation angles remain low, which justifies that assumption and $r = 1 - \varepsilon$.

The connection from IRT evaluations to building parameters can be shown by two examples: Schott, Biegel and Wilkinson [184] use the IRT-measured surface temperatures to classify building rooftops into five different heat loss classes. In comparison to a ground survey, the method leads to the same result in 63 % and to significant errors in only 1 % of the investigated roofs, showing that this method helps to identify "structures which could profit from retrofit activities" [184]. For drive-by IRT recordings, Monien et al. [189] present an approach that includes their correction and mapping onto 3D building model façades. However, they conclude that the use is currently restricted to a consistent visual presentation with the purpose of drawing attention to the issue of energy efficiency, i.e. a qualitative application.

This thesis presents improved evaluation methods for aerial infrared thermography building up on the findings outlined above.

2.6.4. Building Typologies

Where measured values do not provide all required parameters for building energy modelling or data acquisition is too expensive for a particular project, default val-

ues are necessary. Some of these values are defined by technical standards, and others are available in building typologies like those from the TABULA project. They were developed for 20 European countries [197] and provide building archetypes for residential buildings of different age and size classes. Besides their contribution to bottom-up stock models in UBEM and even on country scale, the archetypes "are used as showcase examples to illustrate the effect of energy saving measures". Furthermore, the "common TABULA approach provides a framework for cross-country comparisons of building features, measures and energy performance" [197].

For Germany, Loga et al. [151] present the typology in a report on exemplary measures to improve residential building energy efficiency. Table 2.2 lists the 50 different archetypes with which they describe the German building stock. Of the four size classes single family house (SFH, free-standing buildings with 1 to 2 dwelling units), terraced house (TH, like SFH, but not free-standing), multi-family house (MFH, buildings with 3 to 12 dwelling units), and apartment block (AB, buildings with more than 12 dwelling units), only SFH and MFH have a representation in each of the 12 age classes. Sub-types specify particular archetypes for some age and size class combinations if buildings were built in the German Democratic Republic (E) as opposed to the general, nation-wide archetypes (N). Furthermore, they extend AB to high-rise building (HR) as fifth size class and SFH to a light-frame (LF) SFH for the 1969…1978 age class.

Each archetype building characterisation includes an exemplary picture as well as information on the heated area, the number of storeys, and the number of apartments. Furthermore, typical heating equipment (in multiple variations) as well as layer constructions and U-values of the envelope components (rooftops or attic floors, exterior wall, windows, and basement ceiling or floor plate) are given. For all of these parts, a conventional and an advanced retrofit scenario is given, completed by the respective reduction potential in final and primary energy demand. Indications if a rooftop or the attic floor and a basement ceiling or the floor plate form the envelope of the heated zone can also be found in the report.

Table 2.2.: *German building archetypes as specified by Loga et al. [151]. See text for explanations of the abbreviations.*

Age class	Size class				
	SFH	TH	MFH	AB	HR
1859	N		N		
1860…1918	N	N	N	N	
1919…1948	N	N	N	N	
1949…1957	N	N	N/E	N	
1958…1968	N	N	N/E	N	N
1969…1978	N/LF	N	N	N/E	N/E
1979…1983	N	N	N	E	E
1984…1994	N	N	N	E	
1995…2001	N	N	N		
2002…2009	N	N	N		
2010…2015	N	N	N		
2016…	N	N	N		

The typology offers no data about the statistical distribution of the included values from the building stock. Therefore the uncertainty of archetype component parameters used in the model of a particular existing building is unknown. A remedy can be found e.g. in the older typology of the Ministry of Building and Housing of the Land of North Rhine-Westphalia [198] that lists different envelope component compositions with U-value ranges and sporadic qualitative information on their commonness (“rare”, “predominant”, etc.). Regional differences in typical constructions, although not covering the whole territory of Germany, are pictured by the “catalogue” of the Centre for Sustainable Building in a detailed report [199], which is more descriptive, but less standardised than the TABULA publication.

All in all, typologies are important in all settings where available data about the building stock is incomplete. Therefore, TABULA is an essential part of the TEASER package (see Section 2.5.4) and is in that context used for data enrichment purposes within this thesis. This is in line with the state of the art in practical applications. Ludwig [200] uses LOD2 models and the German typology to cal-

culate building-individual heat demands on a large scale. An important data gap in this case is that information about renovation measures already implemented is entirely missing.

2.6.5. Heat Transfer Coefficient and Inverse Modelling Methods

Another approach for mitigating inaccuracies in building modelling is to exploit time series data. This is done by several recently developed methods that deliver a heat transfer coefficient (HTC) in the wider sense, i.e. a parameter relating whole building heat loss to the temperature difference between interior and exterior [12]. Examples are the co-heating test, for which Jack et al. [201] delivered reliability evidence, the QUB method [202], and the energy signature method [203]. These approaches measure the energy performance directly and do not need the geometry or similar preliminary knowledge of the building. However, the HTC (which can also be calculated from building parameters following ISO 13789 [157]) cannot be the only source of information for individual envelope component refurbishment because it does not distinguish between the contributions of different building parts. Furthermore, solar gains and air exchange need to be accounted for with additional measurements and modelling effort. While the co-heating test and the QUB method build up on dedicated measurements in an unoccupied building, the energy signature method works without disturbing the occupants, but requires a long time series of metered data and has disadvantages regarding accuracy. Other ways to avoid laborious measurement campaigns are grey-box regression [204] or modelling based on data from smart meters or building automation systems [205, 206]. These models do not necessarily fill white-box (physical) models, but can also or with even better performance be combined with black-box and grey-box modelling approaches as mentioned in the introduction of Section 2.5. Their application is limited by the need for long time series of data manually read from meters or recorded from specifically installed equipment. A

further spread of smart meters and smart home devices may make them more useful in the future, also in the case of small building retrofit preparations for which extensive preparatory measurement work is currently unreasonably costly. Nevertheless, the idea of an HTC value for benchmarking is picked up later in this thesis.

3. Project Overview, Test Sites, and Complementary Work

As this thesis was embedded into an overarching project, the methods and the results that are presented in it build up on numerous complementary works by other researchers and/or completed as a team. In the following, the concept of the project is introduced (Section 3.1), followed by an introduction to the case study building and the case study quarter in Sections 3.2 and 3.3 respectively. In order to separate the actual contributions of the dissertation from others' work in the project, the latter is summarised in this chapter, starting with the use of aerial imagery to reconstruct the geometry of buildings in Section 3.4. Section 3.5 introduces how movements of points on building surfaces can be measured using satellite radar. Finally, Section 3.6 explains an approach to analyse internal layer structures of walls using microwave radar.

3.1. Concept of the Project

This dissertation emerged from the scientific project "Building Tomograph" jointly executed by four research institutes. The common goal was to test the applicability of various remote sensing technologies for the energetic analysis of existing buildings. As part of the project, remote sensing methods were applied to case studies on two scales, a single-family house in Morschenich and a city quarter in

Berlin-Moabit. Both case studies are presented in the following sections. In Figure 3.1 and Figure 3.2, the workflow from the different measurement technologies towards energy simulations are shown for the single building and the quarter respectively. In both cases, data from different technologies is acquired. The task of this thesis was to investigate the data's suitability to be collected, analysed, and used as parameters for energy simulations.

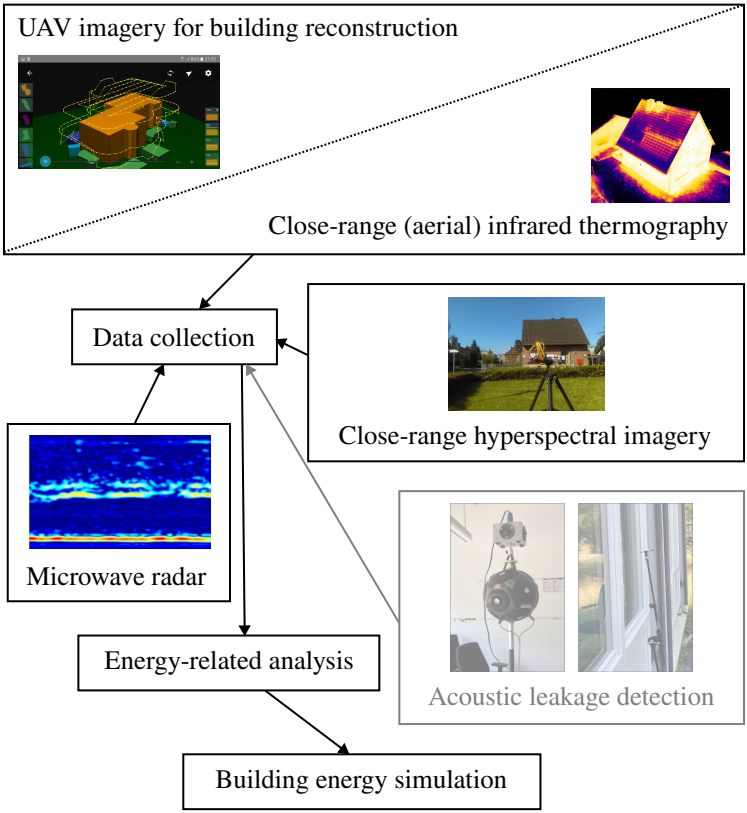

Figure 3.1.: *Overview of measurement methods and workflow envisaged in the Building Tomograph project for the single-building scale (with illustrating images from the final report [9]).*

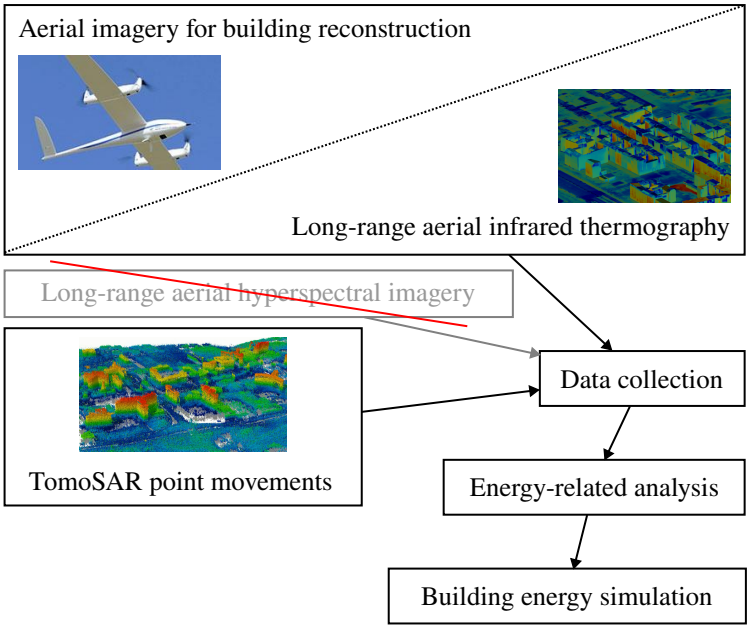

Figure 3.2.: *Overview of measurement methods and workflow envisaged in the Building Tomograph project [9] for the district scale. Images: plane © DLR; TomoSAR by Zhu and Bamler [207], licensed under CC BY 3.0 DEED.*

For the case study quarter, measurement methods envisaged for the project were long-range aerial images with visible-band, thermal, and hyperspectral cameras as well as TomoSAR, a satellite-based method. Hyperspectral imagery could not be acquired due to difficulties with flight approvals. For the case study building, close-range imagery of the same three types was taken. Additionally, microwave radar was used for wall structure assessment. The idea of acoustic air leakage detection was investigated in the project, but not applied to the case study building [9]. All measurement methods are introduced in more detail further below in this chapter.

3.2. Case Study Building in Morschenich

This section introduces the case study building. Furthermore, it presents the measurements performed to gather reference values for the experimental remote sensing methods and the simulations. Finally, it lists the remote sensing technologies applied to analyse the building.

3.2.1. Building Description

Located in the former village of Morschenich (now called Bürgewald) in western Germany, about halfway between Aachen and Cologne, the single family house used as a case study building was sold to a mining company and abandoned in the face of an approaching lignite surface mine. It was available for research purposes in 2018 and 2019. Although the house is about 25° off from a north-south alignment (see Figure 3.3), its façades are named by their approximate cardinal orientation throughout this thesis. Figure 3.4 shows exterior views on the building.

The building was built in the 1960s (with double-glazed uPVC windows installed in the mid-1990s) and consists of two heated storeys as well as a basement and an attic, both of which are unheated. The sectional view from the construction plans in Figure 3.5 illustrates this design. While the footprint covers about 81 m^2, the net heated area reaches 117 m^2. Figure 3.6 contains the floor plans of the heated storeys and names some of the rooms.

Some of the building's properties were specified in a dossier provided by the owner. However, the information is neither complete nor necessarily reliable, as it is largely based on construction plans rather than on as-built conditions. To gather knowledge about the U-values of the envelope parts, it was therefore amended by on-site inspections, including drillings and material tests. Together with a 3D model of the geometry that was manually reconstructed from laser scans, the data

Figure 3.3.: *Location of the case study building in the village of Morschenich. Background: basemap.de Web Raster, © GeoBasis-DE / BKG 2023, CC BY 4.0.*

Figure 3.4.: *Exterior views on the case study building from a southern (left) and a north-eastern (right) perspective during the preparation of the first and second measurement campaign respectively.*

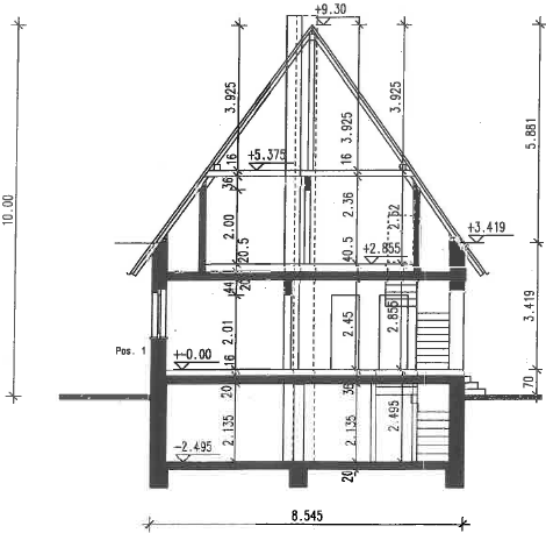

Figure 3.5.: *Sectional view from a southern perspective, taken from the construction plans of the case study building.*

was collected in an EnergyPlus Input Data File (IDF). This served as a reference for the remote sensing evaluation [13]. The Tables 3.1 and 3.2 cover the relevant contents of the file including U-values calculated from standard material properties. Table 3.1 lists the different construction types present at the house. Table 3.2 shows in which building parts they were found. It becomes apparent that the walls that are less exposed to sunlight (Northern and Western façade) have better thermal insulation and that measures were taken to reduce heat losses through the roof. The small unheated spaces mentioned in Table 3.2 are visible between the bedroom and the roof on both sides of the house in both the sectional view in Figure 3.5 and the floor plan of the first storey in Figure 3.6b.

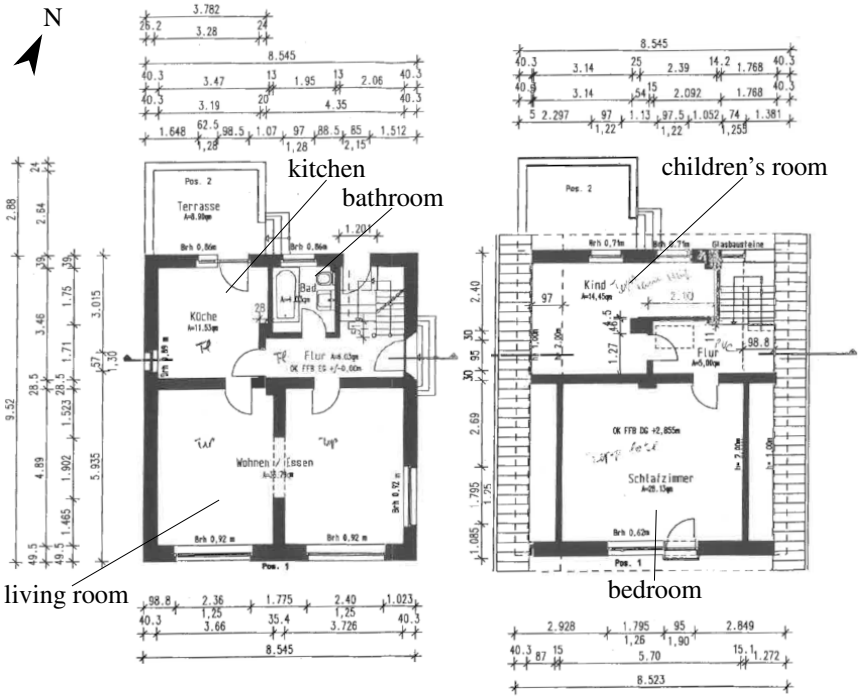

(a) *Ground floor.* **(b)** *First floor.*

Figure 3.6.: *Construction floor plans of the two heated storeys of the case study building with room labellings.*

Table 3.1.: *Best knowledge about the composition of wall (W), ceiling (C) and roof (R) constructions of the case study building (heated/inside to unheated/outside) and U-values (U, in* $\mathrm{W\,m^{-2}\,K^{-1}}$*) calculated from these.*

Type	Composition/layers	Source(s)	U
W1	Hollow blocks (pumice), air, brick facing	Dossier, drilling	1.01
W2	Hollow blocks (pumice), brick facing	Dossier, drilling	1.19
W3	Brickwork, air, brick facing	Dossier, drilling	1.34
W4	Brickwork, brick facing	Dossier, drilling	1.74
W5	Hollow blocks (pumice)	Inspection	1.45
W6	Brickwork (interior walls)	Inspection	-
C1	Carpet, timber floor boards, concrete	Dossier	2.68
C2	Tiling, floating screed, concrete	Dossier	3.13
C3	Concrete, mineral wool	Dossier	0.29
C4	Wooden hatchway	Inspection	4.55
R1	Plasterboard, mineral wool, roof tiles	Inspection	0.28
R2	Roof tiles	Inspection	6.73

Table 3.2.: *Best knowledge about construction types and areas A of the different building parts of the case study building. Construction types are explained in Table 3.1.*

Building part	Construction type(s)	A in $\mathrm{m^2}$
Attic roof	R2	73.8
Attic façades	W4	14.7
Attic floor	C3 (96.8 %), C4 (3.2 %)	46.9
Roof of heated space	R1	30.4
Northern façade (heated zone)	W2	41.3
Southern façade (heated zone)	W3	38.3
Western façade (ground floor)	W1 (95.8 %), W4 (4.2 %)	28.0
Eastern façade (ground floor)	W3 (95.8 %), W2 (4.2 %)	28.0
Basement ceiling	C1 (57.7 %), C2 (42.3 %)	81.4
Interior borders of small unheated spaces	W5 (54.5 %), C2 (37.9 %), W6 (7.6 %)	40.2
Exterior borders of small unheated spaces	R2 (78.9 %), W4 (15.6 %), W2 (5.5 %)	30.4
Interior walls (heated zone)	W6	157.7
Interior ceiling (heated zone)	C1 (81.3 %), C2 (18.7 %)	66.2

3.2.2. Measurement of Dynamic Thermal Behaviour

As the actual heat use of the case study building before its abandonment is unknown, two measurement campaigns delivered data for validating building energy models. During both, the thermal behaviour of the building in presence of internal heat loads was monitored. The measurements taken during the first campaign in April 2018 were successfully reproduced by an EnergyPlus model created from the IDF [13]. However, the amount of measured values was not considered sufficient for a reliable validation. A second campaign was conducted in February 2019. The building was heated for several days using distributed electrical heaters and fans. It was kept at an approximately constant mean interior temperature of above 30 °C for seven days. Afterwards, it was exposed to free cooling. Meanwhile, interior air temperatures, heating loads and weather conditions were monitored. Figure 3.7 exemplarily shows a temperature sensor in the kitchen, outdoor sensors for solar radiation (pyranometer) and combined temperature and humidity, and how the entry to the basement was closed with plastic foil to hinder air exchange [10].

The measured temperatures of several rooms and the average temperature of the heated zone are plotted along with the overall electric load in Figure 3.8, giving an impression about the temperature range within the building during the campaign. As the most powerful heater was placed in the kitchen for technical reasons, that room is warmer than all others throughout the heating phase. The other rooms are largely within a range of 5 K until solar radiation through the large windows pushes the bedroom temperature up between February 15 and 17. After heaters were switched off on February 17, leaving the air-distributing fans and the measurement equipment as the remaining electric loads, the kitchen temperature assimilates quickly.

Figure 3.7.: *Exemplary parts of the setup for monitoring the conditions during the case study measurement: Temperature sensor in the kitchen (a), combined outdoor sensor for temperature and humidity (b), sealing of the basement entry (c), and solar radiation sensor a few metres off the building (d) [10].* *Copyright © 2019 Solar-Institut Jülich der FH Aachen.*

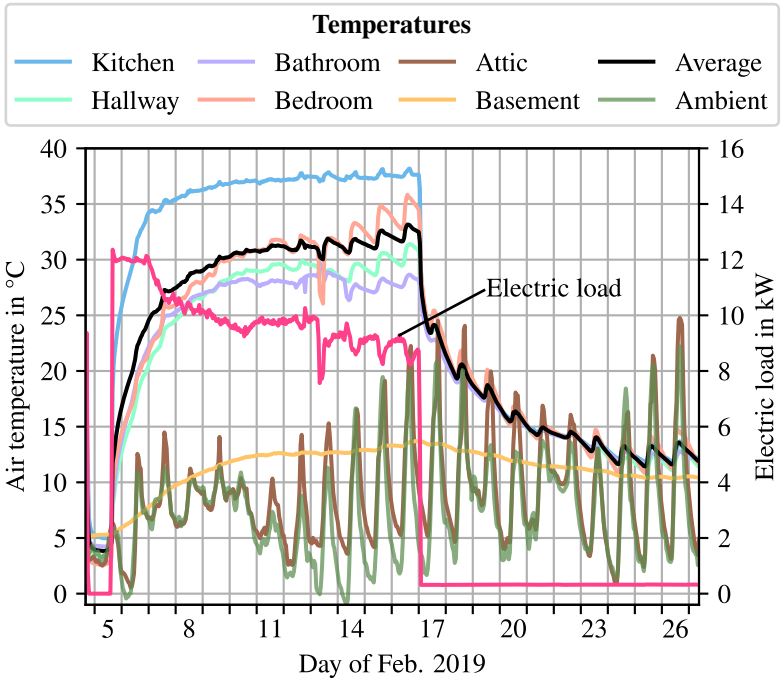

Figure 3.8.: *Measured temperatures of selected rooms and volumetric average for the heated part of the case study building during the second measurement campaign, along with the total electric load of all appliances (heaters, fans, measurement equipment).*

3.2.3. Applied Methods

Most of the remote sensing technologies originally designated to be part of the project [8] were applied to the case study building. This section briefly summarises their application and how the data from their results could benefit building energy analyses.

Photogrammetric Determination of Exterior Envelope Geometry

The external geometry was reconstructed with a photogrammetry-based method. As pictured in Figure 3.9, images were taken with an off-the-shelf single-lens reflex camera equipped on a UAV. In a semi-automatic process, a selection of images was processed to a point cloud of the building using the commercial software Agisoft Photoscan. The subsequent processing steps are described in Section 3.4.

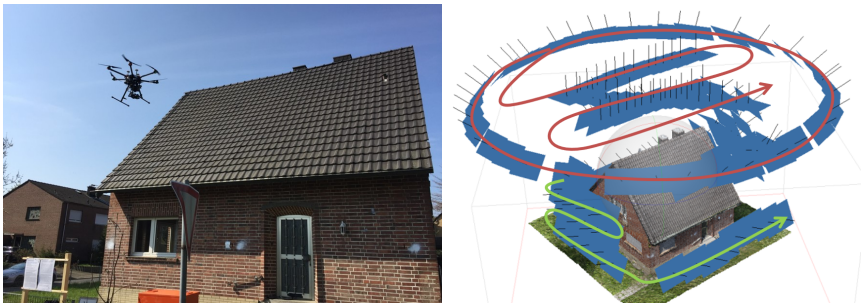

Figure 3.9.: *Acquisition and processing steps of the photogrammetric determination of exterior envelope geometry on the case study building: UAV flight (left) [9], UAV flight paths, position and orientation of 152 manually selected images, and point cloud generated from them (right).*

Close-range Aerial Infrared Thermography

With the goal of quantitatively analysing infrared thermography, infrared images were taken both from UAVs and from stationary cameras at the case study site. Their purpose is to give insights into the thermal properties of the building envelope in terms of U-values of wall and roof parts [176]. Within the project, the UAV images could be mapped onto the point cloud of the building envelope (see Figure 3.10), but the quantitative processing of them did not lead to productive results suitable for this thesis. Instead, a model calibration approach was developed independently from the application on the case study building by Patel et al. [177]. As a consequence, thermal imaging is treated here only for the district scale as introduced in Section 3.4.

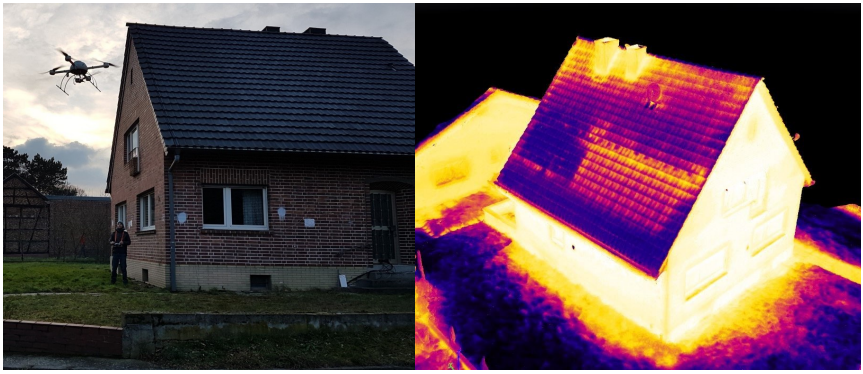

Figure 3.10.: *IR image acquisition from UAV on a winter early morning (left) and point cloud of the case study building (of Figure 3.9) textured from the results using Pix4D Mapper (right) [9].*

Internal Wall Structure Assessment Using Microwave Radar

A complementary technology that allows to identify the internal wall structure is microwave radar. The method is introduced more detailed in Section 3.6. It

was applied to one wall of the case study building from a fixed rack with movable scanning antennas (see Figure 3.11). Although this thesis contributes an important module of a possible connection between microwave radar measurements and energy assessments, the workflow was not yet developed far enough to use the case study application of the measurement technology in the exemplary modelling of the building.

Figure 3.11.: *Rack with movable antennas for microwave radar scans of the interior structure of an exemplary case study building wall [9].*

Hyperspectral Imaging

Hyperspectral cameras contain imaging sensors that are able to record radiation in numerous narrow and contiguous spectral bands at the same time. Using the reflection of solar radiation, the differences resulting from the chemical composition of the reflecting surface make material identification, e.g. of roof materials, possible [8, 208]. Pictures of the case study building envelope with hyperspectral images were successfully used to classify pixels semantically. For example, as depicted in Figure 3.12, roof parts were identified. However, that information was also available from the photogrammetry-based method (see Section 3.4) and the resolution of the hyperspectral images is very coarse. Therefore, hyperspectral imaging results were not included into the methods presented in this thesis.

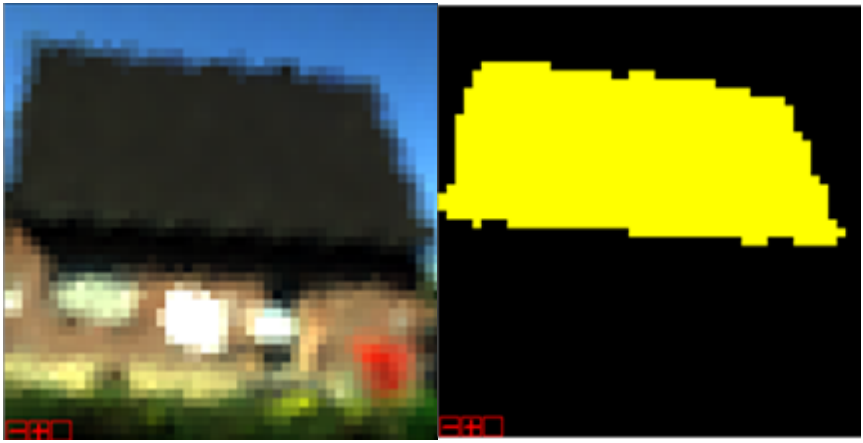

Figure 3.12.: *Visible representation of a hyperspectral image of the case study building (left) and automatically detected roof pixels (right) [9].*

Selected Modelling Input

Only the data in the photogrammetry-based geometry model serves as an input for the exemplary modelling of the case study building presented in this dissertation. However, the modelling methods used are designed to cover results from the remaining technologies as well as soon as they reach a technology readiness suitable for an integration into the process. This also includes the acoustic approach for air leakage estimation developed by Kölsch [209] which could not be tested on the case study building.

3.3. Case Study Quarter in Berlin-Moabit

The case study quarter is located in the Moabit neighbourhood of Berlin as pictured in Figure 3.13. The main reason for choosing the area was the availability of historical TerraSAR-X satellite recordings. Their analysis is presented in Section 3.5. In addition, both visual and infrared aerial images were evaluated (see Section 3.4). Based on the textured 3D model(s) resulting from these evaluations, a comparative analysis of urban building energy modelling (UBEM) approaches was performed, involving the application of the methods of SimStadt and the SHD (specific heat demand) approach (see Section 2.5.5). In the corresponding publication [11], the characteristics of the quarter are summarised:

> It is a good example for an urban area where heat energy modelling based on consumption data is not possible. The reasons are the very heterogeneous energy sources used for heating (oil, gas and district heating) as well as data protection regulations that make data unavailable. [...] There are 208 buildings in total. Of these, 71 % (161 buildings) are primarily used for residential purposes, most of them being large multifamily buildings. The rest are used for industry, offices, retail or education. Garages and other non-heated buildings make up

Figure 3.13.: *Aerial view of the case study quarter in Berlin-Moabit with the investigated area delineated in red. Background: © Geoportal Berlin / Digitale farbige Orthophotos 2019 (DOP20RGB), dl-de/by-2-0.*

12 % of the stock. In terms of age, 63 % of the buildings were built before 1910, while the rest were built mostly between 1953 and 1996. The five newest buildings are from 2008 and 2016.

3.4. Reconstruction of Buildings from Aerial Imagery

Information on as-built geometry is essential to analyse existing buildings. Aerial RGB imagery processed by photogrammeric methods can be a source for the 3D data on which the modelling approach presented in this thesis is based and was used for the exemplary applications. For the single building, images were acquired from unmanned aerial vehicles (UAVs, see Section 3.2.3). For the city quarter, a small airplane carried the cameras. The method of Frommholz et al. [171] was applied on both use cases, with six steps leading from aerial imagery to a CityGML file with 3D building envelope polygons:

1. creation of a digital surface model (DSM: a map of the highest elevation of all objects on the earth's surface), a digital terrain model (DTM: like DSM, but without vegetation and man-made structures) and a 3D point cloud from the RGB images;
2. projection of the point cloud to the ground plane and extraction of walls by local linear regression, leading to a closed footprint polygon;
3. reconstruction of roofs within the footprint by plane local regression;
4. creation of building envelope polygons in 3D space by intersecting the vertically extruded walls with the ground (from the DTM) as well as with the roof plane patches;
5. texturing of wall and roof polygons from original images;

6. detection of windows on wall textures and separation of wall and window polygons.

As elaborated in previous publications [11, 14], the method differed slightly between the two use cases regarding steps 1, 2, 4 and 6: For the city quarter, step 1 was executed including a commonly used possibility to filter out vegetation with an additional near-infrared (NIR) channel of the images [210]. For the single building, a commercial photogrammetry software was used. Because the resulting 2D wall shapes in step 2 were not complete for the city quarter due to line-of-sight-obstructing vegetation, footprints from the digital cadastre ALKIS served as the main source for the façade outlines. They were refined using the point cloud data afterwards. The model of the single building was originally created with roof overhangs by extending the roof planes, exploiting DSM data after step 4, but these parts of the model are not used within this dissertation. In step 6, windows were detected using a pattern-based approach for segmentation [171] on city quarter façades. On the single building, a colour-based approach was applied [14].

The resulting CityGML models are visualised in Figures 3.14 and 3.15 respectively. For the district case, window detection delivered visibly good results only where the conditions regarding tree coverage and texture resolution were beneficial. Still, it was more accurate than the usual assumptions of a constant window-wall ratio [11]. On the single building, 11 of the 12 main windows were successfully detected (see Figure 3.16). Issues regarding visibility (because of roof overhangs) and texture colors (because of roof overhangs and markings on the wall) kept the rest from being recognised as well. Furthermore, as described in a contribution to the *Building Simulation 2019 Conference* [14], the accuracy of the UAV position data measured by GPS turned out to be insufficient for achieving high precision in the point cloud. Due to image orientation residuals, the photogrammetry software compressed the point cloud in comparison to the real building, resulting in an underestimation of the building size in a first CityGML representation. As a countermeasure, the actual horizontal dimensions of the building were

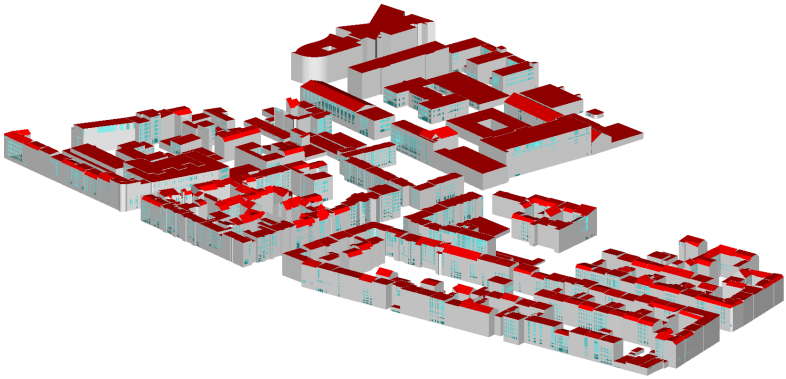

Figure 3.14.: *CityGML LOD3 model of the case study quarter as 3D representation in FZKViewer [79].*

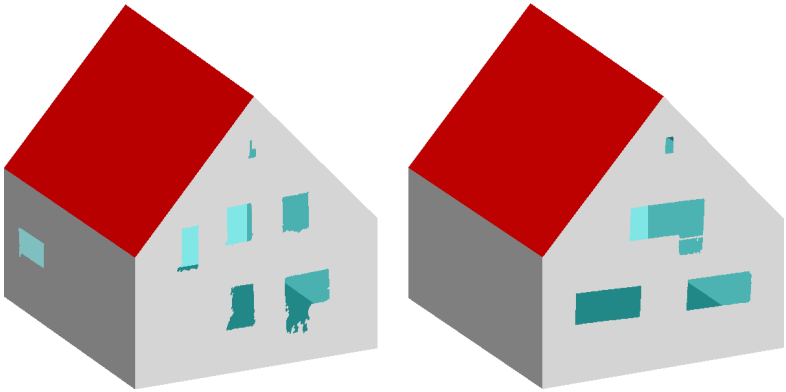

Figure 3.15.: *CityGML LOD3 model of the case study building from northern (left) and southern (right) perspective as 3D representation in FZKViewer [79].*

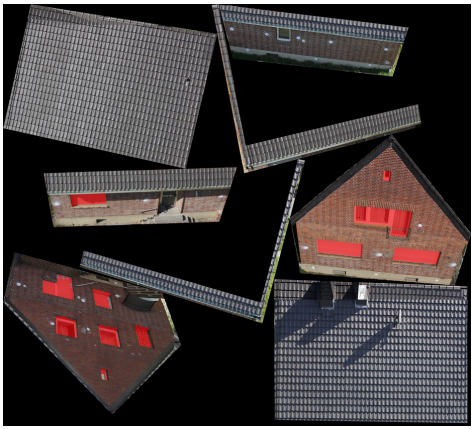

Figure 3.16.: *Textures of the case study building model surfaces with detected windows marked red [14].*

introduced into the point cloud generation process as reference lengths. As it can be seen in Table 3.3 that compares measured and modelled values, that countermeasure brought the model size into an acceptable range for the second RGB point cloud and CityGML version. To avoid these additional measurements, incorporating automatically logged differential GPS (DGPS) or real-time kinematics (RTK) data from the UAV are a favourable solution. Neither the UAV flights (with a more accurate positioning system) nor steps 5 and 6 of the 3D reconstruction process could be repeated within the scope of the project. As a remedy, the window polygons from the undersized 3D model were projected onto the more accurate geometry, resulting in the CityGML representation shown in Figure 3.15. The methods developed in this dissertation, including the simulation process presented in Section 4.3, were tested with that data.

Table 3.3.: *Geometry of the case study building: readings for different data sources and measurement methods, mostly already published in Gorzalka et al. [14].*

Data source	Wall length			Building	Wall inclination	
	West	South	North	height	North	South
Plan	9.520 m	8.545 m	8.545 m	9.300 m	90°	90°
Manual measurement	9.480 m	8.535 m	8.545 m	-	-	-
Laser scan point cloud	9.480 m	8.530 m	8.542 m	9.132 m	90.27°	89.02°
1st RGB point cloud	8.86 m	7.98 m	8.00 m	8.93 m	92.04°	88.45°
1st CityGML model	8.812 m	8.263 m	8.263 m	8.579 m	90°	90°
2nd RGB point cloud	9.456 m	8.506 m	8.510 m	9.132 m	90.35°	89.94°
2nd CityGML model	9.343 m	8.469 m	8.469 m	9.087 m	90°	90°

3.4.1. Thermal Imagery

The 3D model of the city quarter was additionally textured from infrared thermography (IRT). The necessary images, recorded from a height of about 600 m using cameras with nadir and oblique orientations, were independently acquired at night to avoid the influence of sunlight. Figure 3.17 shows the camera setup in the plane and the flight paths. The imagery covers radiation in the 7.5–14 µm band and has a resolution of about 35 cm for the orthogonally captured roofs and less for the obliquely pictured façades. In addition, a complementary orthoimage of the street level was produced. The combination of IR-textured 3D model and orthoimage of the ground leads to the scene visualised in Figure 3.18 [11].

Section 4.2 elaborates how 3D models and district-scale infrared imagery are processed in order to benefit UBEM, with results shown in Section 5.2.

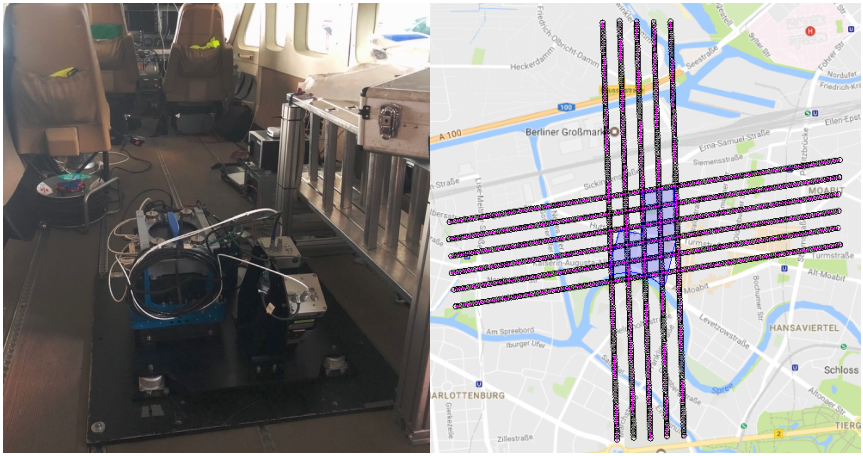

Figure 3.17.: *Setup of cameras with nadir and oblique orientation within the plane (left) and flight paths of March 2019 (right, background: © 2021 GeoBasis-DE / BKG (© 2009), Google) [9].*

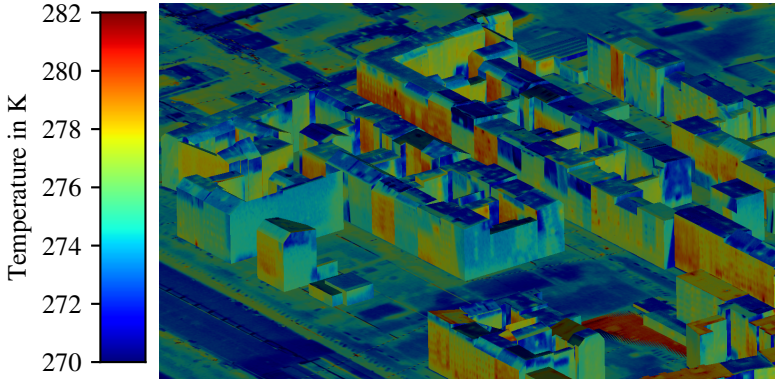

Figure 3.18.: *Northern part of the case study quarter: scene of the IRT-textured 3D model combined with the complementary orthoimage, both coloured depending on the effective blackbody temperatures equivalent to the radiation recorded by the camera.*

3.5. Measurement of Point Movements with TomoSAR

With the goals to identify constructional changes and to observe seasonal movements of buildings and their surfaces, two stacks of historical recordings made by the TerraSAR-X satellite were interpreted using synthetic aperture radar (SAR) tomography (TomoSAR). The satellite is equipped with an imaging microwave SAR with 3.1 cm wavelength [211]. With the words of Zhu et al. [212],

> [t]he general imaging principle of SAR is based on the transmission of pulses and the reception of their echoes reflected back from the surface. Therefore, the location of a pixel in a radar image corresponds to the two-way round-trip time [...] (= range) as well as the mean time of transmission and reception [...] (= azimuth). Since the position of the satellite with respect to time is known from precise orbit determination, the azimuth is referred to an absolute location in 3-D space. The geometric distance [...] from this satellite position to the surface is obtained by scaling the two-way round-trip time with the velocity of light [...].
>
> In the case of a point scatterer, the two radar observations, i.e., the azimuth time and the geometric range, can be extracted from the focused SAR image through point target analysis [...], which yields the center coordinates of the scatterer's signature at subpixel level. If the errors present in this type of observations (atmospheric signal delays including ionospheric and tropospheric delays, geodynamic displacements such as solid Earth tides, continental drift, atmosphere pressure loading, ocean tidal loading, pole tides, ocean pole tides, and atmosphere tidal loading) are corrected by external models and the remaining unknown effects, e.g., time delays induced by cables and electronics, are calibrated for, the outcome are absolute 2-D radar observations.

Scatterers appear where radar beams are scattered in a way that a significant amount of radiation travels back to the satellite afterwards, which mainly occurs at metallic objects or inner edges of structures. The resulting 3D positions of these scatterers are recorded with 1–2 cm accuracy [212, 213], leading to a point cloud of the observed scene. Multiple point clouds of the same region can be fused by matching repeatedly appearing scatterers [212], reaching an accuracy with which millimeter-scale movements can be monitored [214]. Here, the data stacks of one ascending (northward) and one descending (southward) orbit of the satellite were exploited. As the satellite "looks" to the right, western and eastern façades appear only in the ascending and descending stack respectively, completing each other when combined. After fusion and georeferencing one point cloud as a reference, the position of the scatterers in the real world can be observed over time. From evaluating the TerraSAR-X stacks between January 2011 and August 2014 for the case study quarter, periodic movements correlating with the ambient temperature were identified. Figure 3.19 shows the measured phase angle and a sine fit to it over the period of observation for an exemplary scatterer. Changing phase angles are caused by travelling distances varying less than the wavelength and can be traced back to millimeter-scale movements by interferometry. In the result, the

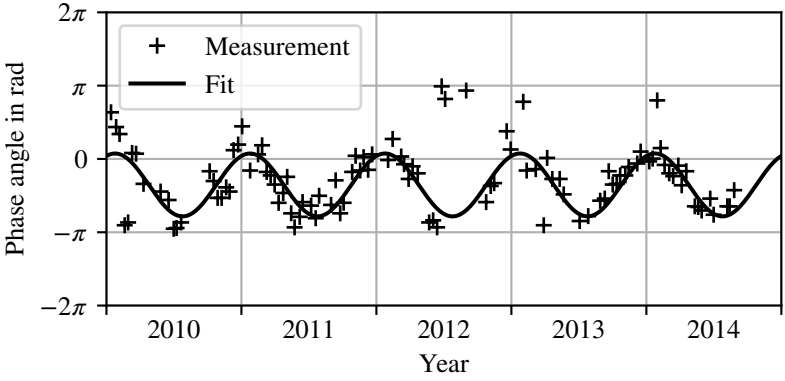

Figure 3.19.: *Measured and fitted deformation phase of an exemplary scatterer over the period of observation.*

correlation of scatterer movements with seasonal temperature changes becomes obvious. Figure 3.20 visualises the vertical amplitudes of all scatterers within the scene, revealing an apparent difference of the amplitudes between buildings. The UBEM-related evaluation methods and results based on TomoSAR data are covered in Sections 4.2.3 and 5.2.2 respectively.

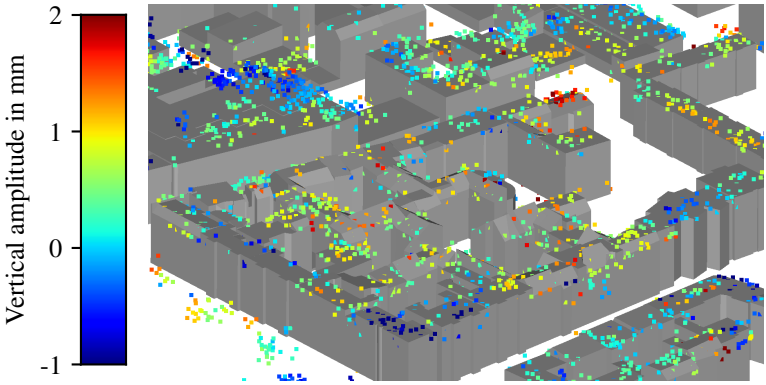

Figure 3.20.: *Scene of 3D model and point cloud of TomoSAR scatterers, coloured depending on their yearly vertical amplitude.*

3.6. Scan of Building Walls Using Near-field Radar

SAR can also be applied at close range, leading to insights about the layer structures of building walls. The method can be used to distinguish structures of inhomogeneous stones [215]. Furthermore, Haas, Peichl and Dill [216] use the technology to detect the number of layers for a wall built from homogeneous material (see Figure 3.21) and are developing an optimisation algorithm to calculate the permittivities of the involved materials. For this purpose, an antenna moves horizontally in steps of 1 cm along the wall in different heights, leading to a scan of the structure. At each position, 1601 equidistant frequency samples in the range of 1–8 GHz are taken. The benefit is that both a high penetration depth

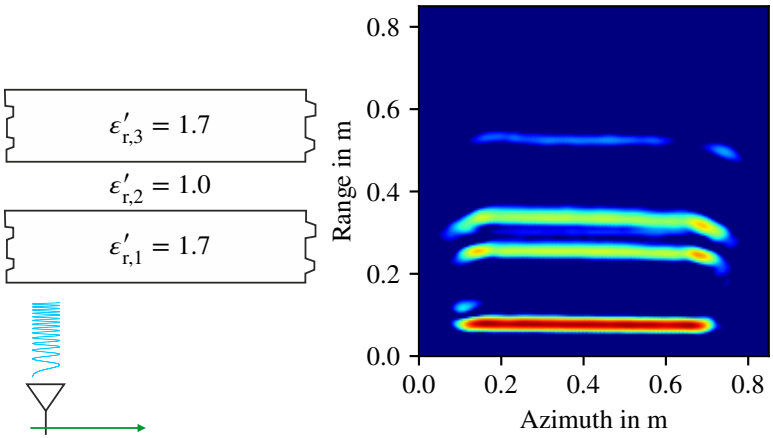

Figure 3.21.: *Radar scan of an exemplary three-layered wall structure consisting of cellular concrete bricks and air: Schematic view of the scan with a broadband horn antenna (left) and the resulting radar image using SAR processing under consideration of the layer permittivities (right). Colours from blue to red indicate increasing reflection amplitudes [216].*

and a clear picture of the nearest layer boundary can be reached through low- and high-frequency radiation respectively. In order to determine material layer permittivities, the method relies on them being constant over the frequency range, which is the case for most building materials [37]. Energetically oriented analyses of walls building up on the results require knowledge about the relationship between layer permittivities and building materials or — even better — thermal conductivities.

The literature review presented in Section 2.3.3 leads to the conclusion that the relationship between permittivity and thermal behaviour within material types is open to be studied. This thesis includes an investigation of correlations between permittivity, thermal conductivity, specific heat and density for different types of bricks and lightweight concrete (see Section 2.3). It is presented in Sections 4.1 (methods) and 5.1 (results).

4. Methods

This chapter explains the methodologies developed and applied as part of this dissertation. They build up on the state of the art as elaborated in Chapter 2 and the complementary work presented in Chapter 3. In the following, the three main fields of the conducted work are covered, starting with the investigation of building materials to facilitate the applicability of microwave radar to wall structure analysis. Afterwards, the creation of building (energy) models based on remote sensing data is described. The third section outlines how those models are processed for simulation purposes, including preparation, code assembly, and application to the case study building. Finally, a method for evaluating the single-building use case based on a sensitivity analysis is outlined.

4.1. Measurement of Permittivity and Thermal Properties for Common Building Materials

As stated in Section 3.6, the applicability of radar scans for energetically oriented analyses of walls requires knowledge about the relationship between layer permittivities and building materials or, even better, thermal conductivities. Section 2.3 concluded that both permittivity and thermal conductivity are based on different microscopic properties, but are correlated to the macroscopic density within building materials that are similar regarding their chemical composition and visible structure. This leads to the hypothesis that there also might be a correlation

between permittivity and thermal conductivity. As a consequence of the lack of literature values to test this hypothesis, measurements of actual materials are required. This section, which is adopted from a previous journal publication [15] for the most part, deals with the methods applied to test the hypothesis and to investigate whether it is possible to determine the thermal properties of building materials from radar measurements. It is embedded into the "Building Tomograph" workflow for a single building as visualised in Figure 4.1. The measurements as well as designing, preparing, and evaluating them regarding the identification of material property values were executed in collaboration with others as declared in the Acknowledgements.

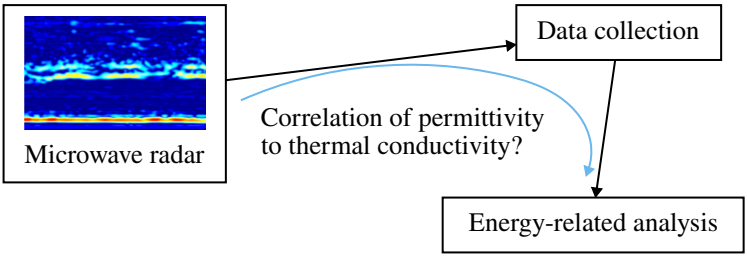

Figure 4.1.: *Investigation into a correlation between permittivity and thermal conductivity of common building materials as part of the overall single-building "Building Tomograph" workflow.*

4.1.1. Sample Collection and Preparation

Material samples were mainly collected in southwestern North Rhine-Westphalia, Germany, by visiting demolition sites and asking for permission to collect stones otherwise up for disposal. Generally, one sample per material type and construction site was prepared for measurement. Exceptions were made in cases of obvious variety within the same material type. All in all, the procedure resulted in samples of 40 burnt clay bricks (32 red, 4 yellow, and 4 with severe scorch

marks), 7 calcium silicate bricks, 2 pieces of aerated autoclaved concrete, and 7 lightweight aerated concrete bricks (5 with open and 2 with closed structure) chosen for measurement.

In order to fit a microwave waveguide (a hollow metallic conductor, see Figure 4.3) as part of a standard setup for permittivity measurements, and to provide smooth and even surfaces for thermal property measurement, each sample stone was shaped into two cuboids (10.9 cm × 5.46 cm × 10 cm and 10.9 cm × 5.46 cm × 5 cm) using a wet-cut masonry saw and grinding tools. To remove the water accumulated in that process, they were oven-dried at 210 °C for 26 hours. It was confirmed that no additional loss of mass occurred within the last two hours to make sure that they were fully dried. To reach a realistic moisture content, the samples were afterwards stored under indoor (office) conditions until their mass remained constant.

Sample densities were calculated as mass divided by net volume (including pores). Due to deviations from perfect cuboid shape, the volume values were double-checked by determining the weight loss in water after all other measurements were completed.

4.1.2. Thermal Property Measurement

The thermal properties of the samples were measured using the transient plane source (TPS) technique, applying a “Hot Disk” device. The method has been shown to be accurate to within ±5 % for the thermal conductivity of building materials. To perform the measurements, a thin Kapton sensor is placed between two samples of the same material as shown in Figure 4.2. The embedded conducting loop is then heated. From the temperature response, the thermal diffusivity, the thermal conductivity, and the volumetric heat capacity of the sample material are derived [217].

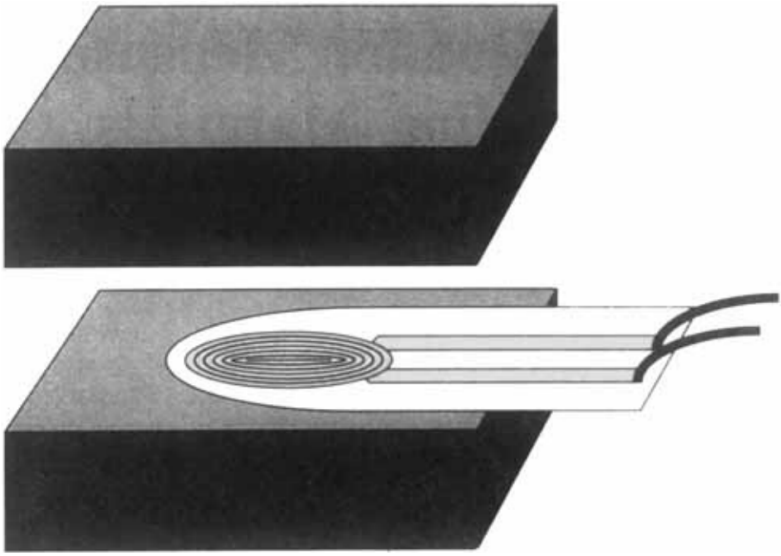

Figure 4.2.: *Principal experimental set-up used for the transient plane source method [217]. Copyright © 1995 John Wiley & Sons Ltd.*

4.1.3. Permittivity Measurement

The waveguide pictured in Figure 4.3 was used to obtain the sample permittivities. A vector network analyser helped to determine the four scattering parameters (transmission and reflection coefficients) for 1601 frequency steps in the range of 1.7–2.6 GHz. With the scattering parameters given, the real and imaginary parts of the stone samples' permittivities were computed with the Nicolson-Ross-Weir method, which requires the knowledge of the length of the sample [218]. In order to reach a better accuracy for the permittivity, the relative permeability was set to 1 (i.e. $\mu = \mu_0$). In the resulting permittivity values, the variation between the various frequency points does not exceed 1 % compared to the overall average. These average values, calculated for the range of 1.7–2.6 GHz, are a good approximation for a total relevant frequency range up to 20 GHz for burnt clay bricks and calcium silicate bricks. Here, the frequency dependence in the permittivity behaviour can

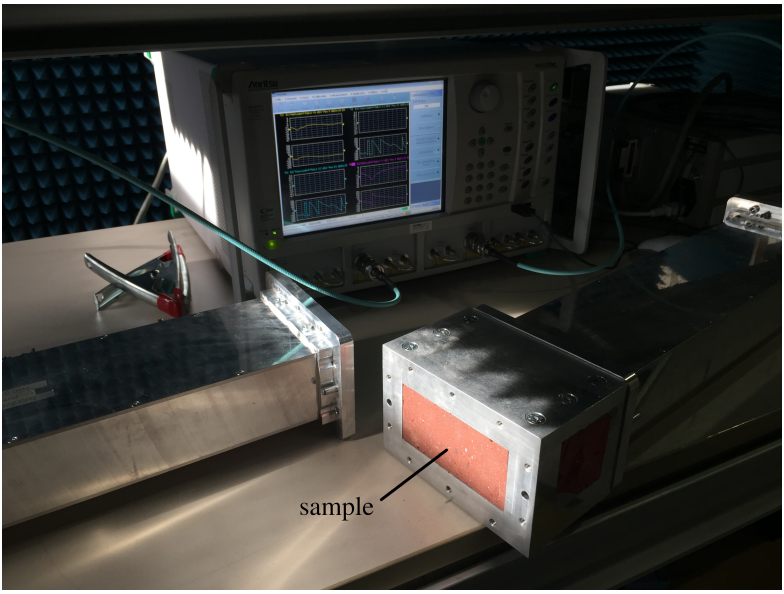

Figure 4.3.: *Burnt clay brick sample in the waveguide in front of the vector network analyser.*

be neglected, which is the case for many solids (in contrast to fluids). Concrete has a high water content and therefore a non-negligible frequency dependence in permittivity according to Ferreira et al. [37]. As a consequence, the extrapolation to the full frequency range cannot be justified there [15].

4.2. Building Modelling and Data Integration

An important part of this thesis was the task of collecting and analysing data from different measurement methods. It is embedded into the overall project as visualised in Figure 4.4.

Collecting differently sourced data into a single building model requires a persist-

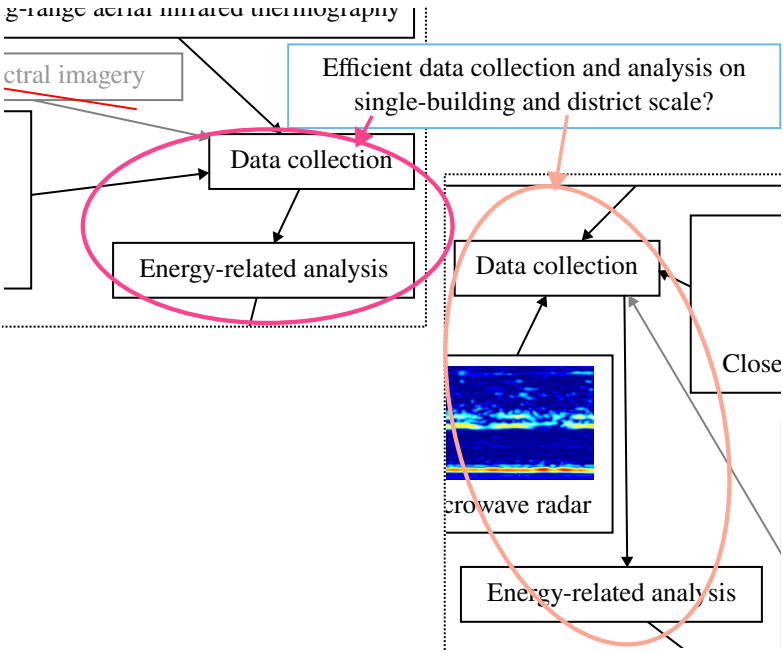

Figure 4.4.: *Energy-related building modelling and data integration as part of the overall "Building Tomograph" workflows shown in Figures 3.1 (for the single-building scale, upper left) and 3.2 (for the district scale, lower right).*

ent and interfaceable information structure. A Python class model was considered suitable, given the advantages of custom class definitions, "pickling" data for later use, and numerous complementary open-source tools written in the same language. Figure 4.5 shows a universal markup language (UML) [110] class diagram of the model components. It covers the subset of the model's classes, variables, functions, and interrelations which are relevant for and therefore mentioned using an accentuated font style in the following subsections. They describe how models are generated from CityGML files, how infrared surface textures and TomoSAR scatterers are evaluated with the help of the model, and what attributes are provided for additional data sources.

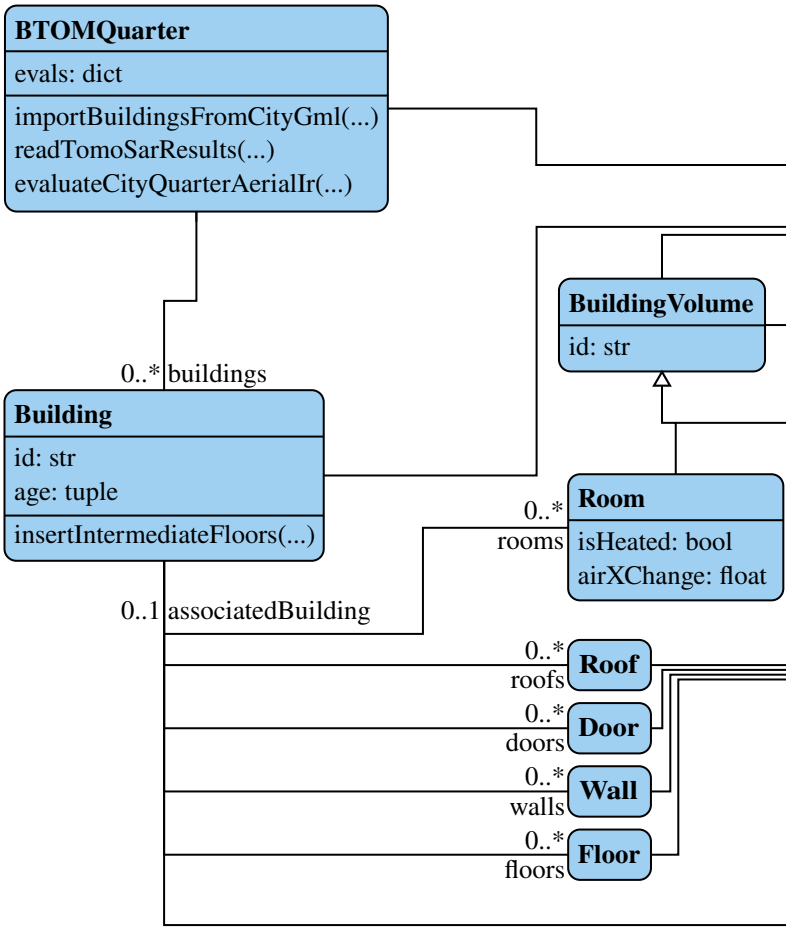

Figure 4.5.: *UML diagram of the Python class model.*

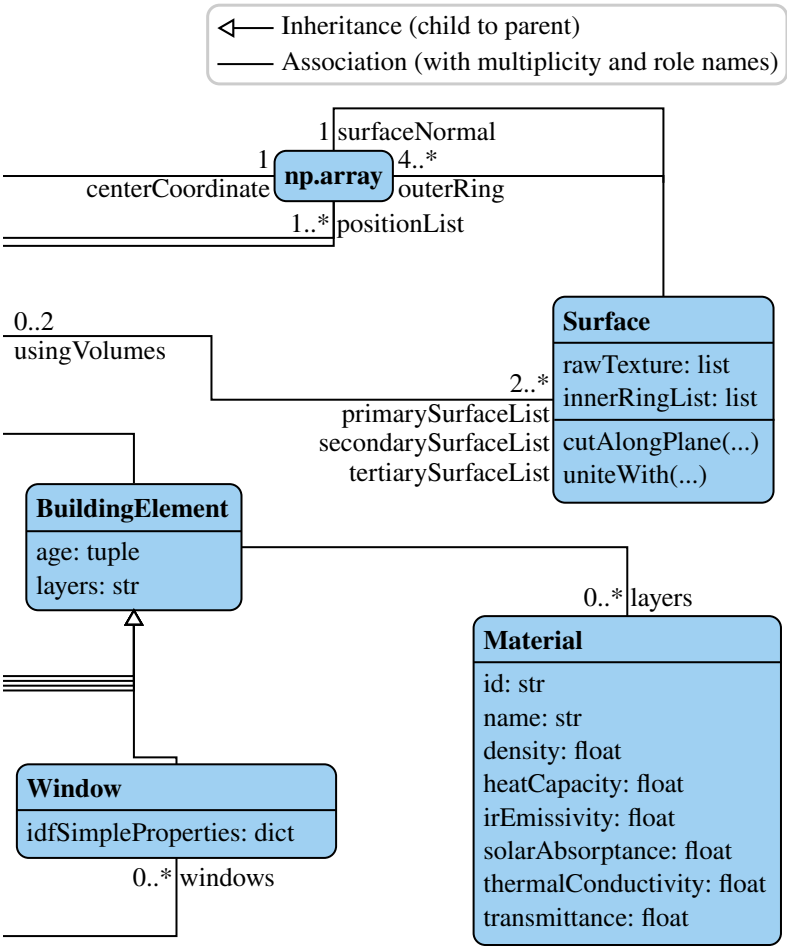
Inheritance (child to parent)
Association (with multiplicity and role names)
1
surfaceNormal
1
np.array
4..*
centerCoordinate
outerRing
1..*
positionList
0..2
usingVolumes
Surface
rawTexture: list
innerRingList: list
2..*
primarySurfaceList
secondarySurfaceList
tertiarySurfaceList
cutAlongPlane(...)
uniteWith(...)
BuildingElement
age: tuple
layers: str
0..*
layers
Material
id: str
name: str
density: float
heatCapacity: float
irEmissivity: float
solarAbsorptance: float
thermalConductivity: float
transmittance: float
Window
idfSimpleProperties: dict
0..*
windows

4.2.1. Model Generation from CityGML Files

From complementary work in the project, building geometries were available in the CityGML format (see Sections 2.4 and 3.4 for details about the format and the data generation method respectively). As a consequence, the structure of the Python class model is based on the CityGML structure. By `importBuildingsFromCityGml()`, each building in the CityGML file is translated into a `Building` object in Python. To avoid high floating point inaccuracies caused by global coordinates, the first coordinate in the file serves as the centre of a local coordinate system (`centerCoordinate`) for the whole `BTOMQuarter` that the `buildings` are collected in. The coordinates are stored as NumPy (`np`) `array` objects in such a way that equal positions of different parts of a building refer to the same array instance. This reduces the computing effort when looking for neighboured elements and makes sure the values remain consistent after any transformation operation. Each CityGML surface results in a `BuildingElement` representation of the respective type (`Roof`, `Door`, `Wall`, `Floor` or `Window`) by creation of a `Surface` from its boundaries and a second one with opposite orientation. Thereby, each element is initialised as a closed but flat volumetric object. The inner surfaces form the borders of a `Room` filling the space in between. All these `BuildingVolume` representations, i.e. elements (`roofs`, `doors`, `walls`, `floors` and `windows`) and `rooms`, define the geometry of their `associatedBuilding`. Elements reference to their front/main, back (if existing), and remaining border surfaces in `primarySurfaceList`, `secondarySurfaceList` and `tertiarySurfaceList` respectively. Surfaces in turn store the `usingVolumes` on both sides. The surface orientation and its normal vector (`surfaceNormal`) are derived from the sequence of points in the polygonal contour `outerRing`. As defined in the CityGML encoding standard, exterior boundaries (outer rings) are listed counter-clockwise and interior boundaries (inner rings in `innerRingList`) clockwise "when looking in opposite direction of the surface's normal vector" [75, p. 88]. Throughout, CityGML IDs are preserved for the `id` attributes of the objects and the overarching objects collect references to its geometry-defining positions in a `positionList`.

Even though CityGML files may include different levels of detail and more data than semantically annotated geometry, the current implementation of the import routine is limited to the scope needed for the LOD3 files that were processed for this thesis. For future applications, it may need to be extended to cover more parts of the CityGML specification or other file formats.

After first evaluations showed issues regarding non-planar roofs, the algorithm described in the following was designed based on Alam et al. [219] to create plane roof surfaces while keeping walls vertical. Due to interdependences between neighbouring buildings, the Python implementation includes the identification of shared wall parts, a task required anyway by the envisaged application in building energy simulation. After performing the latter, each coordinate array is assigned to multiple planes that must cut through it. Per roof surface, a single plane is established. Wall objects that must be within one plane (because they are located above each other within the same building or represent walls shared by different buildings) are lumped. At this point, some of the surfaces may still be non-planar. The subsequent plane fit starts with the walls, keeping verticality where possible and making sure that invariable coordinate values (those assigned to more than three planes) remain fixed. Ground surface coordinates are then projected onto the horizontal plane that contains the lowest position of each building. The previous values are stored as terrain intersection line. Afterwards, planes are fitted to the roof surface coordinates, without changing previously defined wall planes. Remaining windows are projected to the wall surfaces around them. Coordinate array identities remain unchanged throughout, but get assigned new number values if necessary. This ensures that edges shared by neighbouring surfaces remain closed. Finally, the previously identified common walls are divided such that the actually shared parts are defined by a single surface object instance that is attributed to wall elements of two different buildings. During this process performed by `Surface.uniteWith()`, the respective texture arrays are cut, keeping textures only for the parts exposed to the environment. No textures are assigned to shared surfaces, but the original textures are kept in `rawTexture` as a reference.

4.2.2. Evaluation of Infrared Surface Textures

This subsection elaborates the approach to evaluate aerial IRT for the application in the case study quarter in Berlin-Moabit (see Section 3.3) as previously published in *Energy & Buildings* [11], presented at the *Workshop 3D-Stadtmodelle* [16], and implemented in the `BTOMQuarter` function `evaluateCityQuarterAerialIr()`.

For preparation, the pixel temperatures of the IRT-textured 3D model presented in Section 3.4 were replaced by radiance values, making use of Planck's law (see Equation (2.7)), weighted with the spectral response β of a microbolometer sensor given by Christian [220, p. 19], i.e.

$$L = \int_{8\,\mu\mathrm{m}}^{14\,\mu\mathrm{m}} \frac{2 \cdot v_1^2 \cdot h \cdot \lambda_w^{-5}}{\exp\left(\frac{v_1 \cdot h}{k \cdot \lambda_w \cdot T}\right) - 1} \cdot \varepsilon_\lambda\left(\lambda_w\right) \cdot \beta\left(\lambda_w\right) \mathrm{d}\lambda_w. \tag{4.1}$$

To derive actual surface temperatures, an evaluation approach was designed, building up on the theoretical considerations in Section 2.6.3. Figure 4.6 visualises the phenomena included. The resulting application of Equation (2.33) leads to

$$\begin{aligned} L = &\left(\varepsilon_{\mathrm{dir}}(\vartheta_{\mathrm{obs}}) \cdot L_{\mathrm{bb}}(T_{\mathrm{s}}) + \sum_i \frac{1 - \varepsilon_{\mathrm{dir}}(\vartheta_i)}{\pi} \cdot L_{\mathrm{b}}(\omega_i) \cdot \cos\vartheta_i \cdot \omega_i\right) \\ &\cdot \tau(h_{\mathrm{f}}, 0°)^{\frac{d}{h_{\mathrm{f}}}} + L_{\mathrm{u}}(h, 0°) \cdot \frac{d}{h_{\mathrm{f}}} \cdot \tau(h_{\mathrm{f}}, 0°)^{\frac{d}{h_{\mathrm{f}}}-1} \\ = &\, L_0 \cdot \tau(h_{\mathrm{f}}, 0°)^{\frac{d}{h_{\mathrm{f}}}} + L_{\mathrm{u}}(h_{\mathrm{f}}, 0°) \cdot \frac{d}{h_{\mathrm{f}}} \cdot \tau(h_{\mathrm{f}}, 0°)^{\frac{d}{h_{\mathrm{f}}}-1}, \end{aligned} \tag{4.2}$$

which accounts for different atmospheric path lengths following Byrnes and Schott [185] and Macleod [186] using the ratio of the distance between surface and camera d to the standard flight height h_{f} and assumes Lambertian BRDF behaviour as defined in Equation (2.39). This correction is the first step of the evaluation and makes it possible to replace each texture pixel with the respective L_0 value, i.e.

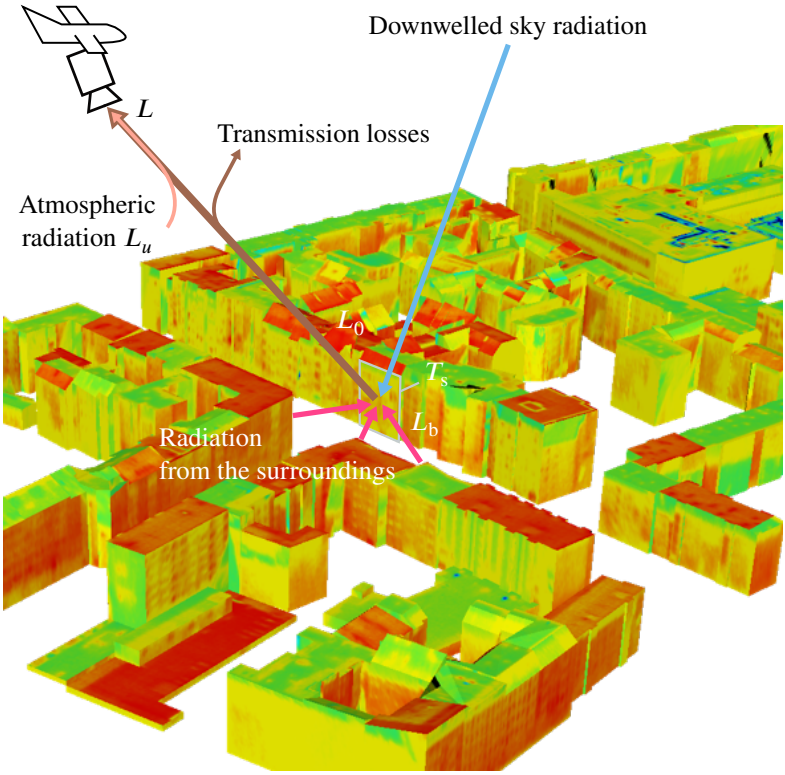

Figure 4.6.: *Thermal radiation propagation in an urban context, as modelled in Equations* (2.33) *and* (4.2) *[16].*

the total radiance leaving the surface into the direction of the camera. As the data was not sufficient for Macleod's angular calibration technique, all atmospheric parameters (L_u, τ, and also L_d) were calculated by MODTRAN and adjusted for the microbolometer spectral response. The required atmospheric conditions were derived from data provided by DWD [221] and ICOS [222] for the nearby Lindenberg Meteorological Observatory and completed by MODTRAN's default "mid-latitude summer" atmospheric conditions.

In a second step, the hemisphere in front of each texture pixel is discretised into solid angle segments ω_i as visualised in Figure 4.7. Raytracing determines the next surrounding object in each direction. The L_0 pixel value of a thus hit object is assumed to be constant for all observation directions and directly gives $L_b(\omega_i)$. This means that background objects are considered Lambertian radiators. Without this assumption, the resulting equation system becomes too complex for the application. If raytracing does not find a surface in a direction ω_i, $L_b(\omega_i)$ is equal to the downwelled sky radiance.

Applying the obtained background radiance for the calculation of $L_{bb}(T_s)$ in the third step requires knowledge about surface emissivities. As the surface materials of the scene could not be classified from the available data, literature values for the emissivities of obviously prevalent surface materials as specified in Table 4.1were used. Surface types are included in the data model.

The IRT-measured temperature of a surface T_s is defined as the temperature equivalent to its *average* blackbody radiance calculated in the third step, again accounting for the the sensor's spectral response. Windows are excluded in the process. The averaging is aimed at compensating the error resulting from discretising the hemisphere when obtaining background radiance.

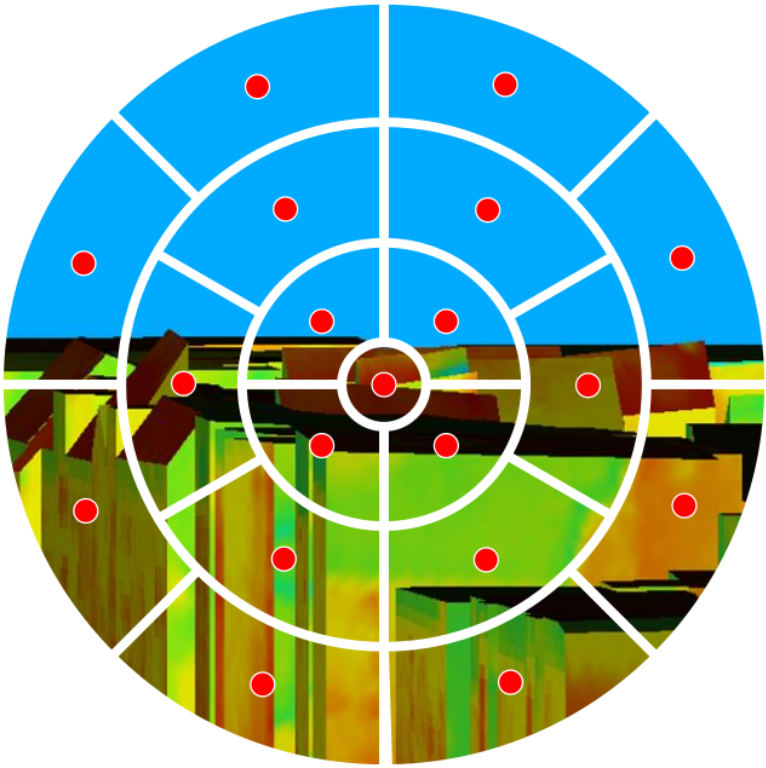

Figure 4.7.: *Simplified visualisation of hemisphere discretisation into solid angle segments for background radiation analysis [16].*

Table 4.1.: *Emissivity values for different surface types.*

Surface type	Prevalent material	$\varepsilon_{\mathrm{dir}}(0°)$	Source
Façade	Plaster	0.91	[191]
Flat roof (slope $< 5°$)	Bitumen	0.96	[191]
Tilted roof (slope $> 5°$)	Red roof tiles	0.90	[223]

4.2.3. Assignment of TomoSAR Scatterers

As described in Section 3.5 and depicted in Figure 3.20, the 3D positions of the scatterers mapped by TomoSAR are known. As a consequence, their movements can be directly connected to the likewise localisable model surfaces by the function `readTomoSarResults()`.

The hypothesis to test on the quarter of Berlin-Moabit was that roofs above unheated attics have larger seasonal movements. For the evaluation, the scatterers located above the eaves height and within or at most 0.5 m (which is half the TomoSAR raster length) outside the 2D footprint polygon of a building were assigned to it (see Figure 4.8 for an example). Furthermore, the buildings were manually investigated for signs of an apartment in the uppermost storey, like large windows and roof terraces, in the 3D model and Apple Maps [224].

4.2.4. Auxiliary Data for Single Buildings

With the goal of a better modelling accuracy for single buildings, additional information is introduced into the Python model after importing the geometry from the CityGML file. First, the storey-separating ceilings are detected by exploiting the window polygons. For that purpose, windows are grouped into storeys depending on overlapping vertical coordinates. Furthermore, they are classified as common or French windows using a threshold height of 1.8 m. For storeys with French windows, the lowest window edge directly gives the vertical position of the floor. For other storeys, the common window cill height of 0.85 m according to DIN 5034-4 [225] is the distance between the median of the lower window edges and the floor. By applying the median instead of the arithmetic mean, possible staircase windows are cancelled out. In case of missing attic windows, the height of the uppermost storey may still be undefined at this point. As a remedy, it is derived from the average height of other storeys. The floor-to-ceiling height of the basement is obtained from plans, owners or inhabitants. With an additional

Figure 4.8.: *TomoSAR scatterer selection for the building at Rostocker Str. 35. Background: © Geoportal Berlin / Digitale farbige TrueOrthophotos 2020 (TrueDOP20RGB) - Sommerbefliegung), dl-de/by-2-0.*

fixed value for the ceiling slab thickness (e.g. 0.3 m), all ceiling positions can be derived. `insertIntermediateFloors()` separates the building into storeys, dividing overarching surfaces by `cutAlongPlane()`. Volumetric room objects for each storey are created in the Python model, introducing the slabs without their thickness to maintain consistency within the model. Instead, following the conventions mentioned in Section 2.4.1, the room object borders are defined in the middle of the slab for borders between two heated storeys and on the slab surface towards the unheated storey otherwise. The necessary information on the heating status (`isHeated`) is again introduced by owners or inhabitants. So are, if possible, the years of construction of the building as a whole and of the individual windows as well as the specifications needed to choose default airtightness values for unheated spaces according to ISO 13789 [157]. For example, an air exchange rate between the unconditioned space and the exterior of $n_{ue} = 1\,h^{-1}$ is suggested if "[a]ll joints between components [are] well-sealed [and] no ventilation openings [are] provided" and $n_{ue} = 10\,h^{-1}$ is recommended for rooms that are "[n]ot airtight due to numerous open joints, or [have] large or numerous permanent ventilation openings" [157, p. 15].

4.2.5. Provision of Attributes for Additional Data Sources

Apart from the three data sources presented above, the model is also prepared for the integration of additional measurement methods. All measurement evaluations are stored in a central `evals` dictionary of the `BTOMQuarter`. This enables the selection of particular results in case multiple evaluations were executed, e.g. with different radiation models for IRT. Apart from that, some already provided parameters can contain a-priori or measured knowledge. The `airXChange` attribute stores the air exchange rate of rooms. Simplified window properties are collected in `idfSimpleProperties`. The `age` parameter of whole buildings or elements contains information on their earliest and latest possible year of construction. `layers` of `Material` instances can be attributed to building elements.

Each material is identified by `id` and `name` and contains the relevant properties of `density`, `heatCapacity`, `irEmissivity`, `solarAbsorptance`, `thermalConductivity` and `transmittance`.

4.3. Simulation

Performing thermal simulations with a building energy model based on remote sensing was one of the most important goals of this dissertation project. This section, partly reproducing previous publications [17, 18], encompasses how the questions filling the gap in the "Building Tomograph" workflow (see Figure 4.9) of how to enrich missing data and how to interface the existing data model with a simulation environment, were answered. It starts with describing how TEASER

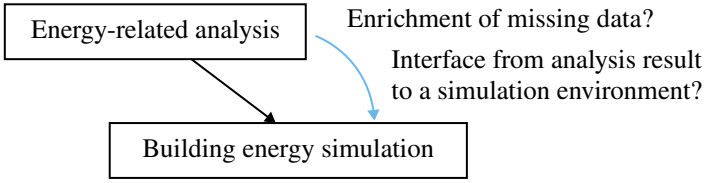

Figure 4.9.: *"Building Tomograph" workflow completion from energy-related data analysis to building energy simulation.*

(see Section 2.5.4) was adjusted to generate suitable building energy simulation models from the information stored in Python. Afterwards, the contributions made to several components of the AixLib library (see Section 2.5.3) are introduced. Finally, the calculations for which the simulation model was used are presented.

4.3.1. Model Preparation with TEASER

The application of TEASER in the context of this thesis was motivated by its potential to be a data enrichment tool and an interface between Python and Modelica models at the same time. For its implementation into the workflow, the first step consists of a conversion between the data of the Python class model described in Section 4.2 and the TEASER data structure outlined in Section 2.5.4. This was solved by making it possible to introduce previously known data into the archetype model generation of TEASER. Furthermore, as TEASER was originally created for parametrising simplified building models for calculations on district scale, several features were altered or added to make it more suitable for the tasks of this work regarding single building modelling and simulation:

1. a representation of borders between adjacent zones;
2. a possibility to adapt the boundary conditions of the exported Modelica model, including non-constant soil temperatures and a partly customizable interface;
3. a new estimation approach for interior thermal masses that accounts for the newly added zone borders.

Zone borders

So far, TEASER has featured `OuterWall`, `Rooftop`, `GroundFloor`, `Window`, and `Door` elements modelling building elements between a zone and the exterior. Additionally, the `InnerWall`, `Ceiling`, and `Floor` elements are used to describe the vertical and horizontal interior thermal masses for the zone. Following the principle for the inner elements, `InterzonalWall`, `InterzonalCeiling`, and `InterzonalFloor` were introduced for modelling borders to other zones on the same floor, on a floor above, and on a floor below respectively. Upon export to the AixLib ROM, they are lumped to a single element per adjacent zone using the

established algorithms of TEASER. The workflow of enriching data of an only geometrically described building in TEASER and exporting it to Modelica is described in the following and visualized in Figure 4.10.

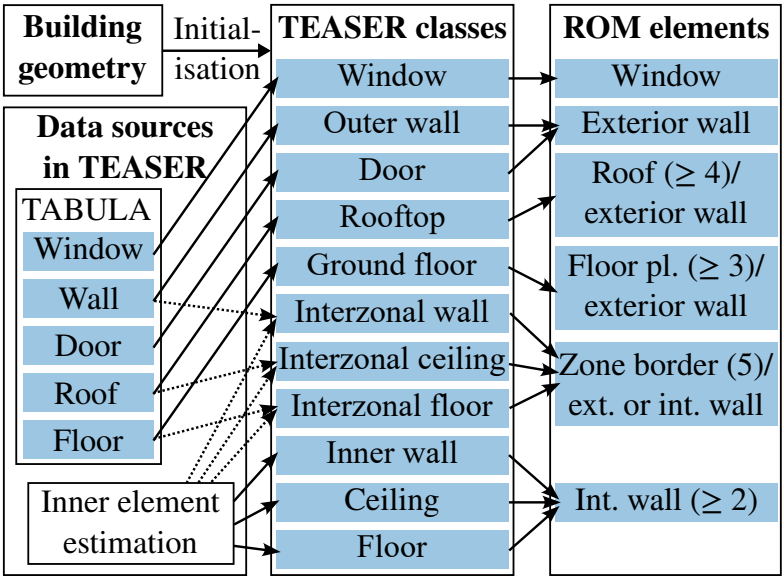

Figure 4.10.: *Visualisation of the data sourcing process for the ROM in TEASER. Numbers in parentheses represent the number of ROM elements. For example, "Floor pl. (≥ 3)/exterior wall" means the ground floor is exported to a floor plate element from* `ThreeElement` *on and is lumped to the exterior wall element for lower-order models.*

One of the arguably most important features of TEASER is the availability of default layers and thermal properties for the building elements, e.g. from the TABULA typology. This enables the user to add energetically relevant data for a building for which only the envelope geometry was known before. So far, all boundaries to the exterior had their counterparts in TABULA and were mapped to default layers and U-values from that database. For inner elements, although not covered by TABULA as such, typical elements for each of TABULA's building age periods are available in TEASER, too. Lacking a proper state-of-the-art

approach, Lauster [107] implemented an algorithm estimating their size based on the number of floors and usual room lengths and widths for the given use conditions, assuming that the uppermost border of a zone is the rooftop, the lowermost is the ground floor, and that each room has one outer wall.

As they can either be borders to unconditioned zones or to other conditioned zones, the new interzonal elements do not have a direct counterpart in TABULA. Therefore, depending on whether the associated thermal zones are equally conditioned or not, the elements are mapped either to the default respective outer or inner type element. Due to the hierarchical system of TEASER (see Figure 2.8), each zone border is created for each of both zones. The resulting Python objects are assigned equal properties. Default layer sequences are reversed for the border elements of unconditioned thermal zones. This is also considered when calculating the RC parameters for the ROM using the asymmetrical algorithm of VDI 6007 Part 1 (as shown in Figure 2.9). In the process, the room that is "more conditioned" (which has to be specified by the user, e.g. due to higher setpoint temperatures) is considered the interior. If the use conditions are equal, the border is modelled adiabatic and lumped to the inner elements on both sides. Although the creation of two separated element objects for one physical zone border means that care has to be taken to keep the model consistent if changes are made after data enrichment, the export to AixLib uses only one of the two elements due to the implementation presented in Section 4.3.2.

Interior Thermal Mass Estimation

As a matter of fact, the previously available approach to estimate the size of inner walls, floors, and ceilings (see Section 2.5.4) does not consider interzonal elements. Keeping it would increase the tendency of TEASER to overestimate interior thermal masses caused by Equation (2.31) implying that all rooms have only one outer wall. However, the typical length and width of a room defined by the usage as done by Lauster [107] is considered to be still the best base for

the calculation. Using the number of floors and rooms that the zone should have depending on its area and height, the new `'typical_minus_outer'` option in TEASER estimates the area of inner elements by subtracting all bordering elements (considering their tilt) from the overall surface area of the typical rooms separately for walls, floors, and ceilings, while avoiding that values fall below $0\,\mathrm{m}^2$.

Interface to the AixLib ROM

In addition to the previously existing Modelica file templates for `OneElement` to `FourElement` models, a `FiveElement` zone parameter template was added to cover the parameters of the new interzonal elements. The user can choose for which pairs of zones (e.g. depending on heating and cooling setpoints) interzonal heat transfer should be considered. Other elements are treated as inner elements on each side. If exporting to a ROM with less than five elements, interzonal elements are lumped to the exterior wall element if an unheated zone is on the other side or to the interior wall element otherwise. Furthermore, an option to introduce custom `Multizone` templates was added to allow introducing more individual boundary condition settings like custom weather file readers, internal gains, or setpoint tables, since all three of them were needed to reproduce the boundary conditions of the case study buildings.

Specification of Archetype Components

When setting up a residential building model, TEASER loads the components and properties of the respective age and size class archetype building. In the adjusted workflow, attributes like area, orientation, and layer structure are transferred from the Python class model to its TEASER representation.

4.3.2. FiveElement ROM Assembly in AixLib

In addition to the necessary customisation of the template files defining the interface between TEASER and AixLib/Modelica, the AixLib components for reduced order calculations were refined.

Initially, three possible approaches for the integration of heat exchange with adjacent zones into the ROM were considered:

1. an approach to consider the heat flow as part of the equivalent temperature, as suggested by VDI 6007 Part 1 [109];
2. the introduction of elements modelling the heat flow to adjacent zones in combination with a vectorisation of all other elements;
3. the introduction of a fifth element without modifications to the rest of the ROM.

In collaboration with the administrators of the GitHub repositories of AixLib and TEASER, option 3 was finally selected for open-source contribution. In the following, all approaches are introduced and the decision is justified.

Option 1: Equivalent Temperature

The standard VDI 6007 Part 1 [109] that the ROM builds up on mentions adjacent zones. It suggests lumping heat flow through borders to adjacent rooms with the heat flow to the exterior using an equivalent temperature

$$\vartheta_{\mathrm{eq,adj}} = \vartheta_{\mathrm{air,adj}} + \frac{\dot{Q}_{\mathrm{rad,se,adj}}}{\alpha_{\mathrm{cv,se,adj}} \cdot A_{\mathrm{se,adj}}}, \tag{4.3}$$

where $\vartheta_{\mathrm{air,adj}}$ is the air temperature in the adjacent room, $\dot{Q}_{\mathrm{rad,se,adj}}$ is the sum of the radiant heat sources and sinks onto the adjacent room's wall surface $A_{\mathrm{se,adj}}$, and

$\alpha_{\text{cv,se,adj}}$ is the convective heat transfer coefficient on that surface. $\vartheta_{\text{eq,adj}}$ is supposed to be merged into the equivalent temperature calculation of the `TwoElement` model.

Option 2: `FiveElementVectorized`

Elements modelling the heat flow to adjacent zones were introduced in a previous publication [17] in combination with a vectorisation of all other elements as `FiveElementVectorized`. The resulting configuration is visualised in Figure 4.11. It covers zone borders and vectorised (i.e. multiple) components per type implemented as arrays. As a result, the calculation core gets an additional interface (for the zone borders). Furthermore, the existing scalar interfaces are replaced by vectorised ones where necessary. Internally, RC element calculation modules are combined to arrays, representing the differently oriented RC elements for rooftops, exterior walls, and zone borders modelled in TEASER. To keep the existing modelling approach for radiative heat exchange between different component types (see Equation (2.22)), the previously scalar resistance modules have to be converted to two-dimensional arrays. New modules have to be created for radiative heat exchange between elements of the same type, connecting different entries of each RC module array.

Selected Option 3: FiveElement ROM

Trying to stick as much as possible to the design principles previously applied in the model, option 1 was ruled out: Equation 4.3 does not fit to the implementation of a largely simplified equivalent temperature calculation entirely based on boundary conditions. Furthermore, interconnecting $\dot{Q}_{\text{rad;se;adj}}$ from within the core ROM with the far side of the other zone and vice-versa would result in modelling the same building element twice, but lumped with different other elements

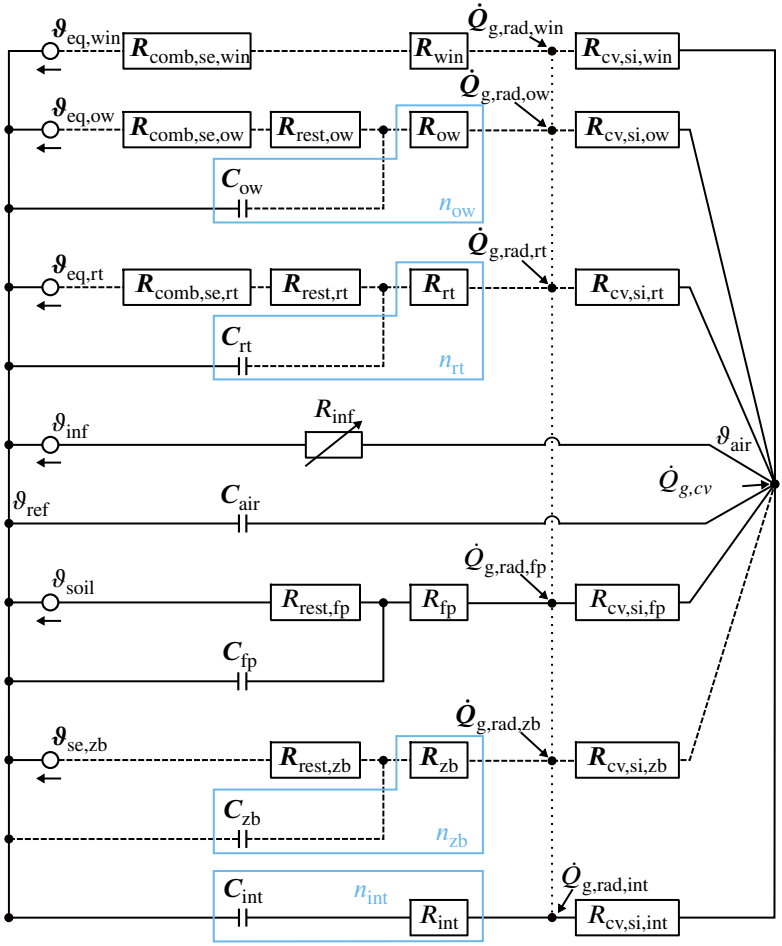

Figure 4.11.: *Thermal network representation of the* `FiveElementVectorized` *model (option 2), analogous to the* `ThreeElement` *network in Figure 2.7. Dashed lines and bold variables indicate parallel connections and components modelled as arrays. The dotted line indicates the resistances for radiation exchange between each pair of interior surfaces.*

and therefore with different boundary conditions. This would not only risk physically false results, but also simulation crashes.

When option 2 was implemented for use in a previous publication [17], it was found that it required significant changes to the core RC model and is not compatible to the established IBPSA core library. Additionally, the benefits of a more detailed model were considered not worth the increase in calculation time, as the ROM is mostly used for simplified modelling.

Option 3 was chosen to be the most suitable for open-source publication as a consequence. The thermal network (shown for three elements in Figure 2.7) was complemented with a possibility to connect multiple thermal zones, in this regard following the vectorisation idea in option 2. Each zone border element is modelled as part of the RC model of the zone with the lower index through the `Multizone` model (see Figure 2.6) to avoid double modelling. In the adjacent zone, the heat flow is directly connected to the surface area. The resulting thermal network is shown in Figure 4.12. In the figure, array connections are represented by dashed lines. The dotted line between the interior surface nodes stands for the pairwise connection of the nodes by resistances for radiation heat exchange.

Changes to Ground Temperature Consideration

Other than in previous versions of the AixLib ROM, the temperature on the outer surface of the ground floor element $\vartheta_{\mathrm{soil}}$ is not necessarily a constant here. It can also be connected to a table in a file, a sine function, or the `AixLib.BoundaryConditions.GroundTemperature.GroundTemperatureKusuda` model that was already a part of AixLib. This feature is particularly relevant for the case study building model, since soil temperatures were measured on site.

In simulations which lump the floor element into the outer wall representation, the ground temperature is considered in the equivalent temperature calculation. As a consequence, a contribution to the IBPSA core library was made to add

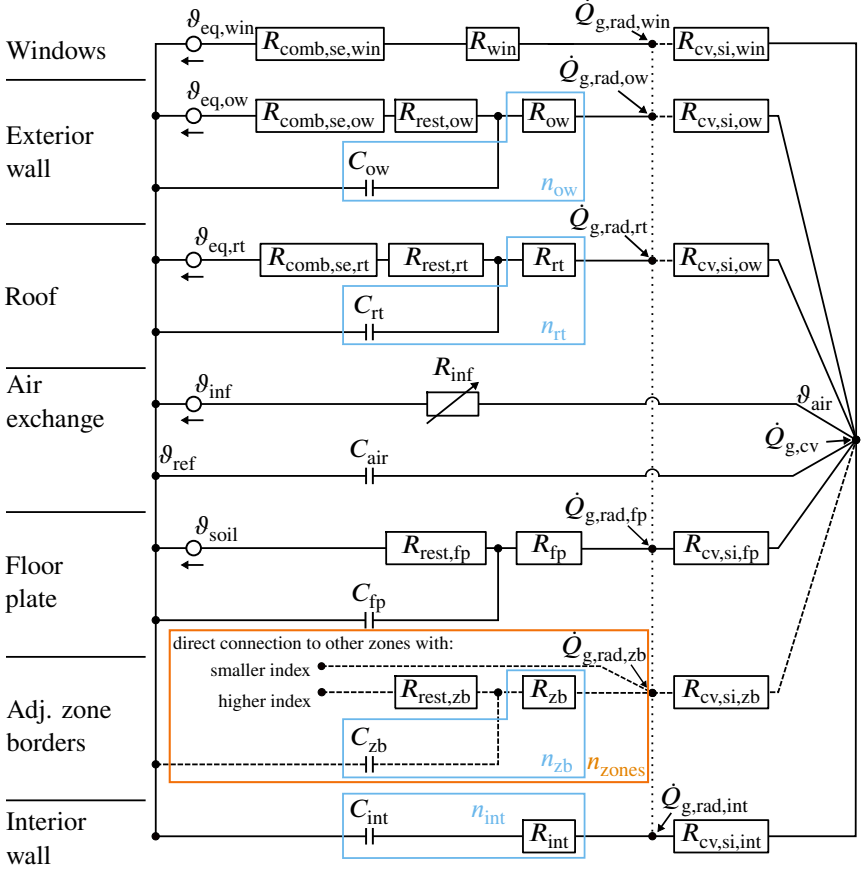

Figure 4.12.: *Thermal network representation for the new `FiveElement` implementation in AixLib, with the fifth element modelling heat exchange with adjacent zones. Refer to the List of Symbols for an explanation of the variables and indices.*

the possibility of non-constant soil temperatures into the equivalent temperature calculation module [226].

Weather Data and Long-wave Radiation on Exterior Surfaces

Radiation from the environment (i.e. terrestrial long-wave radiation) contributes to the equivalent air temperature defined in VDI 6007 Part 1 [109]. Nevertheless, Lauster and Müller [117] and TEASER only consider atmospheric long-wave radiation (represented by ϑ_{bs} in Equation (2.28)), which tends to be lower. This assumption can be justified by the non-availability of terrestrial long-wave radiation in the common TMY3 weather files [227] and the small contribution of long-wave heat exchange to the overall amount. However, it is included in the DWD test reference years [158] for which an import module was developed in order to gather more realistic weather information for German locations. Hence, the approach defined in VDI 6007 Part 1 [109] was implemented except for two of its elements: First, as the necessary data is not included in the TEASER model, the influences of the horizon elevation were left out. Second, the radiation-dependent radiant heat transfer coefficient was not implemented to avoid non-linear equations in Modelica. This leads to

$$\Delta\vartheta_{\mathrm{eq,lw},i} = \left(\sqrt[4]{\frac{-E_{\mathrm{ter,lw}}}{0.93 \cdot \sigma}} \cdot \left(1 - F_{\mathrm{sky},i}\right) + \sqrt[4]{\frac{E_{\mathrm{atm,lw}}}{0.93 \cdot \sigma}} \cdot F_{\mathrm{sky},i} - T_{\mathrm{amb}} \right) \cdot \frac{\varepsilon_{\mathrm{se}} \cdot h_{\mathrm{rad,se},i}}{h_{\mathrm{comb,se},i} \cdot 0.93}, \tag{4.4}$$

where $E_{\mathrm{ter,lw}}$ is the terrestrial long-wave radiation (defined downward and therefore always negative), $E_{\mathrm{atm,lw}}$ is the atmospheric long-wave radiation, $\varepsilon_{\mathrm{se},i}$ is the long-wave emissivity of the exterior surface i, and

$$F_{\mathrm{sky},i} = \frac{1 + \cos\gamma_{\mathrm{tilt,se},i}}{2} \tag{4.5}$$

is the sky view factor of the surface, calculated from its tilt angle $\gamma_{\text{tilt,se},i}$.

4.3.3. Model Application to the Case Study Building

In principle, a working AixLib/Modelica simulation model can be generated following the steps described above. To demonstrate that this low-effort and highly automatable approach based on remote sensing can produce a dynamic thermal building model, it is applied to the case study building described in Section 3.2. Altogether, the process can be summarised as visualised in Figure 4.13.

Model Generation

The suitability of AixLib's `TwoElement` configuration for dynamic simulations was already demonstrated and verified by Lauster [107] using the standards VDI 6007 Part 1 [109] and ASHRAE 140 [228] , revealing minor limitations in case of sudden changes in the boundary conditions due to the model reduction steps. These steps are partly avoided here. Furthermore, the measured thermal behaviour of the case study building was subject only to two sudden changes in interior loads. This leads to the conclusion that the presented steps from measurement to model generation promise to deliver a good representation of the existing case study building. For a case-specific application like this, appropriate weather data must be collected and additional knowledge about the investigated building may be included.

In this case, simulation models were created in six different variations in order to determine the sensitivity of the simulation results to differences in the building parameters. An overview of the parameters can be found in Table 4.2. Regarding the U-values, variations 1 to 3 use the values given in the TABULA typology [197] for the non-refurbished state that are implemented in TEASER. Variation 4 contains the best knowledge from building plans and on-site investigations about

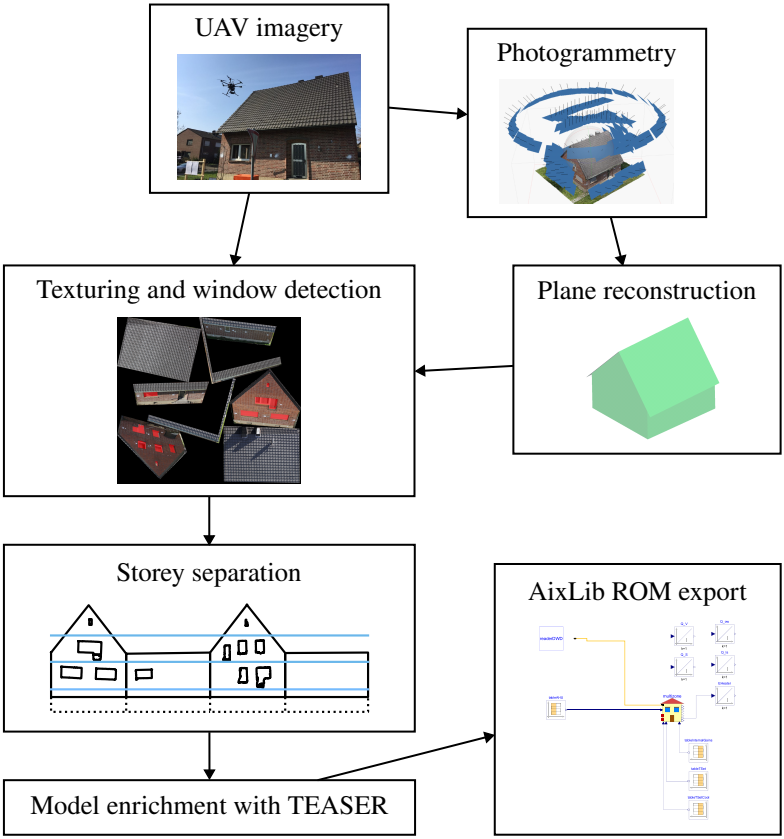

Figure 4.13.: *Generation process for the dynamic thermal model of the case study building. The last three steps were actively developed as part of this dissertation.*

Table 4.2.: *Mean heat transfer coefficients (U-values) for roof parts, exterior walls (EW), attic floor (AF), basement ceiling (BC), and windows (Win) as well as window SHGCs of different simulation model variations for the case study building. For envelope parts of unheated spaces (if different, indicated by values in brackets), any insulation layers were removed from the typology entries.*

Var. no.	U-value source	(Mean) U-values in $W\,m^{-2}\,K^{-1}$					SHGC
		Roofs	EW	AF	BC	Win	
1	TABULA	0.9 (3.2)	1.2	0.8	1.1	1.9	0.6
2	TABULA	0.9 (3.2)	1.2	0.8	1.1	1.9	0.6
3	TABULA	0.9 (3.2)	1.2	0.8	1.1	1.9	0.6
4	Best guess	0.4 (6.7)	1.3 (1.8)	0.5	1.1	1.9	0.6
5	Best case	0.7 (3.2)	0.9 (1.7)	0.7	0.8	1.9	0.6
6	Worst case	1.8 (3.2)	1.7	1.3	1.3	1.9	0.6

the walls (exterior and interior) and the roof of the building as available from the IDF model (see Section 3.2.1). The actual compositions of the building parts in contact to soil and of the basement ceiling are unknown. So, it also falls back to TABULA values there. Variations 5 and 6 reflect the best and worst case respectively when considering the building typology of the state of North Rhine-Westphalia (NRW) [198], where "best case" means "best insulation". They are a remedy for the unavailability of uncertainty information on TABULA's archetype building components and represent the boundary of the confidence region for the thermal parameters of the building. Window U-values are always $1.9\,W\,m^{-2}\,K^{-1}$, which is the value of the window archetypes representing the knowledge that they were replaced in the mid-nineties.

To assess the model's sensitivity for their sizes, the variations also differ in the properties of interior surfaces. They cover different estimation approaches for interior thermal masses, resulting in the areas for the three zones listed in Table 4.3. Variation 1 is based on the approach previously implemented in TEASER (see Section 4.3.1). Variation 2 uses the newly implemented version presented in Section 4.3.1. Although that approach does not overestimate thermal mass as much

Table 4.3.: *Surface area of the interior elements of each zone and source for the materials and thermal properties assigned for the six model variations.*

Var. no.	Interior element surface in m^2			Material/layer data source
	Attic	Basement	Main zone	
1	0	171.15	501.52	TABULA
2	0	136.62	388.69	TABULA
3	0	81.68	265.05	TABULA
4	0	81.68	265.05	Best knowledge
5	0	81.68	265.05	TABULA
6	0	81.68	265.05	TABULA

as TEASER's original one, the values are still higher than the actual values of the building as found in variations 3 to 6. The attic has no inner walls, so its interior element surface area is always $0\,m^2$. The data source for their physical properties was chosen analogous to the U-values in Table 4.2. Because the NRW typology does not contain information about interior constructions, TABULA values are used for both variation 5 and 6.

In all cases, the model consists of three thermal zones: attic, basement, and one heated zone that covers all the living area in the ground and first floor. Two small unheated spaces between the roof and a part of the first floor are modelled as part of the heated zone as they are not visible from the outside.

Simulation

To test the overall approach described in this thesis, the exterior conditions (temperature and solar radiation as well as the temperature of the surfaces in contact to soil) recorded during the measurement campaign were applied. For all variations, heating setpoints (to very high temperatures) and usage profiles (to zero) were set in such a way that they do not influence the simulation. Instead, the measured loads of the installed heaters were defined as internal gains. Air exchange rates

were kept at the default value for the conditioned zone. For the unconditioned zones, they were set to 10 h^{-1} for the attic and 1 h^{-1} for the basement, following the recommendations in Table 7 of ISO 13789 [157]. Table 8 in the same standard is the source for the interior surface heat transfer coefficients of non-vertical surfaces. They are set to 5.0 $W\,m^{-2}\,K^{-1}$ for upwards and 0.7 $W\,m^{-2}\,K^{-1}$ for downwards heat flow. The default value in TEASER mentioned in Section 2.5.4 is valid for full-year simulations and therefore not a good choice for a simulation in which the direction of the heat flow does not change.

The model was simulated from January 18, 8:00 to March 1, 16:00, giving it time to stabilise under constant weather conditions until the start of the measurement on February 4 (the actual building was unheated at the time). The comparison with measured values is presented in Section 5.3.1 of the following chapter.

Heat Demand and Heat Transfer Coefficient

In addition to the simulation, the annual heat demand for the existing building and for a refurbishment scenario were determined. Finally, the HTC of the whole building was calculated, simulating a steady state situation. The results of the calculations are presented and discussed in the following chapter.

4.4. Evaluation of Single-building Use Case

Before a new method for modelling an existing building is applied to a particular use case, the uncertainty of its results regarding that application needs to be known. For the toolchain presented here (consisting of UAV-based geometry assessment as well as subsequent energy parameter enrichment and simulation model generation, as pictured in Figure 4.13), several pieces of input variables are either based on assumptions or uncertain. This raises the question how the

uncertainty in these variables affects the results. The comparison between measured and simulated values for the case study model enriched with archetypal values as described in Section 4.3.3 cannot substantiate a general applicability of the method. Therefore, a sensitivity analysis is performed to evaluate how the model results react to changes in the input parameters. This section presents the model output and input parameters considered for an illustrative use case and the variance-based method applied for the sensitivity analysis.

4.4.1. Use Case for Illustration

The use case for analysing the sensitivity of the model is a retrofit decision for a single-family house, with the case study building used to provide exemplary values. The method presented in this dissertation generates uncertain information about the building regarding

- geometry: while the outer envelope of the building can be accurately modelled, the determination of window areas and borders of the heated zone is subject to significant uncertainty;
- building physics: standard U-values and airtightness replace missing measurements;
- solar gains: apart from window geometries, standard g-values are used;
- HVAC equipment: no data is collected, and simulation does not cover it.

Not all items of this list are relevant for the evaluation of the method. As the approach aims neither to model the HVAC equipment nor the operation of the building at this point, these aspects are not considered in the sensitivity analysis. Instead, the space heating demand for a full year under the standard interior and exterior conditions defined by DIN V 18599-2 [95] is used as the main indicator.

Expected energy savings and compliance to energy efficiency requirements (by law or for subsidies) are of particular relevance for retrofit decisions. For the latter, the energy demand after retrofit as well as meeting requirements for envelope thermal transmittance are relevant in case of a full retrofit, at least in Germany [229]. Demand calculations based on the geometry determined by a simplified method and typology thermal transmittance are in line with current guidelines [230]. As a consequence, the risk of not meeting energy efficiency guidelines can be neglected for the sensitivity analysis here. Instead, the insulation measures proposed by Loga et al. [151] for the TABULA project as "advanced retrofit" are assumed to be applied to the case study building, and **the expected energy savings are calculated**.

In literature, the term "energy performance gap" refers to the large differences between actual energy savings through retrofits and theoretical demand calculations observed in practise. It has been traced back preliminarily to inaccuracies in modelling of building characteristics and of occupant behaviour [231]. Modelling the occupant behaviour correctly is not relevant for the non-inhabited case study building. This part is therefore put aside, which is equivalent to the assumption that the retrofit decision is made by occupants who use their building perfectly in line with the standard conditions. With regard to the method presented in this thesis, some of the uncertain building model parameters mentioned above may cause performance deviations.

1. The geometry of the heated zone and the areas of envelope components affect heat demand both before and after retrofit through uncertain thermal losses and solar gains.

2. Using standard values for air leakage leads to uncertain infiltration losses before retrofit, but due to compulsory airtightness assessment not post-retrofit.

3. Unknown properties of the basement ceiling and thermal bridges affect heat losses through certain parts of the envelope primarily before retrofit.

The case study analysis considers the parameter variations listed in Table 4.4 and illustrated in Figures 4.14 and 4.15. The U-value ranges mirror the best/worse cases as of Table 4.2 for outer walls and basement ceiling (U_{ow} and U_{bc}) and additionally include the best guess values for rooftop and attic floor (coupled values for U_{rt} and U_{af}). The heights above ground for basement ceiling h_{bc} and attic floor h_{af} are varied independently, but within the same range such that the lowest position of the basement ceiling is at ground level. The window-wall ratio (WWR) is varied from 80 % of the measured value up to the value of 0.3 that is, although usually too high, often applied in UBEM [11]. For the factor F_G that reduces basement ceiling U-value and infiltration air changes at 50 Pa n_{50}, the range between low and high quality provided by DIN V 18599-2 [95] for existing buildings with no airtightness assessment and unheated basement is applied. In addition, the interior surface area is uncertain. The inner wall area is varied to reach an overall interior area (including the constant ceiling area between first and second floor) in the range provided by Table 4.3. In addition, it is scaled with the difference between attic floor and basement ceiling height. Window U-value and SHGC are not varied due to the availability of standard values for common window types.

Table 4.4.: *Parameter variations for the sensitivity analysis.*

Parameter	Pre-retrofit		Post-retrofit
	Lower border	Upper border	
1a. U_{rt}	$0.4\,\mathrm{W\,m^{-2}\,K^{-1}}$	$1.8\,\mathrm{W\,m^{-2}\,K^{-1}}$	$0.14\,\mathrm{W\,m^{-2}\,K^{-1}}$ (fixed)
1b. U_{af}	$0.5\,\mathrm{W\,m^{-2}\,K^{-1}}$	$1.3\,\mathrm{W\,m^{-2}\,K^{-1}}$	
2. U_{ow}	$0.9\,\mathrm{W\,m^{-2}\,K^{-1}}$	$1.7\,\mathrm{W\,m^{-2}\,K^{-1}}$	$\left(U_{bc,pre}^{-1} + 6.86\,\mathrm{m^2\,K\,W^{-1}}\right)^{-1}$
3. U_{bc}	$0.8\,\mathrm{W\,m^{-2}\,K^{-1}}$	$1.3\,\mathrm{W\,m^{-2}\,K^{-1}}$	$\left(U_{bc,pre}^{-1} + 3.43\,\mathrm{m^2\,K\,W^{-1}}\right)^{-1}$
4. WWR	0.072	0.3	= pre-retrofit
5. h_{bc}	0.01 m	1.51 m	= pre-retrofit
6. h_{af}	5.32 m	6.82 m	= pre-retrofit
7. F_G	0.65	0.75	0.85 (fixed)
8. n_{50}	$6\,\mathrm{h^{-1}}$	$10\,\mathrm{h^{-1}}$	$2\,\mathrm{h^{-1}}$ (fixed)
9. A_{int}	$265.05\,\mathrm{m^2}$	$501.52\,\mathrm{m^2}$	= pre-retrofit

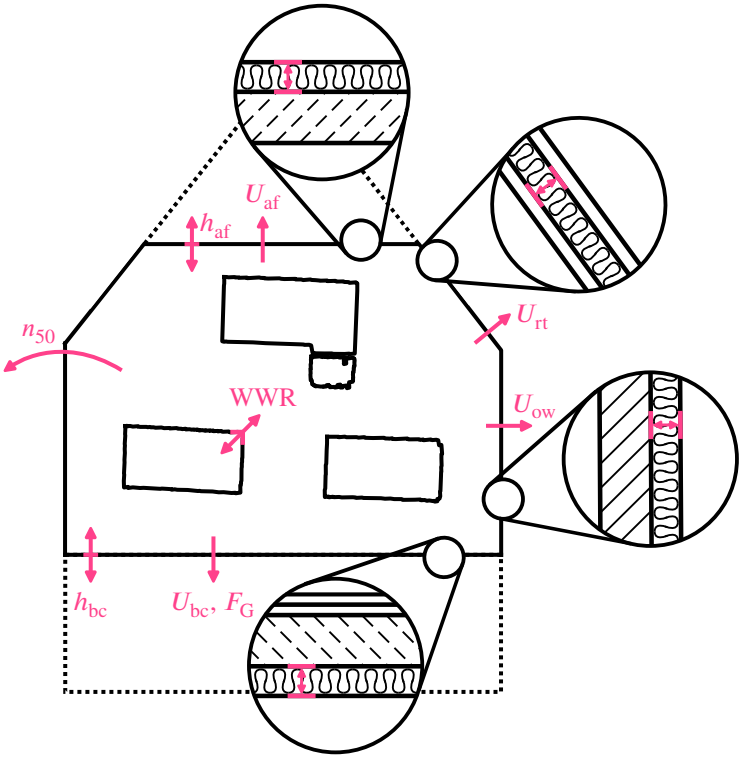

Figure 4.14.: *Envelope-related parameters varied for the sensitivity analysis and layer thicknesses adapted for reaching the varied U-values, illustrated on the south façade of the case study building (pre-retrofit case).*

After retrofit, the insulation proposed as "advanced retrofit" by Loga et al. [151] is added to the exterior walls and below the basement ceiling. Tilted roof, attic floor, and windows are fixed at the respective TABULA U-value, following the assumption that the relevant components are exchanged. For F_G and n_{50}, the DIN V 18599-2 [95] standard values for state-of-the-art retrofits are used. The geometry remains unchanged. This results in less varied parameters, which is clearly visible in Figure 4.15 when compared to Figure 4.14.

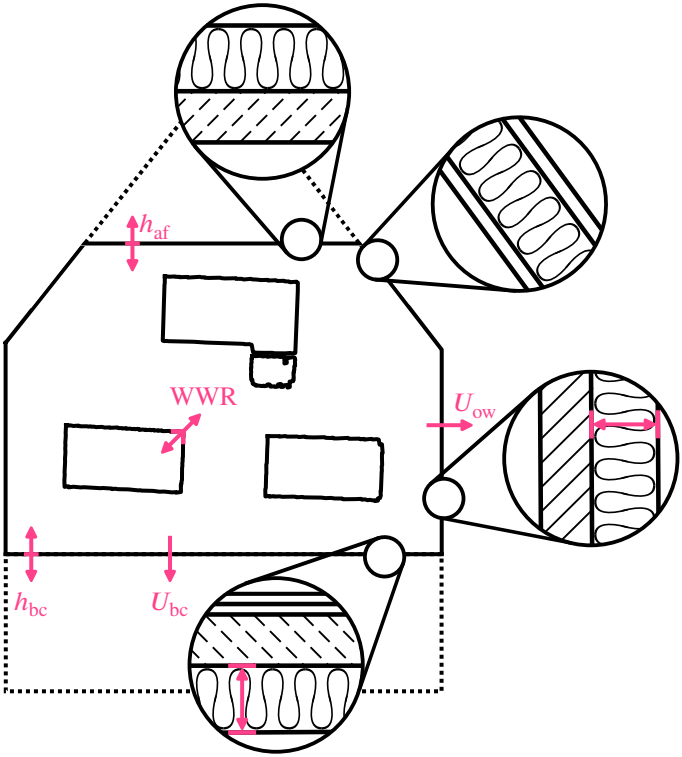

Figure 4.15.: *Envelope-related parameters varied for the sensitivity analysis and layer thicknesses adapted for reaching the varied U-values, illustrated on the south façade of the case study building (post-retrofit case).*

To reduce the model complexity and uncertainty caused by the basement zone, the heat exchange through the basement ceiling is simplified using the standard approach of temperature correction [95]. It effectively causes a reduction of the U-value by F_G, which is why it is converted into equivalent additional insulation of the basement ceiling in the model. Similarly, ambient air temperatures are assumed for the attic, but no solar gains and reduced convection are considered for that part of the thermal zone envelope. All in all, the `FiveElement` ROM is replaced by a single-zone `FourElement` representation.

4.4.2. Variance-based Method Implementation

In his dissertation about "Monte Carlo Based Uncertainty and Sensitivity Analysis for Building Performance Simulation", Burhenne [232, p. 159] presents four methods for global sensitivity analysis (emphasis addded):

> The **scatter plot method** is used for a first visual inspection and ranking of the analyzed parameters. If many parameters are analyzed, the **elementary effects method** is used for identifying the most influential ones for further investigation (i.e., factor fixing). Furthermore, the μ^*-σ plot provides insights into the model structure (i.e., nonlinearities and interactions between parameters can be identified). As a subsequent step, the **variance-based method** is applied for detailed quantitative analysis with the computation of first-order and total sensitivity indices for the set of the most influential parameters. Finally, **Monte Carlo filtering** can be applied to determine the regions of the model inputs (e.g., design specifications and boundary conditions) that lead to the desired model output (e.g., an energy demand below a certain threshold).

Furthermore, Burhenne [232, p. 159] identifies sampling based on Sobol' sequences as the most appropriate sampling technique. Similarly, Menberg, Heo

and Choudhary [233] conclude that the variance-based method is suitable for a detailed quantitative analysis. As this is relevant here and no preliminary analysis is needed, the method is chosen for the task. Algorithms for Sobol' sampling and variance-based analysis are included in the open-source Sensitivity Analysis Library (SALib) by Herman, Usher and Iwanaga [234, 235], which was applied for this dissertation.

For a detailed explanation of the algorithmic procedure, the reader is referred to Appendix A.3.1. In short, sensitivities are calculated based on efficiently drawing N samples out of the the k-dimensional parameter space (Table 4.4 opens $k = 9$ dimensions), where N is a power of two. The method applied needs $N \cdot (k + 2)$ evaluations of the target function. In the use case presented here, the target function is the calculation of energy savings through a full-year simulation of both the pre-retrofit and the post-retrofit state. Each simulation requires several seconds to run. Regarding the problem fact that the number of samples is unknown in advance, but sensitivity estimators converge for high values of N, advice is given by Burhenne [232, p. 160]: "For most building performance simulation problems, convergence can be defined to be reached when the estimator falls within the range of the reference results ±5 %. A practicable Monte Carlo termination rule is when the estimator is within this range for the last three sample sizes where the largest sample size is used as the reference result." However, this rule might be difficult to reach for very small estimators according to Burhenne. In that case, convergence of the sum of total sensitivities for all influencing variables $\sum_i S_{\mathrm{T}i}$ is said to be sufficient.

5. Results and Discussion

This chapter presents and discusses the results of the measurements and calculations performed within the scope of this dissertation. Starting off with the smallest scale, Section 5.1 covers the material investigations to facilitate the applicability of radar scans for energetically oriented analyses of walls. In the context of large-scale UBEM, the evaluations of IRT and TomoSAR in the case study quarter are presented by Section 5.2. Section 5.3 focuses on the generation of a (simulation) model for the case study building and the simulated interior temperatures during the measurement campaign as well as methods for whole building evaluation. Finally, Section 5.4 presents the results of a sensitivity analysis for the single-building use case.

5.1. Building Material Investigations

The results of the experiments described in Section 4.1 presented in the following were already published in *Materials and Structures* [15]. In comparison to that article, the contents of this section are only modified to a minor degree.

The experiments gave material properties for all 56 samples mentioned in Section 4.1.1. 40 of them were burnt clay bricks (BCB) of different type and colour, including four (partly) scorched ones. Additionally, seven calcium silicate bricks (CSB), two autoclaved aerated concrete (AAC) and seven lightweight aggregated concrete (LAC) (five with open and two with closed structure) samples

were measured. Only a few samples had to be excluded because they did not fill the waveguide due to damages.

Table A.1 in the Appendix contains the average measured values for the properties of each sample. In this section, the results are presented and discussed. The imaginary part of the measured permittivities ε_r'' showed to be small, with the exception of a non-significant tendency to higher values for calcium silicate bricks. As the imaginary part of the complex permittivity was not considered for the expected correlation between density/heat transfer and permittivity (see Sections 2.3 and 4.1), the following analysis focuses exclusively on the real part.

5.1.1. Measured Material Properties and Interrelations

Figure 5.1 shows an overview of measured values for thermal conductivity (Figure 5.1a) and volumetric heat capacity (Figure 5.1b) over permittivity for each investigated sample. A positive correlation is visible in both cases. For thermal conductivity and permittivity, the different materials are clearly clustered: Measurements for all BCB types form a highly correlated group. LAC with open structure and AAC values are grouped at lower values for both permittivity and thermal conductivity. LAC with closed structure and CSB samples have lower and higher thermal conductivity values than the BCB group respectively. The overall correlation coefficient is 0.703. Regarding volumetric heat capacity and permittivity, all material types are included in the slightly asymptotic-looking interrelation with a correlation coefficient of 0.849.

For analysing the contributions of the theoretically relevant quantities (as presented in Section 2.3) to these already high correlations, the different plots in Figures 5.2 to 5.4 visualise the measurement results in greater detail. Furthermore, they allow to observe from which measured quantities the variations originate. The plots are discussed in the following. As a complement, relevant correlation values are summarised in Table 5.1.

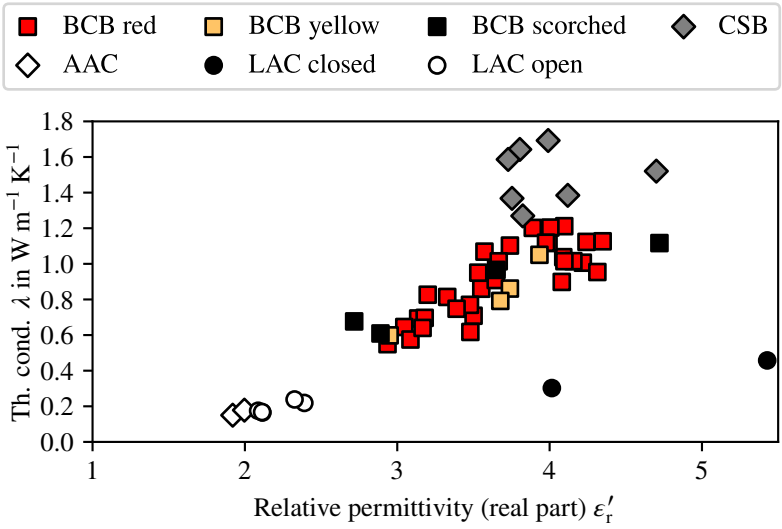

(a) *Thermal conductivity over relative permittivity.*

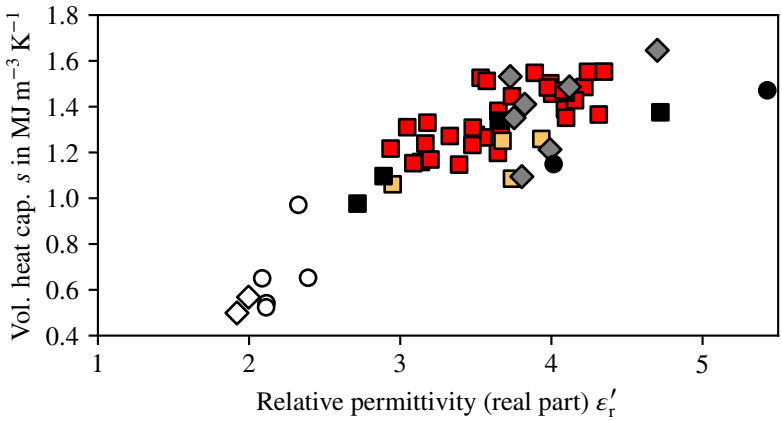

(b) *Volumetric heat capacity over relative permittivity.*

Figure 5.1.: *Thermal properties and permittivities of investigated samples.*

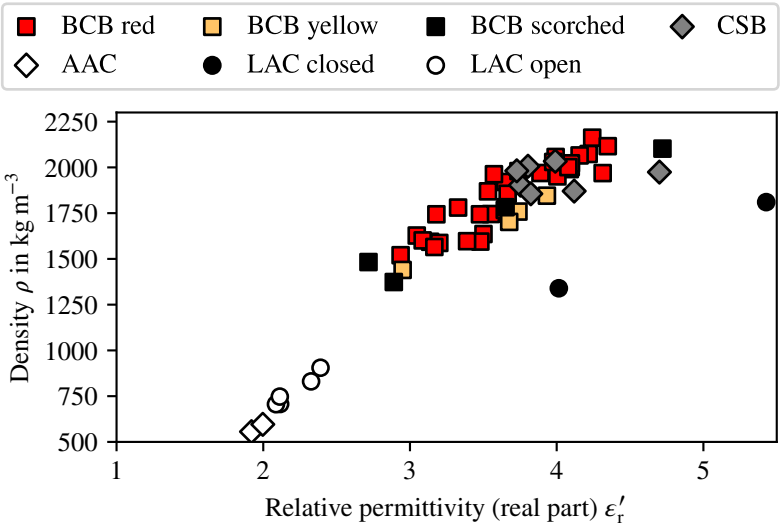

(a) *Density over permittivity.*

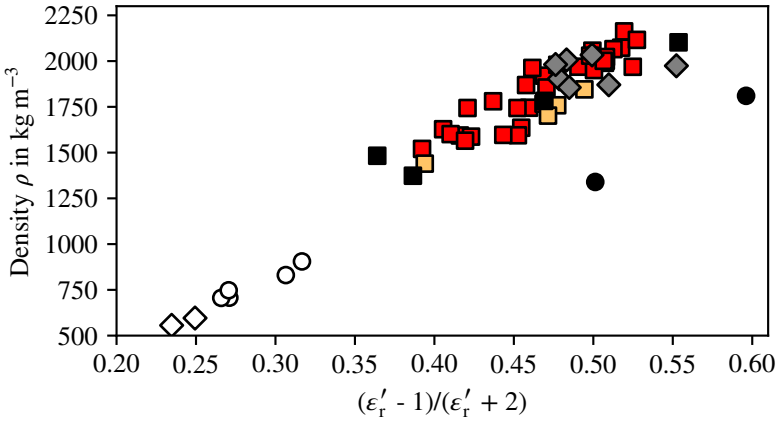

(b) *Density over left side of Clausius-Mossotti equation.*

Figure 5.2.: *Densities and permittivities of investigated samples.*

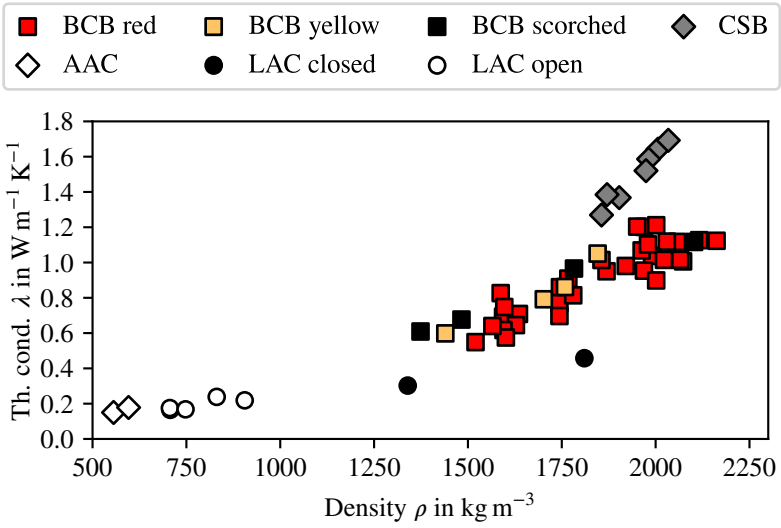

(a) *Thermal conductivity over density.*

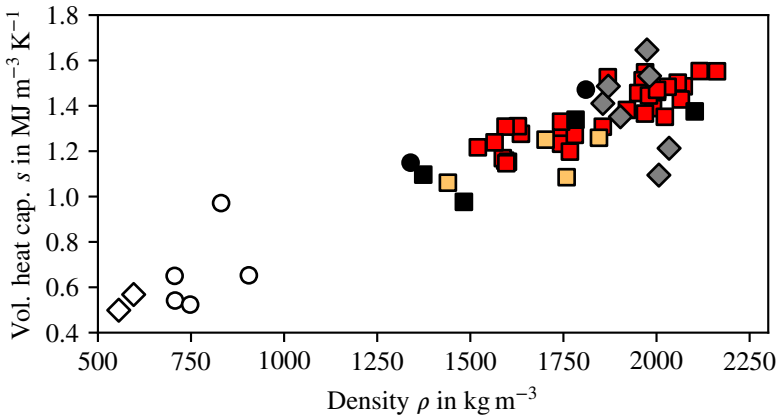

(b) *Volumetric heat capacity over density.*

Figure 5.3.: *Thermal properties and densities of investigated samples.*

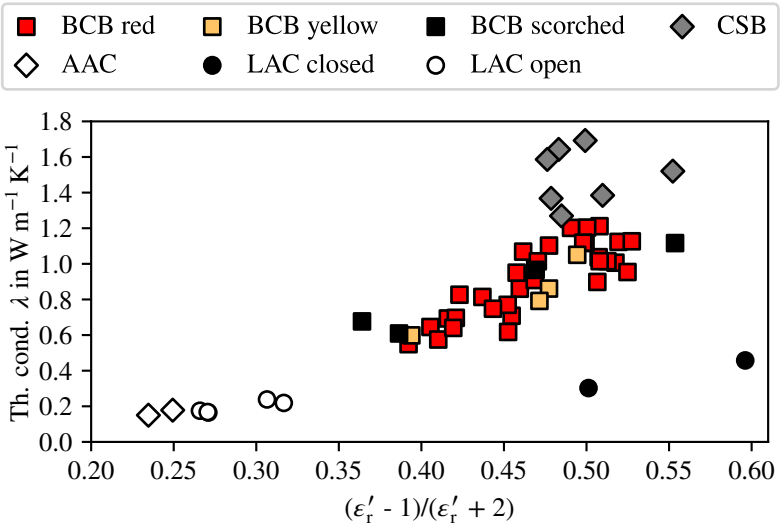

(a) *Thermal conductivity over left side of Clausius-Mossotti equation.*

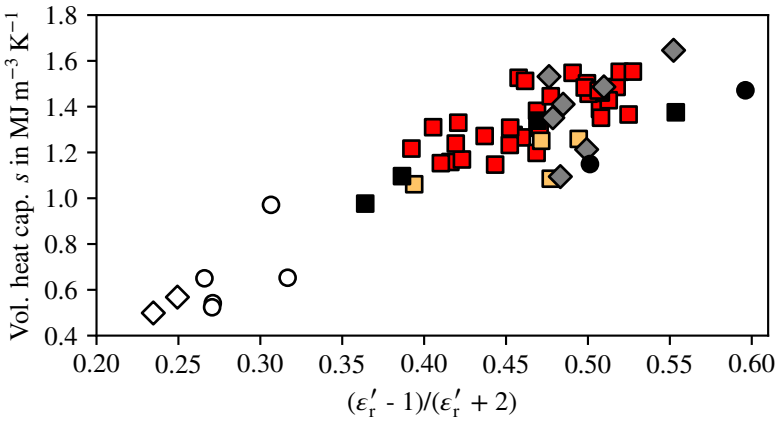

(b) *Volumetric heat capacity over left side of Clausius-Mossotti equation.*

Figure 5.4.: *Thermal properties and* $(\varepsilon_r' - 1)/(\varepsilon_r' + 2)$ *of investigated samples.*

Table 5.1.: *Relevant correlation values between material properties from the sample measurements for all stones and within samples of similar material. CM(ε_r') stands for the left side of Clausius-Mossotti equation applied to the real part of the relative permittivity $(\varepsilon_r' - 1)/(\varepsilon_r' + 2)$.*

Parameters	All	BCB	CSB	LAC & AAC
$\varepsilon_\mathrm{r}' \leftrightarrow \rho$	0.874	0.914	0.105	0.989
$\mathrm{CM}(\varepsilon_\mathrm{r}') \leftrightarrow \rho$	0.929	0.917	0.099	0.992
$\rho \leftrightarrow \lambda$	0.853	0.898	0.977	0.979
$\rho \leftrightarrow s$	0.924	0.861	−0.361	0.942
$\mathrm{CM}(\varepsilon_\mathrm{r}') \leftrightarrow \lambda$	0.749	0.842	0.063	0.965
$\varepsilon_\mathrm{r}' \leftrightarrow \lambda$	0.703	0.833	0.063	0.976
$\mathrm{CM}(\varepsilon_\mathrm{r}') \leftrightarrow s$	0.895	0.734	0.544	0.947
$\varepsilon_\mathrm{r}' \leftrightarrow s$	0.849	0.718	0.557	0.938

Permittivity to density

While Figure 5.2a again shows a slightly asymptotic-looking interrelation between permittivity and density, it becomes almost linear when replacing permittivity by the left side of the Clausius-Mossotti equation (Equation (2.16)) in Figure 5.2b. As a consequence, the correlation coefficient rises from 0.874 to 0.930. The LAC with closed structure samples show strikingly off-correlation values, presumably because metallic contents of blast furnace slag aggregates increase their permittivity compared to other similarly dense materials.

Density to thermal parameters

When looking at thermal conductivity and density (Figure 5.3a), the samples of different stone types have similar slope and show high internal consistence between the material properties, which is confirmed by the correlation values in Table 5.1. Volumetric heat capacity and density are shown as highly correlated in total by Figure 5.3b and Table 5.1, but the sample values are more scattered.

Taking only calcium silicate bricks into account, the positive correlation disappears.

In total, the overall correlation between thermal conductivity and density is smaller than between volumetric heat capacity and density. This is presumably caused by material-specific factors with a significant influence on heat conduction, such as grain sizes and interior structure. A theoretic relationship considering these contributions might describe the behaviour better, but its development would be beyond the scope of this work.

Permittivity to thermal parameters

The interrelations between permittivity and density and between density and thermal parameters help to draw a connection between permittivity and thermal parameters. As Figure 5.4b and the correlation value of 0.895 show, volumetric heat capacity values of the investigated materials can be estimated from permittivity values. The scattering of the values is high, but the influence of thermal capacity on building energy demand is limited anyway. The advantage of using the left side of the Clausius-Mossotti equation is that it gives a linear relationship when comparing Figure 5.1b and Figure 5.4b.

Deriving values for thermal conductivity from permittivity is feasible. For a linear fit to the left side of the Clausius-Mossotti equation $(\varepsilon_r' - 1)/(\varepsilon_r' + 2)$, the residual standard deviation is $0.259\,\mathrm{W\,m^{-1}\,K^{-1}}$ (relative value: 30.0 %) for the thermal conductivity over all samples. The value decreases to 13.2 % or $0.105\,\mathrm{W\,m^{-1}\,K^{-1}}$ if the existence of calcium silicate bricks and lightweight aggregated concrete with closed structure can be ruled out in advance. This is also illustrated by Figure 5.4a. Regarding closed-structure LAC, it was very hard to classify the samples when talking to practitioners; it seems to be a rarely used material. Furthermore, both samples were found as parts of interior walls. CSB bricks are indeed common in exterior walls. Their aforementioned tendency to have higher ε_r'' values may give

a hint towards their existence upon measurement if no other source (like old plans or owner's knowledge) is available.

All in all, the hypothesis of an interrelation between permittivity and thermal parameters is at least partly confirmed. More samples are needed to get a better understanding. Especially, more of the non-BCB stones mentioned here, other materials that appear in exterior walls, and specimens from other regions would be helpful for an improvement of the database.

5.1.2. Measurement Accuracy

The TPS measurements were repeatedly performed by the Hot Disk device to prevent dynamic effects of the surrounding temperature. Furthermore, the samples were repeatedly measured in different seasons. The variation of repeatedly measured values lies mostly well within the uncertainty mentioned in Section 4.1.2. Some exceptions can be traced back to inhomogeneous material or very low thermal conductivity. There was no systematic influence of the season. In conclusion, it seems reasonable that the uncertainty of ± 5 % determined by Log and Gustafsson [217] applies here, too.

Table 5.2 compares the measured values to the standard material parameters available from CIBSE Guide A. Measured thermal conductivities are smaller than in the guide for all material types but CSB, which is consistent with the guide's statement that "[p]articular masonry products can have thermal conductivities significantly lower than the corresponding values given" [47, p. 4]. When concerning Figure 5.3a, the CIBSE values for BCB are at the upper end of the scattered sample values. The same is valid for BCB and CSB volumetric heat capacity, while measured volumetric heat capacity matches the tabulated values very well for AAC and LAC. Anyway, repeating the measurements with another measurement device may allow to exclude systematic errors as a reason for the mentioned deviations. As the deviations mostly have the same direction and are similarly

Table 5.2.: *Comparison between material properties tabulated in CIBSE Guide A [47] (C) and linear fit to measured thermal properties (M) for the respective densities. CIBSE values for AAC are interpolated to the measured average density.*

Material	ρ in kg m^{-3}	λ in W m^{-1} K^{-1}		s in MJ m^{-3} K^{-1}	
		M	C	M	C
BCB	1300	0.46	0.75	1.01	1.09
	1500	0.63	0.85	1.13	1.26
	1700	0.80	1.00	1.25	1.43
CSB	2000	1.61	1.50	1.34	1.68
AAC	576	0.16	0.20	0.53	0.48
LAC open	720	0.17	0.26	0.61	0.60
	870	0.22	0.30	0.75	0.73
LAC closed	1760	0.44	0.66	1.43	1.48

large within a material, their possible influence on the correlation between permittivity and thermal parameters is not important for testing the hypothesis of its existence.

Regarding permittivity, the two cuboids per sample were measured independently. Repeated measurements of individual cuboids show clearly lower deviation than different cuboids of the same sample stone. The overall standard deviation of repeated measurements to the average value is about 1.5 %, which can be considered as uncertainty of the values. Values for comparison are available from the field of communication propagation. As stated in Section 2.3.1, an overview is available from an Ofcom project [31]. Specifically, Yahalom et al. [38] and Leschnik and Schlemm [39] list ε'_r values of 3.3 to 5.3 for bricks at 5 GHz and 2.45 GHz respectively, which is confirmed by ITU-R Recommendation P.2040-1 [40] giving $\varepsilon'_\mathrm{r} = 3.75$ at 1–10 GHz and by Abel and Wallace [41]. Only one value ($\varepsilon'_\mathrm{r} = 3.98$ at 2.45 GHz) for calcium silicate bricks was found in the literature [39]. Regarding lightweight concrete, values between 2 and 3 at 0–5 GHz can be found [36, 42]. For aerated concrete, ε'_r values of 2.04 at 2.45 GHz and of 2.26

at presumably 60 GHz were published [39, 236]. Although all these sources do not specify the density of their samples, the measurements presented here can be considered plausible as they fall within the range of the literature values. In addition, it should be emphasised again that great care was taken to create realistically dry materials, since high or unknown moisture contents influence the permittivity values considerably.

Regarding the density measurements, the type B uncertainty [237] resulting from reading the spring scale sums up to about 1 %. Density values were only obtained for a qualitative comparison and are irrelevant for the direct correlation between permittivity and thermal parameters.

All in all, the uncertainties of the material parameters are significantly smaller than the dispersion of the values and do not interfere with the conclusion on the hypothesis.

5.2. Case Study Quarter

Remote sensing recordings of the case study quarter included aerial IRT and TomoSAR. The surface temperatures evaluated through the former and the seasonal point movements measured by the latter are analysed and set into the context of UBEM by this section.

5.2.1. Surface Temperatures and U-values

In the following, the results of estimating surface temperatures from aerial IRT recordings of the case study quarter according to Section 4.2.2 are presented and checked against two state-of-the-art UBEM methods, namely SimStadt and the SHD approach (see Section 2.5.5). Large parts of this section originate from a collaborative publication on comparing different UBEM approaches [11].

Estimating U-values from the surface temperatures [184] determined according to the methodology presented in Section 4.2.2 would need a high amount of assumptions. To avoid this, the surface temperatures are used as indicators for building envelope insulation quality that can be obtained from remote sensing and compared to the results of the SHD approach and of SimStadt (both methods are presented in Section 2.5.5). Higher surface temperatures suggest higher U-values of the envelope because of higher heat transmission losses through the building envelope. In SimStadt, the U-values are intermediate results based on information from the IWU typology and material properties and are used for calculating the heat demand. The SHD approach uses specific heat demands of the IWU typology archetype buildings. The respective U-values are considered for the comparison although they do not influence the calculated heat demand directly. As a consequence of the different U-value assignment procedures and of a disagreement in identified archetypes for 27 % of the CityGML buildings, the U-values vary between the SHD approach and SimStadt even though both are based on the same typology.

Figure 5.5 shows the U-values of both approaches plotted against the mean IR-measured temperatures of all wall and roof surfaces for each building. As the U-values are based on typologies, they are discretely distributed. Furthermore, the SHD approach does not assign U-values to non-residential buildings and uses another definition of buildings coming from ALKIS that aggregates multiple CityGML buildings to a single one. This causes a large difference in the number of data points between Figure 5.5a and Figure 5.5b. Correlation coefficients of below 0.1 for all four cases (evaluating roofs or walls and SHD approach or SimStadt) lead to the conclusion of no correlation between the assigned U-values and the measured surface temperatures. The physical relationship between the *actual* values of these parameters is only indicated by two outliers with low U-values for the roofs and low surface temperatures. They represent the two most recently (2016) built residential buildings in the case study area. However, two data points are not sufficient to draw any further conclusions.

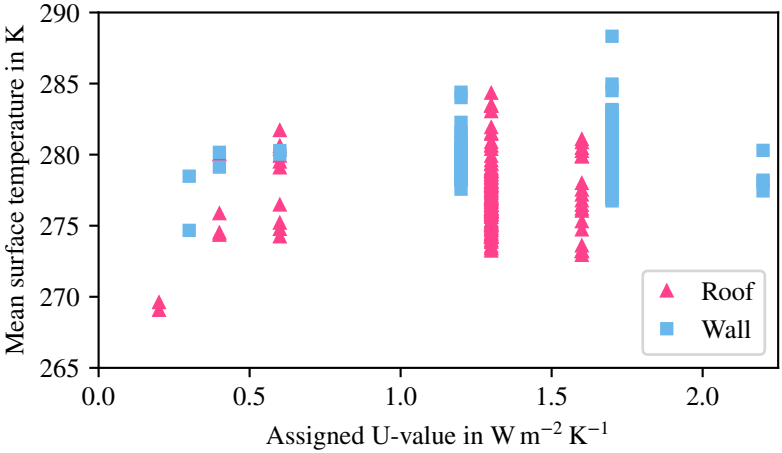

(a) *SHD approach.*

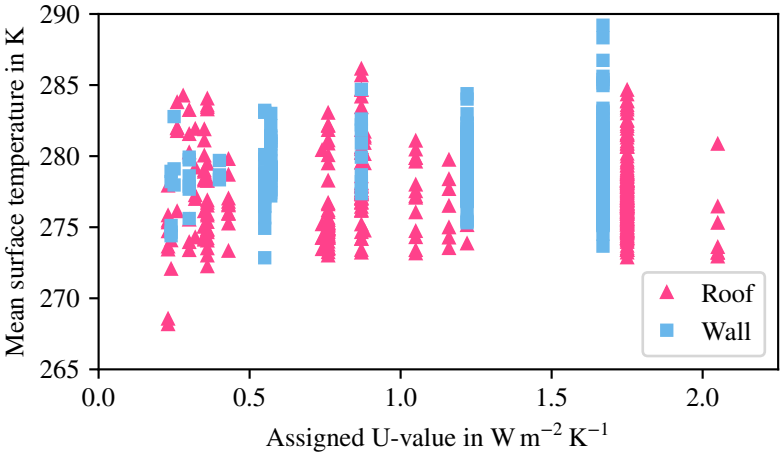

(b) *SimStadt.*

Figure 5.5.: *IRT-measured mean surface temperatures per building plotted against the U-values assigned by state-of-the-art UBEM approaches.*

The lack of correlation between the surface temperatures and the U-values indicates errors and uncertainties in measurement and/or the UBEM approaches. Some possible sources are listed in the following, but as they all depend on how the assumptions in the methods match the local conditions and ground truth data was not available, they cannot be quantified. The typology approaches make use of typical U-values, but the assignment of types to buildings depends on different geometric attributes of the building and can therefore lead to errors. Furthermore, refurbishments and/or more atypical building design may lead to differences between assumed and actual values. Consequently, since the building stock may have developed energetically in the last decades, the statistical value of "typical" values is uncertain. On the other hand, thermographically measured surface temperatures are not necessarily a reliable indicator for thermal transmittance as the corresponding indoor temperature is unknown and because of the non-stationary nature of the heat flow through the building envelope. Additionally, the measurement is influenced by the uncertainty of the camera itself as well as by atmospheric conditions, the radiation properties of surface materials, and radiance from surrounding objects and the sky.

Figure 5.6 shows the pairs of U-values and surface temperatures only for the roofs of residential buildings for which indicators for an apartment in the uppermost storey (see Section 4.2.3) lead to the assumption that the attic is inhabited and therefore heated. The focus on these roofs avoids a huge part of the uncertainty caused by the influence of indoor temperatures, surface radiation properties, and radiance from surrounding objects on the surface temperatures of walls. For both UBEM approaches, a certain grouping of several temperature values for equal U-values can be observed. From the outer appearance of the respective buildings, no physical background that would explain the phenomenon could be identified. However, some observations are striking:

1. The two clusters at about $0.4\,\mathrm{W\,m^{-2}\,K^{-1}}$ with temperatures above and below 275 K respectively both belong to comparatively new building complexes with flat roofs. The lower temperatures represent larger parts of the

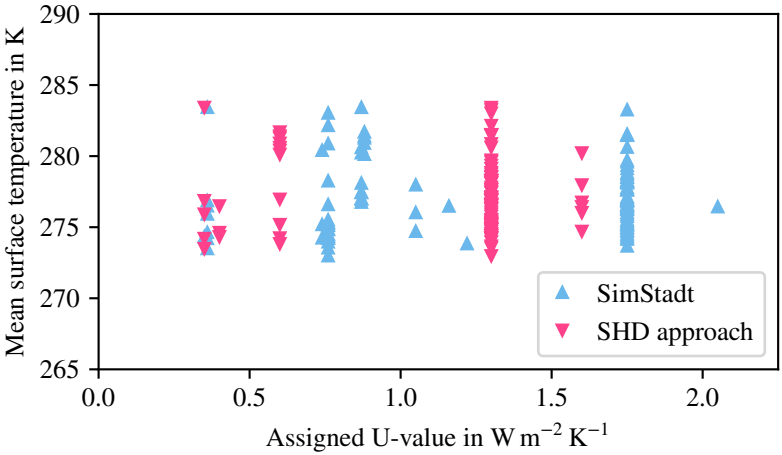

Figure 5.6.: *IRT-measured surface temperatures of residential building roofs (mean value per building) plotted against the U-values assigned by state-of-the-art UBEM approaches.*

complexes, while the higher temperatures are measured for very small, less tall parts. The temperature gap could for example be caused by different convective behaviour above the surfaces.

2. A remarkable share (9 out of 14) of the roofs with SimStadt U-values around 0.8 W m^{-2} K^{-1} and mean measured surface temperatures below 276 K have roof terraces that seem to be recently added, which points towards well-insulated roofs as one of the reasons for the low temperatures.

3. The outlier at about 0.4 W m^{-2} K^{-1} and 284 K results from a small low-rise building in between two much higher ones.

4. The large amount of values at 1.3 W m^{-2} K^{-1} and 1.76 W m^{-2} K^{-1} for the SHD approach and SimStadt respectively represents buildings originally built before 1919. For these, insulation and surface materials may have undergone multiple refurbishments in the meantime.

These challenges and observations lead to difficulties in the interpretation of the results, but also show the opportunities for future development of the approaches. Considering the findings of Schott, Biegel and Wilkinson [184] that buildings can be subdivided into U-value classes based on IRT, it is suggested that typologies can serve as a valuable source of a-priori information for such a method, e.g. for retrofit classification of building surfaces [17]. In this way, combining remote sensing and archetype approaches may improve the U-values used for modelling and simulation and thereby increase the reliability of UBEM results.

However, the results show that additional research and development is required to reduce uncertainties in IRT: First, segmentation methods may serve to reduce the analysed wall and roof surfaces to the part covered by the predominant material that the used emissivity is valid for. Second, these materials and their radiative properties, preferably including their dependence on the viewing angle, need to be known and individually assigned to the buildings, for example using hyperspectral techniques (as presented e.g. by Roessner et al. [238]). Third, more efficient algorithms may improve the modelling of the reflection of radiance from surrounding objects. Finally, deriving information about indoor temperatures could help calculating the relation between U-values and surface temperatures. One possible indicator are features visible on the 3D model textures (as done manually for heated attics here), analysed using machine learning. In the following, it is pointed out how TomoSAR evaluations may also be a potential source for the required information.

5.2.2. Seasonal Movements and Heated Attics

The seasonal scatterer movements measured through TomoSAR (see Section 3.5) were connected to the model roof surfaces of the case study quarter buildings as described in Section 4.2.3. As a result, the average vertical amplitudes of scatterers on the surfaces could be evaluated. The hypothesis was that buildings with unheated attics show a larger seasonal amplitude due to more thermal expansion

caused by larger changes in the temperature of interior materials. To test this hypothesis, the building stock was filtered for buildings whose uppermost storey could comparatively clearly be classified as heated or unheated by the aforementioned visual analysis. The result of the classification is pictured in Figure 5.7. Figure 5.8 shows the distributions of the yearly amplitudes of the vertical movements of rooftops with heated and unheated attics below them. It makes use of a per-building median to cancel out outliers that may result from neighbouring buildings or metallic structures on the outside.

The tendency towards higher amplitudes in the case of non-heated attics is obvious from the figure. However, the difference between the mean values of the distributions is low at 0.312 mm, which is about the sum of the standard deviations of 0.165 mm for heated and 0.146 mm for non-heated attics. As a consequence, this analysis can only hint towards the possibility of detecting heated attics with TomoSAR. There are several aspects contributing to a considerable uncertainty. First, the ground truth of the heating status of the attics is only assumed from visible inspections. Second, the binary differentiation between non-heated and heated attics does not reflect the nature of the phenomenon. In reality, the amplitude depends on the distance between attic floor and gable and on the structure and the materials used for the roof frameworks. In the case study quarter, the relatively uniform structure of the building stock with a high number of similarly built pre-1919 buildings makes this factor less important. Finally, for tilted roofs, scatterers have different distances to the floor of a non-heated attic or may even be on roof surface parts directly above the heated storey below the attic.

As a conclusion, the results suggest that the hypothesis of larger yearly vertical amplitudes of scatterer movements above non-heated attics is reasonable and that TomoSAR may have the potential to help identifying heated attics, thereby improving UBEM as indicated in Section 5.2.1. Nevertheless, a study with a larger set of buildings including ground truth information about the actual conditions of the attics is needed for the proof of practical applicability. If such applicability is given, the amplitudes may be used as sole indicator or be combined with textures

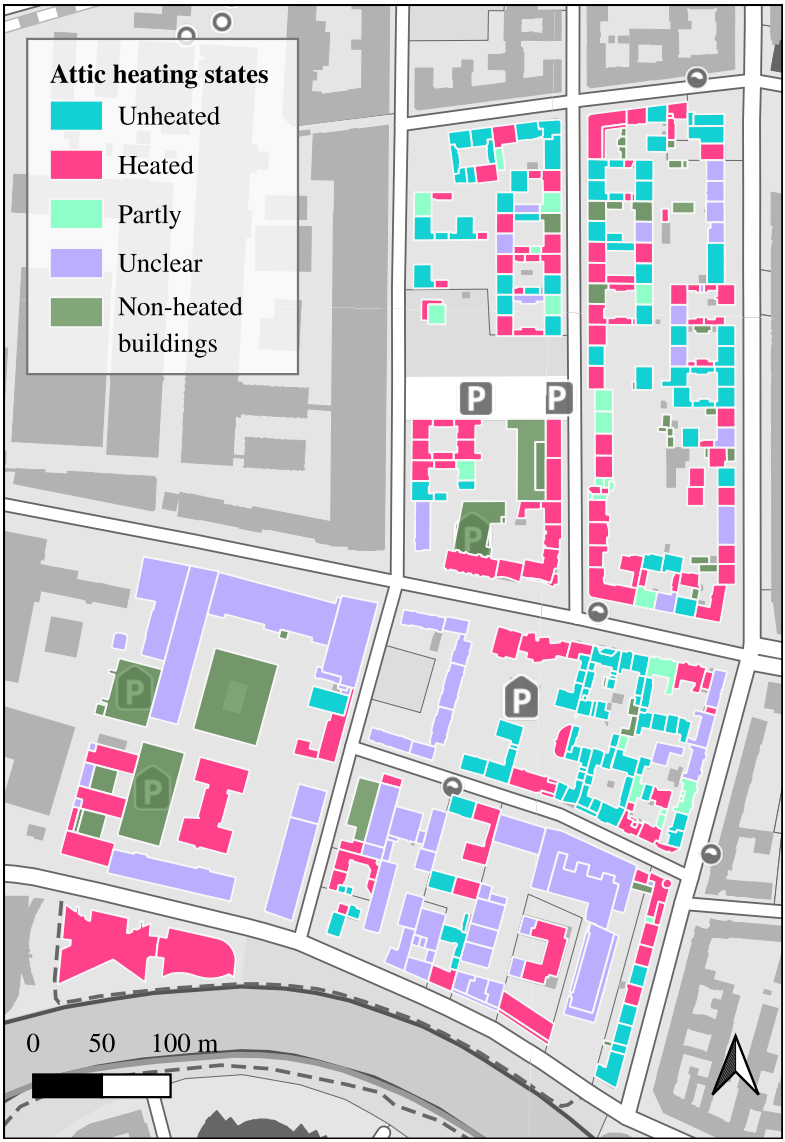

Figure 5.7.: *Result of a manual classification of the buildings in the case study area regarding the heating states of the attic. Background: basemap.de Web Vektor, © GeoBasis-DE / BKG 2024, CC BY 4.0.*

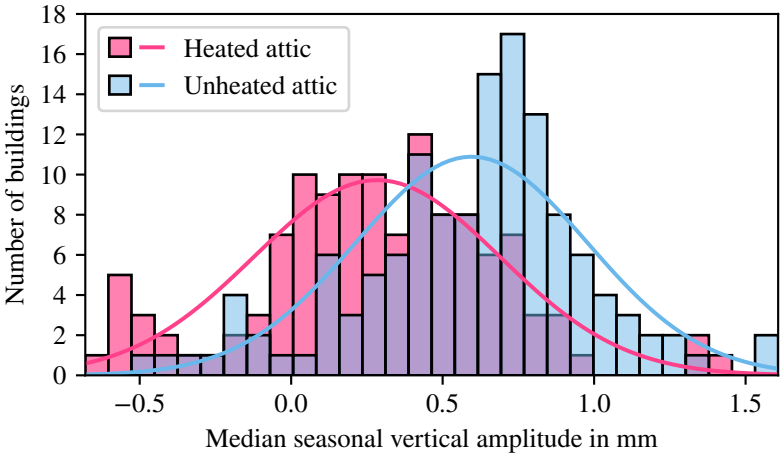

Figure 5.8.: *Distribution of the per-building median of TomoSAR-measured yearly amplitudes (bars) of scatterers on roofs for supposedly heated and non-heated attics in the case study area and corresponding normal distributions (lines).*

or 3D data in a machine-learning-based algorithm if sufficient training data can be generated. However, the existence of historical satellite data for an area to be investigated is required, which is not generally the case. In fact, Berlin was chosen for the project because of their availability.

5.2.3. Relevance for Practical Application

The practical relevance of the methods presented is focused on modelling a larger number of buildings, e.g. in a district or city, without having access to building properties that need to be individually assessed. Starting from three-dimensional building geometries that are already available in a large number of regions [86] or can be derived as presented in Section 3.4, thermal properties need to be enriched to the parts of the geometry. If building age classes are known from the cadastre, (or, as in Germany, from the census [239]), this can be done using a state-of-the-art archetype approach (see Section 2.5.5).

Data about refurbishments, heated attics, and window sizes are usually not available. Although these features may be investigated before building new infrastructure (like district heat networks), feasibility studies usually do not go into that depth and would profit from conveniently accessible datasets. Remote sensing could contribute here with

- windows detected from aerial imagery;
- heated attics assessed through TomoSAR evaluations;
- information derived from aerial thermal infrared about building elements (roof and/or wall parts) being insulated in the past.

A combination of the three could significantly reduce uncertainty in UBEM applications in early phases of heat infrastructure planning. As shown in the previous sections, some issues regarding technical feasibility remain.

5.3. Case Study Building

The first step in modelling the case study house separates the storeys as described in Section 4.2.4, making use of the window positions depicted in Figure 3.16. Figure 5.9 shows the resulting wall polygons and ceiling heights. The basement floor-to-ceiling height was introduced with a measured value of 2.07 m. Taking the actual conditions of the building and default air exchange rates according to ISO 13789 [157] into account, the internal volume is separated into three zones:

1. the unconditioned attic with an air exchange rate of $10\,\mathrm{h}^{-1}$ resulting from open joints between roof tiles;
2. the unconditioned basement with an air exchange rate of $1\,\mathrm{h}^{-1}$ due to small ventilation openings, but no localised open joints;
3. the heated zone including ground floor and first floor.

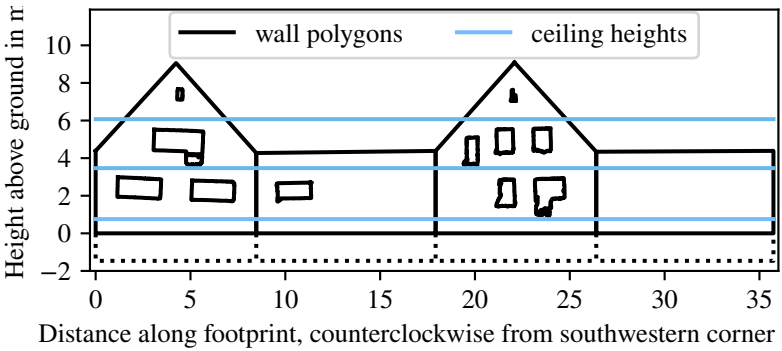

Figure 5.9.: *Projected wall polygons with ceiling heights automatically detected from window positions. Dotted lines mark wall polygons below ground [17]. Note that the inclination of the window polygons result from the projection between the CityGML models described in Section 3.4.*

This process was already presented with preliminary results at the *Building Simulation 2019* Conference [14]. In that context, it was found that the preliminary CityGML model underestimated the actual size of the building. As elaborated in Section 3.4, the point cloud was corrected afterwards and the new CityGML representation used here was generated.

Through the overall process illustrated in Figure 4.13, simulation models for the case study building were generated for use in Modelica. Figure 5.10 shows the graphical representation for the top level of the model. The variations described in Section 4.3.3 were each processed into Modelica representations to perform three different types of computations. First, the measurement campaign was simulated using the recorded exterior conditions and heat loads. Second, the annual heat demands for the existing building and a refurbishment scenario of each variation were determined using the local test reference year. Third, the HTC of the whole building was calculated, simulating a steady state situation. In this section, which is based on and partly reproduces previous contributions to the *Buildings* journal [17] and the *International Modelica Conference* [18], the results are presented and discussed.

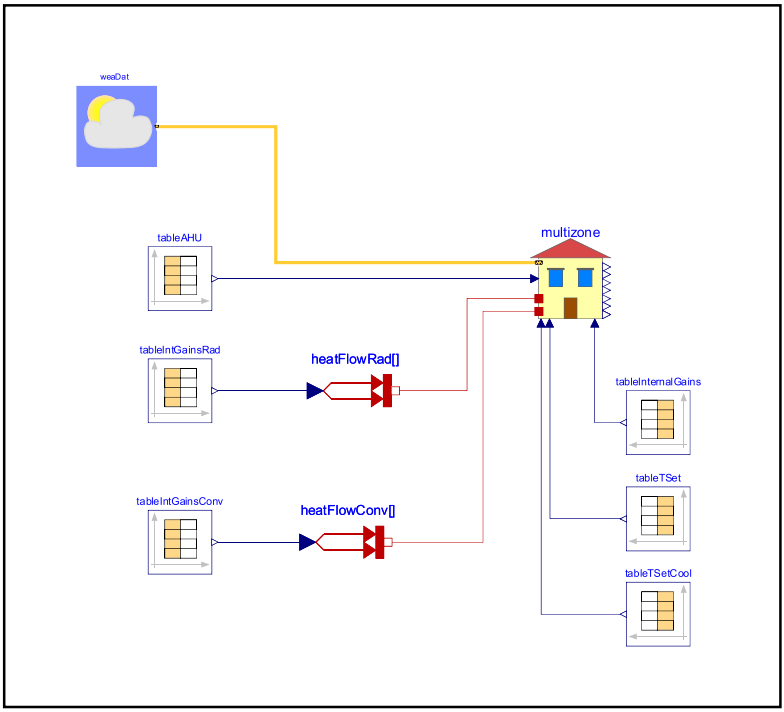

Figure 5.10.: *Graphical representation of the top level of the Modelica simulation model to reproduce the measurement campaign. The details of the* `multizone` *block are shown in Figure 2.6.* `weaDat`*,* `tableIntGainsRad`*, and* `tableIntGainsConv` *contain the exterior conditions as well as radiative and convective interior gains respectively. The other tables are filled with blank values.*

5.3.1. Simulation of the Measurement Campaign

To test the ability of the model to reproduce the dynamic thermal behaviour of the building, the simulated interior temperatures of the model variations 1 to 4 (see Section 4.3.3 for details of the simulation setup) are compared to the measured ones. Figure 5.11 shows measured and simulated values of the mean air temperature for the heated zone of the building over the course of the campaign. The comparison of the five graphs leads to several observations that allow conclusions on the suitability of the model:

1. For the conditioned zone, the results show that the two variations with automatically estimated interior surfaces areas (1 and 2) fit very well to the measurement in periods without a steep increase or decrease of the temperature (February 11 to 16 and 22 to 26). Variation 3 with the actual surface areas shows a tendency to overheat (February 7 to 12) and cool down too much (February 20 to 26). However, given that the thermal properties of the building were taken from the typology rather than from actual values, differences to the measured temperatures are not relevant for an evaluation of the model.

2. Variation 4 containing the best knowledge of the actual building shows an overall good agreement to the measured temperatures, especially when considering that the zone is actually divided into six rooms of which one (the kitchen, located in the ground floor) heated up much more quickly than the others and kept a temperature of about 37 °C from February 9 until the start of the cooldown due to the placement of the largest heater (see Figure 3.8). Furthermore, the influence of the fans (intended to homogenise air temperatures) on convection was not modelled. The root-mean-square error (RMSE) for the hourly temperature difference between February 5, 15:00 and February 26, 24:00 is 1.13 K. Obvious deviations occur during warm-up (too slow until February 8, slight overheating afterwards; overall RMSE 1.51 K between February 5, 15:00 and February 13, 11:00) and

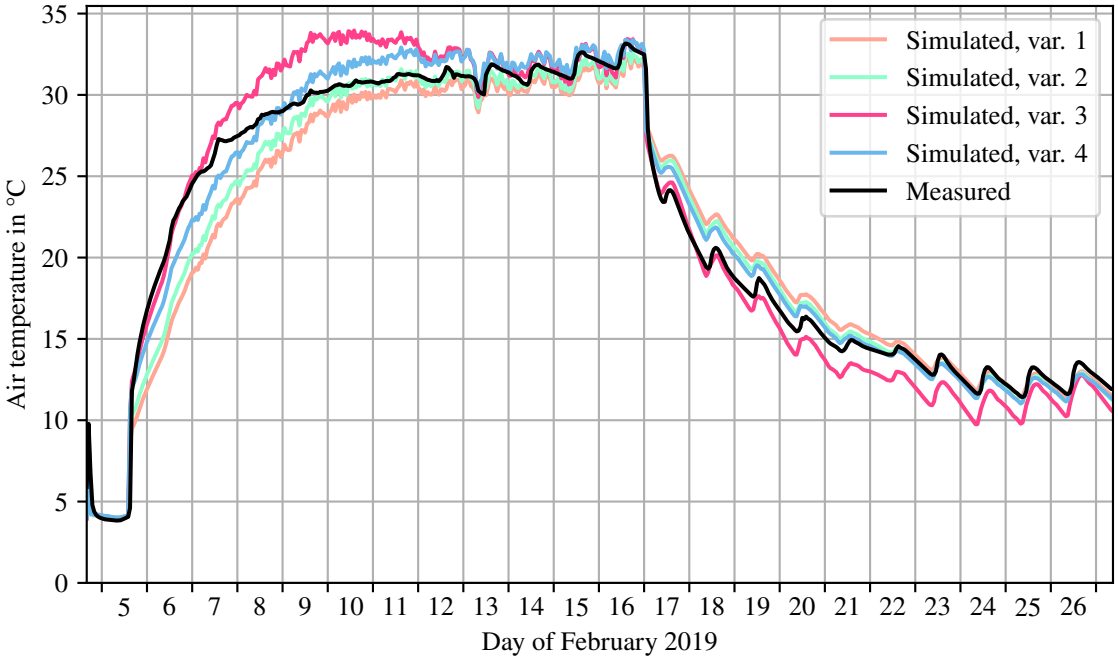

Figure 5.11.: *Mean air temperature of the heated zone of the case study building during the measurement campaign in February 2019, measured and simulated using model variations 1 to 4 (see Section 4.3.3).*

cooldown (overall RMSE 0.90 K between February 17, 1:00 and February 26, 24:00). In the period of approximately constant temperature between February 13, 12:00 and February 16, 24:00, the simulated temperature is mostly overestimating the measured temperature to a minor degree with an RMSE of 0.59 K. A possible explanation for the mismatch in the speed of heating up and cooling down is that the simplified resistance-capacitance representation of the exterior walls in Modelica cannot exactly model the dynamic behaviour of the actual walls. They are mostly composed of light-weight concrete with low heat capacity on the inside and bricks with high heat capacity on the outside and therefore will store heat further outside than their model representation and react faster to changes in the heat flow from the building interior.

3. The sensitivity to changing interior masses is also interesting. Here, the reduction by 22.5% from variation 1 to 2 has an only minor impact. The additional reduction by 31.8% (approximately the same absolute reduction) to variation 3 changes the model behaviour to a far larger extent. Although this calls for further investigations into the sensitivity of the ROM, the different variations are comparable in times with dynamic loads in the magnitude of those appearing in usual application cases, i.e. interior temperatures of conditioned zones being kept within a range of a few K.

4. In the original publication on TEASER, Remmen et al. compare dynamic heat loads of a German archetype model to a detailed model of a similar Belgian house to assist "in achieving a better understanding of assumptions made and limitations of the archetype approach" and call for extending "[s]uch detailed model comparisons [...] to additional archetypes in future research" [108]. The agreement between simulated and measured values is better for the measurement at the case study building, which points towards the applicability of the overall approach, at least for this specific age and size class.

In Figure 5.12, the mean air temperatures of the unheated zones (basement and attic) are visualised. Here, the difference in daily fluctuations of the basement temperature between measured (almost no fluctuation) and all four simulated air temperatures (about 1–5 K) might be the result of an overestimated air exchange rate or of the model neglecting the vertical temperature distribution in the heated zone.

As simulated attic temperatures are very similar, the lines for variation 3 and in part 4 largely cover the others. A poor performance of variation 4 is apparent between February 13 and February 18 during night times. Possible reasons are the same as for the deviations in basement temperatures. Variation 3 compensates these issues by a higher-than-actual U-value ($0.84\,\mathrm{W\,m^{-2}\,K^{-1}}$ instead of $0.52\,\mathrm{W\,m^{-2}\,K^{-1}}$) for the interzonal ceiling.

5.3.2. Determination of the Heat Demand

The annual heat demands for all six model variations of Table 4.2 were calculated by running simulations for the complete DWD test reference year under the standard interior and exterior conditions defined by DIN V 18599-2 [95].

Additionally, a retrofit scenario for each of them was created using the additional insulation layers applied by the TABULA advanced retrofit scenario (30 cm to the rooftop and attic floor, 24 cm to the outer walls, and 12 cm to the basement ceiling; each with a thermal conductivity of $0.035\,\mathrm{W\,m^{-1}\,K^{-1}}$) and inserting new windows with a U-value of $0.80\,\mathrm{W\,m^{-2}\,K^{-1}}$ [151].

First of all, this approach calls for a comparison between the results of the simulation and of the DIN V 18599-2 [95] monthly evaluation method. Following the conventions used by the standard (see Section 2.5.2), Figure 5.13 compares the contributions to the heat demand $Q_{\mathrm{h,dem}}$ as annual sums of the heat sources from internal gains $Q_{\mathrm{int,source}}$ and solar gains through the windows $Q_{\mathrm{sol,tr}}$ and of the heat losses by transmission Q_{t} and by ventilation Q_{v} for both the cases with

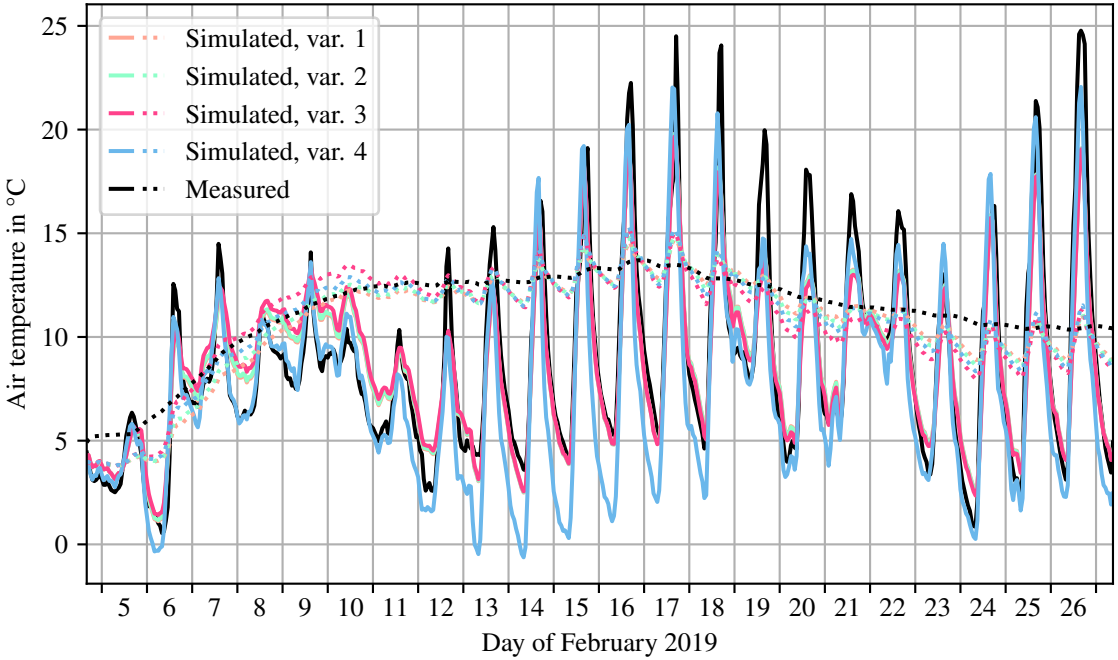

Figure 5.12.: *Mean air temperatures of the unheated zones of the case study building (solid lines: attic, dotted lines: basement) during the measurement campaign in February 2019, measured and simulated using model variations 1 to 4 (see Section 4.3.3).*

and without retrofit, exemplarily for variation 6. Heat bridges are not covered by the AixLib ROM. The transmission losses due to them $\Delta Q_{\mathrm{t,hb}}$ are therefore pictured separately. It must be noted that the different contributions do not simply sum up to the annual demand due to the monthly evaluation. For example, solar gains in summer contribute to the annual sum of heat gains through the windows, but do not reduce the heat demand significantly. To a lesser extend, deviations in the transmission and ventilation losses between simulation and monthly balance in months with a very low heat load do influence the contribution bars in the figures, but not the annual sum. Appendix A.2 contains figures with a more detailed monthly evaluation. From the comparison, it is concluded that the demand calculated by annual simulation matches the monthly balance values satisfyingly well.

Figure 5.14 shows that the difference in internal thermal mass between variations 1 to 3 have a minor impact on the annual heat demand, presumably due to the set-point reduction of the heating during the night. On the one hand, the small difference between variations 3 and 4 shows that the case study building is a good representative of its TABULA type. On the other hand, the high difference between the heat demands of variations 5 and 6 may give a feeling for the width of the distribution of energy performances of buildings with similar age and construction type and illustrate that the randomly chosen case study building could as well have been more or much less energy-efficient. The deviations of $-20\,\%$ and $+34\,\%$ to the demand of variation 3 indicate the magnitude of the confidence region. Even though the demands in the retrofit scenarios do not differ considerably between best and worst case, owners would choose their retrofit options based on savings compared to the status quo. This emphasises the high importance for the *difference* between the heat demands in the existing state and a potential retrofit scenario, an aspect that is further discussed in Section 5.4 about the model sensitivity.

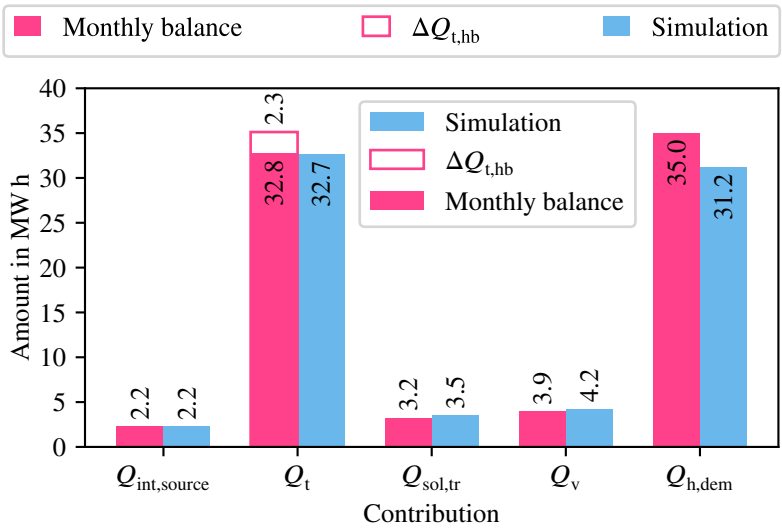

(a) *Without retrofit.*

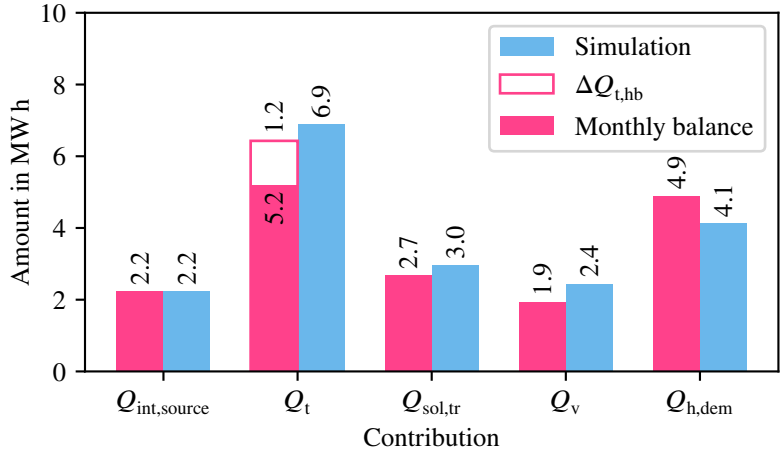

(b) *Advanced retrofit scenario.*

Figure 5.13.: *Contributions to annual heat demand calculated by monthly energy balance (DIN V 18599-2 [95]) and simulation.*

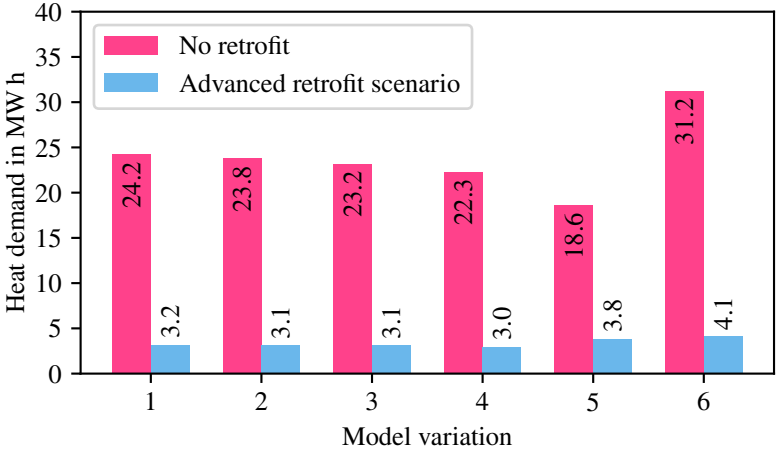

Figure 5.14.: *Simulated heat demand of the case study building in its existing state and in retrofit scenarios for all six model variations presented in Section 4.3.3.*

5.3.3. Determination of the Heat Transfer Coefficient

Figure 5.16 shows calculated and measured HTC values for the case study building. The measured one was derived as the ratio of heating power supplied and air temperature difference for a period during the measurement campaign with approximately constant ambient and interior air temperatures. Although the boundary conditions neither for the co-heating test nor for the QUB method (see Section 2.6.5) could be fulfilled during the case study, the result is considered reliable due to the high number of measurement equipment that indicate nearly steady-state conditions for a period before sunrise on February 11 (3:00 to 8:00, see Figure 5.15).

For the steady state simulation results, the soil temperature was assumed equal to the ambient temperature, which reflects the situation during the measurement. Nevertheless, values are generally below the summed value of transmission and ventilation HTC calculated following ISO 13789 [157]. The ISO standard does not account for interior thermal masses, which results in equal values for the

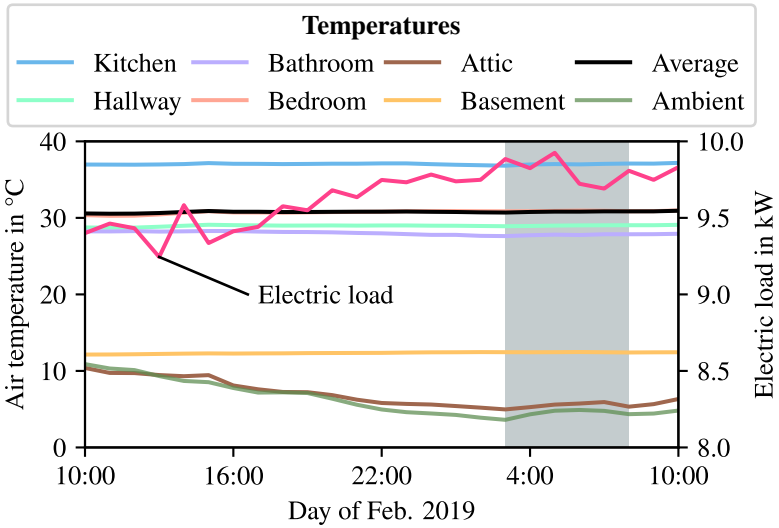

Figure 5.15.: *Measured temperatures of selected rooms and volumetric average for the heated part of the case study building, along with the total electric load of all appliances (extraction from Figure 3.8), with HTC evaluation period marked in grey.*

model variations 1 to 3. The AixLib simulation model includes radiative heat transfer between interior surfaces of envelope components and interior component surfaces. On the one hand, this leads to slightly decreasing HTC values from variation 1 to 3. On the other hand, it increases thermal resistances between interior surface and zone air temperature, causing the difference to the calculated values.

All in all, HTC values simulated through the realistic model variations (1 to 4) are within a 14 % range below the measured value. As the circumstances (simple geometry of the building, relatively accurate U-values in the model) are beneficial, this range cannot be taken as the general uncertainty of the method. For example, increased convection caused by the fans causes an increase in the measured HTC. For variation 3, increasing the internal convection coefficients of the

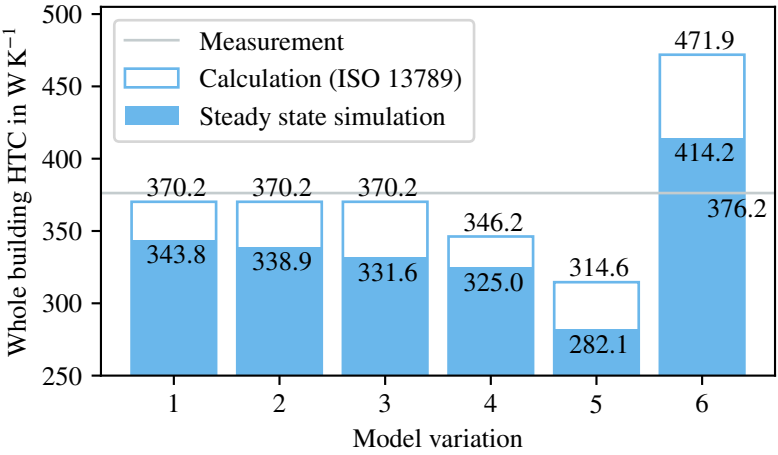

Figure 5.16.: *Comparison of HTC values (including ventilation) from a steady-state simulation and from a calculation according to ISO 13789 for the model variations (see Section 4.3.3) with the measured value of the case study building.*

heated zones by 4 W m^{-2} K^{-1} (which is equivalent to an increase in the wind speed of 1 m s^{-1} when concerning ISO 6946 [115]) results in a simulated HTC value of 376.7 W K^{-1}. Furthermore, the best-/worst-case model variations (5 and 6) lead to a difference to the measured value of −25 % and +10 % respectively. As a consequence, accurate U-values measured by infrared thermography or other techniques would increase the reliability of determined values considerably. However, the fact that the HTC does not account for solar gains, air infiltration, and interior thermal masses makes it measurable through the presented method with smaller uncertainty than the heat demand. This is also illustrated by the low or non-existing differences between variations 1 to 3.

5.4. Model Sensitivity

With the aim of assessing the building model generation method presented in this thesis, an approach to calculate the sensitivity towards different input parameters was presented in Section 4.4. The results of this sensitivity analysis are presented in the following.

Three different output quantities are investigated for the case study of the single-family house in Morschenich: the annual demand of both pre-retrofit and post-retrofit state as well as the annual savings reached by retrofit, defined as the difference between the two demand values. Although this section presents results for the sensitivity of these three values towards different input parameters, the results do not allow conclusions on general data requirements for demand calculations or for retrofit investment decisions, but only on the sensitivity of the method presented.

5.4.1. Convergence

The sensitivity analysis is based on sampling the parameter space. As a consequence, the validity of results can only be made sure if they converge for a sufficient number of subsequent sample sizes. Burhenne [232, p. 160] (as described in Section 4.4.2) accepts convergence if estimators from three subsequent sample sizes are within a range of $\pm 5\,\%$ compared to the estimator for the largest sample size as a reference result. Figure 5.17 includes the estimators for total sensitivity of the pre-retrofit heat demand towards all input parameters listed in Table 4.4 and the sum of these estimators $\sum_i S_{\mathrm{T}i}$ over a range of sample sizes from $N = 2$ to $N = 2048$ as well as the respective deviation to the final value at $N = 2048$ as a reference value. The graphics show that convergence is reached without exception.

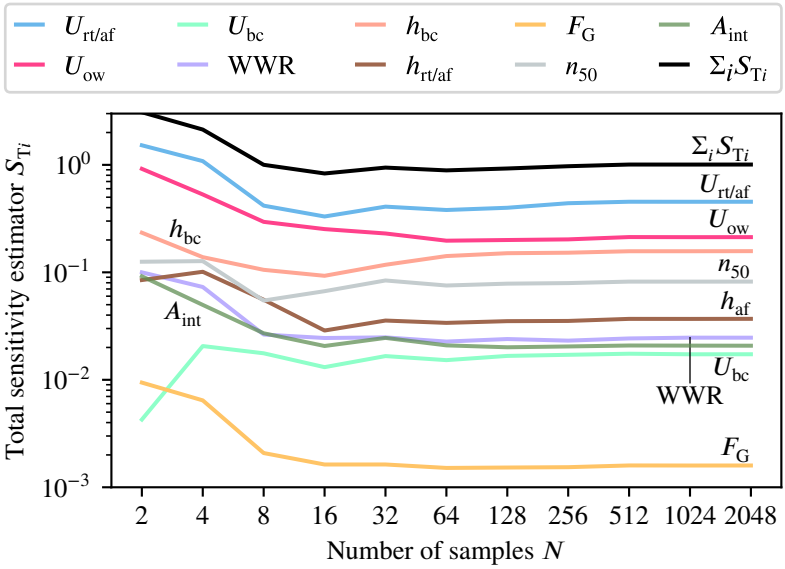

(a) *Total sensitivity estimators.*

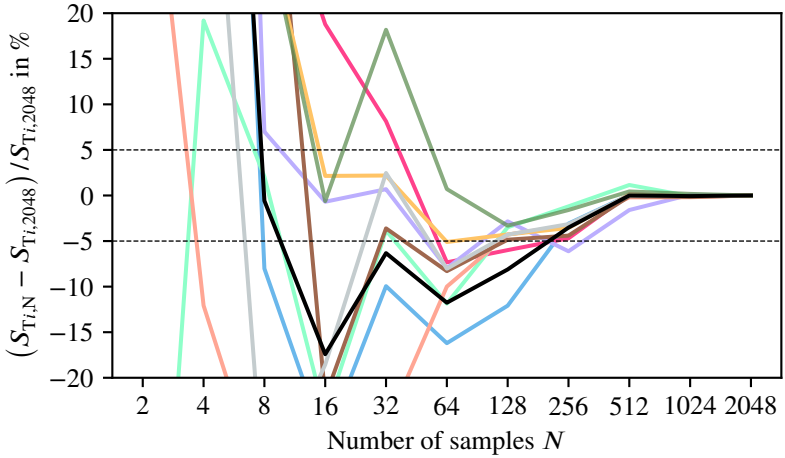

(b) *Deviation of total sensitivity estimators to the respective reference results.*

Figure 5.17.: *Convergence of total sensitivity estimators regarding pre-retrofit heat demand.*

Appendix A.3.2 contains similar graphics for the estimators of total and first-order sensitivities regarding all three output quantities. Convergence is reached for almost all values with a few exceptions. The **total sensitivity** estimator does not fully converge for $S_{\mathrm{T,WWR}}$ regarding energy savings. However, deviation at $N = 512$ is only slightly above the threshold and the estimator has a small value at $S_{\mathrm{T,WWR},2048} = 1.94 \times 10^{-3}$, which is why the result is considered acceptable. The **first-order sensitivity** estimators do not converge for the input parameters A_{int}, WWR and F_{G} regarding both pre-retrofit demand and savings. In all cases, values are small (< 0.03). Due to the disproportionally high computation effort for higher sample sizes and the convergence fulfilling Burhenne's alternative criterion of $\sum_i S_i$ within $\pm 5\,\%$ for four subsequent sample sizes, the results are considered acceptable for evaluating the model generation method as a whole.

5.4.2. Sensitivity of Demand Values

The goal of the sensitivity analysis is to find the influence of the several input parameters on the model output. Three different model outputs were considered.

Pre-retrofit Demand

Table 5.3 lists the sensitivity estimators regarding pre-retrofit heat demand for all input parameters, ranked by their importance. Figure 5.18 shows the same values as a bar diagram to visualise the share of variance explained by each parameter. The first conclusion to be drawn from similar values for first-order and total sensitivities is that interactive effects play a minor role in the model. Furthermore, it becomes obvious that U-values account for about two thirds (68 %) of the variance in pre-retrofit heat demand. U-values of roof, attic floor, and outer wall are particularly important. Storey positions and airtightness also account for a considerable share of variance. All in all, a mean heat demand of 29 732 kW h and a variance of $(3278\,\mathrm{kW\,h})^2$ is observed in the sample. These values, taken from

Table 5.3.: *Final estimators for the sensitivity analysis regarding pre-retrofit heat demand.*

Rank	Parameter	S_i	S_{Ti}
1	$U_{rt/af}$	4.52×10^{-1}	4.54×10^{-1}
2	U_{ow}	2.09×10^{-1}	2.13×10^{-1}
3	h_{bc}	1.54×10^{-1}	1.57×10^{-1}
4	n_{50}	8.22×10^{-2}	8.20×10^{-2}
5	h_{af}	3.52×10^{-2}	3.69×10^{-2}
6	WWR	2.27×10^{-2}	2.47×10^{-2}
7	A_{int}	1.99×10^{-2}	2.08×10^{-2}
8	U_{bc}	1.74×10^{-2}	1.73×10^{-2}
9	F_G	1.68×10^{-3}	1.59×10^{-3}
Sum		0.9936	1.0069

A and B matrices of the Sobol' samples (see Section A.3.1), converge faster than sensitivity estimators as depicted in Figure A.18 in the Appendix.

Post-retrofit Demand

Ranked sensitivity estimators regarding post-retrofit heat demand are summarised in Table 5.4 and Figure 5.19. Again, differences between first-order and total sensitivities are small, which points to small interactive effects. In the absence of uncertainty in $U_{rt/af}$, n_{50}, and F_G and almost entirely in U_{bc} and U_{ow}, the prevalence of geometric parameters is not surprising. WWR being ranked higher here than h_{bc} and $_{af}$ is presumably caused by a combination of two effects: First, the difference of wall and window U-values is still at about $0.7\,\mathrm{W\,m^{-2}\,K^{-1}}$, but the relative relevance of the higher heat losses are bigger now. Second, solar gains have an increased relevance during the heating period after retrofit. A similar effect is observed for the absolute values. The sample shows a mean heat demand of 5577 kW h and a variance of $(612\,\mathrm{kW\,h})^2$. Although the absolute value is clearly lower than for pre-retrofit, relative deviation is similar.

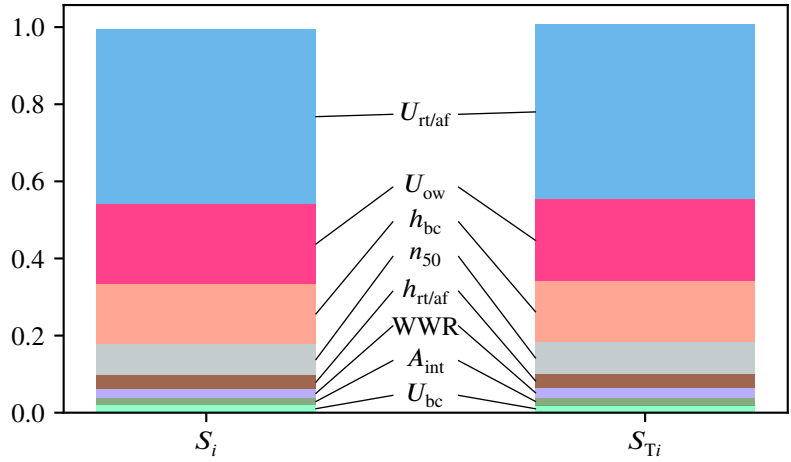

Figure 5.18.: *Stacked bar diagram of final estimators of first-order and total sensitivities regarding pre-retrofit heat demand. Sensitivities towards F_G are not labeled due to very small values.*

Table 5.4.: *Final estimators for the sensitivity analysis regarding post-retrofit heat demand.*

Rank	Parameter	S_i	S_{Ti}
1	WWR	7.26×10^{-1}	7.33×10^{-1}
2	h_{bc}	2.32×10^{-1}	2.40×10^{-1}
3	h_{af}	2.77×10^{-2}	2.84×10^{-2}
4	A_{int}	3.15×10^{-3}	3.27×10^{-3}
5	U_{bc}	2.90×10^{-3}	2.87×10^{-3}
6	U_{ow}	1.19×10^{-3}	1.10×10^{-3}
Sum		0.9921	1.0085

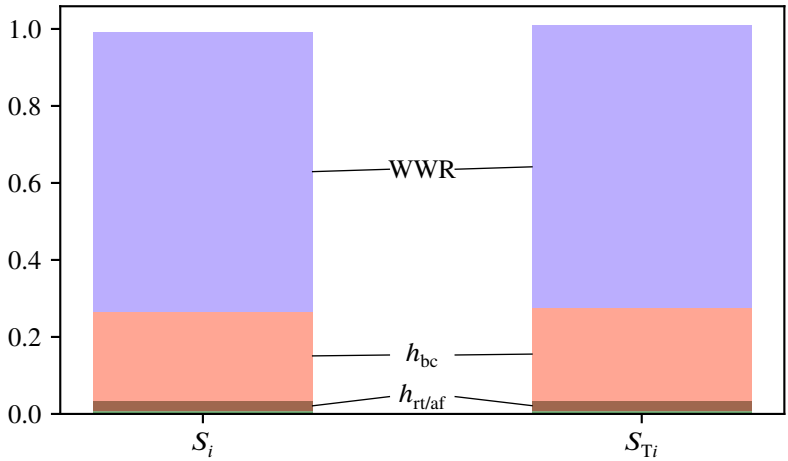

Figure 5.19.: *Stacked bar diagram of final estimators of first-order and total sensitivities regarding post-retrofit heat demand. Sensitivities towards A_{int}, U_{bc}, and U_{ow} are not labeled due to very small values.*

Savings

Mean savings in the sample are 24 155 kW h, with a variance of $(3096\,\mathrm{kW\,h})^2$. The savings are the difference between pre-retrofit and post-retrofit demand values. Influences of both output quantities can be observed in sensitivities regarding energy savings. However, as the order of magnitude in pre-retrofit variance is higher than for post-retrofit, the estimators displayed in Table 5.5 and Figure 5.20 are similar as for pre-retrofit values. The most obvious example is the WWR, which also has an invalid first-order estimator $S_{\mathrm{WWR}} < 0$. $S_{\mathrm{WWR}} \approx 0$ is most likely caused by larger windows resulting in higher demand values pre-retrofit (due to low window U-values), but lower demand values post-retrofit (due to solar gains). These two effects nearly cancel out when looking at the difference, and the estimation method applied is not robust regarding first-order estimators falling below zero.

Table 5.5.: *Final estimators for the sensitivity analysis regarding heat demand savings by retrofit.*

Index	Parameter	S_i	S_{Ti}
1	$U_{rt/af}$	5.06×10^{-1}	5.08×10^{-1}
2	U_{ow}	2.27×10^{-1}	2.32×10^{-1}
3	h_{bc}	1.03×10^{-1}	1.06×10^{-1}
4	n_{50}	9.21×10^{-2}	9.19×10^{-2}
5	h_{af}	2.74×10^{-2}	2.93×10^{-2}
6	A_{int}	1.91×10^{-2}	2.00×10^{-2}
7	U_{bc}	1.67×10^{-2}	1.66×10^{-2}
8	WWR	-3.13×10^{-4}	1.94×10^{-3}
9	F_G	1.89×10^{-3}	1.79×10^{-3}
	Sum	0.9930	1.0078

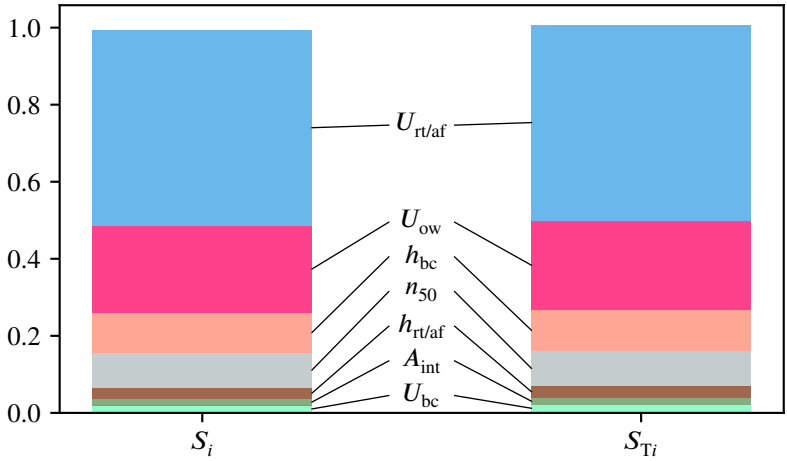

Figure 5.20.: *Stacked bar diagram of final estimators of first-order and total sensitivities regarding savings by retrofit. Sensitivities towards F_G and WWR are not labeled due to very small values.*

5.4.3. Robustness

The initial question of the sensitivity analysis was how robust the results are towards the uncertainty in assumed or measured model parameters. The findings presented above show a variance equivalent to 10 % of pre-retrofit demand and savings by retrofit for the case study example. It is mainly caused by uncertainty regarding the U-value of important building elements. Geometric parameters are of minor importance, but accurate window size data is crucial for precise post-retrofit demand calculations.

These results show that reliable data from the parts of the project approach (see Figure 3.1) that were not yet implemented in the case study evaluation workflow, namely infrared thermography and microwave radar for the measurement of exterior elements, hyperspectral imagery for surface classification, and acoustic leakage detection, would have different impact on the robustness of the results. Better data about exterior elements from IRT and radar could reduce uncertainty about U-values significantly. Surface classifications could improve data about window sizes and therefore about post-retrofit demand, but given the expensive sensors and their coarse resolution (see Section 3.2.3), improvements in state-of-the-art evaluations based on visual images or laser scans seem more promising for the task. Air leakage detection would not have an obvious high impact for the given case study. However, it could not only improve results in cases where ventilation losses are higher, but also simplify leakage detection after retrofit if the compulsory airtightness assessment after retrofit fails.

5.5. Practical Relevance

The previous sections suggest that to a large extend of about two thirds, envelope thermal quality explains the variance in demand values calculated by applying the method presented in this dissertation consisting of

1. taking RGB images of the building during a pre-planned UAV flight;
2. photogrammetrically evaluating these pictures, generating a point cloud representing the building envelope;
3. automatically reconstructing the wall, roof, and window surfaces out of the point cloud;
4. detecting storey ceilings from window positions;
5. assigning typical constructions (and recommended retrofit options) considering the building age and type;
6. simulating the resulting model for a full year with standard boundary conditions.

Geometric parameters are mainly relevant for post-retrofit demand, but the order of magnitude in post-retrofit variance is lower than for pre-retrofit and for savings by retrofit. Although the uncertainty ranges of input parameters were chosen in the absence of objective distributions, the stark difference in quantitative sensitivity estimators point toward their ranking being valid for an evaluation of the method. However, it must be stressed again that the results cannot be interpreted as general data requirements for demand calculations or for retrofit investment decisions, but only regarding the sensitivity of the method presented and applied to the case study building.

Looking at the high importance of envelope thermal quality for both pre-retrofit demand and energy savings, it becomes clear that the overall reliability of the building analysis approach would benefit from an increased accuracy in the measurement of U-values by complimentary remote sensing techniques. However, as stated in Section 2.6.2, measurements through quantitative infrared thermography [176] currently must be considered more uncertain than typology values. Other standard procedures [156, 175] are too laborious for the goal of a fast, automatable, and hence inexpensive approach.

6. Conclusion

The preceding chapters presented different aspects of how remote sensing can contribute to fast, reliable and automatable energy assessments in the building stock. The scale of the applications ranges from district level to single buildings and material investigations for use on individual construction elements. This conclusion summarises the research presented in the dissertation and checks the results against the initial hypothesis that the investigated remote sensing methods have the potential to be used in automatable workflows that reduce the effort to gather data about existing buildings in a quality that is sufficient to inform the decision process about measures like efficiency improvements, district heat networks, and renewable energy implementations.

6.1. District and Municipal Scale

For a case study quarter in Berlin-Moabit, infrared thermography and TomoSAR scatterer amplitudes were evaluated with the help of a semantically annotated polygonal 3D model of the building stock generated from oblique aerial imagery.

IRT polygon textures were corrected for atmospheric influences, different surface emissivities, viewing directions, and reflected radiance from the surroundings to derive average surface temperatures. The availability of the textured model was

highly beneficial for the task and improves the applicability of IRT for district-scale building analysis and for incentivising retrofits by making heat losses visible. Nevertheless, no correlation was observed between the measured surface temperatures and the typical U-values for the corresponding building ages and types. Most likely, this is caused by independent uncertainties in measurement results and typology respectively. If these uncertainties are reduced by improvements in data acquisition and evaluation systems, aerial IRT is expected to be applicable for estimating urban façade and roof U-values or for detecting already executed energy retrofits, which would close an important data gap for district heat projects and municipal heat planning.

TomoSAR has been found to be applicable to analyse roof surfaces for seasonal movements and may classify the respective buildings into having heated or unheated attics, which is relevant for estimating the heated volume of a building and therefore for calculating its heat demand. The availability of this information would thereby contribute to the reduction of uncertainty in IRT or similar UBEM evaluations and would enable urban planners to detect potential for additional living space in densely populated areas. The method is particularly interesting because it does not require dedicated measurements. However, its applicability is restricted to regions where sufficient historical satellite recordings are available.

6.2. Single-building Scale

With the help of a custom Python class model, a dynamic energy simulation model for a single-family house in Morschenich was generated from UAV imagery, typology values, and simple additional information as well as on-site measurements. The steps presented in this thesis complete a collaboratively developed highly automated workflow shown in Figure 4.13. For this purpose, the UBEM-oriented combination of the open-source tools TEASER [108] and AixLib [104] was adapted for improved applicability on single-building scale. Most importantly, a

more detailed modelling of building elements relevant for heat loss, including zone borders, was made possible. The model of the case study building was applied to simulate its dynamic thermal behaviour during a measurement campaign consisting of heating the building up from ambient temperature, keeping it at an approximately constant temperature, and letting it cool down freely. The results show an accurate reproduction of the internal temperatures.

Heat demand estimates can be assessed by simulating the thermal performance of the building during a test reference year. The model also allows to calculate whole building heat transfer coefficients. They match values according to ISO 13789 [157] well and deviate from the measured value by between $-8\,\%$ and $-12\,\%$. As this is also possible after adapting the model components according to standard retrofit options, the overall approach allows to calculate pre- and post-retrofit heat demands or heat transfer coefficients quickly, automatically, and therefore inexpensively. Hence, it enables the user to compare possible savings of potential refurbishment scenarios.

The relevant standards and legislation consider typical U-values and simplified geometry measurements appropriate to some extent. This includes the archetype values and photogrammetric methods used for the presented approach. Taking this into account, it is already close to practical applicability. Some improvements still would be beneficial. In a sensitivity analysis, it was found that envelope thermal quality explains the largest part of variance in pre-retrofit demand and savings by retrofit for an exemplary application to a single-family house. The accuracy of heat demand and therefore retrofit saving estimates would benefit substantially from U-values measured on site. Furthermore, the importance of solar gains for post-retrofit demand calls for a better window detection process.

6.3. Single-wall Scale (Material Investigations)

On the scale of single building elements, the method envisaged for application includes scans with microwave SAR and calculates wall layer permittivities based on the resulting imaging data [15]. As a part of this thesis, the question was raised if a correlation between permittivity and thermal material properties (thermal conductivity and volumetric specific heat) exists for relevant building materials. If so, measured permittivities would allow conclusions to be drawn about the energetic quality of the scanned elements.

By investigating 56 samples of typical construction materials, the hypothesis of a correlation between permittivity and thermal material properties (thermal conductivity and volumetric specific heat) was mostly confirmed. As a result, the derivation of specific heat and, for all materials but calcium silicate bricks and lightweight aggregated concrete, thermal conductivity from known permittivity values is feasible. U-values and RC parameters can be derived from these using the found material property relationships [240]. As a consequence, microwave SAR is able to non-destructively investigate building elements for energy-related purposes. Practical applicability is still limited because of the difficult handling of measurement devices and a complicated result analysis process, which are topics of further research.

6.4. Outlook

All in all, the remote sensing techniques and data processing methods covered in this dissertation can enhance the knowledge about the energy performance conditions of the building stock. In a next step, they should be advanced to practical implementation in order to exploit their potential for promoting energy efficiency measures.

On district scale, the combination of infrared thermography, dynamic simulation and different approaches for finding building age classes is promising. It demands (feasible) improvements of the technology and validation studies [19]. If these improvements are reached, the method could substantially increase the applicability of UBEM by providing reliable input data. With the results, it could contribute to the development of future heat supply strategies. Due to the easily understandable principle and the accessibility of infrared visualisations, the important task of communicating necessary measures to the public is a promising use case already now.

On single-building scale, the next step would be the development and validation of a widely applicable technical system that implements the presented approach of combining UAV-based measurement and semi-automatic data evaluation with owner or user interaction. It could benefit from improved semantical detection of building envelope components, opening up the possibility of providing custom-tailored energy efficiency recommendations with low effort. If commercially available, this would increase attention to heat loss issues and lower barriers to solutions for both residential and non-residential applications.

Regarding microwave radar for wall structure analysis, future activities to combine it with close-range infrared thermography are envisaged. Additional research investigating additional materials as well as the influence of moisture and further technical development of the measuring equipment are required for wider and practical applicability respectively. Such developments may also be combined with and thereby contribute to improve the aforementioned single-building assessment approach, given that the presumably substantial reduction of uncertainty justifies the increased effort compared to using typology values. In that context, the technology could serve to exemplarily investigate representative building parts on a single building or within a district and increase the overall accuracy of single-building analyses or typology applications. Envisaged future research also includes investigating the applicability for measuring moisture content.

Bibliography

[1] National Institute of Standards and Technology. *CODATA Recommendeed Values of the Fundamental Physical Constants: 2018*. 2018. URL: https://physics.nist.gov/cuu/pdf/wall_2018.pdf (visited on 17th Mar. 2021).

[2] R. Becker et al. „Enabling BIM for Property Management of Existing Buildings Based on Automated As-is Capturing“. In: *Proceedings of the 36th International Symposium on Automation and Robotics in Construction (ISARC)*. Ed. by M. Al-Hussein. International Association for Automation and Robotics in Construction (IAARC), 2019, pp. 201–208. DOI: 10.22260/ISARC2019/0028.

[3] European Environment Agency. *Greenhouse gas emissions from energy use in buildings in Europe*. 2023. URL: https://www.eea.europa.eu/en/analysis/indicators/greenhouse-gas-emissions-from-energy (visited on 15th Feb. 2024).

[4] IPCC. *Climate Change 2014: Synthesis Report. Contribution of Working Groups I, II and III to the Fifth Assessment Report of the Intergovernmental Panel on Climate Change*. Geneva, Switzerland: IPCC, 2015.

[5] A. Power. „Housing and sustainability: demolition or refurbishment?“ In: *Proceedings of the Institution of Civil Engineers - Urban Design and Planning* 163.4 (2010), pp. 205–216. DOI: 10.1680/udap.2010.163.4.205.

[6] T. Kuramochi et al. „Ten key short-term sectoral benchmarks to limit warming to 1.5°C“. In: *Climate Policy* 18.3 (2018), pp. 287–305. DOI: 10.1080/14693062.2017.1397495.

[7] European Commission. *A Renovation Wave for Europe - greening our buildings, creating jobs, improving lives: COM/2020/662 final*. Brussels, Belgium: Communication from the Commission to the European Parliament, the Council, the European Economic and Social Committee and the Committee of the Regions, 2020.

[8] J. Estevam Schmiedt et al. „Remote sensing techniques for building models and energy performance studies of buildings“. In: *EBC Annex 71: Building energy performance assessment based on in-situ measurements: First expert meeting*. Loughborough, United Kingdom, 2017.

[9] Deutsches Zentrum für Luft- und Raumfahrt. *Gtom – Messsystem für schnelle und genaue energetische Analysen von Gebäudehüllen für Gebäude und Quartiere. Öffentlicher Schlussbericht*. Cologne, Germany, 2021.

[10] C. Schorn and J. Göttsche. *Gtom: Gebäudetomograph – Messsystem für schnelle und genaue energetische Analysen von Gebäudehüllen für Gebäude und Quartiere, Teilvorhaben: Durchführung und Auswertung von Validierungsmessungen. Schlussbericht*. Jülich, Germany, 2020.

[11] I. Dochev et al. „Calculating urban heat demands: An analysis of two modelling approaches and remote sensing for input data and validation“. In: *Energy and Buildings* 226 (2020), p. 110378. DOI: 10.1016/j.enbuild.2020.110378.

[12] R. Fitton et al. *Building energy performance assessment based on in-situ measurements Challenges and general framework*. Leuven, Belgium: KU Leuven, 2021.

[13] P. Gorzalka et al. „Building Tomograph – From Remote Sensing Data of Existing Buildings to Building Energy Simulation Input“. In: *EBC Annex 71: Building energy performance assessment based on in-situ measurements: Fifth expert meeting*. Innsbruck, Austria, 2018.

[14] P. Gorzalka et al. „Remote Sensing For Building Energy Simulation Input – A Field Trial“. In: *Proceedings of Building Simulation 2019: 16th Conference of IBPSA*. Ed. by V. Corrado, E. Fabrizio, A. Gasparella and F. Patuzzi. Building Simulation Conference proceedings. IBPSA, 2020, pp. 4094–4101. DOI: 10.26868/25222708.2019.210186.

[15] P. Gorzalka et al. „Material investigations to facilitate the applicability of microwave radar to energy-related wall structure analysis“. In: *Materials and Structures* 54.3 (2021). DOI: 10.1617/s11527-021-01716-8.

[16] P. Gorzalka. „Luftbildbasierte 3D-Modelle und energetische Quartiersanalyse am Beispiel Berlin-Moabit“. In: *Workshop 3D-Stadtmodelle*. Ed. by Kommission & Arbeitskreis 3D-Stadtmodelle. 2019.

[17] P. Gorzalka, J. Estevam Schmiedt, C. Schorn and B. Hoffschmidt. „Automated Generation of an Energy Simulation Model for an Existing Building from UAV Imagery“. In: *Buildings* 11.9 (2021), p. 380. DOI: 10.3390/buildings11090380.

[18] P. Groesdonk, D. Jansen, J. Estevam Schmiedt, B. Hoffschmidt and J. E. Schmiedt. „Integration of Heat Flow through Borders between Adjacent Zones in AixLib's Reduced-Order Model“. In: *Proceedings of the 15th International Modelica Conference*. Ed. by D. Müller, A. Monti and A. Benigni. Linköping, Sweden: Linköping University Electronic Press, 2023, pp. 577–588. DOI: 10.3384/ecp204577.

[19] P. Gorzalka et al. „Collecting Data for Urban Building Energy Modelling by Remote Sensing and Machine Learning“. In: *Proceedings of Building Simulation 2021: 17th Conference of IBPSA*. Ed. by D. Saelens, J. Laverge, W. Boydens and L. Helsen. Building Simulation Conference pro-

ceedings. IBPSA, 2022, pp. 1139–1146. DOI: 10.26868/25222708.2021.30184.

[20] P. Groesdonk, B. Kölsch, N. Patel and J. Estevam Schmiedt. „Drohnenbasierte dynamische quantitative Infrarotthermographie in der energetischen Analyse von Gebäuden“. In: *Zerstörungsfreie Materialprüfung. DACH-Jahrestagung 2023, 15.-17. Mai 2023, Friedrichshafen, Graf-Zeppelin-Haus*. DGZfP-Berichtsband. Berlin, Germany: DGZfP, 2023.

[21] H. Hens. *Building physics: heat, air and moisture: Fundamentals and engineering methods with examples and exercises*. 3rd ed. Berlin, Germany: Ernst & Sohn, 2017. DOI: 10.1002/9783433608548.

[22] D. W. Hahn and M. N. Özisik. *Heat conduction*. 3rd ed. Hoboken, NJ, USA: Wiley, 2012. DOI: 10.1002/9781118411285.

[23] ISO 80000-7:2019-08. *Quantities and units: Light and radiation*. Technical standard. International Organization for Standardization, 2019.

[24] F. T. Ulaby and D. G. Long. *Microwave Radar and Radiometric Remote Sensing*. Norwood, MA, USA: Artech House, 2015.

[25] B. Schumacher, H.-G. Bach, P. Spitzer and J. Obrzut. „Electrical Properties“. In: *Springer Handbook of Materials Measurement Methods*. Ed. by H. Czichos, T. Saito and L. Smith. Berlin and Heidelberg, Germany: Springer, 2007, pp. 431–484. DOI: 10.1007/978-3-540-30300-8_9.

[26] H. Eifert. *Bauen in Stein: Die Historie der mineralischen Baustoffe in Deutschland und Umgebung*. Düsseldorf, Germany: Verlag Bau + Technik, 2015.

[27] W.-R. Metje. „Anorganische Bindemittel“. In: *Baustoffkenntnis*. Ed. by W. Hiese. Neuwied, Germany: Werner Verlag, 2007, pp. 151–204.

[28] H. Knoblauch and U. Schneider. *Bauchemie*. 6th ed. Neuwied, Germany: Werner Verlag, 2006.

[29] W.-P. Ettel. „Beton“. In: *Baustoffkenntnis*. Ed. by W. Hiese. Neuwied, Germany: Werner Verlag, 2007, pp. 249–366.

[30] W. Pützschler. „Gesteinskörnungen/Zuschläge für Mörtel und Beton“. In: *Baustoffkenntnis*. Ed. by W. Hiese. Neuwied, Germany: Werner Verlag, 2007, pp. 205–248.

[31] dB Spectrum Services Ltd, Red-M Ltd and Radio Communication Research Unit of CCLRC Rutherford Appleton Laboratory. *Ofcom project SES-2005-08: Predicting coverage and interference involving the indoor-outdoor interface: Final Report*. 2007.

[32] B. Davis et al. „Complex permittivity of planar building materials measured with an ultra-wideband free-field antenna measurement system“. In: *Journal of Research of the National Institute of Standards and Technology* 112.1 (2007), pp. 67–73. DOI: 10.6028/jres.112.005.

[33] A. Safaai-Jazi, S. M. Riad, A. Muqaibel and A. Bayram. *Ultra-wideband Propagation Measurements and Channel Modeling: DARPA NETEX Program Report on Through-the-Wall Propagation and Material Characterization*. Blacksburg, VA, USA, 2002.

[34] I. Cuiñas and M. G. Sánchez. „Permittivity and Conductivity Measurements of Building Materials at 5.8 GHz and 41.5 GHz“. In: *Wireless Personal Communications* 20.1 (2002), pp. 93–100. DOI: 10.1023/A:1013886209664.

[35] A. H. Muqaibel and A. Safaai-Jazi. „A new formulation for characterization of materials based on measured insertion transfer function“. In: *IEEE Transactions on Microwave Theory and Techniques* 51.8 (2003), pp. 1946–1951. DOI: 10.1109/TMTT.2003.815274.

[36] R. Kubacki. „New Attempt to Building Materials Permittivity Measurements“. In: *Progress In Electromagnetics Research Symposium. Proceedings of PIERS 2014 Guangzhou*. Cambridge, MA, USA: The Electromagnetics Academy, 2014, pp. 2676–2680.

[37] D. Ferreira, I. Cuinas, R. F. Caldeirinha and T. R. Fernandes. „A review on the electromagnetic characterisation of building materials at micro- and millimetre wave frequencies“. In: *The 8th European Conference on Antennas and Propagation (EuCAP 2014)*. IEEE, 2014, pp. 145–149. DOI: 10.1109/EuCAP.2014.6901713.

[38] A. Yahalom, Y. Pinhasi, E. Shifman and S. Petnev. „Transmission through Single and Multiple Layers in the 3-10 GHz Band and the Implications for Communications of Frequency Varying Material Dielectric Constants“. In: *WTOC* 9.12 (2010), pp. 759–772.

[39] W. Leschnik and U. Schlemm. „Dielektrische Untersuchung mineralischer Baustoffe in Abhängigkeit von Feuchte- und Salzgehalt bei 2,45 GHz“. In: *Feuchtetag '99*. Ed. by Bundesanstalt für Materialforschung und -prüfung, Materialforschungs- und -prüfanstalt an der Bauhaus-Universität Weimar and Deutsche Gesellschaft für Zerstörungsfreie Prüfung. DGZfP-Berichtsband. Berlin, Germany: DGZfP, 1999.

[40] ITU-R P.2040-1:2015-07. *Effects of building materials and structures on radiowave propagation above about 100 MHz*. Recommendation. Geneva, Switzerland: Radiocommunication Sector of International Communication Union, 2015.

[41] J. R. Abel and J. W. Wallace. „4-40 GHz Permittivity Measurements of Indoor Building Materials“. In: *2019 IEEE International Symposium on Antennas and Propagation and USNC-URSI Radio Science Meeting*. IEEE, 2019, pp. 105–106. DOI: 10.1109/APUSNCURSINRSM.2019.8888911.

[42] ITU-R P.1238-6:2009-10. *Propagation data and prediction methods for the planning of indoor radiocommunication systems and radio local area networks in the frequency range 900 MHz to 100 GHz*. Recommendation. Geneva, Switzerland: Radiocommunication Sector of International Communication Union, 2009.

[43] M. G. Sánchez and I. Cuiñas. „Building material characterization from complex transmissivity measurements at 5.8 GHz“. In: *IEEE Transactions on Antennas and Propagation* 48.8 (2000), pp. 1269–1271. DOI: 10.1109/8.884501.

[44] J. Lähteenmäki and T. Karttaavi. „Measurement of dielectric parameters of wall materials at 60 GHz band“. In: *Electronics Letters* 32.16 (1996), p. 1442. DOI: 10.1049/el:19960954.

[45] A. R. von Hippel. „Theory“. In: *Dielectric materials and applications*. Ed. by A. R. von Hippel. Cambridge, MA, USA: The M.I.T. Press, 1966, pp. 3–46.

[46] ISO 10456:2007-12. *Building materials and products: Hygrothermal properties: Tabulated design values and procedures for determining declared and design thermal values*. Technical standard. International Organization for Standardization, 2007.

[47] B. Anderson, S. Doran, K. Mina and G. Pettit. „Thermal properties of building structures“. In: *Environmental design*. Ed. by CIBSE. London, United Kingdom: CIBSE, 2006.

[48] J. S. Johnson. „CORRELATION OF ELECTRICAL AND THERMAL PROPERTIES OF BUILDING BRICK“. In: *Journal of the American Ceramic Society* 21.3 (1938), pp. 79–85. DOI: 10.1111/j.1151-2916.1938.tb15749.x.

[49] R. W. Powell. „Heat“. In: *Reports on Progress in Physics* 6.1 (1939), pp. 297–329. DOI: 10.1088/0034-4885/6/1/316.

[50] A. Perinelli, F. Finotti, A. M. Tonelli, L. Ricci and R. Albatici. „Experimental apparatus for the determination of thermal conductivity and humidity in building materials by means of electrical permittivity measurements“. In: *TEMA: Technologies, Engineering, Materials and Architecture* 5.2 (2019), pp. 29–41. DOI: 10.17410/tema.v5i2.226.

[51] A. Borrmann, M. König, C. Koch and J. Beetz. „Building Information Modeling: Why? What? How?“ In: *Building Information Modeling. Technology Foundations and Industry Practice*. Ed. by A. Borrmann, M. König, C. Koch and J. Beetz. Cham, Germany: Springer International Publishing, 2018, pp. 1–24. DOI: 10.1007/978-3-319-92862-3_1.

[52] S. Herle, R. Becker, R. Wollenberg and J. Blankenbach. „GIM and BIM“. In: *PFG – Journal of Photogrammetry, Remote Sensing and Geoinformation Science* 88.1 (2020), pp. 33–42. DOI: 10.1007/s41064-020-00090-4.

[53] G. Piaseckienė. „DIMENSIONS OF BIM IN LITERATURE: REVIEW AND ANALYSIS“. In: *Mokslas - Lietuvos ateitis* 14.0 (2022), pp. 1–11. DOI: 10.3846/mla.2022.16071.

[54] ACCA Software. *The dimensions of BIM – 3D, 4D, 5D, 6D, 7D, 8D, 9D, 10D BIM explained*. 2018. URL: https://biblus.accasoftware.com/en/bim-dimensions/ (visited on 20th Jan. 2023).

[55] I. Kamardeen. „8D BIM modelling tool for accident prevention through design“. In: *Proceedings 26th Annual ARCOM Conference*. Ed. by C. Egbu. Leeds, United Kingdom: Association of Researchers in Construction Management, 2010, pp. 281–289.

[56] S. Jaiswal, A.-Q. Gbadamosi, O. Olawale and B. Oluwayemi. „Enabling Quality in Lean Construction: Integrating the Principles of Total Quality Management with 9D-BIM“. In: *The Eighth International SEEDS Conference 2022: Sustainable Ecological Engineering and Design for Society*. 2022.

[57] J. Darós. *Guia completo: BIM 10D construção industrializada*. 2019. URL: https://utilizandobim.com/blog/bim-10d-construcao-industrializada/ (visited on 20th Jan. 2023).

[58] V. Pereira, J. Santos, F. Leite and P. Escórcio. „Using BIM to improve building energy efficiency – A scientometric and systematic review“. In: *Energy and Buildings* 250 (2021), p. 111292. DOI: 10.1016/j.enbuild.2021.111292.

[59] J. Messner et al. *BIM Project Execution Planning Guide, Version 3.0 Prepublication Draft*. University Park, PA, USA: PennState, 2022.

[60] ISO 16739-1:2018-11. *Industry Foundation Classes (IFC) for data sharing in the construction and facility management industries: Data schema*. Technical standard. International Organization for Standardization, 2018.

[61] E. Fichter. „Automatisierte Erzeugung geometrischer Modelle für die BIM-basierte Gebäudesimulation“. Dissertation. Aachen, Germany: RWTH Aachen, 2022. DOI: 10.18154/RWTH-2022-11049.

[62] K. Aengenvoort and M. Krämer. „BIM in the Operation of Buildings“. In: *Building Information Modeling. Technology Foundations and Industry Practice*. Ed. by A. Borrmann, M. König, C. Koch and J. Beetz. Cham, Germany: Springer International Publishing, 2018, pp. 477–491. DOI: 10.1007/978-3-319-92862-3_29.

[63] R. Volk, J. Stengel and F. Schultmann. „Building Information Modeling (BIM) for existing buildings — Literature review and future needs“. In: *Automation in Construction* 38 (2014), pp. 109–127. DOI: 10.1016/j.autcon.2013.10.023.

[64] R. Volk, T. H. Luu, J. S. Mueller-Roemer, N. Sevilmis and F. Schultmann. „Deconstruction project planning of existing buildings based on automated acquisition and reconstruction of building information“. In: *Automation in Construction* 91 (2018), pp. 226–245. DOI: 10.1016/j.autcon.2018.03.017.

[65] R. J. Scherer and P. Katranuschkov. „BIMification: How to create and use BIM for retrofitting“. In: *Advanced Engineering Informatics* 38 (2018), pp. 54–66. DOI: 10.1016/j.aei.2018.05.007.

[66] C. Franzen et al. „BIM-SIS Adaptive Knowledge Based System for Identification of Stone Damages in Building Information Modeling Working Environment“. In: *Monument Future: Decay and conservation of stone. Proceedings of the 14th International Congress on the Deterioration and Conservation of Stone*. Ed. by S. Siegesmund and B. Middendorf. Halle (Saale), Germany: Mitteldeutscher Verlag, 2020, pp. 977–980.

[67] TragWerk Software Döking+Purtak. *BIM SIS – Schadens Identifikations System*. 2022. URL: https://www.bim-sis.de/ (visited on 19th Jan. 2023).

[68] Trimble. *LOD simply explained: The LOD Kiwi*. 2019. URL: https://constructible.trimble.com/construction-industry/lod-simply-explained-the-lod-kiwi (visited on 19th Jan. 2023).

[69] M. Beirer. *LOIN — Level of Information Need*. 2022. URL: https://www.buildinformed.com/loin-level-of-information-need/ (visited on 19th Jan. 2023).

[70] DIN EN 17412-1:2020-11. *Bauwerksinformationsmodellierung: Informationsbedarfstiefe: Teil 1: Konzepte und Grundsätze*. Technical standard. Deutsches Institut für Normung, 2020.

[71] C. van Treeck, R. Wimmer and T. Maile. „BIM for Energy Analysis“. In: *Building Information Modeling. Technology Foundations and Industry Practice*. Ed. by A. Borrmann, M. König, C. Koch and J. Beetz. Cham, Germany: Springer International Publishing, 2018, pp. 337–347. DOI: 10.1007/978-3-319-92862-3_20.

[72] G. von Spiess. *Energieeffizienznachweise im BIM-Prozess (WEB-Seminar)*. Düsseldorf, 2020.

[73] D. Müller et al. *BIM2SIM - Methodenentwicklung zur Erstellung von Simulationsmodellen aus Daten des Building Information Modeling. Gemeinsamer Endbericht*. Aachen, Germany, 2021. DOI: 10.2314/KXP:1819319997.

[74] D. Jansen. *bim2sim v0.1.0*. 2023. URL: https://github.com/BIM2SIM/bim2sim/releases/tag/v0.1.0 (visited on 27th Sept. 2023).

[75] OGC 12-019:2012-03. *OGC City Geography Markup Language (CityGML) Encoding Standard*. OpenGIS Encoding Standard. Open Geospatial Consortium, 2012.

[76] K. Arroyo Ohori, F. Biljecki, K. Kumar, H. Ledoux and J. Stoter. „Modeling Cities and Landscapes in 3D with CityGML“. In: *Building Information Modeling. Technology Foundations and Industry Practice*. Ed. by A. Borrmann, M. König, C. Koch and J. Beetz. Cham, Germany: Springer International Publishing, 2018, pp. 199–215. DOI: 10.1007/978-3-319-92862-3_11.

[77] R. T. Watson. „Introduction to XML“. In: *XML - Managing Data Exchange*. Ed. by R. Foley. Wikibooks, 2007.

[78] maila-push. *Frankfurt_Street_Setting_LOD3*. 2009. URL: http://misc.gis.tu-berlin.de/typo3-igg/fileadmin/count.php?f=fileadmin%2Fcitygml%2Fdocs%2FFrankfurt_Street_Setting_LOD3.zip (visited on 20th Jan. 2023).

[79] Karlsruher Institut für Technologie. *FZKViewer*. 2021. URL: https://www.iai.kit.edu/1648.php (visited on 4th Mar. 2021).

[80] V. Coors, C. Andrae and K.-H. Böhm. *3D-Stadtmodelle: Konzepte und Anwendungen mit CityGML*. Berlin, Germany: Wichmann Verlag, 2016.

[81] F. Biljecki, H. Ledoux and J. Stoter. „An improved LOD specification for 3D building models“. In: *Computers, Environment and Urban Systems* 59 (2016), pp. 25–37. DOI: 10.1016/j.compenvurbsys.2016.04.005.

[82] TU Delft. *Cities/regions around the world with open datasets*. 2023. URL: https://3d.bk.tudelft.nl/opendata/opencities/ (visited on 27th Sept. 2023).

[83] Chair of Geoinformatics at Technische Universität München. *3DCityDB in Action*. 2023. URL: https://www.3dcitydb.org/3dcitydb/3dcitydb-in-action/ (visited on 27th Sept. 2023).

[84] LVN and Stadt Neuss. *Geofachdaten der Stadt Neuss - CPAWeb3DViewer*. 2022. URL: https://www.geo-neuss.de/CPAWeb3DViewer/CPAWebGLService (visited on 1st June 2024).

[85] Bundesamt für Kartographie und Geodäsie. *Dokumentation 3D Gebäudemodell Deutschland - LoD2 (LoD2-DE): Produktstand 2020*. 2020. URL: https://sg.geodatenzentrum.de/web_public/gdz/dokumentation/deu/LoD2-DE.pdf (visited on 15th Jan. 2021).

[86] N. Milojevic-Dupont et al. „EUBUCCO v0.1: European building stock characteristics in a common and open database for 200+ million individual buildings“. In: *Scientific data* 10.1 (2023), p. 147. DOI: 10.1038/s41597-023-02040-2.

[87] A. Malhotra et al. „A REVIEW ON COUNTRY SPECIFIC DATA AVAILABILITY AND ACQUISITION TECHNIQUES FOR CITY QUARTER INFORMATION MODELLING FOR BUILDING ENERGY ANALYSIS“. In: *BauSIM 2020*. Ed. by M. Monsberger, C. J. Hopfe, M. Krüger and A. Passer. Graz, Austria: Verlag der Technischen Universität Graz, 2020, pp. 543–549. DOI: 10.3217/978-3-85125-786-1-65.

[88] F. Biljecki, J. Stoter, H. Ledoux, S. Zlatanova and A. Çöltekin. „Applications of 3D City Models: State of the Art Review“. In: *ISPRS International Journal of Geo-Information* 4.4 (2015), pp. 2842–2889. DOI: 10.3390/ijgi4042842.

[89] B. Saeidian, A. Rajabifard, B. Atazadeh and M. Kalantari. „A semantic 3D city model for underground land administration: Development and implementation of an ADE for CityGML 3.0“. In: *Tunnelling and Underground Space Technology* 140 (2023), p. 105267. DOI: 10.1016/j.tust.2023.105267.

[90] virtual city systems. *Urbane Simulation*. 2023. URL: https://vc.systems/loesungen/urbane-simulation/ (visited on 27th Sept. 2023).

[91] T. Brüggemann and P. von Both. „3D-Stadtmodellierung: CityGML“. In: *Building Information Modeling*. Ed. by A. Borrmann, M. König and J. Beetz. Wiesbaden, Germany: Springer Vieweg, 2015, pp. 177–192.

[92] A. Foucquier, S. Robert, F. Suard, L. Stéphan and A. Jay. „State of the art in building modelling and energy performances prediction: A review“. In: *Renewable and Sustainable Energy Reviews* 23 (2013), pp. 272–288. DOI: 10.1016/j.rser.2013.03.004.

[93] National Renewable Energy Laboratory. *EnergyPlus*. URL: https://energyplus.net/ (visited on 18th Mar. 2021).

[94] S. Herkel, B. Köhler and D. Kalz. „Energie – Gebäudeperformance in Planung und Betrieb optimieren“. In: *Gebäude.Technik.Digital*. Ed. by C. van Treeck et al. Berlin and Heidelberg, Germany: Springer Berlin Heidelberg, 2016, pp. 243–330. DOI: 10.1007/978-3-662-52825-9_4.

[95] DIN V 18599-2:2016-10. *Energetische Bewertung von Gebäuden: Berechnung des Nutz-, End- und Primärenergiebedarfs für Heizung, Kühlung, Lüftung, Trinkwasser und Beleuchtung: Teil 2: Nutzenergiebedarf für Heizen und Kühlen von Gebäudezonen*. Prestandard. Deutsches Institut für Normung, 2016.

[96] M. Senave and S. Boeykens. „Link between BIM and energy simulation“. In: *Building Information Modelling (BIM) in Design, Construction and Operations*. Ed. by L. Mahdjoubi, C. A. Brebbia and R. Laing. Southampton, United Kingdom: WIT Press, 2015, pp. 341–352. DOI: 10.2495/BIM150291.

[97] L. Brackney, A. Parker, D. Macumber and K. Benne. *Building Energy Modeling with OpenStudio: A Practical Guide for Students and Professionals*. Cham, Germany: Springer, 2018. DOI: 10.1007/978-3-319-77809-9.

[98] Autodesk. *About Energy Analysis for Autodesk® Revit®*. 2017. URL: https://knowledge.autodesk.com/support/revit-products/learn-explore/caas/CloudHelp/cloudhelp/2016/ENU/Revit-Analyze/files/GUID-A4C490A7-A86C-4027-B829-A77AB3211B60-htm.html (visited on 18th Mar. 2021).

[99] R. Pernetti, L. Magnani and A. Magrini. „Energy Performance of Buildings: A Comparison of Standard Assessment Methods“. In: *Nearly Zero Energy Building Refurbishment*. Ed. by F. Pacheco Torgal, M. Mistretta, A. Kaklauskas, C. G. Granqvist and L. F. Cabeza. London, United Kingdom: Springer London, 2013, pp. 177–205. DOI: 10.1007/978-1-4471-5523-2_7.

[100] Bundesamt für Bauwesen und Raumordnung. *Europäische Normungsarbeit zur Gesamtenergieeffizienz-Richtlinie*. 2023. URL: https://www.bbsr-geg.bund.de/GEGPortal/DE/ErgaenzendeRegelungen/EPBD/EuropNorm/cen.html (visited on 31st May 2024).

[101] ISO/TR 52016-2:2017-06. *Energy performance of buildings: Energy needs for heating and cooling, internal temperatures and sensible and latent heat loads: Part 2: Explanation and justification of ISO 52016-1 and ISO 52017-1*. Technical report. International Organization for Standardization, 2017.

[102] H. Erhorn and K. Jagnow. „Bilanzierungsverfahren nach der neuen DIN V 18599 (DIN V 18599-1)“. In: *Bauphysik Kalender 2019*. Ed. by N. A. Fouad. Berlin, Germany: Ernst & Sohn, 2019, pp. 139–170. DOI: 10.1002/9783433609842.ch5.

[103] H. Erhorn. „DIN V 18599: Energetische Bewertung von Gebäuden jetzt umfassend möglich“. In: *Kongress ”Erneuerbare Energien 2006”*. Böblingen, Germany, 2006.

[104] D. Müller, M. Lauster, A. Constantin, M. Fuchs and P. Remmen. „AixLib – An Open-Source Modelica Library within the IEA-EBC Annex 60

Framework“. In: *Proceedings of the CESBP Central European Symposium on Building Physics and BauSIM 2016*. Ed. by J. Grunewald. Stuttgart, Germany: Fraunhofer IRB Verlag, 2016, pp. 3–9.

[105] M. Wetter, D. Blum and J. Hu. *Modelica IBPSA Library v1*. 2019. DOI: 10.11578/dc.20190520.1.

[106] P. Fritzson and V. Engelson. „Modelica — A unified object-oriented language for system modeling and simulation“. In: *ECOOP'98 — Object-Oriented Programming*. Ed. by G. Goos, J. Hartmanis, J. van Leeuwen and E. Jul. Vol. 1445. Lecture Notes in Computer Science. Berlin and Heidelberg, Germany: Springer Berlin Heidelberg, 1998, pp. 67–90. DOI: 10.1007/BFb0054087.

[107] M. Lauster. „Parametrierbare Gebäudemodelle für dynamische Energiebedarfsrechnungen von Stadtquartieren“. Dissertation. Aachen, Germany: RWTH Aachen, 2018. DOI: 10.18154/RWTH-2018-230258.

[108] P. Remmen et al. „TEASER: An open tool for urban energy modelling of building stocks“. In: *Journal of Building Performance Simulation* 11.1 (2018), pp. 84–98. DOI: 10.1080/19401493.2017.1283539.

[109] VDI 6007 Part 1:2015-06. *Calculation of transient thermal response of rooms and buildings - Modelling of rooms*. Guideline. The Association of German Engineers, 2015.

[110] Object Management Group. *OMG Unified Modeling Language (OMG UML): Version 2.5*. 2013. URL: https://www.omg.org/spec/UML/2.5/Beta2/PDF/ (visited on 5th Feb. 2021).

[111] C. L. Beuken. „Wärmeverluste bei periodisch betriebenen elektrischen Öfen: Eine neue Methode zur Vorausbestimmung nicht-stationärer Wärmeströmungen“. Dissertation. Freiberg, Germany: Sächsische Bergakademie Freiberg, 1936.

[112] L. Rouvel. „Berechnung des wärmetechnischen Verhaltens von Räumen bei dynamischen Wärmelasten“. In: *Brennstoff – Wärme – Kraft* 24.6 (1972), pp. 245–262.

[113] L. Rouvel and F. Zimmermann. „Berechnung des instationären thermischen Gebäudeverhaltens Teil 1“. In: *HLH Lüftung/Klima - Heizung/Sanitär - Gebäudetechnik* 3 (2004), pp. 39–46.

[114] VDI 2078:2015-06. *Calculation of thermal loads and room temperatures (design cooling load and annual simulation)*. Guideline. The Association of German Engineers, 2015.

[115] ISO 6946:2017-06. *Building components and building elements: Thermal resistance and thermal transmittance: Calculation methods*. Technical standard. International Organization for Standardization, 2017.

[116] M. Lauster. *GitHub: RWTH-EBC/TEASER: Issue #680 Default inner convection coefficients*. 2021. URL: https://github.com/RWTH-EBC/TEASER/issues/680#issuecomment-786600506 (visited on 1st Feb. 2024).

[117] M. Lauster and D. Müller. „Methoden der Zeitreihenanalyse für die Bewertung von urbanen Gebäudesimulationen“. In: *Bauphysik* 40.6 (2018), pp. 420–426. DOI: 10.1002/bapi.201800030.

[118] A. Chittum and P. A. Østergaard. „How Danish communal heat planning empowers municipalities and benefits individual consumers“. In: *Energy Policy* 74 (2014), pp. 465–474. DOI: 10.1016/j.enpol.2014.08.001.

[119] European Parliament and Council of the European Union. *Directive (EU) 2023/1791 of the European Parliament and of the Council of 13 September 2023 on energy efficiency and amending Regulation (EU) 2023/955 (recast) (Text with EEA relevance)*. Ed. by EUR-Lex. 2023. URL: http://data.europa.eu/eli/dir/2023/1791/oj (visited on 24th June 2024).

[120] C. F. Reinhart and C. Cerezo Davila. „Urban building energy modeling – A review of a nascent field“. In: *Building and Environment* 97 (2016), pp. 196–202. DOI: 10.1016/j.buildenv.2015.12.001.

[121] A. Sola, C. Corchero, J. Salom and M. Sanmarti. „Multi-domain urban-scale energy modelling tools: A review“. In: *Sustainable Cities and Society* 54 (2020), p. 101872. DOI: 10.1016/j.scs.2019.101872.

[122] H. Lim and Z. J. Zhai. „Review on stochastic modeling methods for building stock energy prediction“. In: *Building Simulation* 10.5 (2017), pp. 607–624. DOI: 10.1007/s12273-017-0383-y.

[123] T. Hong, Y. Chen, X. Luo, N. Luo and S. H. Lee. „Ten questions on urban building energy modeling“. In: *Building and Environment* 168 (2020), p. 106508. DOI: 10.1016/j.buildenv.2019.106508.

[124] A. Malhotra et al. „Information modelling for urban building energy simulation—A taxonomic review“. In: *Building and Environment* 208 (2022), p. 108552. DOI: 10.1016/j.buildenv.2021.108552.

[125] A. Malhotra. „DESCity: district energy simulation using CityGML models“. Dissertation. Aachen, Germany: RWTH Aachen, 2023. DOI: 10.18154/RWTH-2023-05656.

[126] V. Coors, M. Betz and E. Duminil. „A Concept of Quality Management of 3D City Models Supporting Application-Specific Requirements“. In: *PFG – Journal of Photogrammetry, Remote Sensing and Geoinformation Science* 88.1 (2020), pp. 3–14. DOI: 10.1007/s41064-020-00094-0.

[127] G. Agugiaro, J. Benner, P. Cipriano and R. Nouvel. „The Energy Application Domain Extension for CityGML: Enhancing interoperability for urban energy simulations“. In: *Open Geospatial Data, Software and Standards* 3.1 (2018), p. 2. DOI: 10.1186/s40965-018-0042-y.

[128] A. Malhotra, M. Shamovich, J. Frisch and C. van Treeck. *E3D Software Tools / Teaserplus*. 2021. URL: https://gitlab.e3d.rwth-aachen.de/e3d-software-tools/teaserplus (visited on 2nd Oct. 2023).

[129] P. Remmen. *GitHub: RWTH-EBC/TEASER: Issue #582 Delete load_citygml*. 2019. URL: https://github.com/RWTH-EBC/TEASER/issues/582 (visited on 1st Feb. 2024).

[130] A. Malhotra, M. Shamovich, J. Frisch and C. van Treeck. „Parametric Study of the Different Level of Detail of CityGML and Energy-ADE Information for Energy Performance Simulations“. In: *Proceedings of Building Simulation 2019: 16th Conference of IBPSA*. Ed. by V. Corrado, E. Fabrizio, A. Gasparella and F. Patuzzi. Building Simulation Conference proceedings. IBPSA, 2020, pp. 3429–3436. DOI: 10.26868/25222708.2019.210607.

[131] L. Fierz. *hues-platform/cesar-p-core: CESAR-P-V2.0.1*. 2021. DOI: 10.5281/zenodo.5148531.

[132] D. Wang, J. Landolt, G. Mavromatidis, K. Orehounig and J. Carmeliet. „CESAR: A bottom-up building stock modelling tool for Switzerland to address sustainable energy transformation strategies“. In: *Energy and Buildings* 169 (2018), pp. 9–26. DOI: 10.1016/j.enbuild.2018.03.020.

[133] T. Hong, Y. Chen, S. H. Lee and M. A. Piette. „CityBES: A Web-based Platform to Support City-Scale Building Energy Efficiency“. In: *The 5th International Workshop on Urban Computing (UrbComp 2016)*. San Francisco, CA, USA, 2016.

[134] Alliance for Sustainable Energy, LLC. *URBANopt SDK Documentation*. 2022. URL: https://docs.urbanopt.net/ (visited on 2nd Oct. 2023).

[135] R. El Kontar et al. „URBANopt: An Open-Source Software Development Kit for Community and Urban District Energy Modeling“. In: *2020 Building Performance Analysis Conference and SimBuild co-organized by ASHRAE and IBPSA-USA*. Ed. by ASHRAE and IBPSA-USA. 2020, pp. 293–301.

[136] D. Robinson et al. „CITYSIM: COMPREHENSIVE MICRO-SIMULATION OF RESOURCE FLOWS FOR SUSTAINABLE URBAN PLANNING“. In: *Building Simulation 2009: Eleventh International IBPSA Confekamerence*. IBPSA, 2009, pp. 1083–1090. DOI: 10.26868/25222708.2009.1083-1090.

[137] EPFL. *CitySim Software*. 2023. URL: https://www.epfl.ch/labs/leso/transfer/software/citysim/ (visited on 2nd Oct. 2023).

[138] ASHRAE 140:2020-. *Method of Test for Evaluating Building Performance Simulation Software*. ANSI/ASHRAE standard. American Society of Heating, Refrigerating and Air-Conditioning Engineers, 2020.

[139] E. Walter and J. Kämpf. „A verification of CitySim results using the BESTEST and monitored consumption values“. In: *Proceedings of the 2nd Building Simulation Applications Conference*. Ed. by M. Baratieri, V. Corrado, A. Gasparella and F. Patuzzi. Bozen-Bolzano, Italy: Bozen-Bolzano University Press, 2015, pp. 215–222.

[140] KAEMCO. *Download. CitySim Pro*. 2023. URL: http://www.kaemco.ch/download.php (visited on 2nd Oct. 2023).

[141] J. F. Rosser et al. „Modelling Urban Housing Stocks for Building Energy Simulation using CityGML EnergyADE“. In: *ISPRS International Journal of Geo-Information* 8.4 (2019), p. 163. DOI: 10.3390/ijgi8040163.

[142] J. A. Fonseca, T.-A. Nguyen, A. Schlueter and F. Marechal. „City Energy Analyst (CEA): Integrated framework for analysis and optimization of building energy systems in neighborhoods and city districts“. In: *Energy and Buildings* 113 (2016), pp. 202–226. DOI: 10.1016/j.enbuild.2015.11.055.

[143] J. A. Fonseca and A. Schlueter. „Integrated model for characterization of spatiotemporal building energy consumption patterns in neighborhoods and city districts“. In: *Applied Energy* 142 (2015), pp. 247–265. DOI: 10.1016/j.apenergy.2014.12.068.

[144] J. A. Fonseca et al. *architecture-building-systems/CityEnergyAnalyst: CityEnergyAnalyst v.3.34.2*. 2023. DOI: 10.5281/zenodo.598221.

[145] S. M. Murshed, S. Picard and A. Koch. „Modelling, Validation and Quantification of Climate and Other Sensitivities of Building Energy Model on 3D City Models“. In: *ISPRS International Journal of Geo-Information* 7.11 (2018), p. 447. DOI: 10.3390/ijgi7110447.

[146] ISO 13790:2008-08. *Energy performance of buildings: Calculation of energy use for space heating and cooling*. Technical standard. International Organization for Standardization, 2008.

[147] R. Nouvel et al. „SimStadt, a new workflow-driven urban energy simulation platform for CityGML city models“. In: *Future buildings & districts sustainability from nano to urban scale*. Lausanne, Switzerland: Ecole polytechnique fédérale de Lausanne (EPFL), 2015. DOI: 10.5075/epfl-cisbat2015-889-894.

[148] D. Monien, A. Strzalka, A. Koukofikis, V. Coors and U. Eicker. „Comparison of building modelling assumptions and methods for urban scale heat demand forecasting“. In: *Future Cities and Environment* 3.0 (2017), p. 2. DOI: 10.1186/s40984-017-0025-7.

[149] V. Weiler, J. Stave and U. Eicker. „Renewable Energy Generation Scenarios Using 3D Urban Modeling Tools—Methodology for Heat Pump and Co-Generation Systems with Case Study Application“. In: *Energies* 12.3 (2019), p. 403. DOI: 10.3390/en12030403.

[150] R. Nouvel, M. Zirak, V. Coors and U. Eicker. „The influence of data quality on urban heating demand modeling using 3D city models“. In: *Computers, Environment and Urban Systems* 64 (2017), pp. 68–80. DOI: 10.1016/j.compenvurbsys.2016.12.005.

[151] T. Loga, B. Stein, N. Diefenbach and R. Born. *Deutsche Wohngebäudetypologie: Beispielhafte Maßnahmen zur Verbesserung der Energieeffizienz von typischen Wohngebäuden*. 2nd ed. Darmstadt, Germany: IWU, 2015.

[152] I. Dochev, H. Seller and I. Peters. „Assigning Energetic Archetypes to a Digital Cadastre and Estimating Building Heat Demand. An Example from Hamburg, Germany“. In: *Environmental and Climate Technologies* 24.1 (2020), pp. 233–253. DOI: 10.2478/rtuect-2020-0014.

[153] VDI 3807 Part 2:2014-11. *Characteristic consumption values for buildings: Characteristic heating-energy, electrical-energy and water consumption values*. Guideline. The Association of German Engineers, 2014.

[154] S. Goy, F. Maréchal and D. Finn. „Data for Urban Scale Building Energy Modelling: Assessing Impacts and Overcoming Availability Challenges“. In: *Energies* 13.16 (2020), p. 4244. DOI: 10.3390/en13164244.

[155] ISO 9972:2014-08. *Thermal performance of buildings: Determination of air permeability of buildings: Fan pressurization method*. Technical standard. International Organization for Standardization, 2014.

[156] ISO 9869-1:2014-08. *Thermal insulation: Building elements: In-situ measurement of thermal resistance and thermal capacitance: Heat flow meter method*. Technical standard. International Organization for Standardization, 2014.

[157] ISO 13789:2017-06. *Thermal performance of buildings: Transmission and ventilation heat transfer coefficients: Calculation method*. Technical standard. International Organization for Standardization, 2017.

[158] Deutscher Wetterdienst and Bundesamt für Bauwesen und Raumordnung. *Ortsgenaue Testreferenzjahre von Deutschland für mittlere, extreme und zukünftige Witterungsverhältnisse: Handbuch*. Offenbach, 2017. URL: https://www.bbsr.bund.de/BBSR/DE/forschung/programme/zb/Auftragsforschung/5EnergieKlimaBauen/2013/testreferenzjahre/try-handbuch.pdf (visited on 9th Nov. 2020).

[159] Bundestag. „Gebäudeenergiegesetz“. In: *BGBl. I (Bundesgesetzblatt Teil I)* 37 (2020), p. 1728.

[160] S. Kelly, D. Crawford-Brown and M. G. Pollitt. „Building performance evaluation and certification in the UK: Is SAP fit for purpose?“ In: *Renewable and Sustainable Energy Reviews* 16.9 (2012), pp. 6861–6878. DOI: 10.1016/j.rser.2012.07.018.

[161] P. van den Brom, A. Meijer and H. Visscher. „Performance gaps in energy consumption: household groups and building characteristics“. In: *Building Research & Information* 46.1 (2018), pp. 54–70. DOI: 10.1080/09613218.2017.1312897.

[162] BEV - Bundesamt für Eich- und Vermessungswesen, ed. *200 Jahre Kataster Österreichisches Kulturgut 1817 - 2017*. Vienna, Austria, 2017.

[163] T. Busen et al. *Bauaufnahme*. mediaTUM - Dokumenten- und Publikationsserver der Technischen Universität München, 2017. DOI: 10.14459/2016md1353273.

[164] A. H. Robinson, J. L. Morrison and P. C. Muehrcke. „Cartography 1950-2000“. In: *Transactions of the Institute of British Geographers* 2.1 (1977), p. 3. DOI: 10.2307/622190.

[165] R. M. Bennett, M. Koeva and K. Asiama. „Review of Remote Sensing for Land Administration: Origins, Debates, and Selected Cases“. In: *Remote Sensing* 13.21 (2021), p. 4198. DOI: 10.3390/rs13214198.

[166] C. Eschmann, C.-M. Kuo, C.-H. Kuo and C. Boller. „High-Resolution Multisensor Infrastructure Inspection with Unmanned Aircraft Systems“. In: *ISPRS - International Archives of the Photogrammetry, Remote Sensing and Spatial Information Sciences* XL-1/W2 (2013), pp. 125–129. DOI: 10.5194/isprsarchives-XL-1-W2-125-2013.

[167] O. Küng et al. „Simplified Building Models Extraction from Ultra-Light UAV Imagery“. In: *ISPRS - International Archives of the Photogrammetry, Remote Sensing and Spatial Information Sciences* XXXVIII-1/C22 (2011), pp. 217–222. DOI: 10.5194/isprsarchives-XXXVIII-1-C22-217-2011.

[168] T. Mill, A. Alt and R. Liias. „Combined 3D building surveying techniques – terrestrial laser scanning (TLS) and total station surveying for BIM data management purposes“. In: *Journal of Civil Engineering and Management* 19.Supplement 1 (2013), S23–S32. DOI: 10.3846/13923730.2013.795187.

[169] M. Johnston and A. Zakhor. „Estimating building floor plans from exterior using laser scanners“. In: *Proceedings of SPIE 6805. Three-Dimensional Image Capture and Applications* (2008), 68050H. DOI: 10.1117/12.766556.

[170] T. L. Garwood et al. „A framework for producing gbXML building geometry from Point Clouds for accurate and efficient Building Energy Modelling“. In: *Applied Energy* 224 (2018), pp. 527–537. DOI: 10.1016/j.apenergy.2018.04.046.

[171] D. Frommholz, M. Linkiewicz, H. Meissner and D. Dahlke. „Reconstructing Buildings with Discontinuities and Roof Overhangs from Oblique Aerial Imagery“. In: *ISPRS - International Archives of the Photogrammetry, Remote Sensing and Spatial Information Sciences* XLII-1/W1 (2017), pp. 465–471. DOI: 10.5194/isprs-archives-XLII-1-W1-465-2017.

[172] S. Malihi, M. Valadan Zoej and M. Hahn. „Large-Scale Accurate Reconstruction of Buildings Employing Point Clouds Generated from UAV Imagery“. In: *Remote Sensing* 10.7 (2018), p. 1148. DOI: 10.3390/rs10071148.

[173] C. Wang et al. „Data acquisition for urban building energy modeling: A review“. In: *Building and Environment* 217 (2022), p. 109056. DOI: 10.1016/j.buildenv.2022.109056.

[174] D. Bienvenido-Huertas, J. Moyano, D. Marín and R. Fresco-Contreras. „Review of in situ methods for assessing the thermal transmittance of walls“. In: *Renewable and Sustainable Energy Reviews* 102 (2019), pp. 356–371. DOI: 10.1016/j.rser.2018.12.016.

[175] ISO 9869-2:2018-08. *Thermal insulation: Building elements: In-situ measurement of thermal resistance and thermal capacitance: Infrared method for frame structure dwelling*. Technical standard. International Organization for Standardization, 2018.

[176] D. Patel, J. Estevam Schmiedt, M. Röger and B. Hoffschmidt. „Approach for external measurements of the heat transfer coefficient (U-value) of building envelope components using UAV based infrared thermography". In: *14th Quantitative InfraRed Thermography Conference (QIRT)*. Berlin: QIRT Council, 2018, pp. 379–386. DOI: 10.21611/qirt.2018.026.

[177] D. Patel, J. Estevam Schmiedt, M. Röger and B. Hoffschmidt. „A Model Calibration Approach to U-Value Measurements with Thermography". In: *Buildings* 13.9 (2023), p. 2253. DOI: 10.3390/buildings13092253.

[178] M. Mahmoodzadeh, V. Gretka and P. Mukhopadhyaya. „Challenges and opportunities in quantitative aerial thermography of building envelopes". In: *Journal of Building Engineering* 69 (2023), p. 106214. DOI: 10.1016/j.jobe.2023.106214.

[179] N. Bayomi, S. Nagpal, T. Rakha and J. E. Fernandez. „Building envelope modeling calibration using aerial thermography". In: *Energy and Buildings* 233 (2021), p. 110648. DOI: 10.1016/j.enbuild.2020.110648.

[180] J. R. Schott. „Methods for estimation of and correction for atmospheric effects on remotely sensed data". In: *Atmospheric Propagation and Remote Sensing II*. Ed. by A. Kohnle and W. B. Miller. SPIE Proceedings. SPIE, 1993, pp. 448–482. DOI: 10.1117/12.154850.

[181] K. Mayer et al. „Estimating building energy efficiency from street view imagery, aerial imagery, and land surface temperature data". In: *Applied Energy* 333 (2023), p. 120542. DOI: 10.1016/j.apenergy.2022.120542.

[182] S. Raetz and R. Denstorff. „Klimaschutz aus der Luft: Thermografiebefliegung in Rheinbach ein voller Erfolg". In: *Stadt und Gemeinde* 68.4 (2013), pp. 120–122.

[183] O. Friman, P. Follo, J. Ahlberg and S. Sjokvist. „Methods for Large-Scale Monitoring of District Heating Systems Using Airborne Thermography“. In: *IEEE Transactions on Geoscience and Remote Sensing* 52.8 (2014), pp. 5175–5182. DOI: 10.1109/TGRS.2013.2287238.

[184] J. R. Schott, J. D. Biegel and E. P. Wilkinson. „Quantitative Aerial Survey Of Building Heat Loss“. In: *Thermosense V*. Ed. by G. E. Courville. SPIE Proceedings. SPIE, 1983, pp. 187–195. DOI: 10.1117/12.934479.

[185] A. E. Byrnes and J. R. Schott. „Correction of thermal imagery for atmospheric effects using aircraft measurement and atmospheric modeling techniques“. In: *Applied optics* 25.15 (1986), p. 2563. DOI: 10.1364/AO.25.002563.

[186] I. Macleod. „An airborne thermal remote sensing calibration technique“. Thesis. Rochester, NY, USA: Rochester Institute of Technology, 1984. URL: https://scholarworks.rit.edu/theses/4354.

[187] A. Berk et al. „MODTRAN6: a major upgrade of the MODTRAN radiative transfer code“. In: *Algorithms and Technologies for Multispectral, Hyperspectral, and Ultraspectral Imagery XX*. Ed. by M. Velez-Reyes and F. A. Kruse. SPIE Proceedings. SPIE, 2014, 90880H. DOI: 10.1117/12.2050433.

[188] M. Vollmer and K.-P. Möllmann. *Infrared thermal imaging: Fundamentals, research and applications*. Second edition. Weinheim, Germany: Wiley-VCH, 2018. DOI: 10.1002/9783527693306.

[189] D. Monien, R. Wilting, E. Casper, M. Brennenstuhl and V. Coors. „WeBest – Automatisierte Korrektur und Mapping von Fassadenthermographien auf 3D-Gebäudemodelle“. In: *Photogrammetrie - Fernerkundung - Geoinformation* 4 (2016), pp. 246–257. DOI: 10.1127/pfg/2016/0298.

[190] L. R. Koirala. „FTIR-Spectroscopic Measurement of Directional Spectral Emissivities of Microstructured Surfaces“. Dissertation. Hamburg, Germany: Helmut-Schmidt-Universität – Universität der Bundeswehr Hamburg, 2004.

[191] VDI 3511:2015-06. *Temperature measurement in industry - Radiation thermometry - Practical application of radiation thermometers*. Guideline. The Association of German Engineers, 2015.

[192] G. Bitelli et al. „Aerial Thermography for Energetic Modelling of Cities“. In: *Remote Sensing* 7.2 (2015), pp. 2152–2170. DOI: 10.3390/rs70202152.

[193] F. E. Nicodemus, J. C. Richmond, J. J. Hsia, I. W. Ginsberg and T. Limperis. *Geometrical Considerations and Nomenclature for Reflectance*. Vol. 160. NBS Monograph. Washington, DC, USA: U.S. Dept. of Commerce, National Bureau of Standards, 1977.

[194] S. Kotthaus, T. E. Smith, M. J. Wooster and C. Grimmond. „Derivation of an urban materials spectral library through emittance and reflectance spectroscopy“. In: *ISPRS Journal of Photogrammetry and Remote Sensing* 94 (2014), pp. 194–212. DOI: 10.1016/j.isprsjprs.2014.05.005.

[195] M. Oren and S. K. Nayar. „Generalization of Lambert's reflectance model“. In: *Proceedings of the 21st annual conference on Computer graphics and interactive techniques - SIGGRAPH '94*. Ed. by D. Schweitzer, A. Glassner and M. Keeler. New York, NY, USA: ACM Press, 1994, pp. 239–246. DOI: 10.1145/192161.192213.

[196] E. Mandanici and P. Conte. „Aerial thermography for energy efficiency of buildings: the ChoT project“. In: *Remote Sensing Technologies and Applications in Urban Environments*. Ed. by T. Erbertseder, T. Esch and N. Chrysoulakis. SPIE Proceedings. SPIE, 2016, p. 1000808. DOI: 10.1117/12.2241256.

[197] T. Loga, B. Stein and N. Diefenbach. „TABULA building typologies in 20 European countries—Making energy-related features of residential building stocks comparable“. In: *Energy and Buildings* 132 (2016), pp. 4–12. DOI: 10.1016/j.enbuild.2016.06.094.

[198] Ministerium für Bauen und Wohnen des Landes Nordrhein-Westfalen. *Verbesserung des Wärmeschutzes im Gebäudebestand des Landes Nordrhein-Westfalen*. Vol. 93,2. Berichte / Ministerium für Bauen und Wohnen des Landes Nordrhein-Westfalen. Düsseldorf, Germany, 1993.

[199] S. Klauß, W. Kirchhof and J. Gissel. *Katalog regionaltypischer Materialien im Gebäudebestand mit Bezug auf die Baualtersklasse und Ableitung typischer Bauteilaufbauten*. Kassel, Germany: Zentrum für Umweltbewusstes Bauen, 2009.

[200] D. Ludwig. „3D-Gebäudemodelle für den kommunalen Wärmeplan – das zentrale Werkzeug für die Wärmewende“. In: *Workshop 3D-Stadtmodelle*. Ed. by Kommission & Arbeitskreis 3D-Stadtmodelle. 2022.

[201] R. Jack, D. Loveday, D. Allinson and K. Lomas. „First evidence for the reliability of building co-heating tests“. In: *Building Research & Information* 46.4 (2018), pp. 383–401. DOI: 10.1080/09613218.2017.1299523.

[202] F. Alzetto, G. Pandraud, R. Fitton, I. Heusler and H. Sinnesbichler. „QUB: A fast dynamic method for in-situ measurement of the whole building heat loss“. In: *Energy and Buildings* 174 (2018), pp. 124–133. DOI: 10.1016/j.enbuild.2018.06.002.

[203] L. Belussi, L. Danza, I. Meroni and F. Salamone. „Energy performance assessment with empirical methods: application of energy signature“. In: *Opto-Electronics Review* 23.1 (2015). DOI: 10.1515/oere-2015-0008.

[204] F. P. Hollick, V. Gori and C. A. Elwell. „Thermal performance of occupied homes: A dynamic grey-box method accounting for solar gains“. In: *Energy and Buildings* 208 (2020), p. 109669. DOI: 10.1016/j.enbuild.2019.109669.

[205] J. Crawley, E. McKenna, V. Gori and T. Oreszczyn. „Creating Domestic Building Thermal Performance Ratings Using Smart Meter Data“. In: *Buildings and Cities* 1.1 (2020), pp. 1–13. DOI: 10.5334/bc.7.

[206] A. Erkoreka, E. Garcia, K. Martin, J. Teres-Zubiaga and L. Del Portillo. „In-use office building energy characterization through basic monitoring and modelling“. In: *Energy and Buildings* 119 (2016), pp. 256–266. DOI: 10.1016/j.enbuild.2016.03.030.

[207] X. X. Zhu and R. Bamler. „TOMOGRAPHIC SAR INVERSION FROM MIXED REPEAT- AND SINGLE-PASS DATA STACKS – THE TERRASAR-X/TANDEM-X CASE“. In: *ISPRS - International Archives of the Photogrammetry, Remote Sensing and Spatial Information Sciences* XXXIX-B7 (2012), pp. 97–102. DOI: 10.5194/isprsarchives-XXXIX-B7-97-2012.

[208] U. Heiden, K. Segl, S. Roessner and H. Kaufmann. „Determination of robust spectral features for identification of urban surface materials in hyperspectral remote sensing data“. In: *Remote Sensing of Environment* 111.4 (2007), pp. 537–552. DOI: 10.1016/j.rse.2007.04.008.

[209] B. Kölsch. „Investigation of an Improved Acoustical Method for Determining Airtightness of Building Envelopes“. Dissertation. Aachen, Germany: RWTH Aachen, 2022. DOI: 10.18154/RWTH-2022-05352.

[210] C. J. Tucker and P. J. Sellers. „Satellite remote sensing of primary production“. In: *International Journal of Remote Sensing* 7.11 (1986), pp. 1395–1416. DOI: 10.1080/01431168608948944.

[211] M. Eineder et al. „Globale Kartierung und lokale Deformationsmessungen mit den Satelliten TerraSAR-X und Tandem-X“. In: *Zeitschrift für Geodäsie, Geoinformation und Landmanagement (zfv)* 1 (2013), pp. 75–84.

[212] X. X. Zhu, S. Montazeri, C. Gisinger, R. F. Hanssen and R. Bamler. „Geodetic SAR Tomography“. In: *IEEE Transactions on Geoscience and Remote Sensing* 54.1 (2016), pp. 18–35. DOI: 10.1109/TGRS.2015.2448686.

[213] U. Balss et al. „Precise Measurements on the Absolute Localization Accuracy of TerraSAR-X on the Base of Far-Distributed Test Sites“. In: *EUSAR 2014; 10th European Conference on Synthetic Aperture Radar*. Berlin and Offenbach, Germany: VDE Verlag, 2014, pp. 993–996.

[214] S. Montazeri, X. X. Zhu, M. Eineder and R. Bamler. „Three-Dimensional Deformation Monitoring of Urban Infrastructure by Tomographic SAR Using Multitrack TerraSAR-X Data Stacks“. In: *IEEE Transactions on Geoscience and Remote Sensing* 54.12 (2016), pp. 6868–6878. DOI: 10.1109/TGRS.2016.2585741.

[215] A. Haas, M. Peichl and S. Dill. „Characterization of building structures with SAR“. In: *EUSAR 2018; 12th European Conference on Synthetic Aperture Radar*. Berlin and Offenbach, Germany: VDE Verlag, 2018, pp. 967–970.

[216] A. Haas, M. Peichl and S. Dill. „Layer determination of building structures with SAR in near field environment“. In: *16th European Radar Conference (EuRAD)*. IEEE, 2019, pp. 209–212.

[217] T. Log and S. E. Gustafsson. „Transient plane source (TPS) technique for measuring thermal transport properties of building materials“. In: *Fire and Materials* 19.1 (1995), pp. 43–49. DOI: 10.1002/fam.810190107.

[218] A. M. Nicolson and G. F. Ross. „Measurement of the Intrinsic Properties of Materials by Time-Domain Techniques“. In: *IEEE Transactions on Instrumentation and Measurement* 19.4 (1970), pp. 377–382. DOI: 10.1109/TIM.1970.4313932.

[219] N. Alam et al. „TOWARDS AUTOMATIC VALIDATION AND HEALING OF CITYGML MODELS FOR GEOMETRIC AND SEMANTIC CONSISTENCY“. In: *ISPRS Annals of Photogrammetry, Remote Sensing and Spatial Information Sciences* II-2/W1 (2013), pp. 1–6. DOI: 10.5194/isprsannals-II-2-W1-1-2013.

[220] S. Christian. „Analysis of Contrast Enhancement Methods for Infrared Images“. Master's thesis. San Luis Obispo, CA, USA: California Polytechnic State University, 2011. DOI: 10.15368/theses.2011.214.

[221] Deutscher Wetterdienst. *DWD OpenData*. URL: https://opendata.dwd.de/climate_environment/CDC/ (visited on 19th Feb. 2021).

[222] D. Kubistin et al. *ICOS ATC CO2 Release, Lindenberg (40.0 m), 2015-10-08-2019-04-30*. 2019. URL: https://hdl.handle.net/11676/cPQQvISFflqinV6lZ7aCaxMW.

[223] J. A. Sobrino et al. „Emissivity mapping over urban areas using a classification-based approach: Application to the Dual-use European Security IR Experiment (DESIREX)“. In: *International Journal of Applied Earth Observation and Geoinformation* 18 (2012), pp. 141–147. DOI: 10.1016/j.jag.2012.01.022.

[224] Apple. *Maps*. 2021. URL: https://www.apple.com/maps/ (visited on 22nd Feb. 2021).

[225] DIN 5034-4:1994-09. *Tageslicht in Innenräumen: Vereinfachte Bestimmung von Mindestfenstergrößen für Wohnräume*. Technical standard. Deutsches Institut für Normung, 1994.

[226] P. Groesdonk. *GitHub: ibpsa/modelica-ibpsa: Issue #1744 Option for non-constant TGround in equivalent air temperature (VDI 6007)*. 2023. URL: https://github.com/ibpsa/modelica-ibpsa/issues/1744 (visited on 1st Feb. 2024).

[227] National Renewable Energy Laboratory. *Weather Data: EnergyPlus*. URL: https://energyplus.net/weather (visited on 8th Apr. 2021).

[228] ASHRAE 140:2007-. *Standard Method of Test for the Evaluation of Building Energy Analysis Computer Programs*. Technical standard. American Society of Heating, Refrigerating and Air-Conditioning Engineers, 2007.

[229] Bundestag. „Gebäudeenergiegesetz“. In: *BGBl. I (Bundesgesetzblatt Teil I)* 37 (2020), p. 1728.

[230] Bundesministerium für Wirtschaft und Energie and Bundesministerium des Innern, für Bau und Heimat. *Bekanntmachung der Regeln zur Datenaufnahme und Datenverwendung im Wohngebäudebestand*. 2020.

[231] S. Cozza, J. Chambers, A. Brambilla and M. K. Patel. „In search of optimal consumption: A review of causes and solutions to the Energy Performance Gap in residential buildings“. In: *Energy and Buildings* 249 (2021), p. 111253. DOI: 10.1016/j.enbuild.2021.111253.

[232] S. Burhenne. „Monte Carlo Based Uncertainty and Monte Carlo Based Uncertainty and Sensitivity Analysis for Building Performance Simulation“. Dissertation. Karlsruhe, Germany: Karlsruher Institut für Technologie, 2013.

[233] K. Menberg, Y. Heo and R. Choudhary. „Sensitivity analysis methods for building energy models: Comparing computational costs and extractable information“. In: *Energy and Buildings* 133 (2016), pp. 433–445. DOI: 10.1016/j.enbuild.2016.10.005.

[234] J. Herman and W. Usher. „SALib: An open-source Python library for Sensitivity Analysis“. In: *The Journal of Open Source Software* 2.9 (2017), p. 97. DOI: 10.21105/joss.00097.

[235] T. Iwanaga, W. Usher and J. Herman. „Toward SALib 2.0: Advancing the accessibility and interpretability of global sensitivity analyses“. In: *Socio-Environmental Systems Modelling* 4 (2022), p. 18155. DOI: 10.18174/sesmo.18155.

[236] COST Telecom Secretariat. *Digital mobile radio towards future generation systems: COST Action 231 final report*. Luxembourg, Luxembourg: European Commission, Directorate-General Telecommunications, Information Society, Information Market, and Exploitation of Research, 1999.

[237] JCGM 100:2008-09. *Evaluation of measurement data — Guide to the expression of uncertainty in measurement: GUM 1995 with minor corrections*. Guideline. Joint Committee for Guides in Metrology, 2008.

[238] S. Roessner et al. „Potential of Hyperspectral Remote Sensing for Analyzing the Urban Environment“. In: *Urban Remote Sensing*. Ed. by X. Yang. Chichester, United Kingdom: Wiley-Blackwell, 2011, pp. 49–61. DOI: 10.1002/9780470979563.ch4.

[239] L. Blanco, M. Aditya, B. Schiricke and B. Hoffschmidt. „Classification of building properties from the German census data for energy analyses purposes“. In: *Proceedings of Building Simulation 2023: 18th Conference of IBPSA*. Ed. by Y. Pan and D. Yan. IBPSA, 2023, pp. 925–932. DOI: 10.26868/25222708.2023.1266.

[240] M. Peichl et al. „Ermittlung eines Wärmedurchgangs von Gebäuden: Deutsches Patent“. DE 10 2020 122 132 B4. 2023.

[241] A. Saltelli et al. *Global Sensitivity Analysis. The Primer*. Chichester, United Kingdom: Wiley, 2007. DOI: 10.1002/9780470725184.

[242] S. Burhenne, D. Jacob and G. P. Henze. „Sampling Based on Sobol' Sequences for Monte Carlo Techniques Applied to Building Simulations“. In: *Proceedings of Building Simulation 2011: 12th Conference of IBPSA*. IBPSA, 2011, pp. 1816–1823. DOI: 10.26868/25222708.2011.1578.

A. Appendix

A.1. Measured Sample Material Properties

Table A.1 contains detailed data for the results presented in Section 5.1.

Table A.1.: *Average measured material property values for each sample (density ρ in $\mathrm{kg\,m^{-3}}$, real part ε_r' and imaginary part ε_r'' of the relative permittivity without unit, thermal conductivity λ in $\mathrm{W\,m^{-1}\,K^{-1}}$, and volumetric specific heat s in $\mathrm{MJ\,m^{-3}}$), sorted by material and density.*

No.	Material	ρ	ε_r'	ε_r''	λ	s
1	BCB red	1520	2.94	0.026	0.55	1.22
2	BCB red	1565	3.17	0.052	0.64	1.24
3	BCB red	1587	3.20	0.041	0.83	1.17
4	BCB red	1594	3.14	0.041	0.69	1.16
5	BCB red	1595	3.48	0.190	0.62	1.31
6	BCB red	1597	3.39	0.098	0.75	1.15
7	BCB red	1601	3.09	0.034	0.58	1.15
8	BCB red	1628	3.05	0.035	0.65	1.31
9	BCB red	1636	3.50	0.067	0.71	1.28
10	BCB red	1744	3.48	0.040	0.77	1.23
11	BCB red	1744	3.18	0.036	0.70	1.33
12	BCB red	1745	3.55	0.054	0.86	1.27
13	BCB red	1767	3.65	0.069	0.91	1.20

No.	Material	ρ	ε_r'	ε_r''	λ	s
14	BCB red	1781	3.33	0.046	0.81	1.27
15	BCB red	1856	3.67	0.041	1.01	1.31
16	BCB red	1869	3.53	0.050	0.95	1.53
17	BCB red	1920	3.65	0.043	0.98	1.38
18	BCB red	1951	4.00	0.066	1.20	1.46
19	BCB red	1963	3.57	0.040	1.07	1.51
20	BCB red	1969	4.31	0.082	0.95	1.37
21	BCB red	1969	3.89	0.053	1.20	1.55
22	BCB red	1980	3.74	0.048	1.10	1.45
23	BCB red	1991	4.09	0.064	1.04	1.39
24	BCB red	2001	4.08	0.058	0.90	1.47
25	BCB red	2002	4.10	0.063	1.21	1.46
26	BCB red	2022	4.10	0.040	1.01	1.35
27	BCB red	2030	3.98	0.047	1.12	1.48
28	BCB red	2057	3.99	0.053	1.12	1.50
29	BCB red	2065	4.16	0.068	1.02	1.43
30	BCB red	2073	4.22	0.079	1.01	1.49
31	BCB red	2116	4.35	0.078	1.13	1.55
32	BCB red	2162	4.24	0.064	1.12	1.55
33	BCB yellow	1440	2.95	0.046	0.60	1.06
34	BCB yellow	1702	3.68	0.110	0.79	1.25
35	BCB yellow	1759	3.74	0.072	0.86	1.09
36	BCB yellow	1845	3.93	0.042	1.05	1.26
37	BCB scorched	1374	2.89	0.036	0.61	1.10
38	BCB scorched	1483	2.72	0.045	0.68	0.98
39	BCB scorched	1783	3.65	0.062	0.97	1.34
40	BCB scorched	2103	4.72	0.176	1.12	1.38
41	CSB	1856	3.82	0.144	1.27	1.41
42	CSB	1871	4.12	0.177	1.38	1.49

No.	Material	ρ	ε_r'	ε_r''	λ	s
43	CSB	1903	3.75	0.123	1.37	1.35
44	CSB	1974	4.70	0.257	1.52	1.65
45	CSB	1981	3.73	0.082	1.59	1.53
46	CSB	2006	3.80	0.097	1.64	1.09
47	CSB	2034	3.99	0.113	1.69	1.21
48	AAC	556	1.92	0.073	0.15	0.50
49	AAC	596	2.00	0.082	0.18	0.57
50	LAC open	706	2.09	0.053	0.18	0.65
51	LAC open	707	2.12	0.051	0.16	0.54
52	LAC open	748	2.11	0.045	0.17	0.52
53	LAC open	831	2.33	0.077	0.24	0.97
54	LAC open	905	2.39	0.079	0.22	0.65
55	LAC closed	1340	4.01	0.144	0.30	1.15
56	LAC closed	1810	5.43	0.187	0.46	1.47

A.2. Monthly Contributions to Heat Demand

The following figures show the monthly contributions to the heat demand of the case study building in model variation 6, complementing the analysis of the annual results in Section 5.3.2.

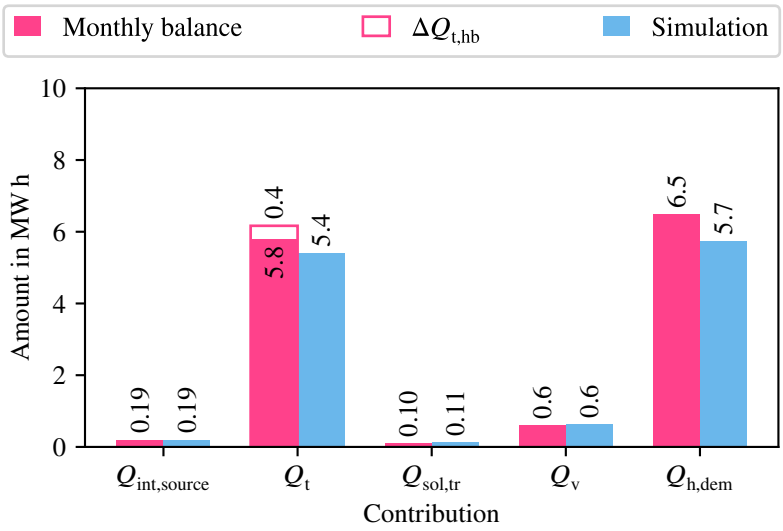

(a) *Without retrofit.*

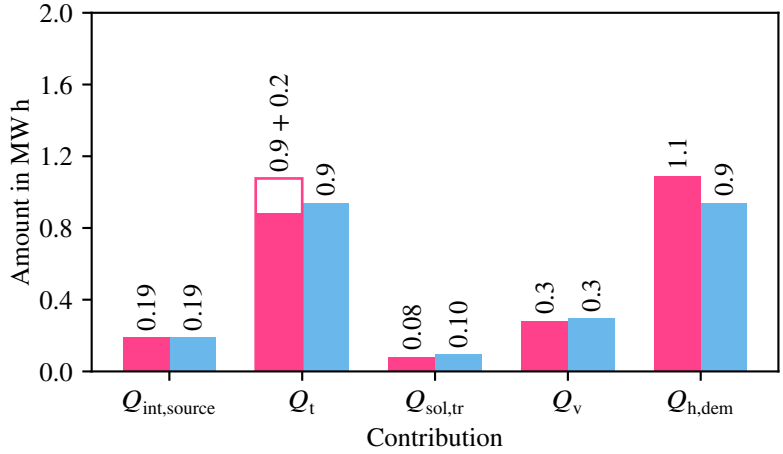

(b) *Advanced retrofit scenario.*

Figure A.1.: *Contributions to January heat demand calculated by monthly energy balance (DIN V 18599-2 [95]) and simulation.*

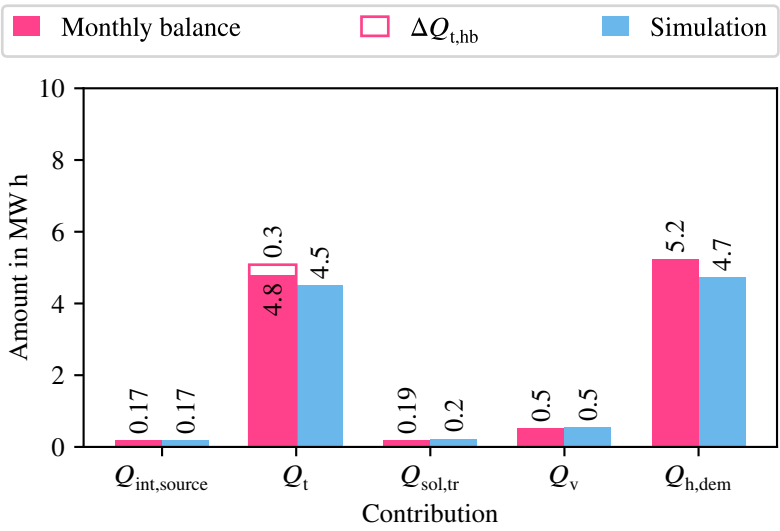

(a) *Without retrofit.*

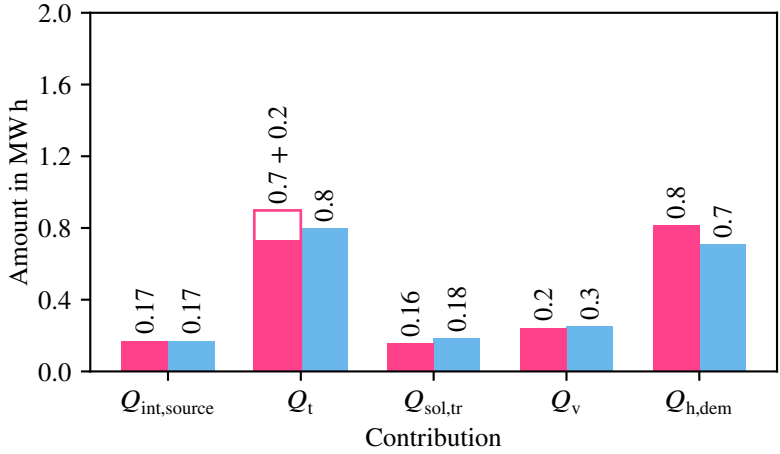

(b) *Advanced retrofit scenario.*

Figure A.2.: *Contributions to February heat demand calculated by monthly energy balance (DIN V 18599-2 [95]) and simulation.*

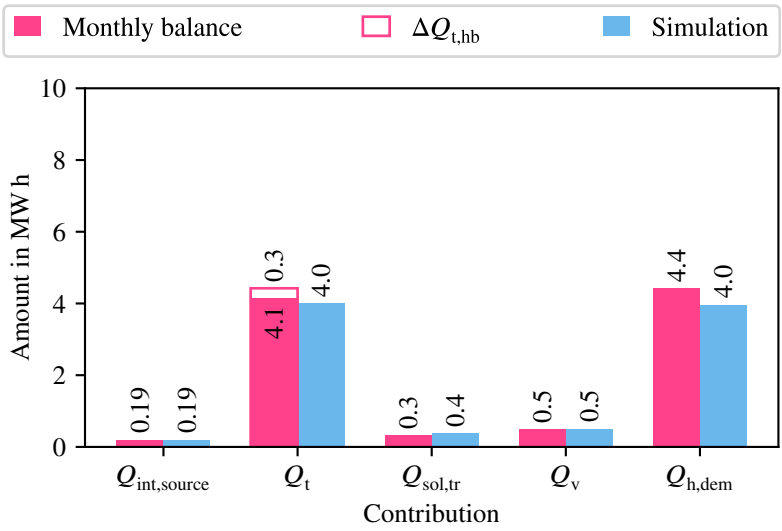

(a) *Without retrofit.*

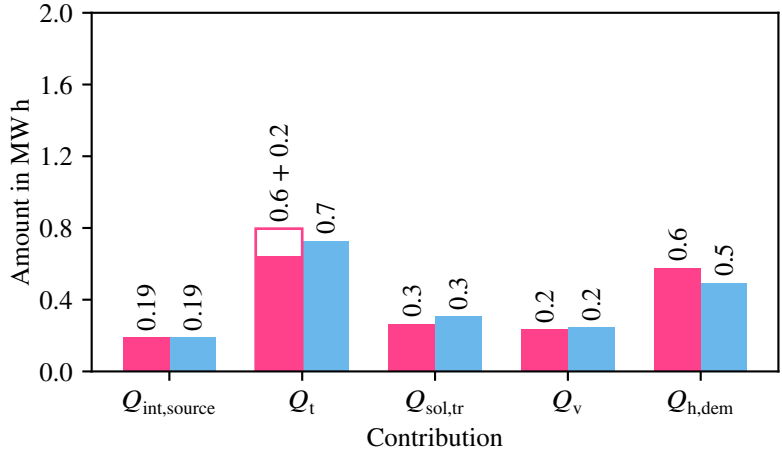

(b) *Advanced retrofit scenario.*

Figure A.3.: *Contributions to March heat demand calculated by monthly energy balance (DIN V 18599-2 [95]) and simulation.*

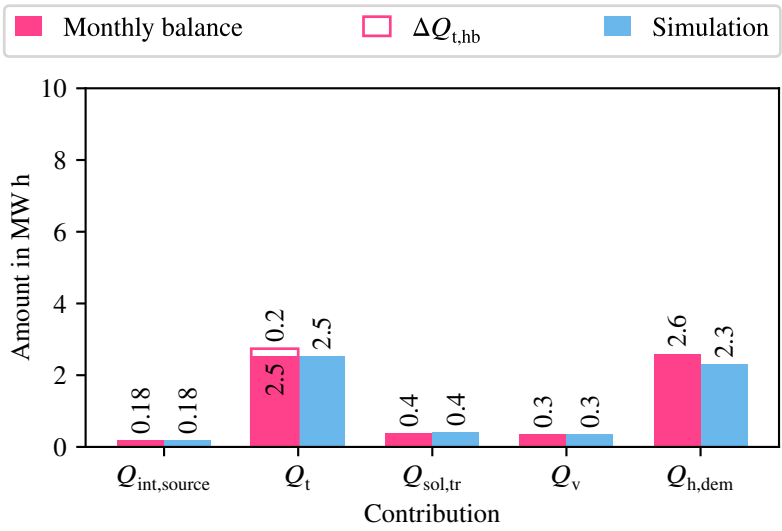

(a) *Without retrofit.*

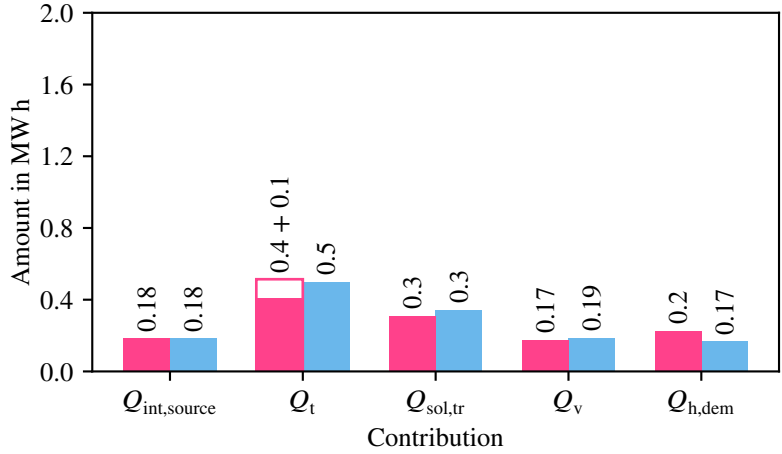

(b) *Advanced retrofit scenario.*

Figure A.4.: *Contributions to April heat demand calculated by monthly energy balance (DIN V 18599-2 [95]) and simulation.*

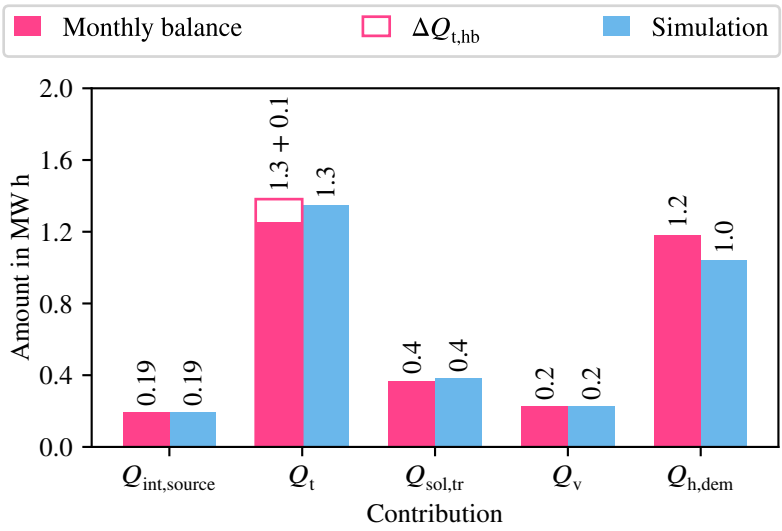

(a) *Without retrofit.*

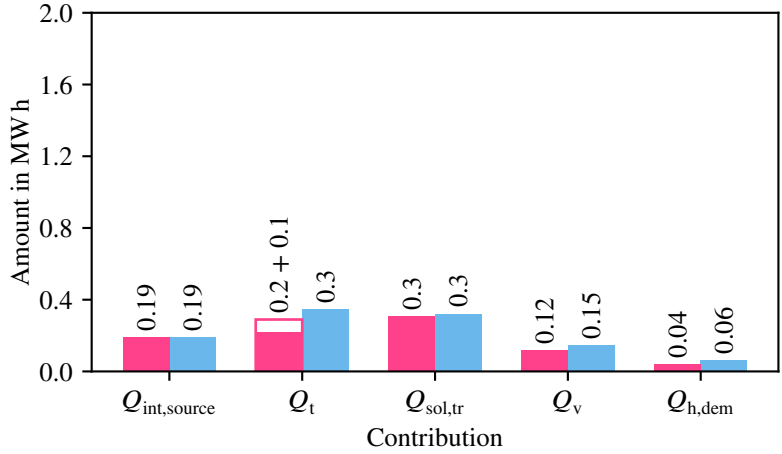

(b) *Advanced retrofit scenario.*

Figure A.5.: *Contributions to May heat demand calculated by monthly energy balance (DIN V 18599-2 [95]) and simulation.*

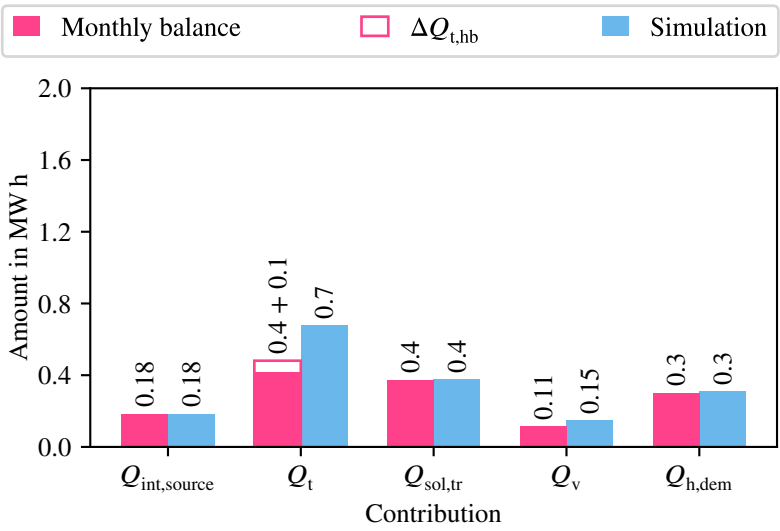

(a) *Without retrofit.*

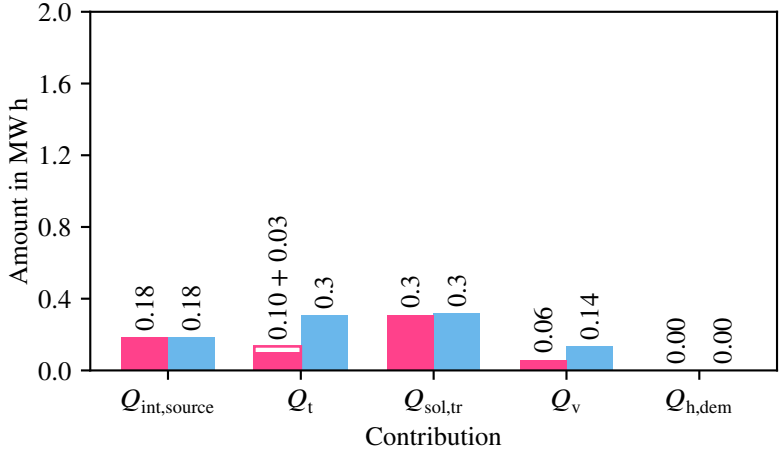

(b) *Advanced retrofit scenario.*

Figure A.6.: *Contributions to June heat demand calculated by monthly energy balance (DIN V 18599-2 [95]) and simulation.*

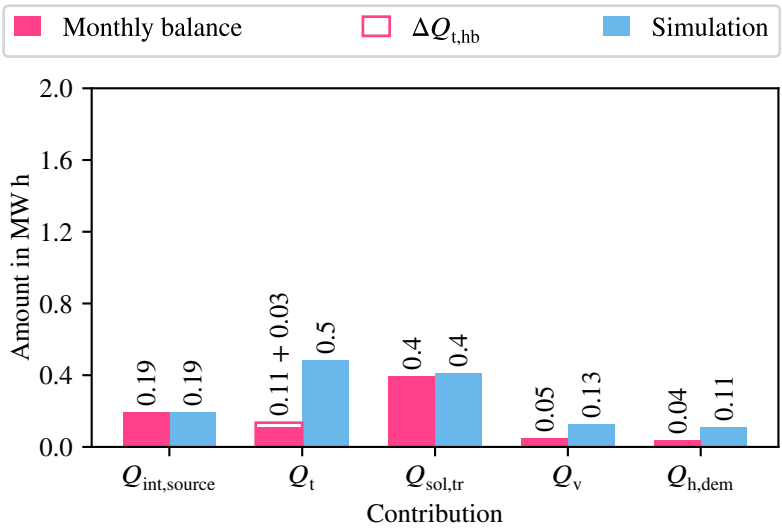

(a) *Without retrofit.*

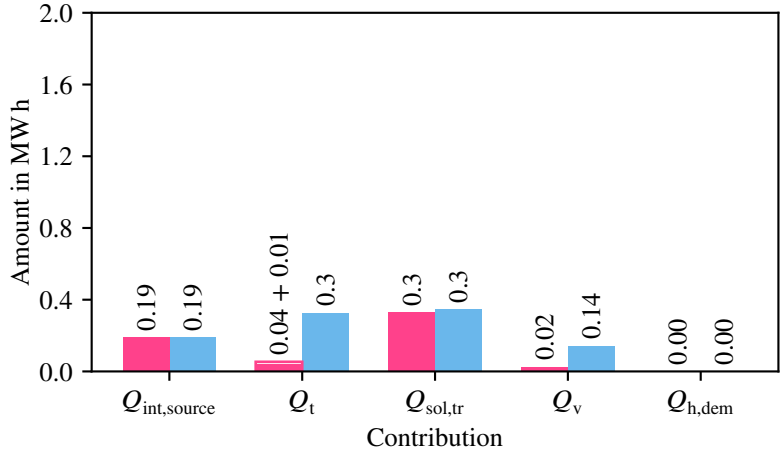

(b) *Advanced retrofit scenario.*

Figure A.7.: *Contributions to July heat demand calculated by monthly energy balance (DIN V 18599-2 [95]) and simulation.*

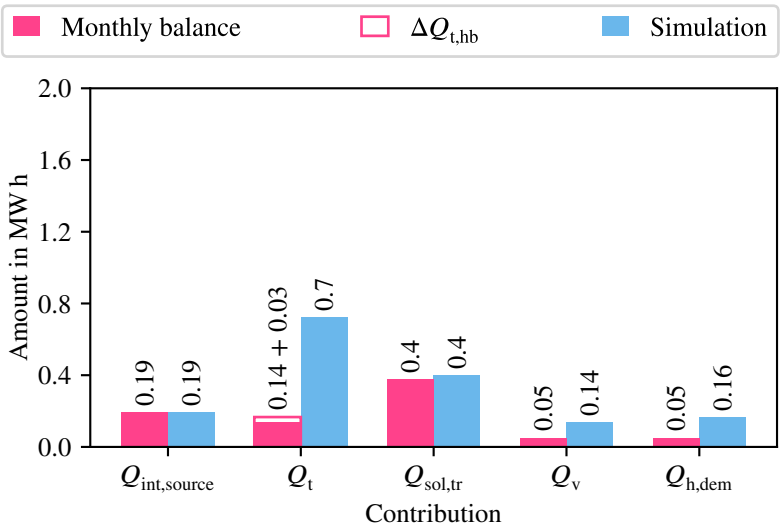

(a) *Without retrofit.*

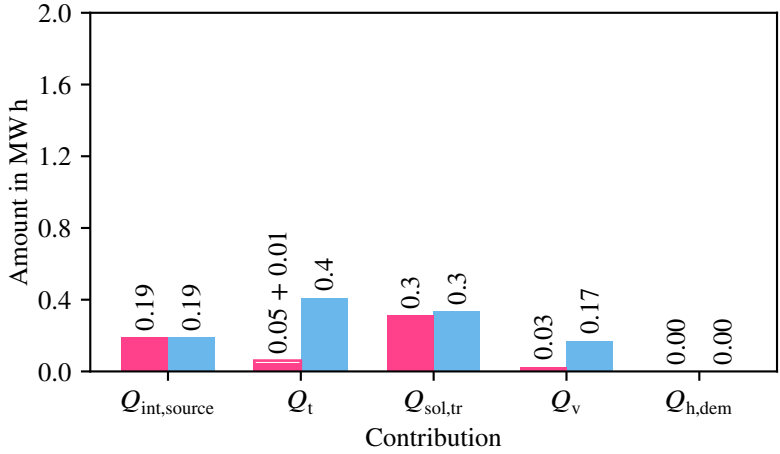

(b) *Advanced retrofit scenario.*

Figure A.8.: *Contributions to August heat demand calculated by monthly energy balance (DIN V 18599-2 [95]) and simulation.*

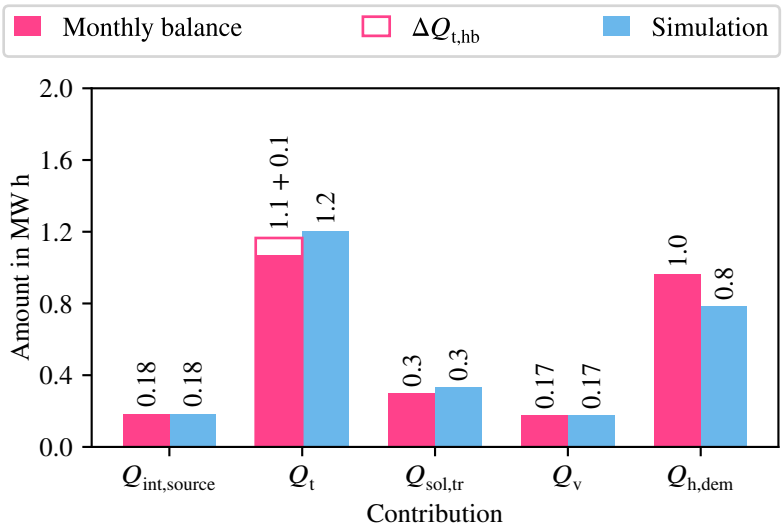

(a) *Without retrofit.*

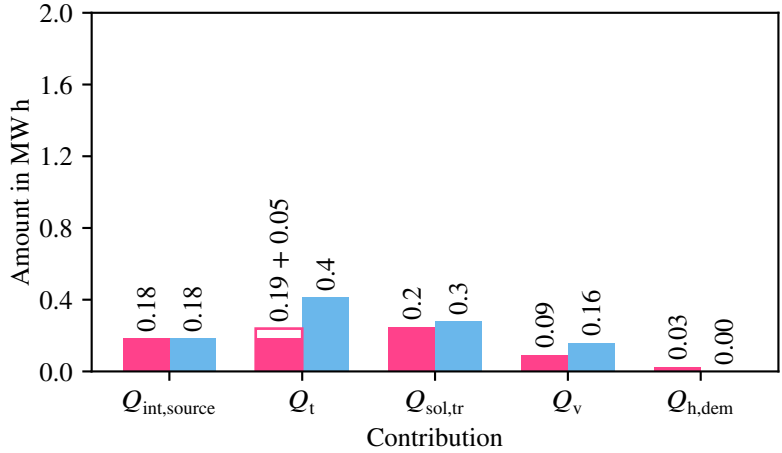

(b) *Advanced retrofit scenario.*

Figure A.9.: *Contributions to September heat demand calculated by monthly energy balance (DIN V 18599-2 [95]) and simulation.*

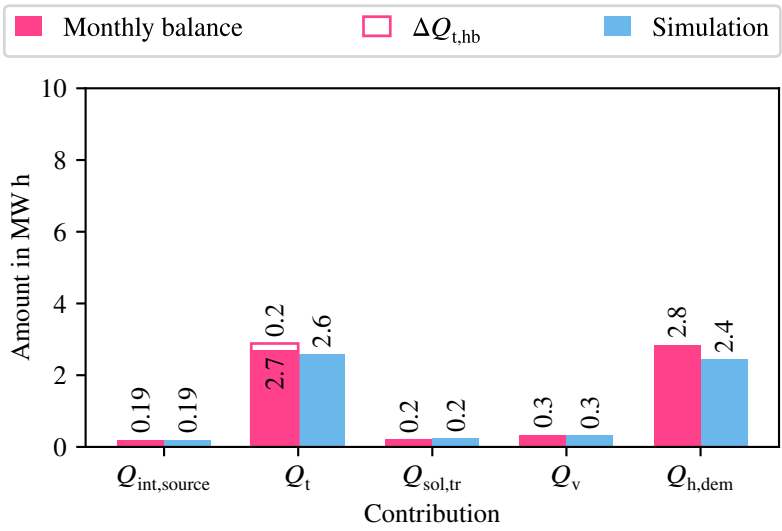

(a) *Without retrofit.*

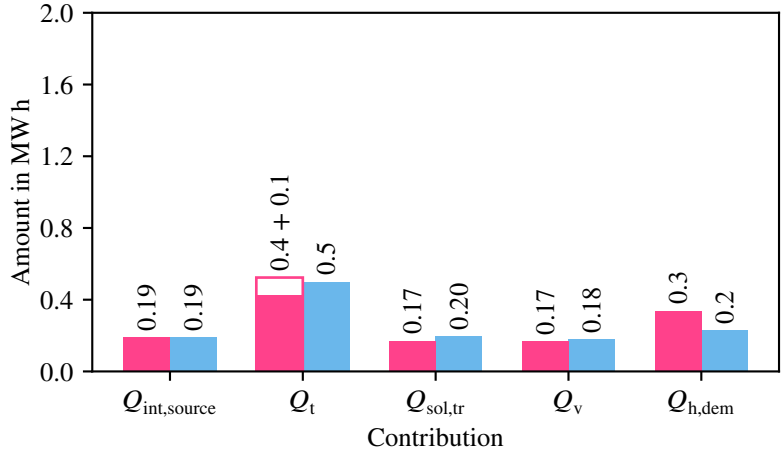

(b) *Advanced retrofit scenario.*

Figure A.10.: *Contributions to October heat demand calculated by monthly energy balance (DIN V 18599-2 [95]) and simulation.*

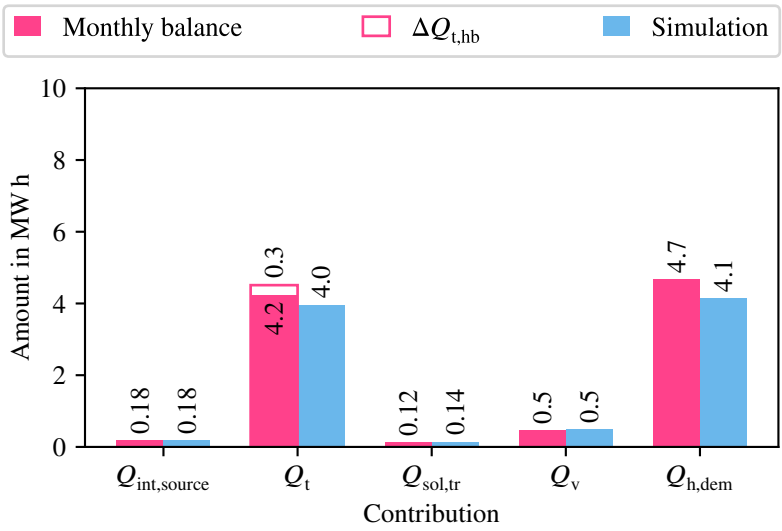

(a) *Without retrofit.*

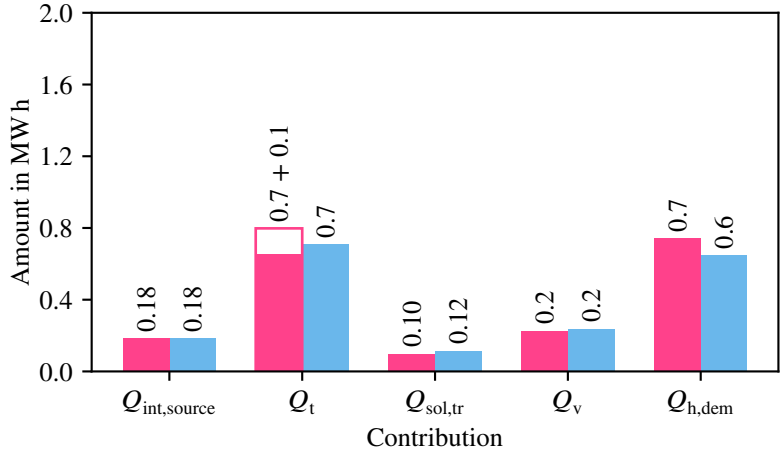

(b) *Advanced retrofit scenario.*

Figure A.11.: *Contributions to November heat demand calculated by monthly energy balance (DIN V 18599-2 [95]) and simulation.*

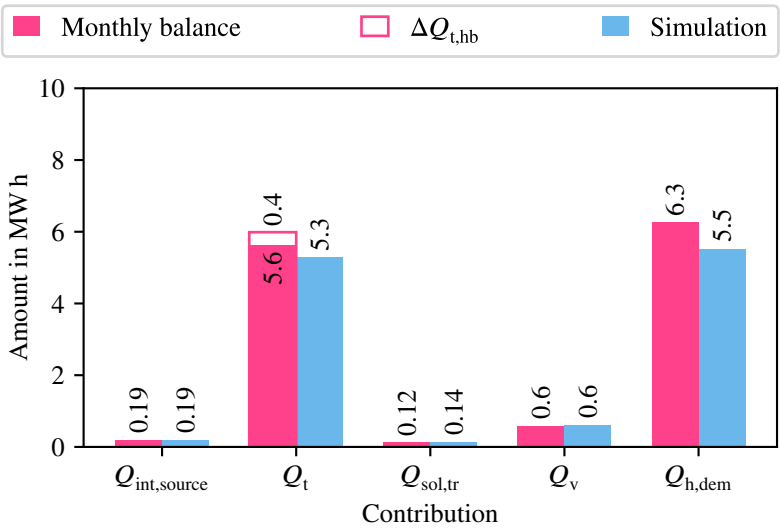

(a) *Without retrofit.*

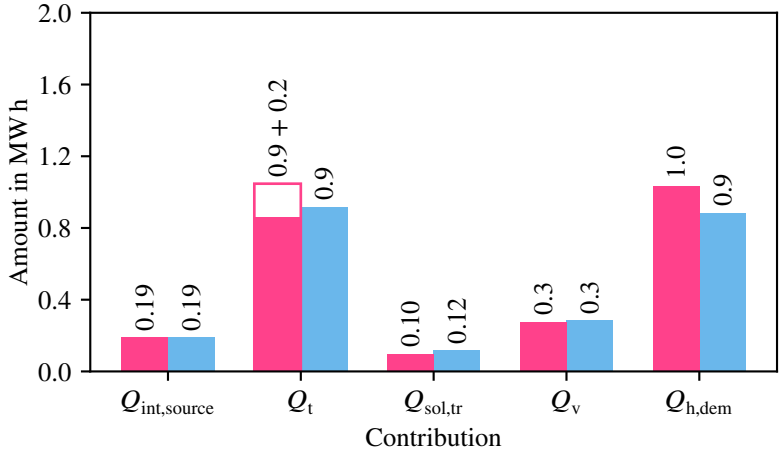

(b) *Advanced retrofit scenario.*

Figure A.12.: *Contributions to December heat demand calculated by monthly energy balance (DIN V 18599-2 [95]) and simulation.*

A.3. Sensitivity Analysis

A.3.1. Principles

This section serves to give a more detailed explanation of the method applied for sensitivity analysis, as presented in Section 4.4.2. After an elaboration of the background regarding what sensitivity analysis is applied for and what its results mean, the calculation procedure for the variance-based method with sampling based on Sobol' sequences is explained.

Background

Sensitivity analysis is a popular method to assess the influence of input parameters on the result of a calculation procedures. Building energy modelling is only one example of its potential applications that appear in several fields as soon as the interaction of different input parameters or their influence on an algorithm is not accessible anymore due to the complexity or magnitude of the mathematical operations [235].

Sensitivity indices of different order are the main outcome of a sensitivity analysis. Summarising the explanation given by Saltelli et al. [241, pp. 20ff.] and assuming a model function

$$Y = f\left(X_1, X_2, ..., X_k\right), \tag{A.1}$$

with output Y and uncertain inputs X_i, the first-order sensitivity index of X_i on Y is calculated as

$$S_i = \frac{V_{X_i}\left(E_{\boldsymbol{X}_{\sim i}}\left(Y|X_i\right)\right)}{V(Y)}. \tag{A.2}$$

In Equation (A.2), $V_{X_i}\left(E_{\boldsymbol{X}_{\sim i}}\left(Y|X_i\right)\right)$ is the conditional variance, i.e. the variance caused by varying solely X_i. It is related to the variance of the function if X_i

is fixed and the vector of all other parameters $\boldsymbol{X}_{\sim i}$ is variable $V_{\boldsymbol{X}_{\sim i}}\left(Y|X_i\right)$ if that value is averaged over all possible values of X_i to $E_{X_i}\left(V_{\boldsymbol{X}_{\sim i}}\left(Y|X_i\right)\right)$, because both values sum up to the total variance of the function

$$V(Y) = E_{X_i}\left(V_{\boldsymbol{X}_{\sim i}}\left(Y|X_i\right)\right) + V_{X_i}\left(E_{\boldsymbol{X}_{\sim i}}\left(Y|X_i\right)\right). \tag{A.3}$$

As a matter of fact, number values of S_i are between 0 and 1. The more influential X_i is on the model function, the higher its first-order sensitivity index. However, their sum does not always add up to 1 due to higher-order effects that appear if a parameter is influential on the model result via one or more other parameters.

These effects are covered by total effect terms to be calculated as

$$S_{\mathrm{T}i} = 1 - \frac{V\left(E\left(Y|\boldsymbol{X}_{\sim i}\right)\right)}{V(Y)} = \frac{E\left(V\left(Y|\boldsymbol{X}_{\sim i}\right)\right)}{V(Y)}. \tag{A.4}$$

According to Saltelli et al. [241, p. 33], "a good, synthetic, though nonexhaustive characterization of the sensitivity pattern for a model with k factors is given by the total set of first-order terms plus the total effects.". The sum of total effects for all parameters will exceed 1 if higher-order effects are present because they are included in the total effects of all variables involved. In the case of models that are purely additive, i.e. no higher-order effects are present, both $\sum_i S_i = 1$ and $\sum_i S_{\mathrm{T}i} = 1$ [241, p. 166f.].

Variance-based Method with Sampling Based on Sobol' Sequences

The variance-base method to calculate first-order and total-effect indices used in this thesis is explained in detail by [241, pp. 164–167] and is "the best available today for computing indices based purely on model evaluations" according to them. In the following, the most important parts of their method are pointed out.

Given the number of samples N and the number of input parameters k, two matrices $\boldsymbol{A}$ and $\boldsymbol{B}$ with k columns and N rows each are created and filled with random numbers. Consequently, $N \cdot k \cdot 2$ numbers are needed for the task. This is where Sobol' sequences become relevant: They are suggested as the source of sequences of quasi-random numbers to fill the matrices. In order to keep the balance properties of the sequence, N needs to be a power of 2 [242].

In $\boldsymbol{A}$ and $\boldsymbol{B}$, the random numbers are replaced by the respective value within the probability distribution of the input parameter in the corresponding column. Matrices $\boldsymbol{C}_i$ are created for every parameter, where all columns are equal to $\boldsymbol{B}$, but the ith column is taken from $\boldsymbol{A}$. Model output vectors are calculated by evaluating the matrices row-wise, giving

$$\boldsymbol{y}_{\boldsymbol{A}} = f(\boldsymbol{A}), \qquad \boldsymbol{y}_{\boldsymbol{B}} = f(\boldsymbol{B}), \qquad \boldsymbol{y}_{\boldsymbol{C}_i} = f\left(\boldsymbol{C}_i\right). \tag{A.5}$$

For that step, $N + N$ function evaluations for matrices $\boldsymbol{A}$ and $\boldsymbol{B}$ plus $k \cdot N$ for the matrices $\boldsymbol{C}_i$ are needed, adding up to a total cost of $N \cdot (k + 2)$ evaluations that is also mentioned in Section 4.4.2.

The method suggested by Saltelli et al. and also implemented in SALib [234, 235] uses the outputs to calculate the first-order indices as

$$S_i = \frac{V\left(E\left(Y|X_i\right)\right)}{V(Y)} = \frac{\boldsymbol{y}_{\boldsymbol{A}} \cdot \boldsymbol{y}_{\boldsymbol{C}_i} - f_0^2}{\boldsymbol{y}_{\boldsymbol{A}} \cdot \boldsymbol{y}_{\boldsymbol{A}} - f_0^2} = \frac{(1/N) \cdot \sum_{j=1}^{N} \boldsymbol{y}_{\boldsymbol{A}}^{(j)} \cdot \boldsymbol{y}_{\boldsymbol{C}_i}^{(j)} - f_0^2}{(1/N) \cdot \sum_{j=1}^{N} \left(\boldsymbol{y}_{\boldsymbol{A}}^{(j)}\right)^2 - f_0^2} \tag{A.6}$$

where

$$f_0^2 = \left(\frac{1}{N} \sum_{j=1}^{N} \boldsymbol{y}_{\boldsymbol{A}}^{(j)}\right)^2 \tag{A.7}$$

is defined as the mean value of all function evaluations over $\boldsymbol{A}$ and $(\cdot)$ denotes a scalar product.

Total order indices are estimated as

$$\begin{aligned} S_{\mathrm{T}i} &= 1 - \frac{V\left(E\left(Y|\boldsymbol{X}_{\sim i}\right)\right)}{V(y)} = 1 - \frac{\boldsymbol{y_B} \cdot \boldsymbol{y_{C_i}} - f_0^2}{\boldsymbol{y_A} \cdot \boldsymbol{y_A} - f_0^2} \\ &= 1 - \frac{(1/N) \cdot \sum_{j=1}^{N} \boldsymbol{y}_{\boldsymbol{B}}^{(j)} \cdot \boldsymbol{y}_{\boldsymbol{C}_i}^{(j)} - f_0^2}{(1/N) \cdot \sum_{j=1}^{N} \left(\boldsymbol{y}_{\boldsymbol{A}}^{(j)}\right)^2 - f_0^2} \end{aligned} \tag{A.8}$$

in a similar manner. For a detailed derivation of these equations, the reader is referred to Saltelli et al. [241, pp. 166f.].

A.3.2. Result Convergence

The following figures show the convergence of all parameters investigated for assessing the model sensitivity in Section 5.4.

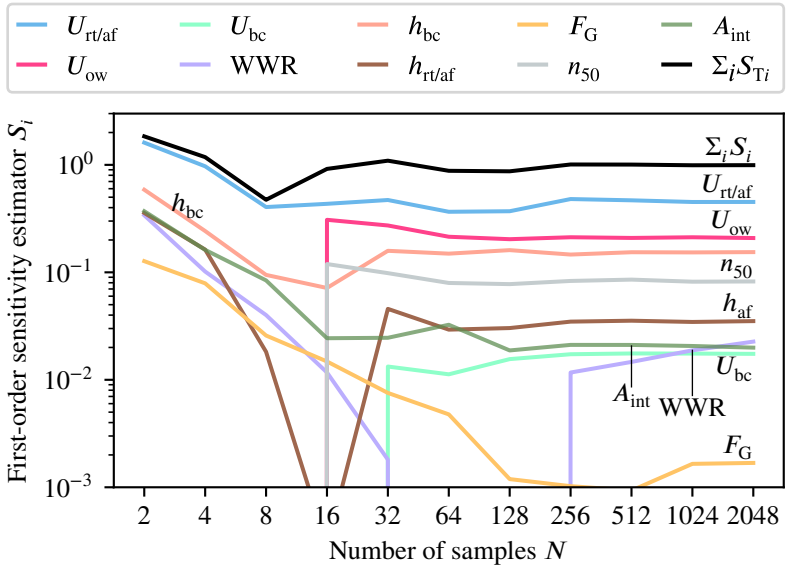

(a) *First-order sensitivity estimators.*

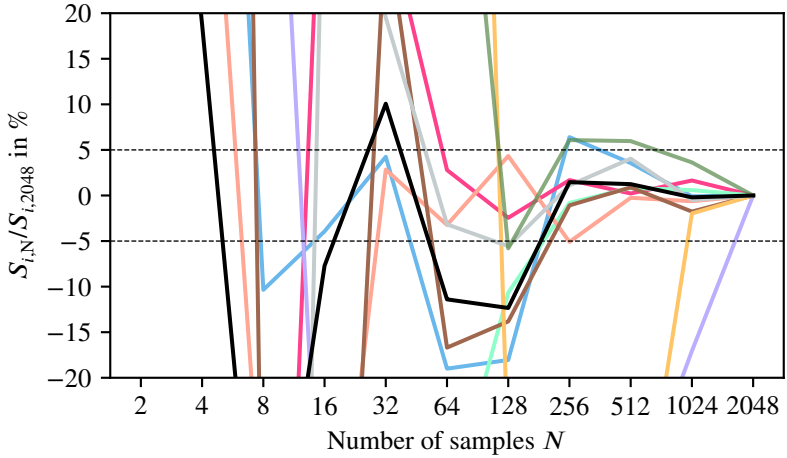

(b) *Deviation of first-order sensitivity estimators to the respective reference results.*

Figure A.13.: *Convergence of first-order sensitivity estimators regarding pre-retrofit heat demand.*

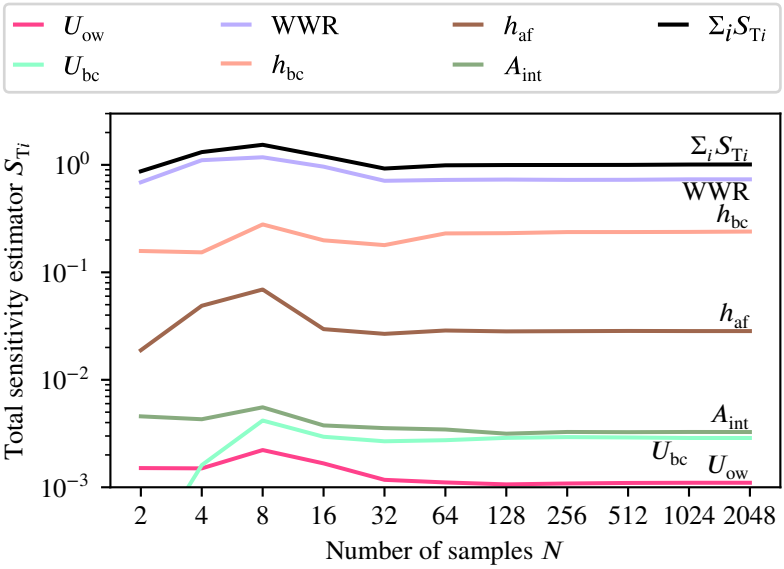

(a) *Total sensitivity estimators.*

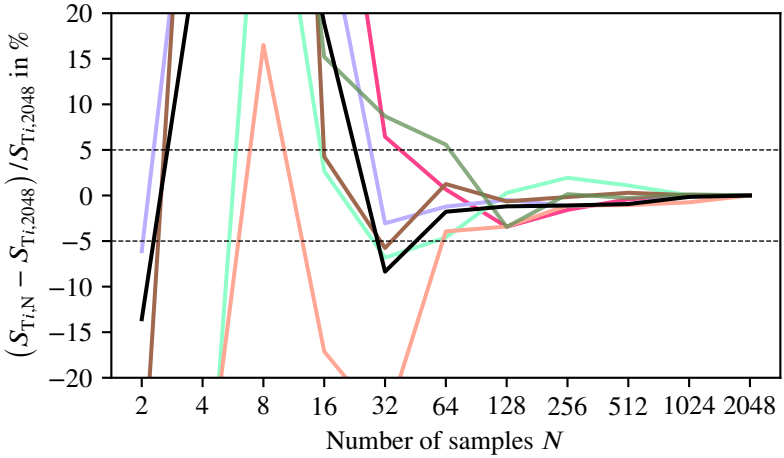

(b) *Deviation of total sensitivity estimators to the respective reference results.*

Figure A.14.: *Convergence of total sensitivity estimators regarding post-retrofit heat demand.*

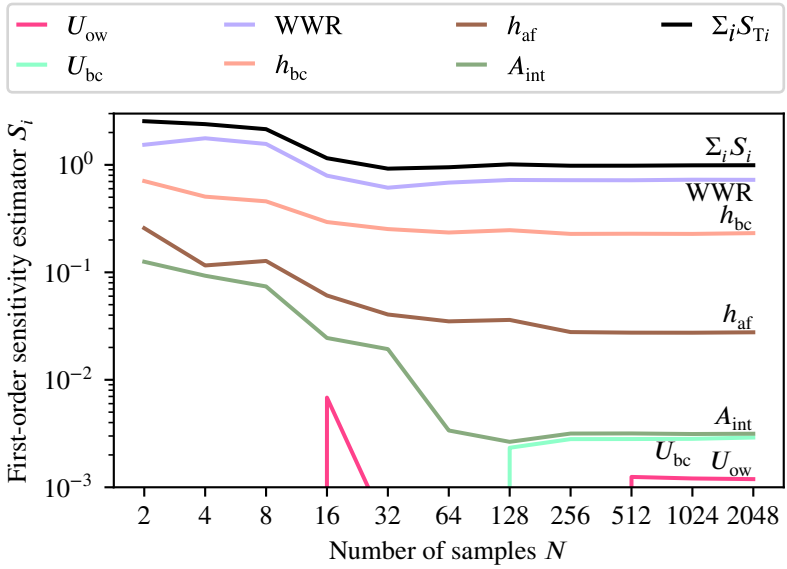

(a) *First-order sensitivity estimators.*

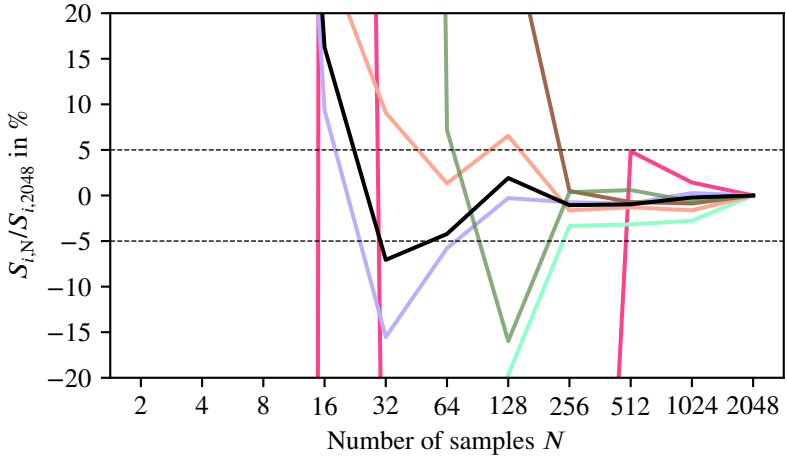

(b) *Deviation of first-order sensitivity estimators to the respective reference results.*

Figure A.15.: *Convergence of first-order sensitivity estimators regarding post-retrofit heat demand.*

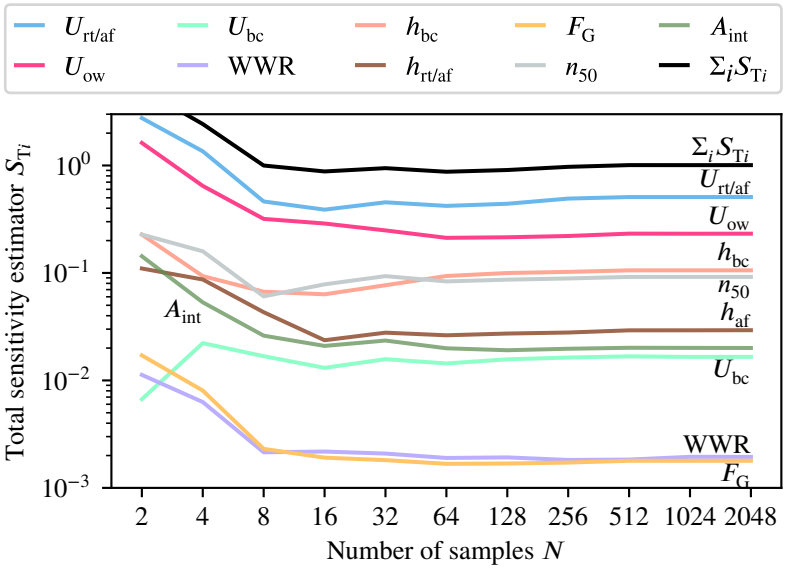

(a) *Total sensitivity estimators.*

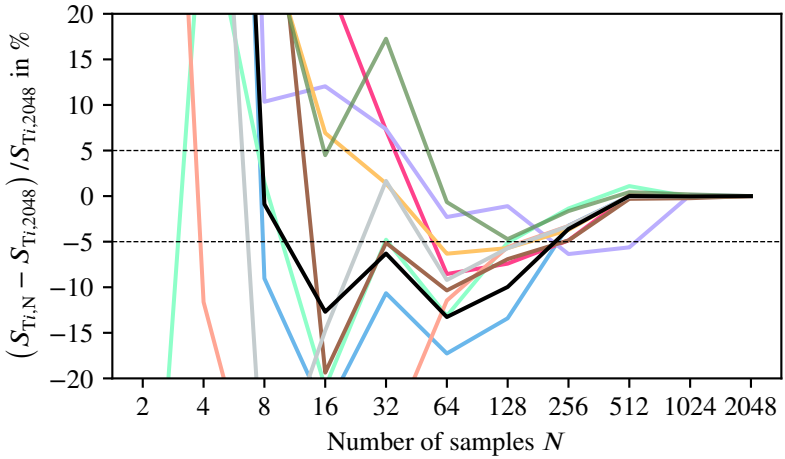

(b) *Deviation of total sensitivity estimators to the respective reference results.*

Figure A.16.: *Convergence of total sensitivity estimators regarding savings by retrofit.*

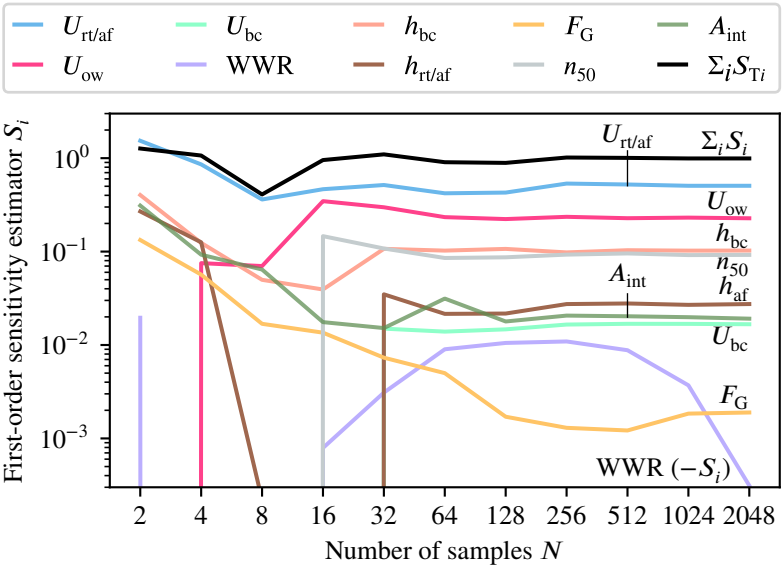

(a) *First-order sensitivity estimators (negative value displayed for S_{WWR}).*

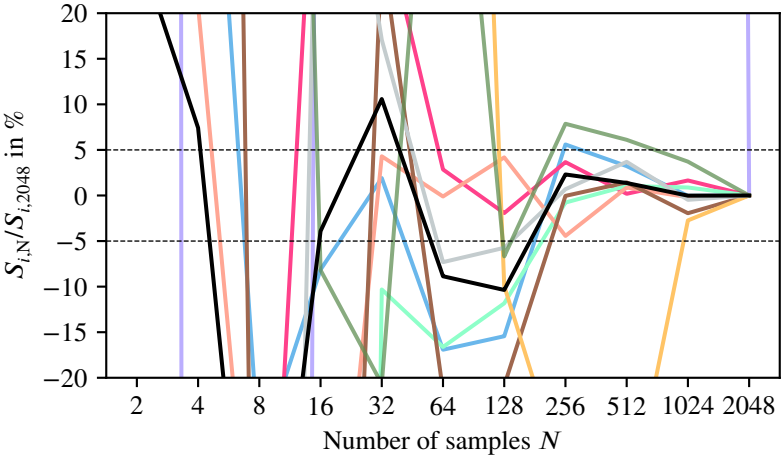

(b) *Deviation of first-order sensitivity estimators to the respective reference results.*

Figure A.17.: *Convergence of first-order sensitivity estimators regarding savings by retrofit.*

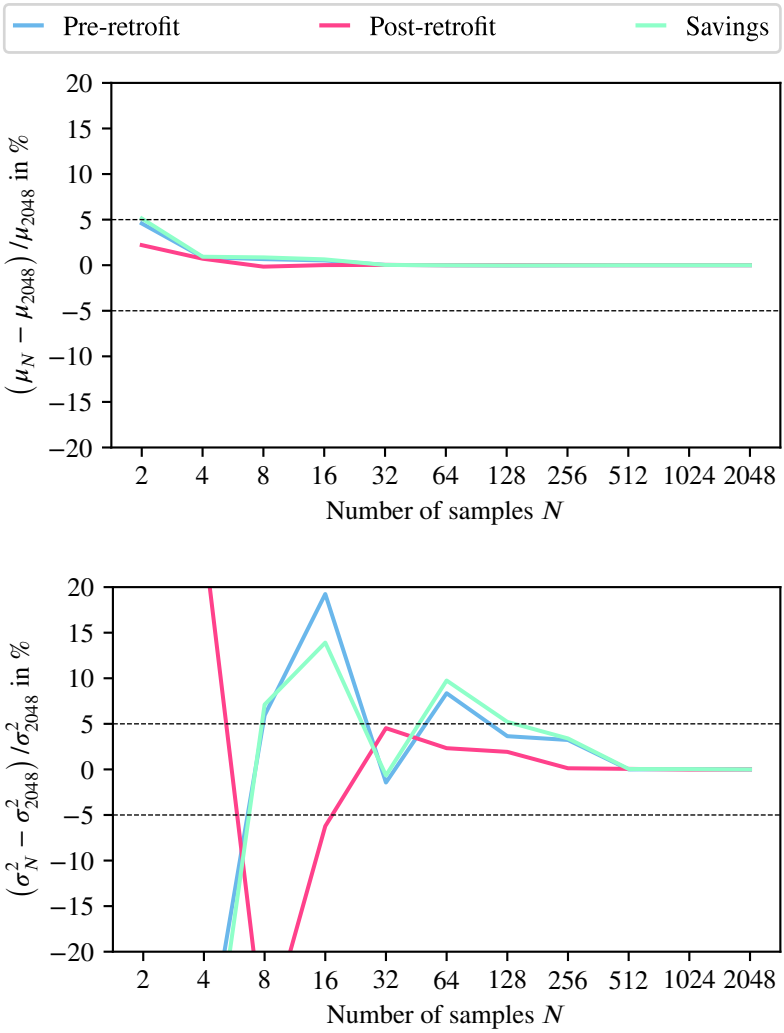

Figure A.18.: *Convergence of mean and variance of the three output quantities over the samples of the sensitivity analysis.*